Mineral Reaction and Deformation in Plagioclase-Olivine Composites: An Experimental Study

Inauguraldissertation

zur
Erlangung der Würde eines Doktors der Philosophie
vorgelegt der
Philosophisch-Naturwissenschaftlichen Fakultät
der Universität Basel

von

Almar A. de Ronde
aus Venhuizen (Niederlande)

Basel, 2004

Genehmigt von der Philosophisch-Naturwissenschaftlichen Fakultät auf Antrag von

Prof. Dr. Renée Heilbronner
(Fakultätsverantwortliche)

PD. Dr. Holger Stünitz
(Dissertationsleiter)

Prof. Dr. Jan Tullis
(Korreferentin)

Basel, den 21 September 2004

Prof. Dr. Hans-Jakob Wirz
Dekan der Philosophisch-
Naturwissenschaftlichen Fakultät

Table of Contents

Abstract

Deformation and metamorphism of rocks are fundamentally interrelated but the ways in which processes of reaction and deformation mutually influence each other are still poorly understood in natural rocks. The aim of this thesis is to investigate relationships between plastic deformation and mineral reactions, by means of rock deformation experiments. Within this broad aim, the thesis focuses on (1) the spatial distribution of deformation and reaction during ductile shear, (2) the effect of mineral reactions on the strength, deformation mechanisms and microstructures of dry rocks and (3) the effect of ductile shear deformation on kinetics and mechanisms of a dry net-transfer reaction.

To these ends, water-deficient plagioclase-olivine composites were studied after shear deformation and hydrostatic experiments inside and outside their chemical stability fields, using a Griggs apparatus. Experiments were performed on anorthite-forsterite (An_{92}-Fo_{93}) and labradorite-forsterite (An_{60}-Fo_{93}) composites at 900°C, confining pressures between 1000-1600 MPa and with constant shear strain rates of $\dot{\gamma} \sim 5\text{x}10^{-5}\text{s}^{-1}$. The hydrostatic and deformed samples were examined by backscattered scanning electron microscopy (BSEM) and transmission electron microscopy (TEM).

At all chosen confining pressures, stable labradorite-olivine composites are found to strain-harden during shear deformation, up to stresses close to the brittle-plastic transition ($\tau \sim$500-780 MPa). Pure olivine and labradorite samples are less strong ($\tau \sim$350 and 100 MPa, respectively) than the labradorite-olivine composites. The pure olivine sample displayed low temperature plasticity, accompanied by some dynamic recrystallisation. The hardening of the labradorite-olivine composites is probably due to the inhibition of grain boundary migration by inter-phase boundaries, which prevent recovery. The prevention of recovery results in labradorite and olivine grains with local high dislocation densities.

At all chosen confining pressures, concurrent plastic deformation and reaction of metastable anorthite-olivine composites results in a pronounced decrease in shear stress ($\tau \sim$150 MPa). The onset of weakening coincides with the formation of fine-grained polyphase reaction products (size ~0.25-1.0 µm). The onset of steady-state flow ($\gamma > 5$, $\tau \sim$200 MPa) is characterised by the coalescence of these products into interconnecting layers. The fine-grained reaction products deform by grain size sensitive creep.

Fabric analysis using the autocorrelation function shows a strong correlation on a sample scale between reaction progress and strain; large shear strain is locally associated with high reaction progress. On a grain scale the applied strain is localised and accommodated in the interconnecting layers of reaction products. Strain accommod-

ation in reaction product layers reduces the strain rate in the reacting anorthite and olivine grains, which, as a result, are able to undergo recovery by dislocation climb.

The reaction weakening mechanism in anorthite-olivine composites is grain size reduction by crystallisation of fine-grained polyphase reaction products, which deform by diffusion-accommodated grain boundary sliding. The reaction causes a change in deformation mechanism from grain size insensitive creep of the anorthite-olivine composite to grain size sensitive creep of reaction products. The measured reduction of shear stress at a constant strain rate confirms this change in the dominant deformation mechanism of the samples.

The growth rates of enstatite and pyroxene-spinel-garnet reaction rims observed around olivine and plagioclase indicate that reaction at hydrostatic and water-deficient conditions is controlled by the limited transport of chemical components. The amount of pressure overstepping in the experiments affects the reaction progress because the rate of nucleation increases exponentially with the Gibbs free energy of reaction (the amount of pressure overstepping for pressure-sensitive reactions). Nevertheless, the studied reactions display a delayed onset of nucleation of new phases (30 to ∼80 hrs), even at pressure overstepping of 700 to 900 MPa.

The plastic deformation of anorthite-olivine composites was found to enhance the studied mineral reactions at water-deficient conditions. This enhancement is shown by the increase of reaction progress as well as the increase of the nucleation and growth rates of reaction rims during deformation. The reaction between anorthite and olivine is enhanced by an increase in the nucleation rate of new phases. The increased nucleation rate may be due to high dislocation densities in the reactant grains that deform by low-temperature plasticity. The mechanical transport of reaction products by grain boundary sliding may change the local equilibrium conditions, which, in combination with slow diffusion and fast nucleation, results in the formation of metastable kyanite.

In summary, this experimental study shows that concurrent plastic deformation and reaction processes in plagioclase-olivine composites positively influence each other: rheological weakening may result from mineral reactions, and the localisation of reaction progress in shear zones can be enhanced by plastic deformation. The results of this thesis imply that concurrent deformation and reaction at water-deficient conditions are of major importance in explaining how and why strain localisation occurs in polyphase rocks under a large range of geological conditions.

Chapter 1

Introduction

…augite appears to be the stable form at high temperatures, hornblende at low temperatures, so that any condition tending to facilitate molecular readjustment at ordinary temperatures must necessarily tend to facilitate the change from augite to hornblende. The enormous pressures brought into operation in the process of mountain-making may not unreasonably be supposed to supply such conditions. (Teall, 1885)

1.1 General background

The fundamental interrelationship between plastic deformation of rocks, e.g. deformation producing permanent alterations in the shape of the rock, and metamorphism, e.g. the recrystallisation of new mineral phases in response to changes in temperature, pressure or volatile content, has long been recognised by many Earth scientists (e.g. Teall, 1885; Zwart, 1963; Mitra, 1978; Brodie and Rutter, 1985; Steffen et al., 2001).

The extent of mineralogical changes may mirror the intensity of rock deformation: metamorphic reactions are often localised in narrow zones of concentrated deformation, i.e. shear zones, while there is limited or no reaction progress in the undeformed country rock (e.g. Kerrich et al., 1980; Marquer et al., 1985). Our understanding of concurrent deformation and reaction processes is of major importance in explaining how and why ductile deformation becomes concentrated in narrow shear zones in the crust and upper mantle (e.g. White et al., 1980; Brewer et al., 1983; Rutter and Brodie, 1988b; Handy, 1989; Drury et al., 1991; Vissers et al., 1991).

Deformation and reaction processes may be mutually dependent. On the one hand syndeformational mineral transformations exert a control on the deformability of rocks (e.g. White and Knipe, 1978). Metamorphic reaction may cause strain weakening, thus contributing to the formation of ductile shear zones. A rock weakening process is essential for preventing a shear zone from widening into the country rock (e.g. White et al., 1980). On the other hand deformation may contribute to mineral reactions in high-grade metamorphic rocks (e.g. Wintsch, 1975, 1985) and enhance the rate of re-equilibration of a rock system to new external conditions. Thus, deformation processes can hinder the preservation of metastable rocks (e.g. Rubie, 1990b) or lead to a positive feedback of further enhanced deformation (e.g. Tsurumi et al., 2003).

The main reaction weakening mechanisms have been reviewed by White and Knipe (1978), Rubie (1983), Brodie and Rutter (1985), Rubie (1990a) and Rutter and Brodie (1995). The crystallisation of fine-grained reaction products, so-called neocrystallisation, is considered to be the most significant reaction weakening mechanism. Studies of peridotite (e.g. Newman et al., 1999), granite (e.g. Kerrich et al., 1980) and eclogite shear zones (e.g. Koons et al., 1987) proposed that deformation tends to be localised in interconnecting layers and aggregates of fine-grained reaction products. The products accommodate deformation by non-frictional grain boundary sliding, e.g. grain size sensitive creep (e.g. Boullier and Gueguen, 1975). Also, the rate of deformation (i.e. strain rate) is inferred to be higher in deforming reaction products (e.g. White, 1979). The mineral transformations can be facilitated by an influx of water as well as a brittle precursor in the initial stages of deformation (Fitz Gerald and Stünitz, 1993; Stünitz and Fitz Gerald, 1993; Handy and Stünitz, 2002). Most studies suggest that the metamorphic grain size reduction induces a change in the deformation mechanism from grain size insensitive dislocation creep of the reactants to grain size sensitive diffusion creep of the products. A general rheological weakening is inferred to be associated with this reduction in grain size (e.g. Poirier, 1980; Hobbs et al., 1990; de Bresser et al., 2001).

Apart from neocrystallisation, other reaction weakening mechanisms include (1) the formation of new weak phases that deform more easily by crystal plasticity (Mitra, 1978; White and Knipe, 1978; Rubie, 1990a), (2) an increase of pore pressures during dehydration reactions, which can lead to brittle failure (Murrell and Ismail, 1976; Rutter and Brodie, 1988a; Paterson, 1989; Olgaard et al., 1995) and (3) transformation-enhanced intracrystalline plasticity (e.g. Poirier, 1985; Meike, 1993).

The occurrence of high reaction progress in permeable shear zones is often attributed to the infiltration of water (e.g. Austrheim, 1987; Klaper, 1990; Keller et al., 2004), because a hydrous fluid is an extremely effective catalyst in mineral reaction and mass transport (e.g. Rubie, 1986). However, shear zones in upper mantle peridotites (e.g. Newman et al., 1999) and granitic basement rocks (e.g. Kerrich et al., 1980) demonstrate that metamorphic reactions also localise in shear zones during ductile deformation under water-deficient conditions. Basement rocks can be dry for long periods of time under metamorphic conditions, with only short and localised periods of fluid infiltration (e.g. Rubie, 1986), and a different facilitation of metamorphic reactions is required when shear zones do not act as a conduit for fluids.

Ductile deformation processes themselves appear to affect reaction kinetics by the generation and movement of dislocations and grain boundaries in minerals. Nucleation of new phases on dislocations is energetically favourable (e.g. Cahn, 1957; Snow and Yund, 1987). The free energy stored in dislocations provides additional driving potential for chemical reactions (e.g. Brodie, 1980; Stünitz, 1998). Plagioclase experiments showed that the migration of high-angle grain boundaries provides high diffusivity paths for the rapid exchange of chemical components during dynamic recrystallisation (Yund and Tullis, 1980, 1991). Tectonic grain size reduction of reactant phases by dynamic recrystallisation results in small grains with high surface area, which may facilitate the nucleation of new phases. Fine-grained materials also have a greater volume of grain boundaries, which decreases the diffusion distances of chemical species. The non-hydrostatic stress conditions during deformation may influence the local reaction equilibrium conditions (e.g. Simpson and Wintsch, 1989; Shimizu, 1992; Wheeler, 1987).

Unfortunately, it is often difficult to thoroughly assess concurrent metamorphic and deformation processes in natural rocks because the complete strain history is seldom recorded. Microstructures may also be overprinted as a result of later thermal, volatile and tectonic events (e.g. Rubie and Thompson, 1985). Most geological studies can only assess the relative timing of deformation and metamorphism (e.g. Spry, 1969; Vernon, 1977).

The interactions between chemical and physical processes in rocks can be studied well in laboratory experiments, because the rheology, deformation mechanisms and reaction kinetics of rocks can be examined under controlled and/or simplified conditions. The resemblance of microstructures produced in experiments to those of naturally deformed rocks can be used to infer chemical and deformation processes under natural conditions. So far, experimental studies on the effects of reaction on deformation have focused on dehydration reactions (e.g. Raleigh and Paterson, 1965; Murrell and Ismail, 1976; Rutter and Brodie, 1988a; Olgaard et al., 1995), hydration reactions (Rutter et al., 1985; Stünitz and Tullis, 2001), and polymorphic phase transitions (e.g. Burnley and Green, 1989; Kirby and Stern, 1993; Meike, 1993; Green and Houston, 1995; Schmidt et al., 2003).

Serpentinite dehydration experiments with controlled pore pressures showed a significant weakening at 500 and 600°C at low strain rates in association with the onset of dehydration to olivine (Brodie and Rutter, 1987; Rutter and Brodie, 1988a). The enhancement of deformability was interpreted as due to the formation of small zones of fine-grained olivine reaction products that deformed by grain size sensitive creep. These experiments point to possible weakening effects of dehydration reactions on the rheology of the crust during prograde metamorphism (e.g. Rubie, 1990a).

Stünitz and Tullis (2001) studied the hydration reaction of plagioclase to zoisite during shear deformation. They observed that wet samples undergoing reaction were weaker than unreacted dry samples at the same experimental conditions. The deformation was localised in narrow shear bands of fine-grained reaction products, which deformed by a granular flow mechanism. They suggested that the plagioclase-zoisite reaction initiated an important weakening mechanism during deformation of plagioclase-bearing rock. In nature, however, the plagioclase hydration reaction is dependent on aqueous fluid infiltration and will only happen when fluid infiltration of the rocks is made possible by pre-existing cracks and micro-fractures.

Experimental studies on the effect of polymorphic reactions in single crystals primarily focused on weakening of rocks by transformation plasticity (e.g. Meike, 1993; Schmidt et al., 2003). Most mineral transformations involve volume changes, which can generate local deviatoric stresses at the grain-scale. Such stresses may assist intracrystalline plastic flow. Experiments have demonstrated a clear minimum of the creep strength of quartz at the α-β quartz transition (e.g. Schmidt et al., 2003). The authors inferred that polymorphic phase transformations could cause a localised reduction in strength of rocks. Other works suggest that reacting minerals under stress can result in transformation faulting, which is a candidate for earthquakes in deeply subducted lithosphere (e.g. Kirby, 1987; Burnley and Green, 1989; Green and Houston, 1995).

The effect of deformation on nucleation rates, growth kinetics and microstructural development during a net transfer reaction with polymineralic reactants and products is virtually unknown. There are no systematic experimental studies on the effect of deformation on the kinetics of chemical reactions in rocks except for studies on polymorphic transformations (e.g. Davis and Adams, 1965; Doukhan and Christie, 1982; Snow and Yund, 1987). Kinetic studies on the calcite-aragonite and sillimanite-kyanite transitions proposed an enhancement of nucleation rate by ductile deformation because increased dislocation densities may lead to an increase of stored plastic strain energy of the minerals (Davis and Adams, 1965; Doukhan and Christie, 1982). Snow and

Yund (1987) observed a ductile deformation-enhanced transformation from calcite to aragonite. The rate of transformation to aragonite was enhanced because of the increased nucleation sites at dislocations and subgrain boundaries that formed during dislocation creep of calcite. The reverse transformation to calcite was inhibited by deformation. Dynamic recrystallisation of aragonite resulted in a substantial grain size reduction. Although the number of nucleation sites increased by the formation of new grain boundaries, the overall transformation decreased because calcite grains could not grow across high-angle aragonite grain boundaries.

1.2 Aim and scope of the study

Two main problems can be distinguished: First, it is generally assumed that reaction weakening of rocks occurs because the crystallisation of fine-grained reaction products changes the dominant deformation mechanism from grain size insensitive creep to grain size sensitive creep. The experimental evidence for this mechanism comes primarily from hydrous reactions, although the localisation of deformation in the upper mantle and lower crust seems to occur under water-deficient conditions. Furthermore, the decrease in strength of the reacting rock during a change in deformation mechanism has never been directly linked to the occurrence of a metamorphic grain size reduction. Secondly, field studies demonstrate that reaction can be localised by ductile deformation in dry natural shear zones. However, the effects of plastic deformation on the nucleation and growth kinetics of a net transfer reaction are virtually unknown.

This thesis aims to address the above problems. The objective is three-fold:

1. To investigate the relation between the distribution of strain and metamorphic reactions in a ductile shear zone.

2. To investigate the effects of mineral reactions on the strength, deformation mechanisms and microstructures of nominally dry rocks.

3. To investigate the effects of ductile shear deformation on the reaction kinetics, mechanisms and microstructures in nominally dry rocks.

In order to achieve these aims, general shear deformation and hydrostatic experiments were performed on plagioclase-olivine composites in and outside the stability fields of the plagioclase-olivine paragenesis.

The rheological properties of pure plagioclase and olivine are well known from other experimental studies (plagioclase: Tullis and Yund (1985); Stünitz and Tullis (2001);

Rybacki and Dresen (2000), olivine: Karato et al. (1986); Chopra and Paterson (1981); Hirth and Kohlstedt (2003)). Therefore, the deformation of reacted and unreacted plagioclase-olivine composites can be compared with the deformation of pure plagioclase and olivine aggregates. The general aspect of the plagioclase-olivine deformation experiments is that the mechanical strength and microstructure of the composites during syndeformational reactions provide information on reaction weakening and strain partitioning in rocks.

Mineral reactions between plagioclase and olivine produce pyroxene-, spinel- and garnet-bearing assemblages. The plagioclase-olivine phase relationships are approximately known from petrological experiments on peridotite phase transitions (e.g. Kushiro and Yoder, 1966; Jenkins and Newton, 1979; Gasparik, 1984; Klemme and O'Neill, 2000) because the chemical equilibrium necessary to obtain typical observed mantle assemblages is difficult to achieve under dry conditions.

A set of hydrostatic comparison experiments has been carried out at the same pressure and temperature conditions as the deformation experiments. The direct comparison of deformed and undeformed plagioclase-olivine composites is aimed to provide understanding of fundamental processes in deformation and metamorphism of rocks, that is, to study the effect of deformation on nucleation, reaction kinetics and microstructures of the mineral transformation process.

The results of the experiments with plagioclase-olivine composites have applications to processes in natural peridotitic rocks. Reactions in the peridotite system are important for controlling the deformation of the upper mantle during crustal thinning and the deformation of oceanic crust and upper mantle lithologies during subduction (e.g. Drury et al., 1991; Vissers et al., 1995).

This thesis presents an extensive dataset on the strength, the deformation and reaction mechanisms and the microstructures of stable and metastable plagioclase-olivine composite rocks. These data provide an insight into metamorphism and deformation in the Earth's crust and upper mantle and will contribute to our understanding of naturally deformed and metamorphosed rocks in general.

1.3 Organisation of the thesis

This is a cumulative thesis, organised around three studies that are to be published separately in international Earth sciences journals (Chapters 3, 4 and 5). Each of these chapters can be read as an individual manuscript.

- Chapter 3 ('Spatial correlation of deformation and mineral reaction in experimentally deformed plagioclase-olivine aggregates') focuses on the quantification of strain and the distribution of reaction in sheared plagioclase-olivine composites, in order to demonstrate the interdependence of reaction and deformation. To determine the correlation between finite strain and the extent of reaction, the microstructures of the samples were analysed using the autocorrelation function. This study is accepted for publication in Tectonophysics (Elsevier).

- Chapter 4 ('Reaction-induced weakening of plagioclase-olivine composites') addresses the effects of mineral reaction on the strength and deformation mechanisms of plagioclase-olivine composites. Plagioclase-olivine composites were deformed in and outside the stability field of the plagioclase-olivine paragenesis. The experimental samples are described in terms of strength, microstructures, deformation mechanisms and reaction progress. This study is to be submitted for publication in the Journal of Geophysical Research (American Geophysical Union).

- Chapter 5 ('Reaction mechanisms and kinetics during plastic deformation of anorthite-olivine composites') focuses on the effects of shear deformation on the reaction kinetics and microstructures of mineral transformation processes. Based on the extended dataset of Chapter 4, a microstructural and kinetic comparison is made between hydrostatic and syndeformational reaction in anorthite-olivine composites. The experimental samples are described in terms of phase relationships, reaction progress and reaction mechanisms. This study is to be submitted for publication in Contributions to Mineralogy and Petrology (Springer-Verlag).

The main conclusions of the entire thesis and directions for future research are summarised in Chapter 6. The applied laboratory techniques for the preparation and execution of experiments on plagioclase-olivine composites in a Griggs apparatus are described in Chapter 2. The compilation of all experiments and analyses in Appendices A, B and C complete this work.

Chapter 2

Experimental techniques

This chapter covers the experimental techniques that were used to prepare and run shear deformation experiments on plagioclase-olivine composites. The experiments were performed at the laboratories of Basel University, Switzerland and Brown University, U.S.A.. First, the methods are described that were used to prepare dense olivine-plagioclase samples, starting with the preparation of pure olivine and plagioclase mineral separates with a specific grain size and the mixing of both minerals to obtain a plagioclase-olivine powder. Secondly, a description of the sample assembly is given, illustrating how the sample assemblies were adapted for the conditions of the experiments. The third section briefly describes the deformation apparatus and the procedure for a typical experiment. The fourth section describes a series of grain growth experiments using a plagioclase-olivine mixture. The goal of these experiments was to determine the optimal pressure, temperature and time conditions for grain growth in the plagioclase-olivine mixture necessary for obtaining dense plagioclase-olivine rock samples. The last sections summarise the experimental problems and propose possible directions for future research.

2.1 Sample preparation

2.1.1 Mineral separation

The plagioclase-olivine samples were prepared from natural rock-forming minerals: anorthite (An_{92}) from the Blumone gabbro (Adamello, Italy), labradorite (An_{60}) from Sonoran single crystals (Sonora, Mexico) and olivine (Fo_{93}) from the Åheim dunite (Åheim, Norway). Except for the labradorite single crystals, anorthite and olivine were separated from their source rock using mineral separation techniques as described by

Hutchison (1974, chap.5). The steps in the mineral separation are illustrated in Figures 2.1 and 2.2.

Anorthite from Blumone gabbro

Blumone gabbro was used as a source rock because it contains unaltered and very fresh anorthite. It is composed of oxides (5%), pyroxene (50%) and anorthite (45%). Anorthite was primarily retrieved using magnetic separation because the oxides and pyroxene have relatively high magnetic susceptibilities compared to feldspars and plagioclases. The entire separation was performed in four steps. First, the rock was carefully crushed by a hammer in order to produce rock fragments passing through a 1 mm sieve. The use of a metal hammer did not result in any metal contamination in the final product. A hand magnet was used to remove the strongly magnetic material (Fig. 2.1a). The residual material was further crushed using an alumina or agate mortar until the rock fragments passed through a 0.5 mm sieve.

The rock powder was processed using a Frantz Isodynamic type magnetic separator. Satisfactory results were obtained when configuring the magnetic separator with 4 Amps, a side tilt of 5° and a forward slope of 15° (Fig. 2.1b). Material with a high magnetic susceptibility is pulled up-slope into the filter tunnel, whereas dominantly anorthite-bearing grains move down-slope. The vibration of the filter tunnel was increased when fine-grained rock powder passed through the apparatus. As a third step, the anorthite and/or anorthite-bearing grains were reintroduced into the magnetic separator using 10 Amps to extract oxide-contaminated anorthite grains.

As a final step, the anorthite fraction was examined under the microscope and remaining impurities were removed manually (Figs. 2.1c,d). The procedure described above proved to be effective, although the amount of anorthite retrieved from Blumone gabbro was relatively small mainly because anorthite was strongly intergrown with other minerals.

Olivine from Åheim dunite

Åheim dunite consists of olivine (80%), pyroxene (10%), oxides and hydrous minerals (5-10%) such as clinochlore, serpentine and talc (Jackson et al., 1992). Olivine was extracted using magnetic, density and manual separation. Specimens of Åheim dunite were crushed using a hammer to produce small 0.5 cm fragments. These fragments were further reduced to 0.5-1 mm sizes using an agate disk mill.

Magnetic separation removed the more magnetically susceptible olivine from most

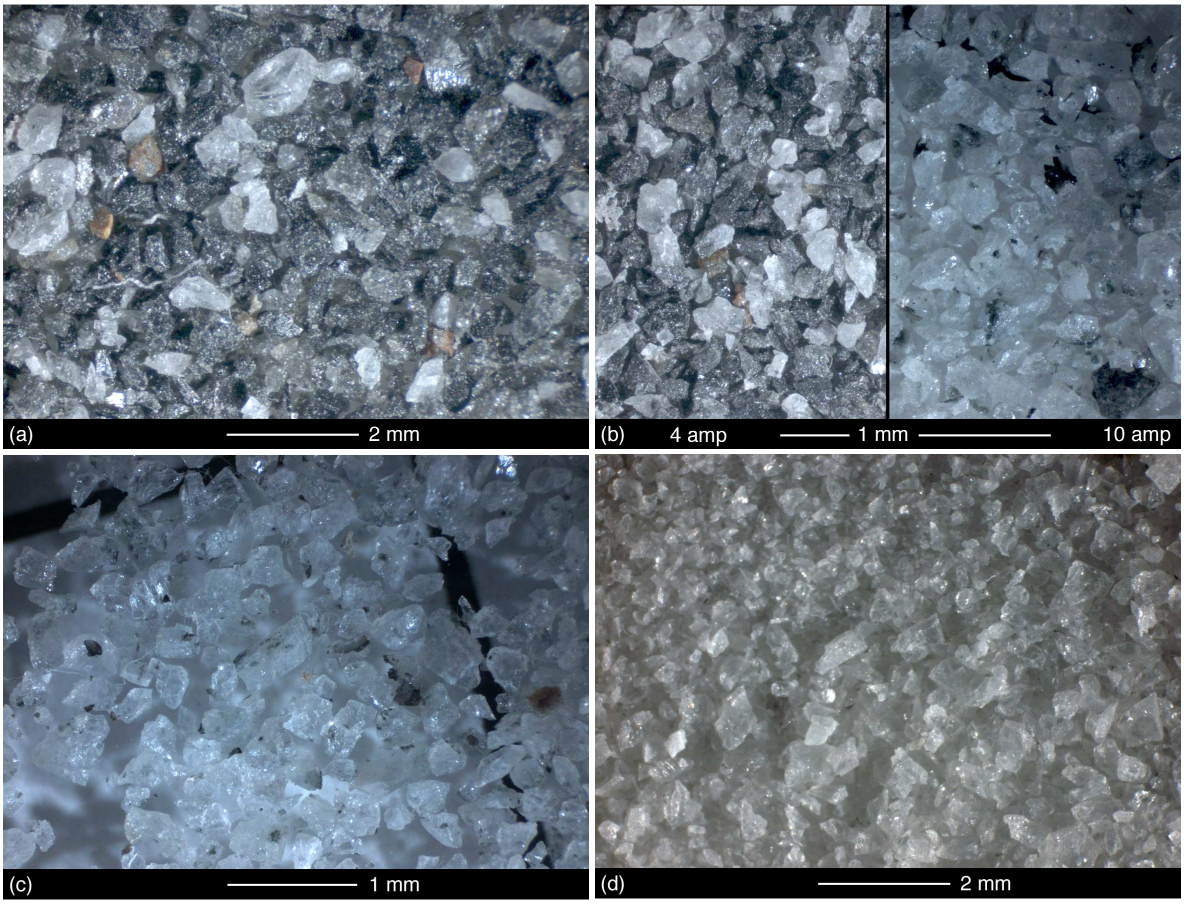

Figure 2.1: Separation of anorthite from Blumone gabbro. The images show minerals that were removed in each step of the separation. A mixture of pyroxene and oxides (dark, brown) and anorthite with inter-growths (white/transparent) were first removed by (a) hand magnet and (b; left) using a magnetic separator at 4 Amps. (b; right) Anorthite grains (white/transparent) with intergrown minerals (dark) were separated with 10 Amps in the magnetic separator. (c) Remaining anorthite grains with impurities were handpicked under the stereo microscope. (d) The pure Blumone gabbro anorthite used in this study.

of the sheet silicates, using 2 Amps, a side tilt of 6° and a forward slope of 15° (Fig. 2.2a). The extracted olivine-bearing material was then put into a flat bowl containing some acetone. By gently shaking the bowl, a large portion of the sheet silicates could be separated from the olivine as these flaky minerals are transported faster in the acetone current. Additionally, density separation was applied (Hutchison, 1974, chap.5) to remove all remaining small sheet silicate fragments, using bromoform as the high-density liquid (ρ=2.89 g cm^{-3}). Olivine (ρ=3.29 g cm^{-3}) sinks through bromoform whereas the sheet silicates remain at the liquid surface (Fig. 2.2b). As many oxides remained, both attached to olivine and as separate particles (Fig. 2.2c), olivine grains were separated manually as well (Fig. 2.2d).

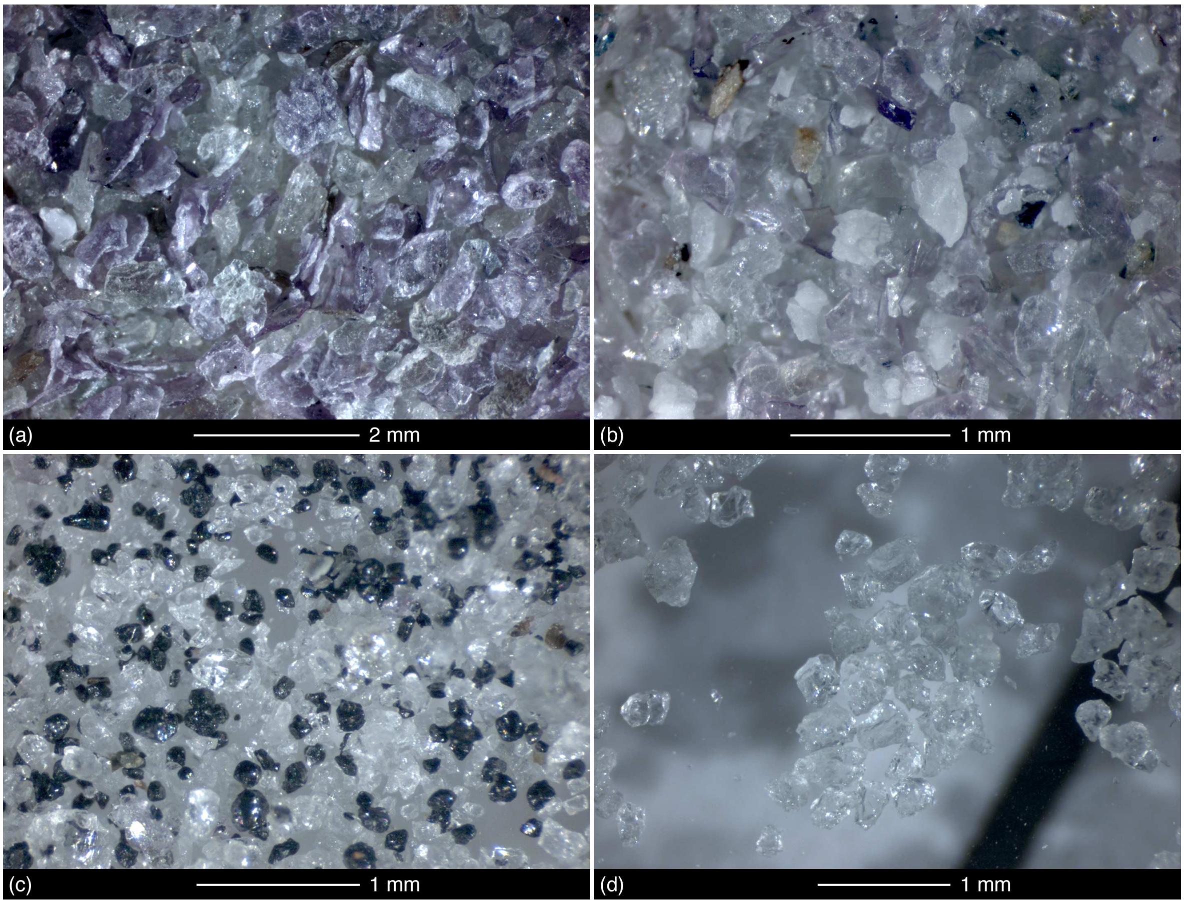

Figure 2.2: Separation of olivine from Åheim dunite. The images show minerals that were removed in each step of the separation. (a) Flakes of sheet silicates (pink; size ∼1.0 mm) removed using a magnetic separator. (b) Finer-grained hydrous minerals (pink; size <0.5 mm) and white granular grains (possibly pyroxene/amphibole) were removed by density separation in bromoform. (c) Oxides, some pyroxene (black; size <0.2 mm) and oxide-contaminated olivine (transparent) were handpicked under the stereo microscope. (d) The pure Åheim dunite olivine used in this study.

2.1.2 Grain size separation

Pure olivine, anorthite and labradorite were ground to fine powders using an alumina mortar. These powders were then sorted within 2-6 and 4-10 µm ranges using a sedimentation method based on Stokes' law of settling. Stokes' law of settling, valid for small grains whose shape approximates a sphere, is given by:

$$v_s = \frac{(\rho_{min} - \rho_{liq}) \cdot g \cdot D^2}{18 \cdot \eta} \tag{2.1}$$

in which v_s is the settling velocity ($cm\, s^{-1}$), g the acceleration of gravity (980 $cm\, s^{-2}$),

ρ_{min} and ρ_{liq} the densities of the mineral and fluid ($g\,cm^{-3}$), D the diameter of the grain (cm) and η the viscosity of the liquid ($g\,cm^{-1}s^{-1}$). The time required for a particle to settle over a vertical distance x is calculated using v_s.

Ethanol was used for olivine settling because ethanol has better grain wetting properties than water and therefore does not cause clustering of fine olivine grains. Anorthite and labradorite were settled in distilled water. The advantage of distilled water over de-ionized water or tap water is that the latter still contain gypsum and other impurities. The sedimentation times that were calculated using equation 2.1, as well as the properties of the minerals and liquids, are given in Table 2.1.

Grain size (μm)	Liquid: water			Liquid: ethanol		
	An_{92}	An_{60}	Fo_{93}	An_{92}	An_{60}	Fo_{93}
10	18	19	14	19	19	15
9	23	23	17	23	24	18
8	29	30	22	29	30	23
7	38	39	29	38	39	30
6	51	53	39	52	54	41
5	74	76	56	75	77	58
4	116	119	87	118	120	91
3	206	211	155	209	214	162
2	462	475	350	471	482	365
1	1850	1899	1398	1883	1928	1461

Table 2.1: Sedimentation times for anorthite (An_{92}), labradorite (An_{60}) and forsterite (Fo_{93}) powders. Times in minutes are calculated for 1-10 μm particles and a sedimentation distance of 10 cm. Viscosities ($\eta \cdot 10^{-3}$ Pa s at 20°C): water = 1.0530, ethanol = 1.200. Densities ($\rho \cdot g\,cm^{-3}$): water = 0.998, ethanol = 0.790, An_{92} = 2.741, An_{60} = 2.696, Fo_{93} = 3.304.

Method

Glass beakers of 500 ml (beaker height = 10 cm) containing the ground mineral powder were filled halfway with the settling liquid. While holding the beaker inside a water-filled Ultrasonic Test Sieve Cleaner (Haver USC 200-90, by Haver & Boecker), the powder was thoroughly stirred using a spatula (plastic preferred over metal) for about five minutes. The beaker was then taken out of the sieve cleaner, filled up to the settling distance (10 cm) and left untouched for the settling time of the largest grain size range of interest. The suspension was then siphoned off until 1 cm of suspension was left in the beaker. The removed suspension was transferred to a second glass beaker, which was held in the ultrasonic stirrer again and refilled with fluid up to the settling distance. The second beaker now contains a grain size fraction ranging from the largest desired grain size up to the smallest. It was left for the time needed to settle the smallest grain size of interest; the suspension was again siphoned off into a third beaker.

After these steps, in the case of a 4-10 µm settling session, beakers 1, 2, and 3 will now contain powders with grain sizes of >11-10 µm, 4-10 µm and <4 µm, respectively. All powders were dried in an oven to hasten evaporation of the liquid, but they were removed from the oven when still moist because complete oven drying results in hard, fine-grained crusts. The moist powders were air-dried and collected. The residual coarse-grained powders were reground and resettled.

Very fine-grained lenses consisting of <1 µm plagioclase and olivine grains were observed in the first samples of this study (Fig. 2.3a, experiments W976 to W1015, Appendix A). These samples were prepared from 2-6 µm powders and the method described above. In order to eliminate such unwanted fine-grained fractions in later samples, 4-10 µm powders were settled repeatedly until the settling liquid appeared clear and transparent.

2.1.3 Mixing of plagioclase and olivine

Powder mixtures were prepared with anorthite-olivine and labradorite-olivine in a 1:2 molar ratio. This is the molar ratio in which forsterite (Fo_{100}) and anorthite (An_{100}) react in the CaO-MgO-$\mathrm{Al_2O_3}$-$\mathrm{SiO_2}$-system. The shear strain and shear strain rate in constant displacement deformation experiments depend on the thickness of the sample. In order to compare the plagioclase-olivine experiments with the plagioclase experiments of Stünitz and Tullis (2001), the sample thickness was intended to be identical to those experiments (0.5 mm). In order to attain this thickness, a volume of 70 mg of Sonoran labradorite was used as the reference volume for one plagioclase-olivine sample. Table 2.2 shows how many grams of each mineral powder were needed to obtain the molar ratio and the required volume.

	An_{60}	An_{92}	Fo_{93}	Fo_{93}	An_{92}	Fo_{93}	An_{60}
Mol	1	1	1	2	1	2	1
Mol. weight$^{(*)}$	271.815	276.930	145.110	290.220	276.930	290.220	271.815
Density (g cm^{-3})	2.696	2.741	3.304	3.304	2.741	3.304	2.696
Weight %	100.00	100.00	100.00	51.17	48.83	51.64	48.36
Volume (*10^{-2}cm^3)	2.597	2.597	2.597	2.597		2.597	
Volume %	100.00	100.00	100.00	46.51	53.49	46.56	53.44
Weight (mg)	70.00	71.17	85.40	39.90	38.07	39.94	37.41

Table 2.2: Molar, volume and weight ratios for olivine and plagioclase powders used for preparation of samples. The volume and weight ratios of 1 sample are based on the volume of 70.0 mg An_{60}. (* 1 AMU = 1.66*10^{-24} gram)

Method

Mineral powder for about 4 to 5 samples was weighed out for each mixing session. The powders were put into a small 10 ml beaker together with a small amount of acetone to create an acetone-plagioclase-olivine slurry. The beaker was held repeatedly in a water-filled ultrasonic stirrer for 2 minutes while the slurry was continuously stirred with a spatula. This procedure caused olivine and plagioclase to mix during the slow evaporation of acetone. It was not possible to let the acetone evaporate completely inside the ultrasonic stirrer because the powder mixture would eventually fume out of the beaker. Therefore the beaker was quickly placed inside a hot oven at 110°C which caused immediately boiling of acetone and fast drying of the powder ('acetone quenching'). The powder mixture was stored in the oven until processed further and it was occasionally stirred with a spatula.

In the beginning of this study, ethanol and distilled water were used for the mixing method instead of acetone. A larger 50 ml beaker was used with more liquid but the same amount of powders. A centrifuge was used to remove the liquid from the mixture. This resulted in an unequal dispersion of olivine and plagioclase inside the mixtures as well as a grain size sorting, even on a micrometer scale. These effects are demonstrated by the presence of very fine-grained lenses and crusts in the end-product rock samples (Fig. 2.3a). The advantage of using acetone as a mixing fluid is that it has better wetting properties than water and ethanol. In the 'acetone quenching' method described above, the fine-grained minerals have less time and space to settle in the slurry and therefore there is not as much grain size sorting.

In most of the samples, plagioclase and olivine of all grain size ranges mixed very well. However the problem of grain size variations and phase partitioning remained to some extent in all samples despite the efforts made (Fig. 2.3). A different method would be advisable in future work (section 2.5).

2.1.4 Forcing blocks

For each experimental sample approximately 78 mg of the plagioclase-olivine powder mixture was placed between two forcing blocks. The forcing blocks are cylindrical cores (diameter = 6.3 mm), cut at 45° to the cylinder axis. The forcing block surface was either plain or had small shallow grooves perpendicular to the shear direction. The grooves served to maintain a good grip on the sample during the experiment. Olivine-rich materials were chosen for the forcing blocks because they do not contain additional

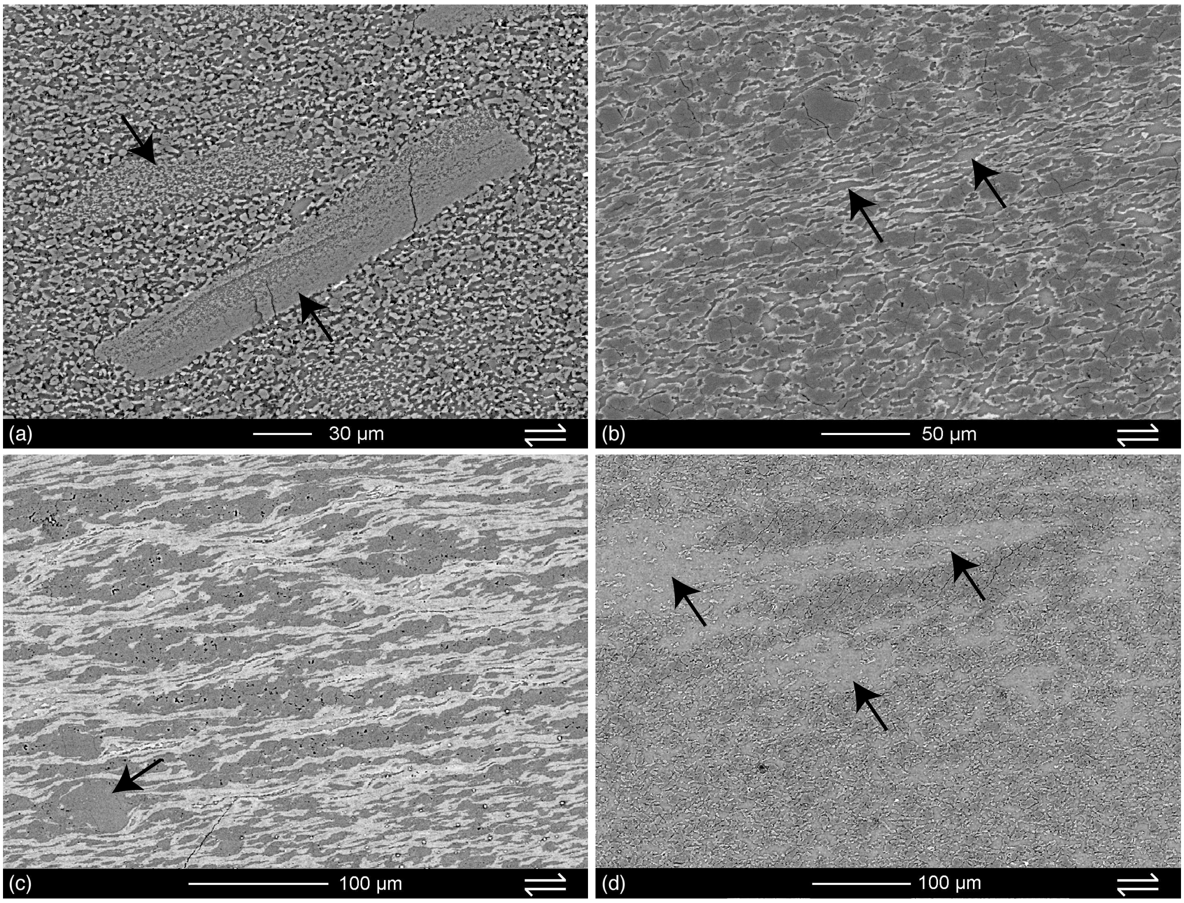

Figure 2.3: Examples of plagioclase-olivine samples with irregularities produced by sample preparation (BSEM-images). The irregularities persist through the experiments and may have been enhanced by deformation. (a) Sample W983 showing lenses and crusts (arrows) of <1 μm sized labradorite and olivine grains. The crusts often have an internal grain size gradation. (b) Detail of the partially reacted matrix in sample W1041. The center of the image is rich in elongated anorthite grains (arrows) whereas the top and bottom dominantly contain coarser-grained olivine. (c) Coarse-grained olivine clasts (size ∼40 μm; dark, arrow) and fine-grained reaction products (size <1 μm, bright) form layers across sample 28AA. Shear bands have developed. (d) Large labradorite lenses in sample 42AA contain finer-grained olivine (arrows). The lenses are adjacent to coarser grained olivine clusters.

chemical components such as aluminium. Hot pressing of the plagioclase-olivine powder between the olivine-rich forcing blocks resulted in a good bonding of the sample with the forcing blocks.

Three different materials were tested as forcing blocks: (1) Åheim dunite, (2) San Carlos single crystal olivine and (3) Balsam Gap dunite. Tables A.1 and A.2 in Appendix A list which material was used in each experiment. Balsam Gap dunite was found to be the most useful forcing block material. It contains few impurities, and any serpentine present on olivine grain boundaries was easily dehydrated during the heat treatment (see following section). Its only disadvantage was occasional fragmentation during preparation. Large olivine grains tended to chip off and break during coring, cutting, polishing and drying.

Forcing blocks were easily prepared from Åheim dunite. However this material was not favoured because it contains numerous hydrous minerals, which are difficult to completely break down during heat treatment (Jackson et al., 1992). Therefore Åheim dunite forcing blocks may have influenced the water content of the samples. One experiment was performed using San Carlos single crystal olivine forcing blocks (17AA, Table A.1). The pistons were difficult to core due to the small size of the San Carlos crystals. It was also difficult to orient the cleavage planes inside the crystals into a hard slip orientation with respect to the main compression direction. Therefore San Carlos single crystals were not used in later experiments.

2.1.5 Jacket and heat treatment

The dunite forcing blocks and sample powders were placed in a jacket of nickel foil (Fig. 2.4). This inner Ni jacket served as an oxygen fugacity buffer of the sample during the experiment (Ni-NiO buffer). An outer Ni tube was used in experiments W975 to W1015 (Appendix A). The Ni tube overlapped the zirconia pistons, creating support and a good vertical sample alignment (Fig. 2.4a). These samples were dried for 6 hours at 1000°C in a CO-CO_2 gas flow mixture at atmospheric pressure. CO-CO_2 gas was used to prevent oxidation of the sample and jacket at high temperatures. CO and CO_2 gases were mixed in 4.68-95.32 vol.% and 3.88-96.22 vol.% ratios, which correspond to oxygen fugacities of $fO_2=0.3116 \cdot 10^{-12}$ (900°C-1000 MPa) and $fO_2=0.493 \cdot 10^{-12}$ (900°C-1500 MPa), respectively.

Folding the inner Ni foil over a bottom and top Ni foil disk after the heat treatment sealed the inner Ni jacket. The disadvantage of this ‘mechanically’ sealed Ni-Ni jacket is the poorly controlled water content in the jacket before and during the experiments. Samples using this type of jacket were put into the sample assembly as quickly as possible after the heat treatment.

The Ni tube was replaced with a Pt tube in subsequent experiments W1026 to W1047 (Appendix A). The Pt tube could be weld sealed using platinum cups on both ends of the sample, which enabled a better control on the water content of the sample (Fig. 2.4b). The Pt tube and cups were welded together prior to the heat treatment, leaving a needle-sized hole open on both sides of the jacket to allow water to escape from the sample during drying. These samples were dried for 12 hours at 1000°C

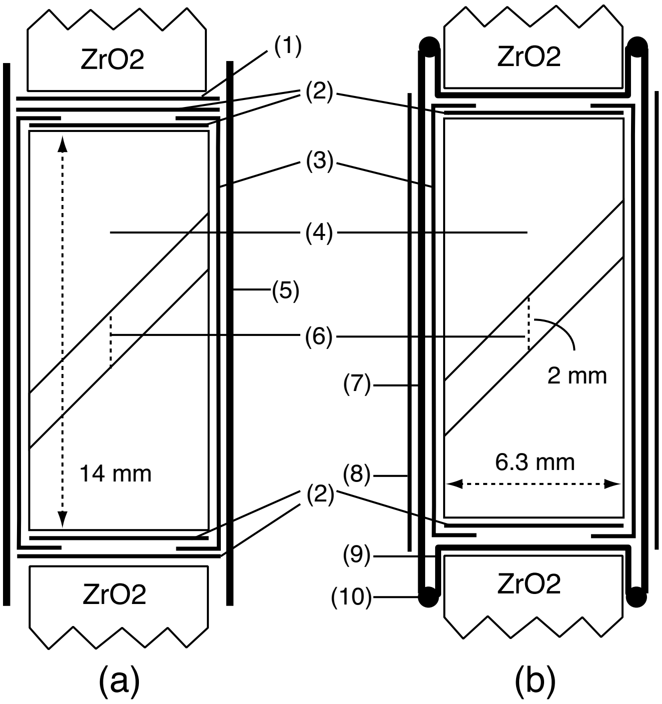

Figure 2.4: Schematic drawings of the sample jackets. (a) Mechanically sealed Ni-Ni jacket. (b) Weld sealed Ni-Pt-Ni jacket. Length of inner Ni foil jacket = 3 mm 'overlap' + 2 mm sample + length of forcing blocks. Length of outer Ni/Pt tube = 4 mm 'overlap' + 2 mm sample + length of forcing blocks. (1) 0.15 mm thick Pt disk, (2) 0.025 mm thick Ni disks. (3) 2 wraps of inner 0.025 mm Ni foil (width = 40 mm) folded over bottom and top Ni disks. (4) 6.3 mm diameter dunite forcing blocks. (5) Outer 0.1 mm thick Ni tube overlapping zirconia pistons. (6) Sample. (7) Outer 0.20 mm thick Pt tube overlapping zirconia pistons. (8) Outer wrap of 0.025 mm thick Ni foil (width = 20 mm), height = 2 mm sample + length of forcing blocks. (9) Pt cup of 0.15 mm thick Pt foil. (10) Weld sealed Pt tube and Pt cup.

in a CO-CO_2 gas flow. The small holes were welded shut immediately after drying to prevent atmospheric water from entering the sample. An additional Ni foil wrap was put around the platinum tubing, making a Ni-Pt-Ni-jacket, when experimental temperatures exceeded 900°C.

Because the plagioclase-olivine powder displayed limited grain growth after hot pressing at 900°C (section 2.4), a different drying and jacketing procedure was chosen for the samples and forcing blocks in experiments 3AA to 55AA (Appendix A). The sample powder was oven-dried at 110°C for at least 3 days which created an 'as-is' plagioclase-olivine powder with some trace amounts of water. The dunite forcing blocks were thoroughly dried for 24 hours at 980-1000°C in a CO-CO_2 gas flow. The CO-CO_2 gas mixture was made using an Analyt Mass Flow Controller with 0.36 mL min^{-1} (CO) and 13.1 mL min^{-1} (CO_2) flow rates (eq. oxygen fugacity at 900°C-1500 MPa). Drying resulted in a 0.50-0.75% weight loss of the Balsam Gap dunite forcing blocks due to the dehydration of hydrous minerals. The as-is sample powder and the dried forcing blocks were assembled quickly into the weld sealed Ni-Pt-Ni-jacket after the forcing block heat treatment.

2.2 Sample assembly

The sample assembly is designed to transmit the confining pressure to the sample inside it. The assembly fits into a 25.4 mm diameter pressure chamber of the confining pressure vessel. Two types of sample assemblies were used in this study: (1) a solid salt sample assembly (SS-assembly, Figs. 2.5 and 2.6) and (2) a molten salt sample assembly (MS-assembly, Fig. 2.7). Detailed descriptions of both assemblies are given by Tullis and Tullis (1986), Gleason and Tullis (1995) and Post and Tullis (1999).

In both assemblies the confining medium is sodium chloride. The jacketed sample fits inside an inner salt liner. The inner salt liner is separated from two larger outer salt pieces by a graphite furnace sleeve. Two soft-fired pyrophyllite sleeves stabilise the furnace within the salt liners. The top and bottom of the furnace are in contact with either copper or graphite disks. The assembly is sealed at the top with a teflon-wrapped lead piece and a metal packing ring. The outer salt pieces have an outer wrap of teflon tape that prevents corrosion of the pressure vessel. The bottom of the assembly consists of an unfired pyrophyllite piece with a central tungsten carbide plug. Zirconia pistons above and below the sample serve to transmit the applied vertical force to the sample.

The furnace, copper and graphite disks and the base plug are connected to a power supply, which provides internal heating of the assembly. The temperature is measured at the sample surface using an S-type Pt-Pt(10%)Rh thermocouple inside protective mullite tubing. The thermocouple enters the assembly through a crushable alumina tube inside the base pyrophyllite and reaches the sample through the outer salt, inner pyrophyllite and graphite sleeves and the inner salt liner. The thermocouple is positioned at the centre of the sample, perpendicular to the shear direction (Fig. 2.6a). The thermocouple mullite tubing is sealed at its elbow and tip using a ceramic cement. An aluminium-oxide ring was inserted inside the graphite-pyrophyllite sleeves to support the thermocouple inside the furnace during experiments with changes in P-T conditions (Fig. 2.6b).

An extra graphite can surrounds the sample and the inner salt liner in the MS-assembly (Fig. 2.7). This configuration allows the containment of molten sodium chloride at temperatures above 980°C. The inner salt liner of the MS-assembly is made shorter than the one in the SS-assembly, by guiding the lower zirconia piston through a bottom soft-fired pyrophyllite piece. The MS-assembly was used in experiments W1026 to W1047 (Table A.2) in which sample hot pressing was performed at 1050°C. The SS-assembly was used in all other experiments.

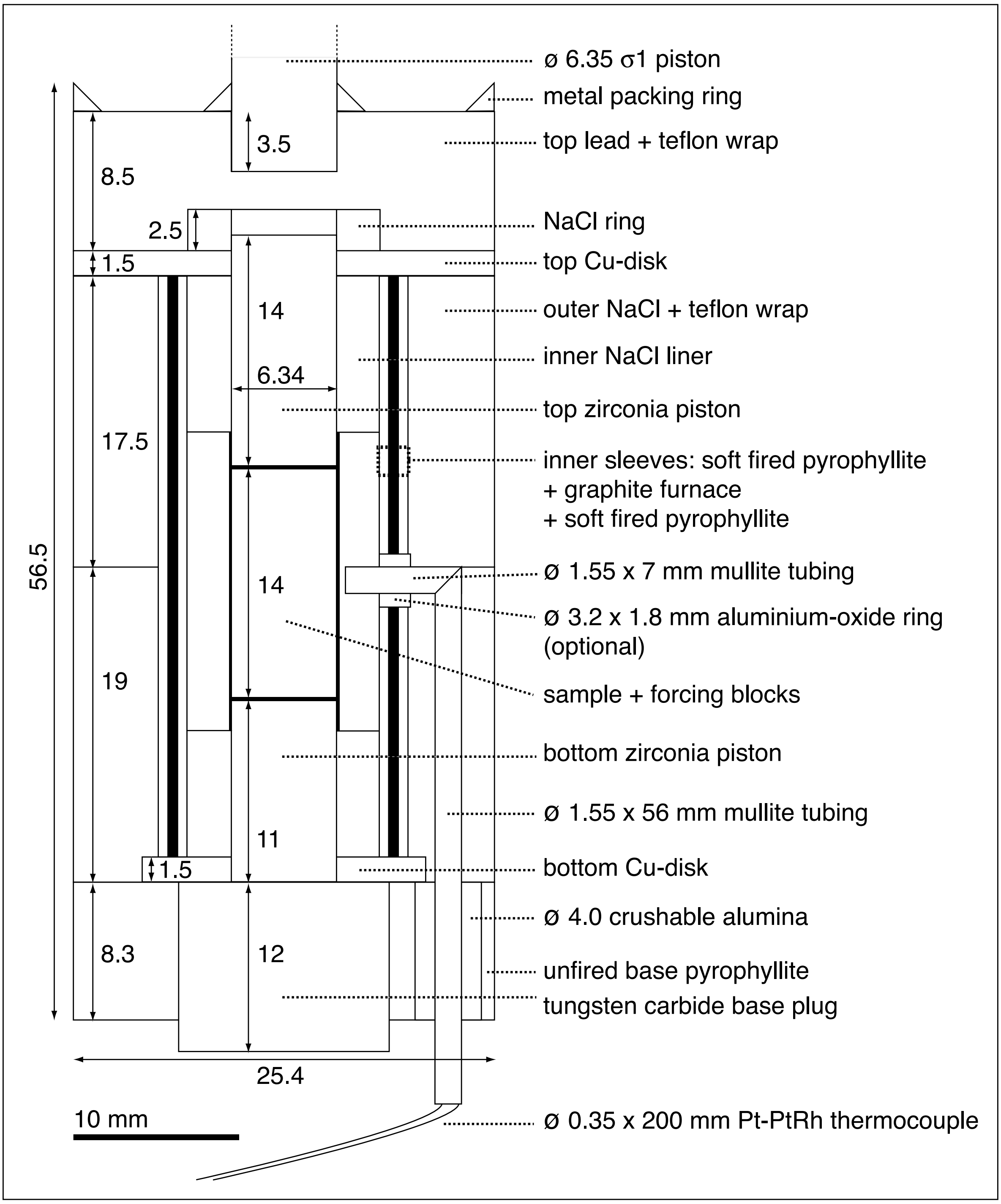

Figure 2.5: Scaled drawing of solid salt sample assembly (SS-assembly) for experiments at Basel University. All lengths in millimetres; vertical lengths may vary with different pressure vessels and base plates. The inner salt liner consists of three parts, and its ID has a smooth fit with the 6.34 mm zirconia pistons. The central salt piece was sanded down by hand to fit the sample. The details of the jacketed sample and forcing blocks are given in Figure 2.4. Drills: 4.1 mm (crushable alumina), 1.7 mm (mullite tubing in NaCl and sleeves) and 3.2 mm (aluminium-oxide ring through sleeves).

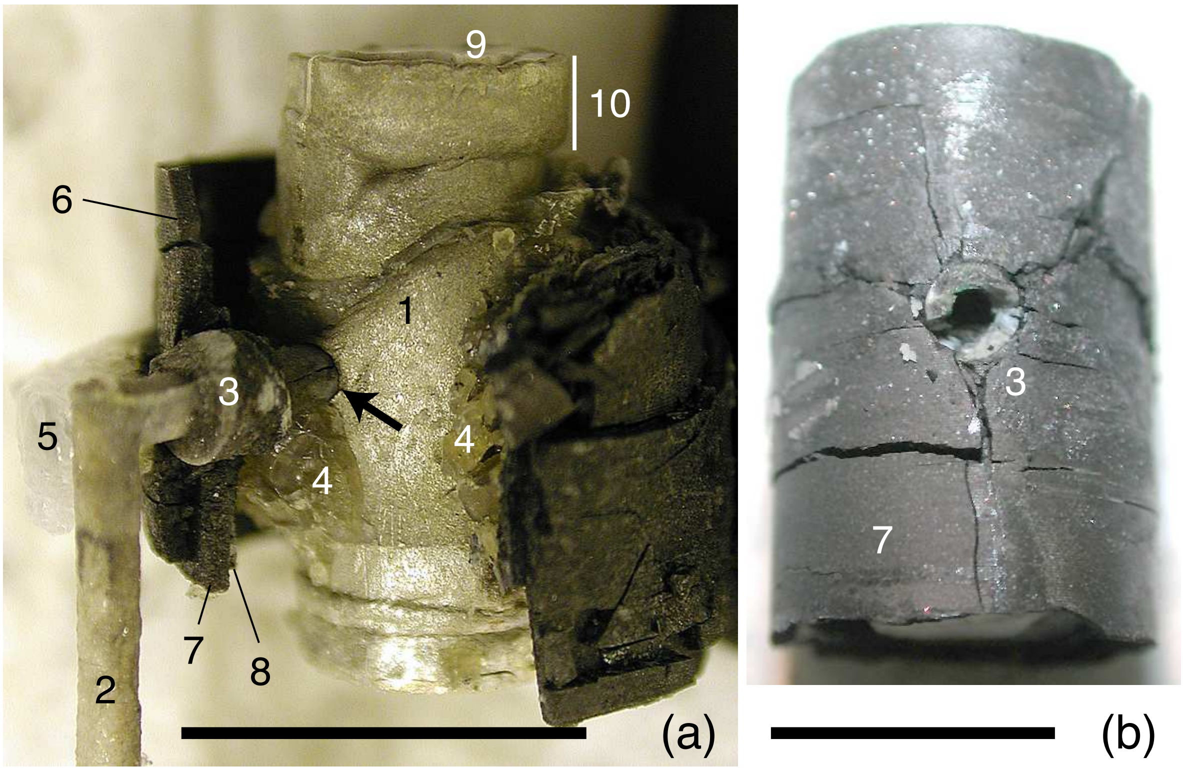

Figure 2.6: Photographs of the SS-assembly after an experiment (scale bars = 10 mm). (a) Sheared sample (1) with the thermocouple bead in its centre (arrow). Thermocouple (2) passes through an aluminium-oxide ring (3). Other parts: inner and outer NaCl (4+5), outer pyrophyllite (6), graphite furnace (7), inner pyrophyllite (8) and top zirconia piston (9) inside a Pt cup (10). (b) Detail of the aluminium-oxide ring (3) inside the graphite furnace (7). The furnace has radiating cracks.

2.3 High pressure-temperature experiments

2.3.1 Rock deformation apparatus

The experiments were performed in a Griggs-type solid confining medium piston-cylinder apparatus at Basel University and Brown University. This apparatus, based on the piston cylinder apparatus of Boyd and England (1960), was designed by D.T. Griggs (Griggs, 1967). It enables rock deformation experiments up to approximately 2.0 GPa confining pressure and 1200°C. A schematic overview of the apparatus is given in Figure 2.8. A detailed description of the apparatus is given by Tullis and Tullis (1986).

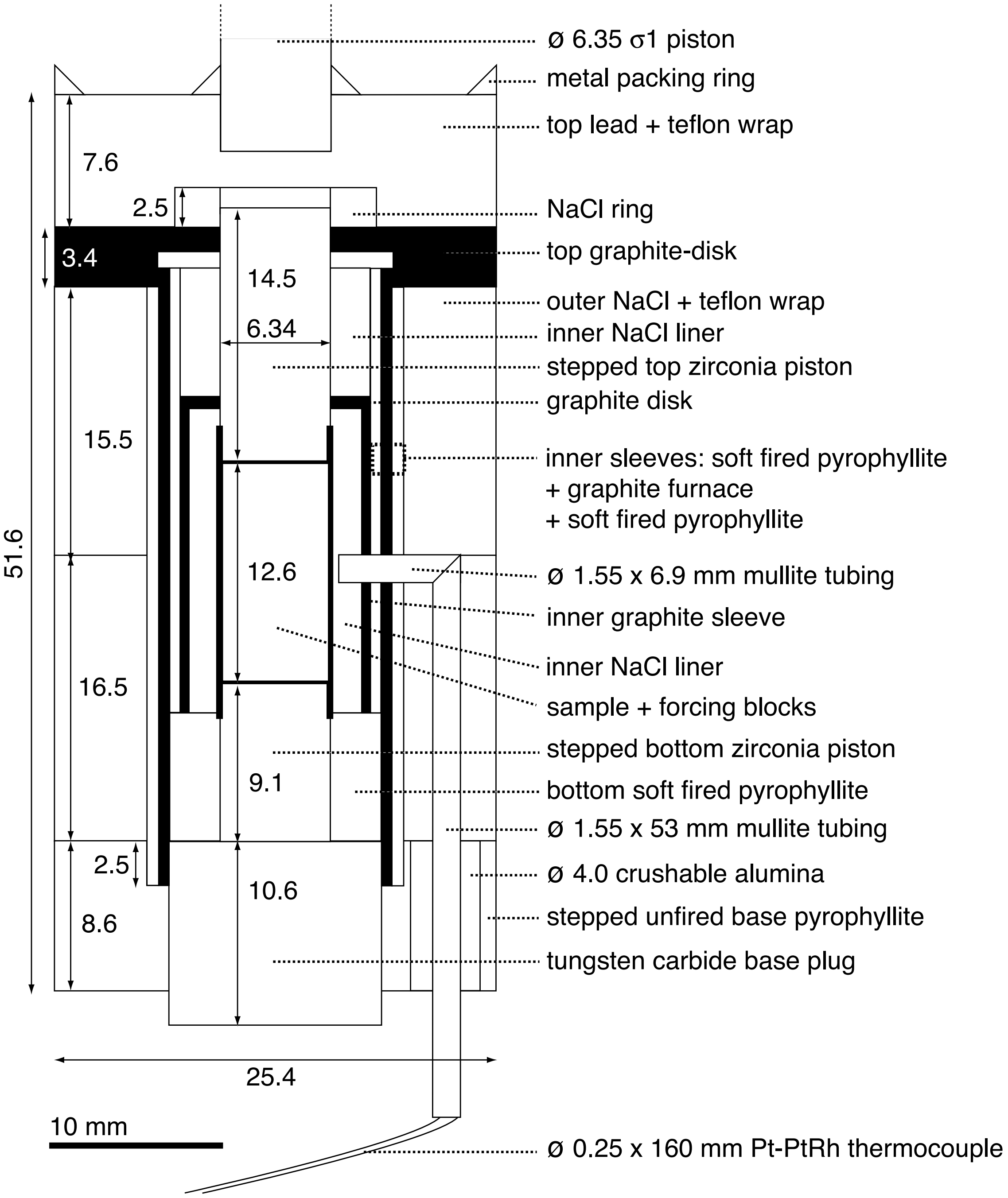

Figure 2.7: Scaled drawing of molten salt sample assembly (MS-assembly) used in experiments at Brown University. Design after Green and Borch (1989) and Gleason and Tullis (1993). All lengths in millimetres; vertical lengths may vary with different pressure vessels and base plates. The inner salt liner consists of two parts; the central salt piece was sanded down by hand to fit the sample. The details of the jacketed sample and forcing blocks are given in Figure 2.4b.

A pressure vessel contains the sample assembly with the rock sample. The confining pressure is generated in the assembly by pumping down a hydraulic ram which presses the confining pressure piston, or σ3-piston, into the pressure vessel chamber. The movement of the hydraulic ram is controlled by pumping oil into oil-chambers above or beneath the hydraulic ram. The confining pressure around the sample is determined by external measurement of the oil pressure in the oil-chambers using a pressure transducer and taking into account the areas of the hydraulic ram and the σ3-piston.

Force is applied on the sample by pressing an inner σ1-piston, which runs concentrically through the σ3-piston, onto the sample assembly. The σ1-piston is displaced by a force actuator, which runs through the hydraulic ram. The force actuator is moved by a constant rate motor on top of a gear train assembly. By choosing different gear combinations in the gear train, different rates of constant actuator displacement are obtained, resulting in different shear displacements rates in the sample shear zone.

The axial displacement of the force actuator is measured using a direct current differential transformer (DCDT). The axial displacement is recalculated as shear displacement along the sample. The axial load on the sample assembly is measured using an external load cell located above the hydraulic ram. The differential stress in the sample is deduced from the axial load by taking into account the surface area of the forcing blocks.

The temperature inside the pressure vessel was measured using a single thermocouple and monitored using a Eurotherm self-tuning temperature controller. The Eurotherm controller can be programmed for any desired temperature path. The pressure vessel and the hydraulic confining pressure ram are cooled with water.

2.3.2 Data processing

The force, displacement and pressure data are recorded as amplified volt signals in an analogue chart recorder. The data are processed using the Fortran program RigS, which calculates shear stress and shear strain. The program corrects the raw data for: (1) elastic distortion of the apparatus with progressive force (distortion correction), (2) reduction of stress-supporting sample area with progressive shear displacement (area correction), (3) internal friction of the assembly and sample jacket (friction correction) and (3) thinning of the sample with progressive shear displacement (thinning correction). The raw data and the mechanical results of all the experiments as well as the source code for the RigS-program are given in Appendix B.

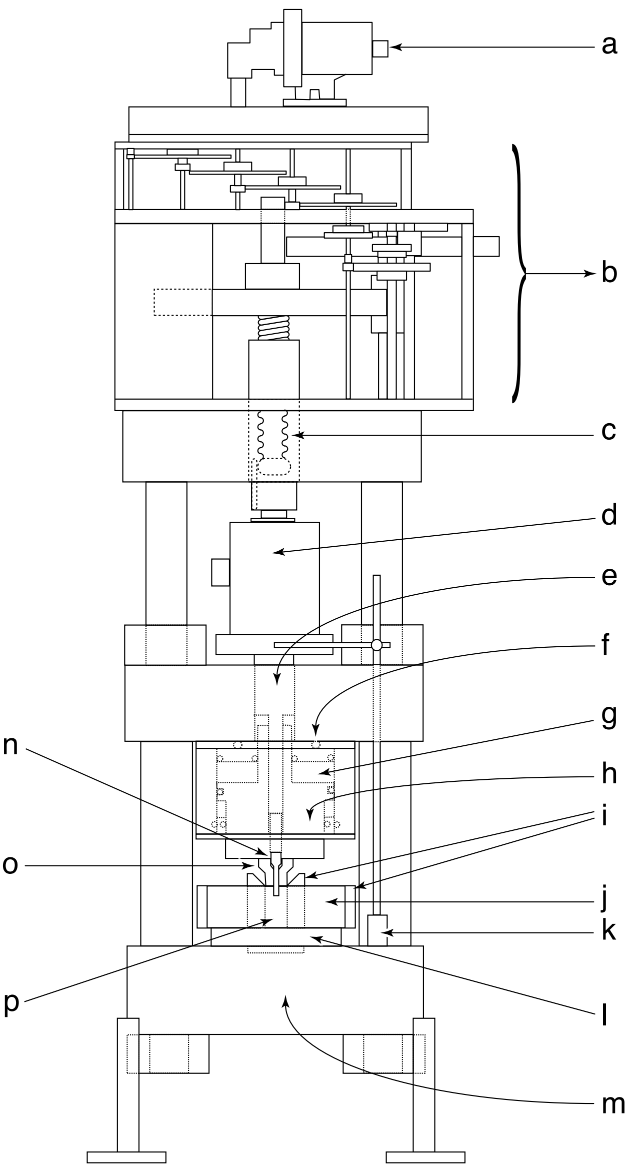

Figure 2.8: Schematic overview of Griggs' solid medium deformation apparatus after Tullis and Tullis (1986). (a) Motor. (b) Gear train. (c) Ball screw. (d) External load cell. (e) Force ram. (f) Water cooling passages. (g) Oil chamber of hydraulic ram, connected to an oil pumping system. (h) Hydraulic confining pressure ram. (i) Water cooling passages of the pressure vessel. (j) Confining pressure vessel. (k) DCDT displacement transducer. (l) Base plate. (m) Apparatus base plate. (n) Force (σ1) piston. (o) Confining pressure (σ3) piston. (p) Sample assembly with rock sample, for details see Figs. 2.5, 2.7 and 2.4.

2.3.3 Execution of an experiment

This section describes how an experiment is executed using the Griggs apparatus. Although slight differences exist between individual experimental runs, Figure 2.9 shows a P-T-t path that is representative for most experiments. After the sample assembly is placed inside the pressure vessel and connected to a base plate, the pressure vessel is positioned within the deformation apparatus. Both the force and hydraulic ram are lowered to make contact with the σ3 and σ1 pistons. This is called the 'initial touch point'.

The confining pressure is slowly increased in one hour to 50 MPa while manually keeping the force ram touching the $\sigma 1$ piston. At 50 MPa, the water-cooling tubes are connected to the pressure vessel, the gear train is set to the 10^{-4} combination (axial displacement rate $\sim 1.5\text{x}10^{-4}\text{mm}\,\text{s}^{-1}$), the top motor is put in place and the pressure vessel base plate is connected to the power supply. The pressure is raised to 100 MPa in ± 0.5 hours. The Eurotherm program is switched on using the program setting called 'path to avoid zoisite' (Table 2.3, Fig. 2.9) and the temperature is raised to 100°C using a ramp rate of $0.5°\text{C}\,\text{s}^{-1}$.

Pressure and temperature are increased alternately, with 0.5-hour breaks between each temperature ramp before raising the confining pressure. At 400 MPa-400°C the force ram is advanced for 0.2 mm. At 500 MPa-600°C, the force ram is advanced until the axial load starts to increase nonlinearly with displacement. This procedure is called the 'fast run-in'. The force ram is then retracted for ± 0.2 mm to unload the sample. From 600°C onward, temperature increase alone causes significant pressure build-up due to the thermal expansion of salt within the sample assembly. The sample stays within the anorthite-olivine stability field throughout the entire process of bringing the sample to high P-T conditions.

The temperature is raised from 900°C to the hot pressing temperature using a ramp rate of $0.2°\text{C}\,\text{s}^{-1}$. In experiments with hot pressing temperatures above 965°C, the temperature may fluctuate because the melting curve of sodium chloride is crossed (Fig. 2.9). As a consequence, the inner salt liners may start to melt. The molten salt undergoes convective flow inside the assembly and causes temperature fluctuations (up to ±30°C), which the Eurotherm controller unsuccessfully tries to compensate.

Hot pressing of the samples is performed for 24-48 hours between 900-1050°C and confining pressures between 700-800 MPa (also see section 2.4), in order to produce a dense plagioclase-olivine rock sample from the plagioclase-olivine powder. After hot pressing, the sample is cooled in 2 hours to 900°C and ~700 MPa. The Eurotherm program is set to keep the temperature fixed at 900°C.

Part	Type	Time	Target (°C)
1	ramp	30 min	900
2	ramp	6 min	965 - 980
3	dwell	20 sec	965 - 980
4	ramp	120 min	900
5	dwell	10 sec	900
6	ramp	3 min	200
7	dwell	10 sec	200
8	ramp	3 min	20
9	end		

Table 2.3: Program for Eurotherm temperature controller: 'path to avoid zoisite'.

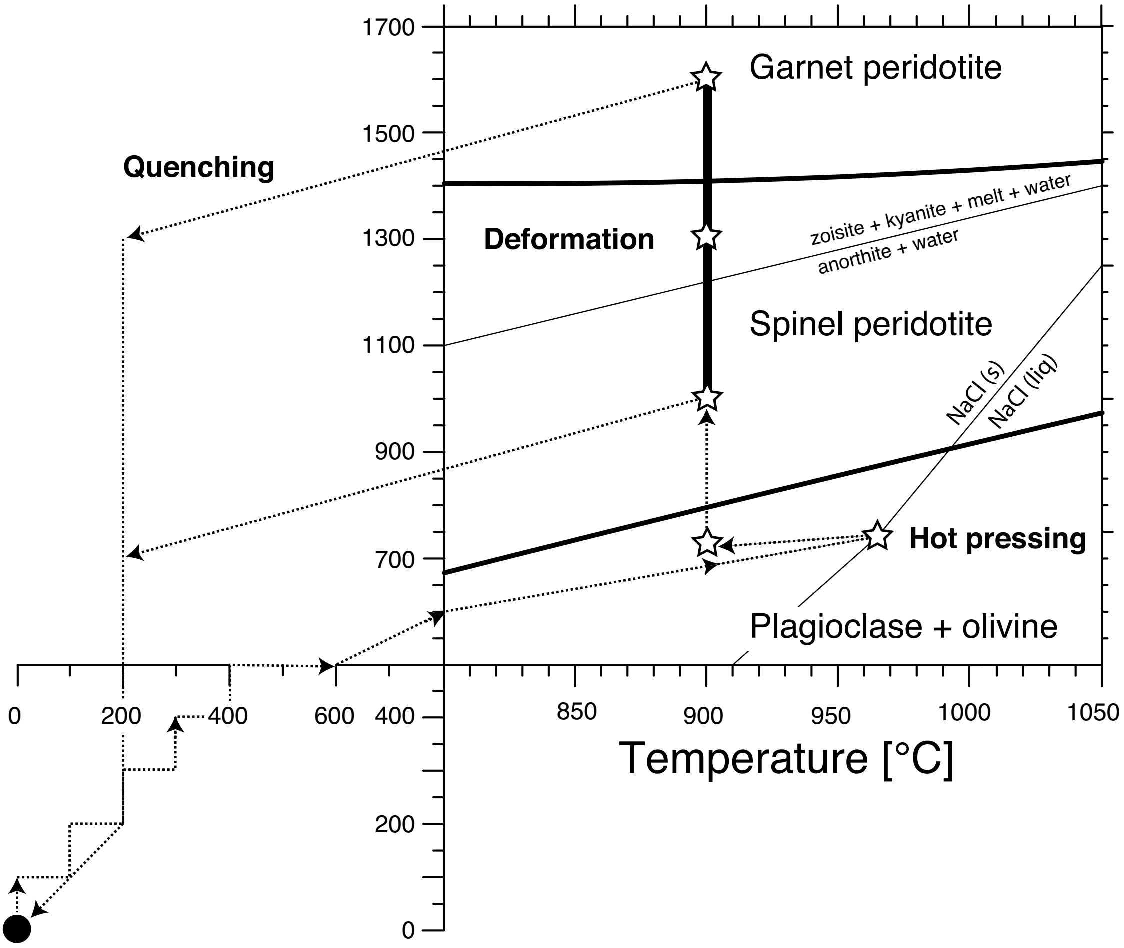

Figure 2.9: Pressure-temperature diagram illustrating the steps in hydrostatic and deformation experiments. Note the change of temperature scale to the left of the pressure-axis. Stars indicate examples of the hot pressing and deformation conditions. Dotted lines with arrows indicate the PT-path taken using the Eurotherm temperature controller. Phase transitions (solid lines): *plagioclase + olivine* → *spinel peridotite* → *garnet peridotite* by the program DOMINO (de Capitani and Brown, 1987; de Capitani, 1994) using the Berman (1988) database and solution models of Fuhrman and Lindsley (1988), Meyre et al. (1997) and Hunziker (2003). NaCl melting curve from Clark (1959), *anorthite + water* → *zoisite + kyanite + melt + water* extrapolated from Goldsmith (1982).

After 0.5 to 1 hour at 900°C, the confining pressure is raised in 1 hour to a confining pressure within the 1000-1600 MPa range. The top motor and gear train are switched to the 10^{-6} gear combination (axial displacement rate ~$1.5\text{x}10^{-6}\text{mm}\,\text{s}^{-1}$). The deformation experiment is started. In case of a hydrostatic experiment, the gear train is left at the 10^{-4} position and motor is not turned on. Depending on the sample length and the length of fast run-in, several hours may be required for the $\sigma 1$ piston to actually reach the hit point with the sample and start true sample deformation (for example 26 hours in sample 28AA, Table A.2).

At the end of a deformation experiment, the motor is turned off and the gear train is switched back to 10^{-4} gear. The Eurotherm controller is activated and cools the assembly from 900°C to 200°C within 3 minutes. This fast cooling causes the sample to be quenched and preserves the microstructures in the rock. The axial load needs to be decreased during quenching and the force ram is backed off using the 10^{-4} gears. The temperature decrease causes a pressure decrease of about 200-300 MPa due to the thermal contraction of the sample assembly. At 200°C the pressure is decreased by 'bleeding' oil from the hydraulic ram oil chambers slowly, in order to prevent horizontal extension cracks in the sample. The force and hydraulic ram are retracted upwards once the experiment is completely de-pressurized and cooled, and the sample is then pressed out of the pressure vessel.

2.4 Grain growth experiments

Porous and dense rocks have different rheological properties and therefore it was considered important to prepare dense and well-annealed plagioclase-olivine samples to be used in the experiments. In laboratory experiments, static grain growth of minerals can be enhanced by high temperatures, pressure, time and intracrystalline water (Tullis and Yund, 1982; Karato, 1989; Evans et al., 2001). The presence of different phases and impurities generally prevents significant grain growth (Tullis and Yund, 1982; Olgaard and Evans, 1988). A number of grain growth experiments were performed in order to determine the optimal P-T-t-conditions for plagioclase-olivine powder hot pressing (Table A.1).

Characteristic microstructures of the plagioclase-olivine powders after the grain growth experiments are shown in Figures 2.10, 2.11, 2.12 and 2.14. The relative amounts of porosity in the samples were estimated from backscattered electron microscope images (BSEM) by assuming that porosity is epoxy-filled and occurs as a black phase in BSEM-images. The porosity area percentages are estimates of their volume fractions (Underwood, 1970).

Grain growth in the dried plagioclase-olivine powders was very limited at 900°C. A sample prepared from 12 hours-dried 4-10 μm powders had 40% of porosity after 24 hours of hot pressing at 600 MPa (Fig. 2.10a). Extending the duration of hot pressing to 48 hours at 740 MPa resulted in 20% porosity in a 24 hr-dried sample (Fig. 2.10b).

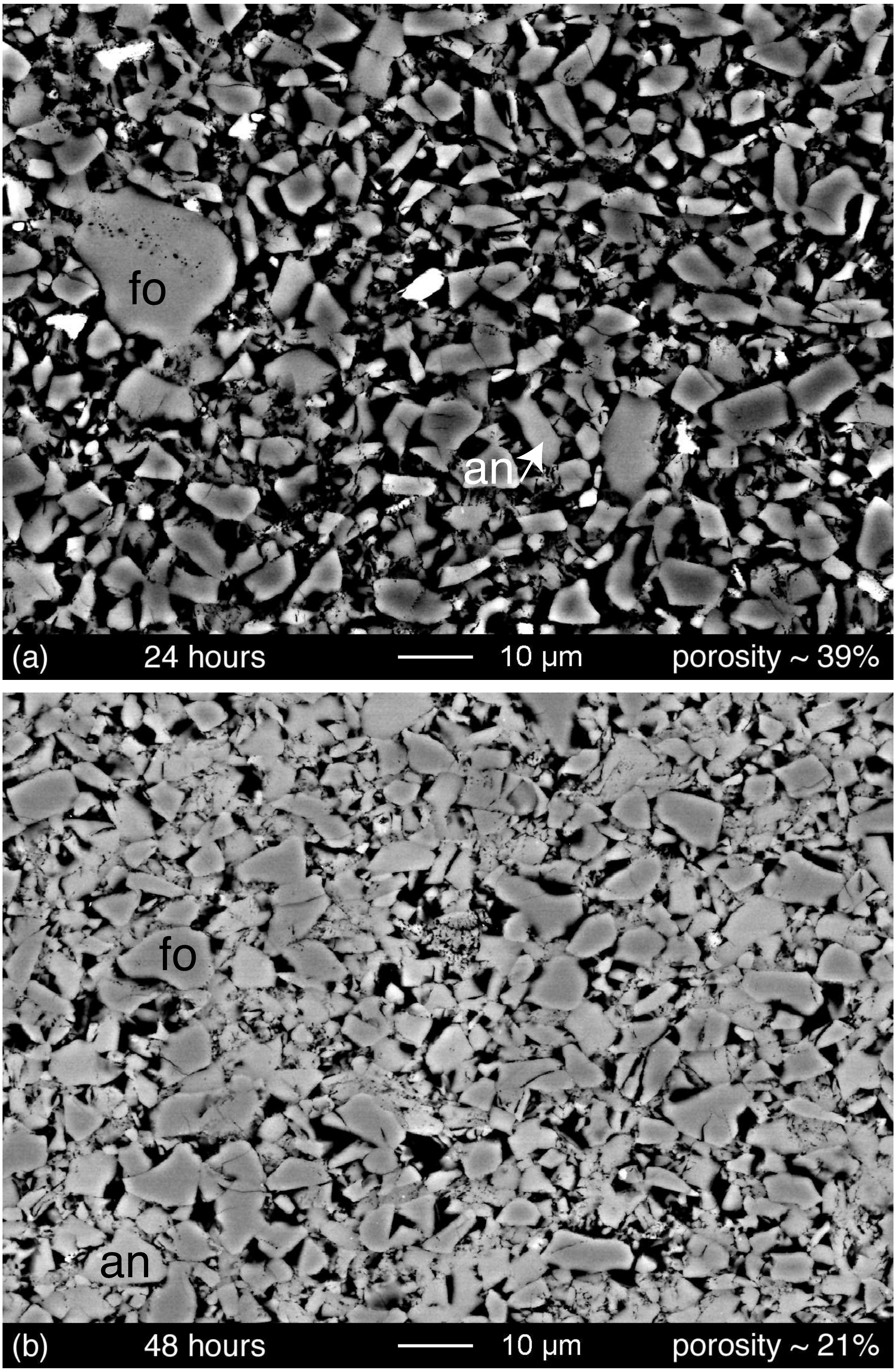

Figure 2.10: Annealing of dried plagioclase-olivine mixtures at 900°C: effect of time (BSEM-images, magnification = 800x). Minerals: plagioclase (an), olivine (fo). (a) 24 hours at P_c= 600 MPa (sample W1015: 4-10 µm powders, 12 hr-drying). Olivine and plagioclase grains are difficult to distinguish in the image. (b) 48 hours at P_c= 740 MPa (sample 3AA: 4-10 µm powders, 24 hr-drying).

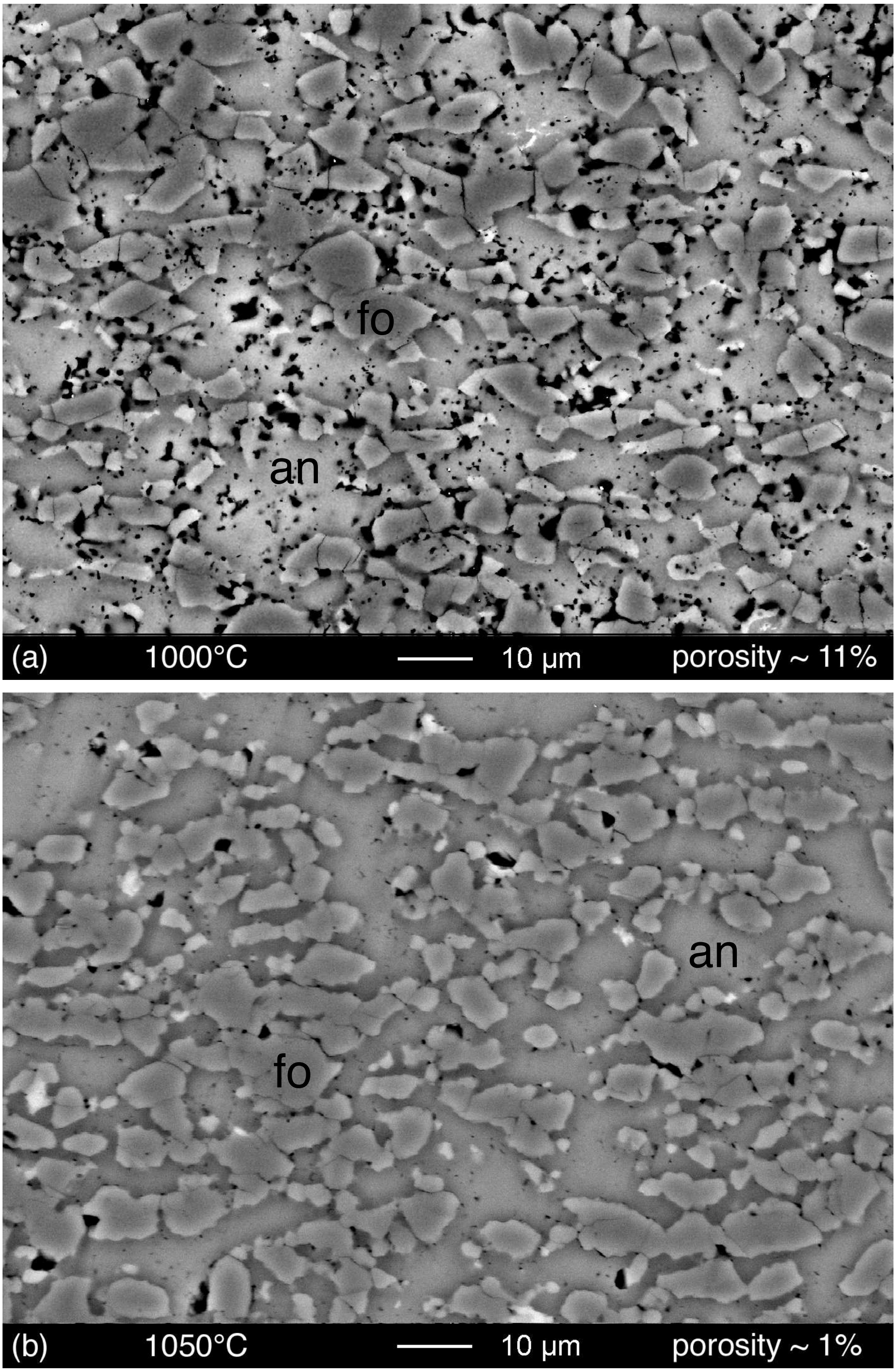

Figure 2.11: Annealing of dried plagioclase-olivine mixtures: effect of temperature (BSEM-images, magnification = 800x). Minerals: plagioclase (an), olivine (fo). (a) 24 hours at 1000°C and P_c= 775 MPa (sample 5AA: 4-10 µm powders, 24 hr-drying). (b) 24 hours at 1050°C and P_c= 750 MPa (sample W1026: 4-10 µm powders, 12 hr-drying).

These samples suggest that grain growth of extensively dried plagioclase-olivine mixtures was limited due to the relatively low temperature of 900°C and the absence water in the plagioclase-olivine grain boundaries.

Temperature and pressure had large effects on the grain growth of plagioclase-olivine mixtures, even if the mixtures were dried for 12 to 24 hours in a CO-CO_2 gas flow. A plagioclase-olivine sample showed a strongly reduced porosity of ~10% after 24 hours at 1000°C and 775 MPa (Fig. 2.11a). A dense sample (porosity of ~1%) formed after 24 hours at 1050°C and 750 MPa (Fig. 2.11b). Plagioclase-olivine samples with the lowest porosity were obtained after hot pressing at high pressures. A sample prepared with 2-6 μm powder was hot pressed for 24 hours at 900°C and 790 MPa first and then kept for another 30 hours at 900°C and 1500 MPa (Fig. 2.12). This reduction of porosity was due to the higher confining pressure of 1500 MPa because there is only limited growth after 24 and 48 hours at 900°C and ±700 MPa (Figs. 2.10). Plotting the sample-porosity versus temperature and pressure indicates that porosity follows an approximately exponential relationship with temperature and pressure (Fig. 2.13).

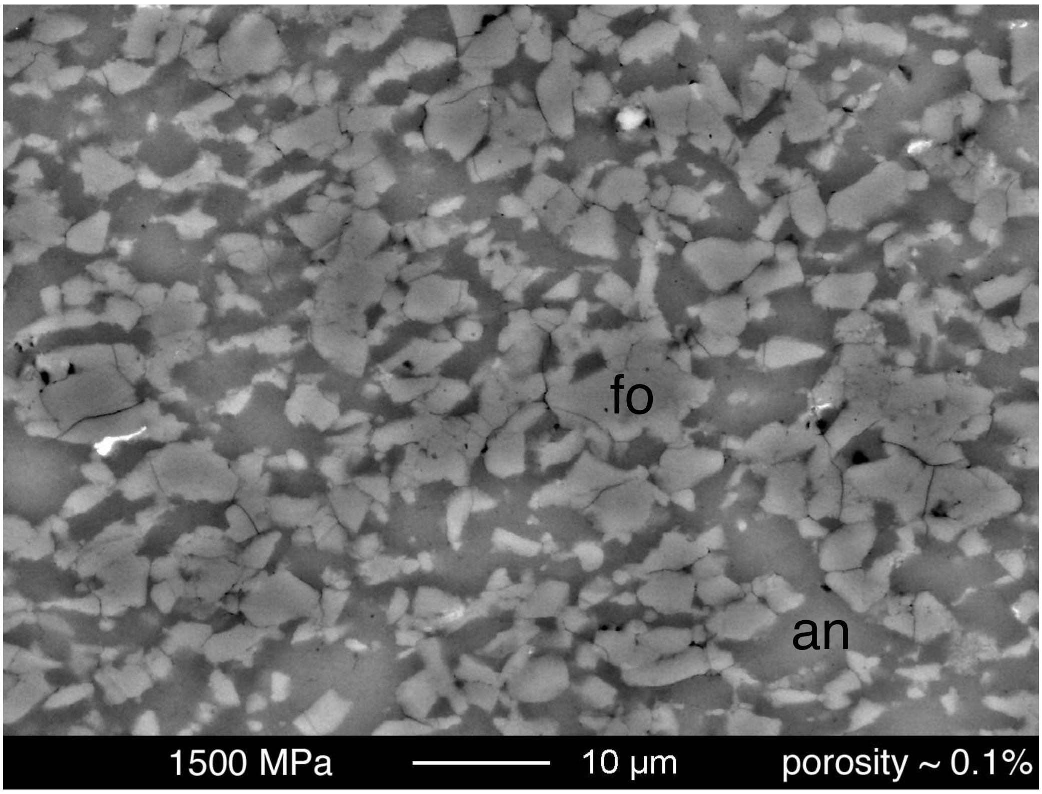

Figure 2.12: Annealing of dried plagioclase-olivine mixtures at 900°C: effect of pressure (BSEM-images, magnification = 800x). Minerals: plagioclase (an), olivine (fo). A dense plagioclase-olivine sample was obtained after 24 hours of hot pressing at 900°C and P_c= 790 MPa, followed by 30 hours at P_c= 1500 MPa (W1045; 2-6 μm powders, 6 hr-drying).

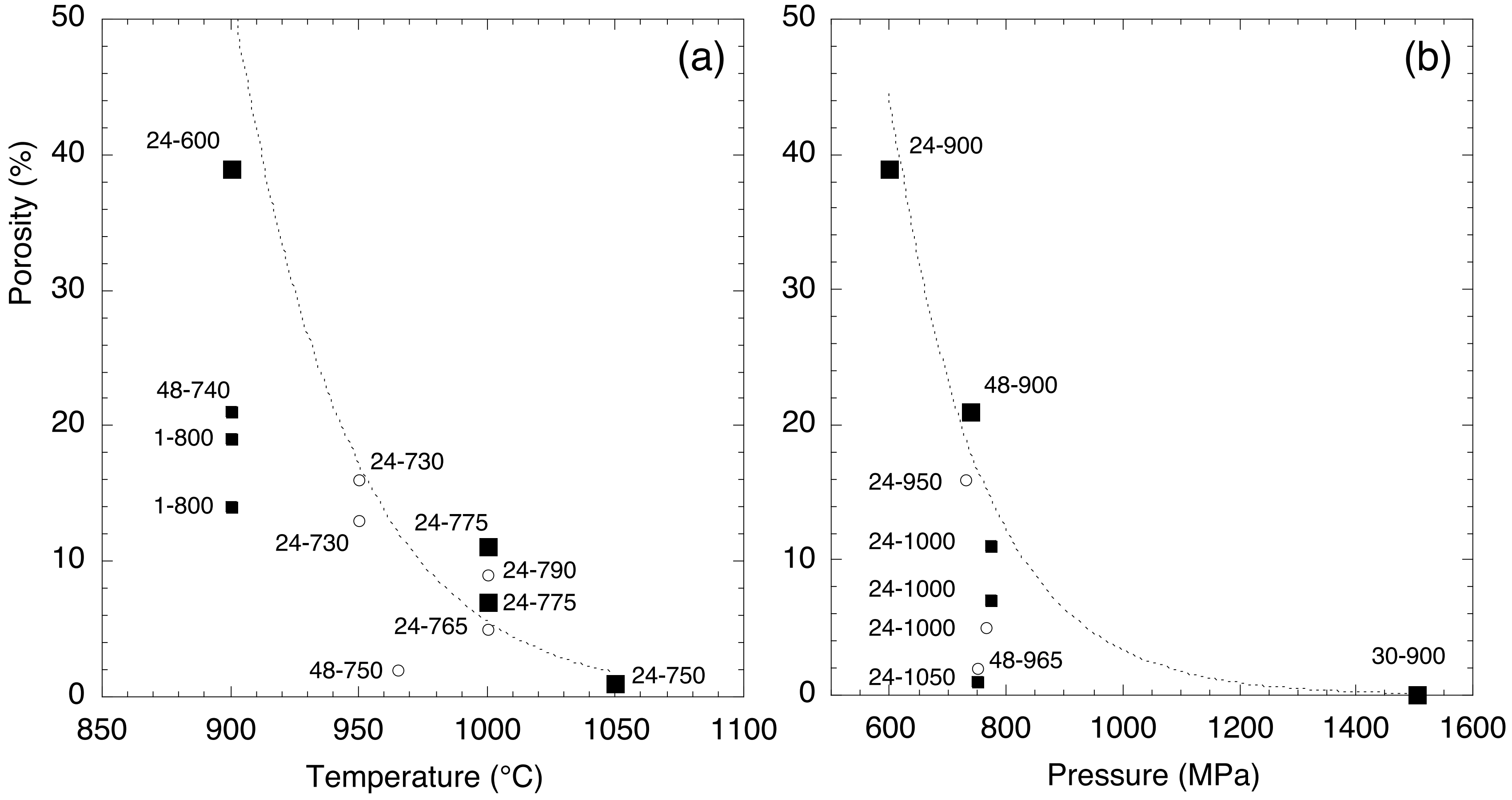

Figure 2.13: Plagioclase-olivine sample porosity versus temperature and confining pressure. Squares: samples dried for 6-24 hours at 1000°C. Circles: as-is samples (oven-dried for >72 hrs at 110°C). Dotted lines are curve fits based on large symbols. (a) Porosity decreases exponentially with temperature in samples that were dried and hot pressed for 24 hours. As-is samples that were hot pressed for 24 hours fit to the same exponential trend. Labels: duration (hr) - P_c (MPa). (b) A strongly decreased porosity is observed in a sample kept at 1500 MPa. An exponential curve fit is suggested for dried hot-pressed samples at 900°C. Labels: duration (hr) - T(°C).

The use of as-is powders instead of dried powders resulted in denser samples at lower temperatures. The porosity of as-is samples slightly decreased from 950°C to 1000°C in 24 hours (Fig. 2.14a-b). Extending the duration of hot pressing to 48 hours at temperatures close to molten salt conditions (i.e. 965°C) resulted in only ∼2% porosity (Fig. 2.14c). The faster grain growth is probably due to the presence of trace amounts of water on the grain boundaries of olivine and plagioclase. Undried Sonoran labradorite powder can contain approximately 0.1 wt.% of absorbed water (Stünitz and Tullis, 2001). The as-is plagioclase-olivine powders may contain 0.05-0.1 wt.% of water after 72 hours of oven-drying at 110°C (see Chapter 4).

Based on the grain growth experiments, the hot pressing conditions for the preparation of dense plagioclase-olivine samples were chosen to be 48 hours at 965°C and 700 MPa. High confining pressures could not be applied to enhance grain growth because the plagioclase-olivine assemblage is only stable at low pressures (Fig. 2.9). Temperatures above ±980°C could not be applied due to the melting of the confining medium and instability of the sample assembly. Therefore a combination was chosen of intermediate temperatures within the 950-980°C range, confining pressures not exceeding 800 MPa and as-is plagioclase-olivine powders. These hot pressing conditions yielded a plagioclase-olivine starting material with an acceptable low porosity of 2% (Fig. 2.14c).

2.5 Problems with the experimental setup

The plagioclase-olivine samples used in this study needed to satisfy specific requirements. The grain size of olivine and plagioclase had to be at least 4 to 10 μm in order to achieve grain size insensitive deformation (Chapter 4). The samples needed to be dry and dense. The hot pressing and deformation of each sample was performed in one experimental run due to the limited availability of mineral powders. The experiments were aimed to be performed at 900°C, based on the plagioclase-olivine phase transitions (Fig. 2.9).

hot pressing temperatures above 980°C were considered to be important to meet these requirements because an increased temperature promotes grain growth even in dry samples. High temperatures during hot pressing caused a practical problem for the experiments. Assemblies needed to be heated and cooled between 900°C-1050°C while staying inside the plagioclase-olivine stability field which jeopardised the stability of the thermocouple. Most failed experiments were due to thermocouple failure during or after

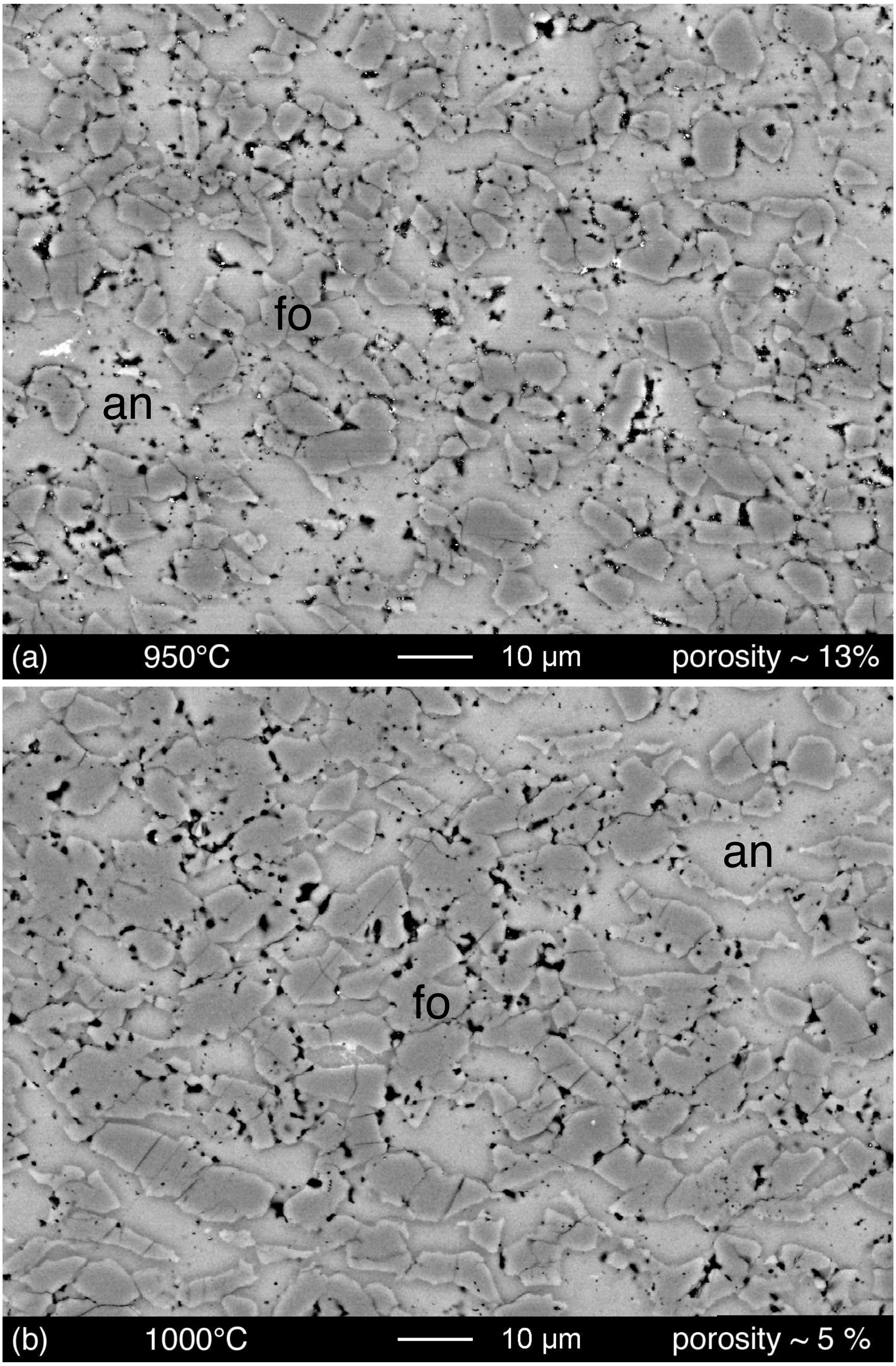

Figure 2.14: Annealing of 'as-is' plagioclase-olivine mixtures (BSEM-images, magnification = 800x). Minerals: plagioclase (an), olivine (fo). Samples were prepared from 4-10 µm powders. 'As-is': oven-dried for >72 hrs at 110°C. (a-b) Effect of temperature (samples 13AA and 16AA): as-is mixtures hot pressed for 24 hours at (a) 950°C-730 MPa and (b) 1000°C-765 MPa indicate that the porosity decreases with temperature.

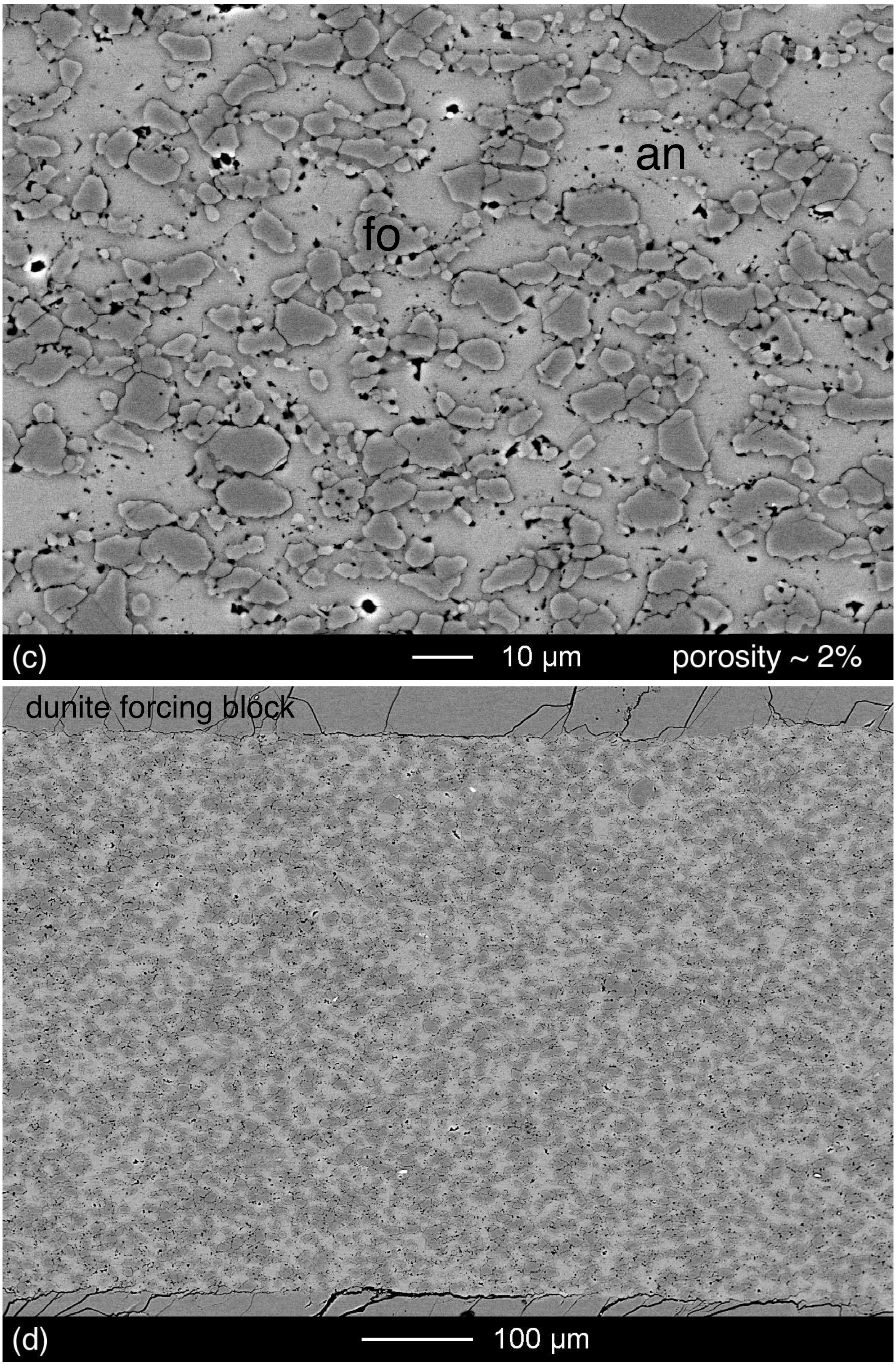

Figure 2.14: (Continued: c; 800x) Effect of time (44AA): a similar porosity as in (b) is achieved by hot pressing as-is mixtures for 48 hours at 965°C and 750 MPa. (d; 150x) A part of sample 44AA, representing the starting material of the deformation experiments. The homogeneously grey dunite forcing blocks can be seen at the top and bottom. The microstructure shows a rather well dispersed distribution of plagioclase (light grey) and olivine (dark grey).

the molten salt hot pressing while raising the pressure to the deformation conditions (Table A.1). The thermocouple typically broke at the site where it passes through the inner pyrophyllite-furnace sleeves. The most plausible explanation for these failures is the difference in thermal expansion and contraction of the pyrophyllite sleeves, graphite furnace and the molten inner salt liner during alternating P-T conditions. In the situations where the molten salt hot pressing and subsequent cooling were successful, the thermocouple tubing probably got damaged during changing temperature conditions and subsequent failed during additional pressurisation.

The following precautions were taken in order to overcome the problem of thermocouple failure while using temperatures near or above the sodium chloride melting curve:

1. Avoiding the MS-assembly altogether because it contains an extra graphite sleeve through which the thermocouple passes (Fig. 2.7). As a consequence the hot pressing temperature was reduced below 1000°C in order to prevent melting of the entire inner salt liner. The duration of hot pressing was increased to 48 hours to ensure sufficient grain growth.

2. Using a K-type chromel-alumel (Cr-Al) thermocouple, which has a flexible and less brittle metal casing (experiments 18AA-21AA, Table A.1). This option was unsuccessful because the thermocouple casing did not hold at partially molten salt conditions.

3. Using an aluminium-oxide ring at the furnace to support the horizontal thermocouple piece (Fig. 2.5). Experiments with an aluminium-oxide ring around the mullite tubing were successful.

4. Allowing a two hour cooling period between high temperatures (>950°C) and 900°C in order to carefully accommodate volumetric changes in the sample assembly. Most of the experiments with slow cooling periods were successful.

5. Increasing the thickness of the Pt-PtRh thermocouple wire from 0.25 to 0.35 mm. This is useful because thicker thermocouple wire is stronger and likely last longer than thin wires.

The combination of heating and cooling of the assembly while crossing the NaCl-melting curve was considered the main cause of the major experimental failures. For this reason, temperatures involving a partially molten inner salt liner (>980°C) were avoided. The final configuration for the experiments was a combination of (1),(3),(4) and (5), which resulted in very stable and successful experimental runs.

The experimental techniques and experiences described in this chapter provide a basis for stable and successful plagioclase-olivine experiments. Future research might benefit from the following suggestions. One limitation in this study was the poorly available quantity of natural Blumone gabbro anorthite. Replacing the Blumone anorthite with a more readily available alternative, in the ideal case single crystals, would simplify sample preparation and would enable the production of plagioclase-olivine mixtures in larger quantities. The advantage of large powder quantities is that the powder mixing can be performed by other techniques, for example using a tumbling apparatus. This technique does not involve fluid-powder interaction and therefore might prevent grain size sorting and phase partitioning.

Cores of plagioclase-olivine rock could be prepared in separate experimental runs, for example using a gas-apparatus in which high temperatures (>1000°C) are easily achieved. The plagioclase-olivine sample cores can be dried separately and cut into fixed dimensions for each experiment. A better characterisation of the starting material would be possible. Separating the sample production and hot pressing from the actual experiment would remove the problem of alternating pressure and temperature conditions and hence simplify the experiment and sample assembly.

Chapter 3

Spatial correlation of deformation and mineral reaction in experimentally deformed plagioclase-olivine aggregates *

3.1 Abstract

Shear deformation of hot pressed plagioclase-olivine aggregates was studied in the presence and absence of mineral reaction. Experiments were performed at 900°C, 1500 MPa and a constant shear strain rate of $\sim 5\text{x}10^{-5}\text{s}^{-1}$ in a solid medium apparatus. Whether the mineral reaction between plagioclase and olivine takes place or not is controlled by choosing the appropriate plagioclase composition; labradorite (An_{60}) does not react, anorthite (An_{92}) does. Labradorite-olivine aggregates deformed without reaction are very strong and show strain hardening throughout the experiment. Syndeformational reaction between olivine and anorthite causes a pronounced strain weakening. The reaction produces fine-grained opx-cpx-spinel aggregates which accommodate a large fraction of the finite strain. Deformation and reaction are localised within a 0.5 mm wide sample. Three representative samples were analysed for their fabric anisotropy R* and shape preferred orientation α^* (fabric angle with the shear plane) using the auto-correlation function (ACF). The fabric anisotropy can be calibrated to quantify strain variations across the sheared samples. In the deformed and reacted anorthite-olivine aggregate, there is a strong correlation between reaction progress and strain: regions

---

*A.A. de Ronde, R. Heilbronner, H. Stünitz, J. Tullis, 2004. Tectonophysics 389 (1-2), 93–109.

of large shear strain correspond to regions of maximum reaction progress. Within the sample, the derived strain rate variations range up to almost one order of magnitude.

3.2 Introduction

Upper mantle and lower crustal deformation involves polyphase aggregates and may occur simultaneously with mineral reactions (White and Knipe, 1978; Rubie, 1983; Brodie and Rutter, 1987; Rutter and Brodie, 1995; Olgaard et al., 1995; Newman et al., 1999; Handy and Stünitz, 2002). In many cases deformation takes place at pressure-temperature conditions that differ from those of the formation of the constituent minerals. In natural mylonites, the association of deformation with the occurrence of metamorphic reactions is well documented, for example in granitic mylonites (Rubie, 1983; Fitz Gerald and Stünitz, 1993; Tsurumi et al., 2003), lherzolites (Newman et al., 1999; Furusho and Kanagawa, 1999) and eclogite facies shear zones (Klaper, 1990). Mineral reactions often lead to the production of new phases with a strongly reduced grain size, allowing the deformation mechanism to change to diffusion-accommodated grain boundary sliding (Boullier and Gueguen, 1975; Kerrich et al., 1980; Rubie, 1983; Rutter and Brodie, 1988b; Stünitz and Fitz Gerald, 1993; Newman et al., 1999; Stünitz and Tullis, 2001).

Although there is qualitative evidence that syndeformational reactions may lead to significant strain weakening, there have been few experimental studies relating mineral reaction to deformation and vice versa, and most of these have focused on dehydration (Murrell and Ismail, 1976; Rutter and Brodie, 1988a; Paterson, 1989; Olgaard et al., 1995) and hydration reactions (Rutter et al., 1985; Stünitz and Tullis, 2001). So far, experimental studies on solid-solid reactions during deformation have only involved polymorphic phase transitions (Kirby, 1987; Burnley and Green, 1989; Green and Houston, 1995).

In order to study the potential effect of syndeformational solid-solid reactions on the strength and the deformation mechanisms of polyphase rocks, we have performed shear deformation experiments on olivine-plagioclase aggregates both within and outside their stability fields. The system plagioclase-olivine was chosen because mineral reactions during deformation of peridotites are considered possible causes for weakening, i.e. strain localisation in the upper mantle (Newman et al., 1999; Handy and Stünitz, 2002).

Shear deformation experiments were carried out at 900°C and a confining pressure of 1500 MPa. At 900°C and 1500 MPa in the CaO-MgO-Al_2O_3-SiO_2-system, the deform-

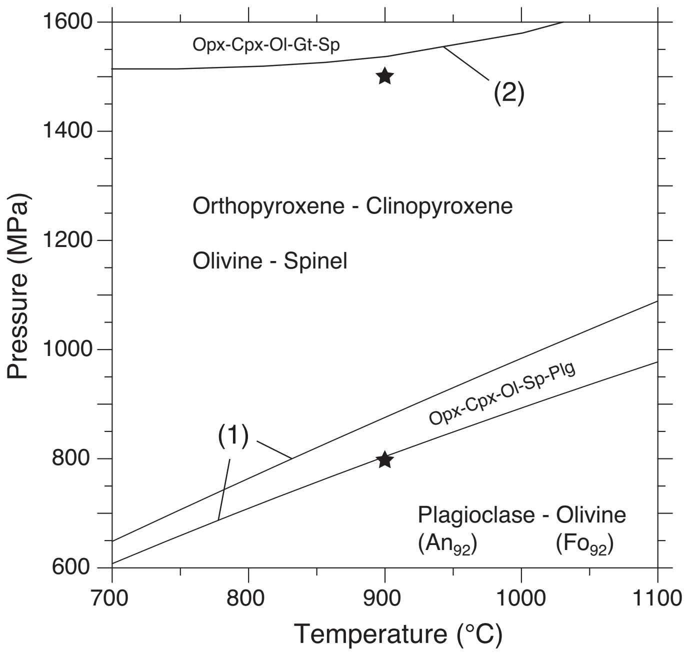

Figure 3.1: Phase diagram for peridotites. The plagioclase to spinel transition (1) is calculated for a (2 Fo_{92})-(An_{92}) bulk composition in the system Na_2O-CaO-FeO-MgO-Al_2O_3-SiO_2 using the program DOMINO (de Capitani and Brown, 1987; de Capitani, 1994) with the Berman (1988) database. The spinel-garnet lherzolite transition (2) is based on a compilation of experimental data of the system CaO-MgO-Al_2O_3-SiO_2 (Jenkins and Newton, 1979; O'Neill, 1981; Gasparik, 1984; Herzberg and Gasparik, 1991; Klemme and O'Neill, 2000). The stars indicate the pressure and temperature conditions of the hot pressing (900°C, 800 MPa) and the deformation experiments (900°C, 1500 MPa).

ation of anorthite-olivine aggregates takes place simultaneously with the multi-variant reaction of anorthite + 2 forsterite = spinel + clinopyroxene + orthopyroxene (Fig. 3.1). For this study, the plagioclase-olivine phase relationships have been calculated using the program DOMINO (de Capitani and Brown, 1987; de Capitani, 1994) and are combined with experimental data from the literature. Three experiments were performed (Table 3.2). (1) A hydrostatic experiment using anorthite (An_{92}) and olivine (Fo_{92}) mixtures at the same conditions as the deformation experiments, to observe possible reaction progress before the onset of deformation. The duration of the hydrostatic experiment is equal to the time during which a regular deformation experiment is exposed to experimental pressure and temperature before the actual run is started. (2) A deformation experiment has been performed using labradorite (An_{60}) and olivine (Fo_{92}) mixtures to study deformation in the absence of reaction. The labradorite-olivine paragenesis has a larger stability field than anorthite-olivine and does not react at 1500 MPa and 900°C. (3) A second deformation experiment has been performed at the same P-T-conditions as (2) using anorthite (An_{92}) and olivine (Fo_{92}) mixtures to study concurrent reaction and deformation (Fig. 3.1). Labradorite and anorthite have similar deformation behaviour (Tullis and Yund, 1999) so that, in terms of intracrystalline plasticity, they should both be valid representatives of a plagioclase phase.

Experiment no.	**1**	**2**	**3**
Sample	An_{92}-Fo_{92}	An_{60}-Fo_{92}	An_{92}-Fo_{92}
Conditions: P(MPa)-T(°C)	1500-900	1480-900	1490-900
Type	hydrostatic	deformation	deformation
Max. γ $^{1)}$	0.0	1.7	4.0
Bulk shear $\dot{\gamma}$ $(\cdot 10^{-5} s^{-1})$ $^{1)}$	0.0	3.2	5.2
Shear displacement (mm)			
-displacement transducer$^{1)}$	0.000	0.827	1.813
-forcing blocks displacement$^{2)}$	0.591	0.309	1.520
Av. shear zone thickness (mm)$^{2)}$	0.492	0.444	0.415
Time (hours)			
-hot pressing (800 MPa-900°C)	24.0	24.0	24.0
-hydrostatic at conditions	30.0	18.2	30.5
-deformation	0.0	12.3	21.2

$^{1)}$ Derived from apparatus data

$^{2)}$ Measured after the experiment on thin section

Table 3.1: Experimental data for the samples used in this study.

The following study focuses on the attempt to quantify strain and the distribution of reaction products in the samples in order to study the interdependence of reaction and deformation. In order to determine the correlation between finite strain and the extent of reaction, the microstructures of the samples were analysed using the autocorrelation function (ACF, Panozzo Heilbronner (1992)). The fabric analysis was then calibrated for finite strain.

3.3 Experiments

3.3.1 Procedure

Plagioclase-olivine samples were prepared by hot pressing 2-6 μm grain size fractions of ground Åheim dunite olivine (Fo_{92}), Blumone gabbro anorthite (An_{92}), and gem quality Sonoran labradorite (An_{60}). The minerals were crushed, handpicked and further ground in an alumina mortar. The grain size fractions of the olivine and plagioclase powders were separated using a sedimentation method in alcohol and water, respectively. Olivine and anorthite or olivine and labradorite were mixed in a 2:1 molar ratio (47:53 volume percent ratio) in alcohol using an ultrasonic stirrer. We placed 77.8 milligrams of the powder mixture inside a nickel jacket, between cylindrical forcing blocks of Balsam Gap dunite which were cut at 45° to the cylinder axis. The forcing block surfaces contained grooves normal to the shear direction in order to maintain a good grip on the sample during the experiment. The samples were then dried for 6 hours at 1000°C in a CO-CO_2 gas mixture. The Ni jackets were mechanically sealed and the samples were subsequently hot pressed in the solid medium apparatus for 24 hours at 800 MPa and 900°C. The hot pressing conditions were at the upper pressure limit within the anorthite-olivine stability field (Fig. 3.1).

The general shear deformation experiments were performed in a modified Griggs apparatus (Tullis and Tullis, 1986) using an all-NaCl sample assembly. The samples were deformed at a constant shear strain rate of $\sim 5\text{x}10^{-5}\text{s}^{-1}$ at 900°C and 1500 MPa. The force and displacement data were processed with a computer program.

Thin sections were prepared normal to the sample-forcing block interface (SFBI) and parallel to the macroscopically observed shear displacement (i.e. XZ-plane of the strain-ellipsoid). The samples were studied in backscattered imaging mode (BSEM) using a Phillips XL 30 scanning electron microscope. The shear displacements in the deformed samples were derived from the offsets of the forcing blocks. Images were taken at a magnification of 1600x, an acceleration voltage of 25 kV and a working distance of 7.0 mm. Continuous series of images were obtained normal to the sample-forcing block interface (SFBI) and parallel to the shear direction.

Table 3.2 lists the details of experiments conducted in this study. We will focus on (1) a hydrostatic experiment in the absence of reaction, (2) a labradorite-olivine experiment to establish the strength of a non-reacting sample and (3) an anorthite-olivine experiment to study the effect of deformation during mineral reaction. The shear stress-shear strain data for the experiments are given in Figure 3.2.

3.3.2 Results

Hydrostatic sample

The hydrostatic anorthite-olivine aggregate (sample 1) did not react and its microstructure is inferred to represent that of the starting material. The microstructure shows a rather well dispersed distribution of plagioclase and olivine in a 46-54 volume percent ratio (Fig. 3.3a). Prior to deformation, olivine and presumably plagioclase have a mean grain size of 3.4±1.2 µm (Fig. 3.3b). In some locations, the sample contains extremely fine-grained (<1 µm grain size) lens-shaped domains of plagioclase and olivine (Fig.

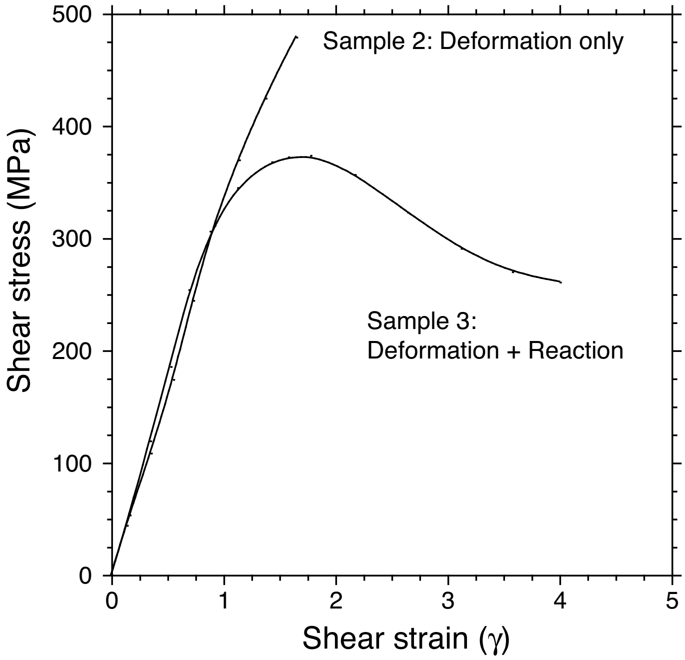

Figure 3.2: Shear stress versus shear strain data for plagioclase-olivine deformation experiments. See Table 3.2 for details. Sample 2: An_{60}-Fo_{92} deformed at 1480 MPa and 900°C without reaction. The sample is very strong and shows no measurable permanent strain. There is strain hardening without yield throughout the experiment. Sample 3: An_{92}-Fo_{92} deformed at 1500 MPa and 900°C with reaction. The sample has a high yield strength and shows weakening of 100 MPa and substantial mineral reaction.

3.3c), sometimes with a gradation in grain size. These domains originate from a crust that formed during settling and drying of the mineral powders. A number of such domains are randomly distributed across the sample.

Deformed samples

The labradorite-olivine aggregate (sample 2) is very strong at 1480 MPa confining pressure, showing an increase of shear stress to 475 MPa (Fig. 3.2). The microstructure of the undeformed material (Fig. 3.3a) and the microstructure of the deformed labradorite-olivine sample (Fig. 3.4a) are similar, indicating that only a small amount of permanent strain has been acquired by the sample. Up to a shear strain of $\gamma = 1.0$, the loading curves of the solid medium experiments are difficult to interpret. Up to that point, samples do not acquire permanent strain. It is also obvious that the anorthite-olivine and labradorite-olivine samples show the same mechanical behaviour up to $\gamma = 1.0$ (Fig. 3.2).

After $\gamma = 1.0$, the anorthite-olivine experiment (sample 3, Fig. 3.2) shows a shear stress maximum of 380 MPa followed by a 100 MPa weakening. From site to site in the sample, variable proportions of olivine and plagioclase have reacted (Fig. 3.4b-d). Reaction products form elongate and laterally continuous streaks and layers, parallel or sub parallel to the shear direction. These layers appear to accommodate large shear strains. Olivine grains are less elongated than anorthite grains and have σ-clast

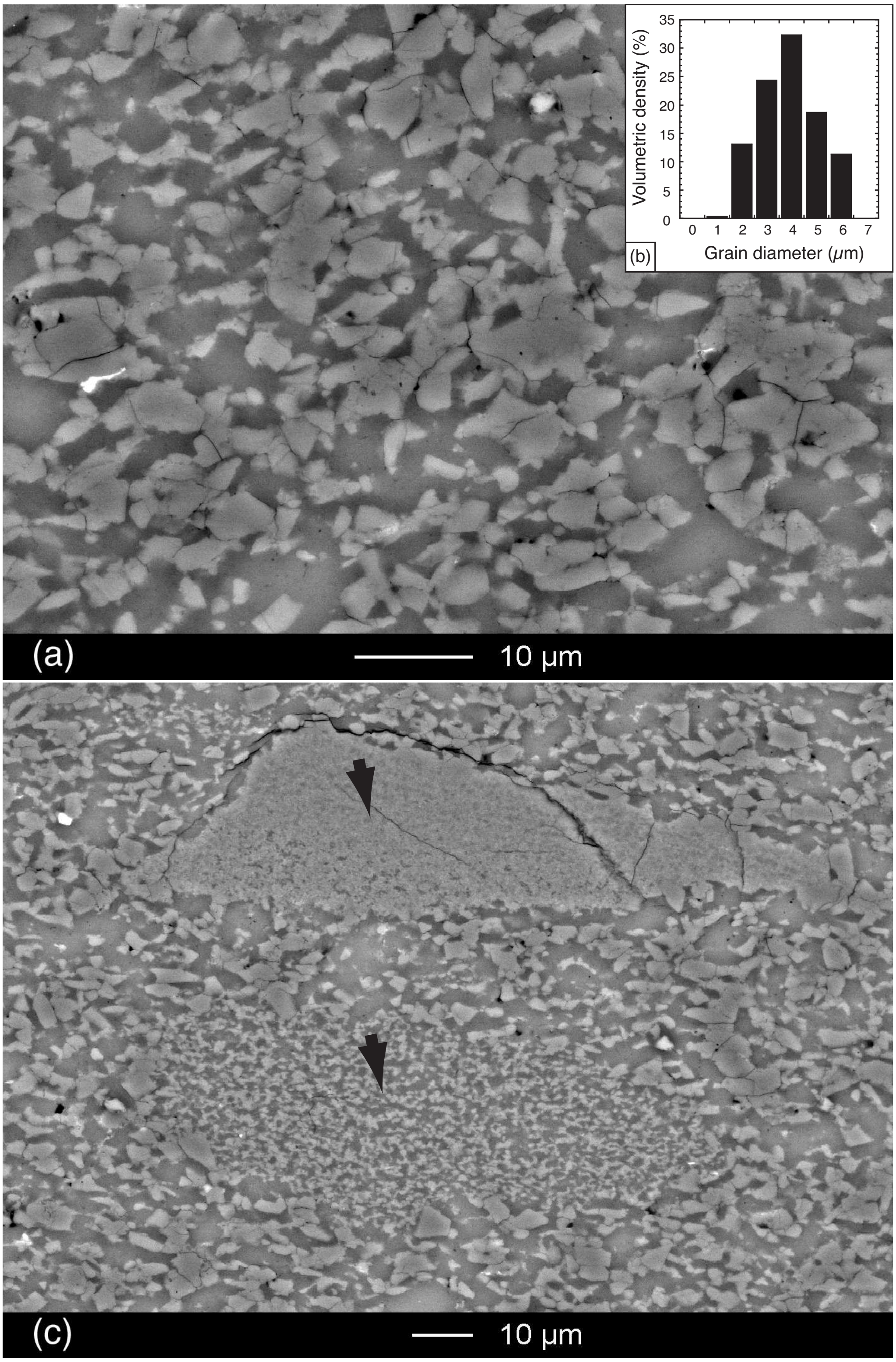

Figure 3.3: SEM backscatter images of the hydrostatic plagioclase-olivine sample 1. Minerals: plagioclase (dark grey), olivine (intermediate grey). (a) Typical microstructure of the An_{92}-Fo_{92} aggregate (46-54 vol. % ratio), representative of the starting material of the deformation experiments. (b) Histogram of volume weighted 3-D grain size distribution of olivine in sample 1, derived from cross-sectional areas and calculated using the program StripStar (Heilbronner, 1998). (c) Examples of fine-grained anorthite-olivine domains (indicated by arrows) of smaller grain size that formed during sample preparation.

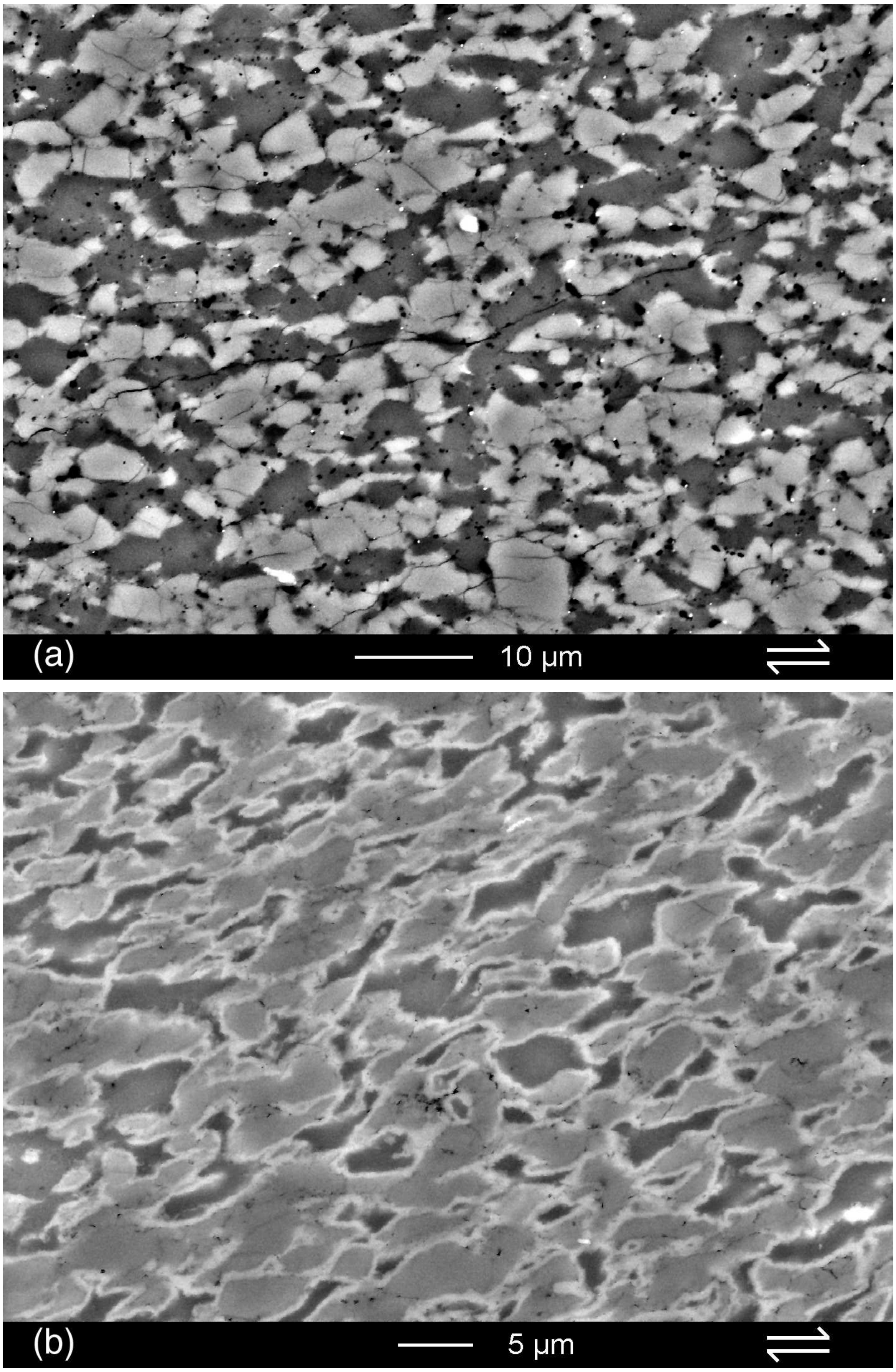

Figure 3.4: Characteristic microstructures of the deformed plagioclase-olivine samples (SEM backscatter images). Sections are prepared parallel to the shear direction and perpendicular to sample-forcing block interface (SFBI). Minerals: plagioclase (dark grey), olivine (intermediate grey) and reaction products (light grey). (a) An_{60}-Fo_{92} aggregate deformed at 1480 MPa (sample 2). Labradorite and olivine are only slightly flattened and slightly horizontally aligned. (b-d) An_{92}-Fo_{92} deformed at 1500 MPa (sample 3). Local variations of deformation intensity are visible as variations of elongation and preferred orientation of plagioclase and olivine grains, indicating increasing deformation and reaction progress from (b) to (d).

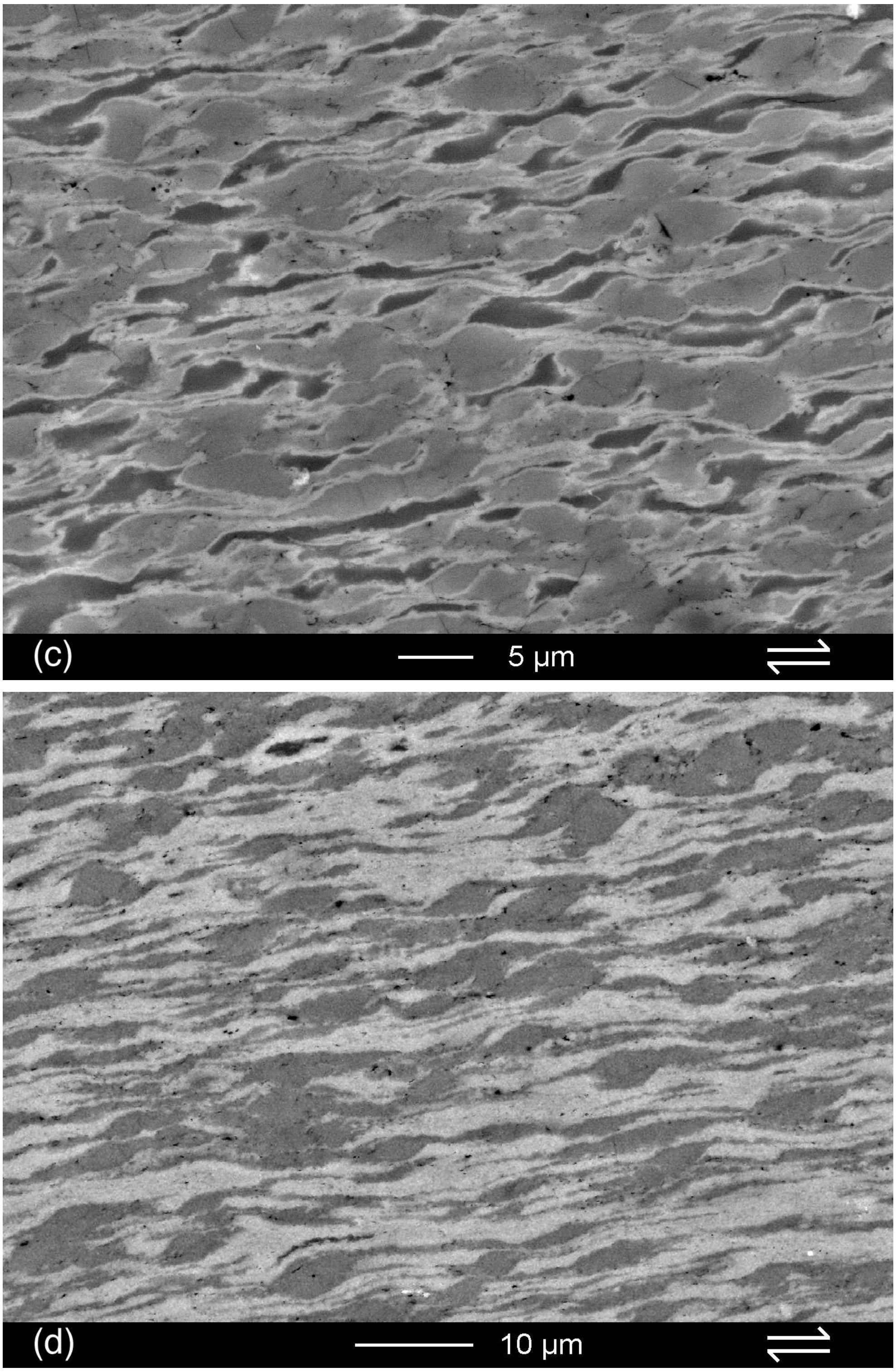

Figure 3.4: (continued) Small white rims around the grains are fine-grained reaction products (orthopyroxene, clinopyroxene and spinel). Reaction is not complete in (b) and (c) whereas (d) shows a site within the sample where plagioclase has reacted completely with olivine to form fine-grained (<1 µm) reaction products (light grey) and residual olivine grains (dark grey). The olivine grains are elongated and have σ-clast geometries with fine-grained recrystallised tails.

geometries (Fig. 3.4d), indicating that olivine is mechanically stronger than anorthite and the reaction products. On the grain scale, the reaction products appear to be the weakest component of the bulk aggregate. Therefore, the weakening of sample 3 is primarily attributed to the formation of fine-grained reaction products.

In an overview of the sheared sample (Fig. 3.5), several fine-grained plagioclase-olivine domains are observed. These domains have been partially deformed and reacted, as indicated by long tails and internal grey level variations. Their preferred orientation may be used as an indicator of strain.

In sample 3, the reaction products are heterogeneously distributed across the sample, indicating a partitioning of deformation and mineral reaction (Figs. 3.4 and 3.6). Large strains, indicated by elongated shapes of olivine and plagioclase grains, and significant reaction progress, indicated by the presence of reaction products, are correlated (compare Figs. 3.4b-d). Strain is typically concentrated between less deformed (more competent) fine-grained domains and near the grooves at the lower SFBI (Figs. 3.5 and 3.6). At these localities, strongly deformed zones or layers are observed, where no plagioclase is left and reaction is most advanced (Fig. 3.4d). Deformation and reaction are at a minimum in the strain shadows of fine-grained domains.

3.4 Microstructural analysis

3.4.1 Method of ACF analysis

We have studied the variation of deformation and the distribution of reaction products in the samples by analysing the autocorrelation function (ACF) of the microstructures. The ACF has been used in a number of microstructural studies on naturally and experimentally deformed rocks (e.g. Panozzo Heilbronner, 1992, 1993; Pfleiderer et al., 1993; Davidson et al., 1996; John and Stuenitz, 1997; Heilbronner, 2002). From the ACF, measures of anisotropy, symmetry and orientation as a function of correlation length (grain size, domain size) can be derived. The ACF technique and a comparison with other methods of fabric analysis is described by Panozzo Heilbronner (1992, 1993). A procedure for calculating local and bulk ACFs of experimentally deformed samples is given by Heilbronner (2002).

Figure 3.7 illustrates the basic steps of the ACF analysis used here. As a first step, a square grid subdivides the area of analysis (Fig. 3.6). The grid size has to be adjusted to the size of the objects (grains, domains) and the desired degree of sensitivity and resolution (Heilbronner, 2002). Here, we used a grid size of 256 x 256

Figure 3.5: SEM backscatter image of a part of the sheared sample 3. The location of the image within the sample is indicated in the top-left (black square). Forcing blocks (FB) are made of dunite and appear homogeneously grey. Grooves in the FBs can be seen at the top and bottom. Minerals: plagioclase (dark), olivine (intermediate grey) and reaction products (light grey). Fine-grained domains (crust flakes) of An_{92}-Fo_{92} occur throughout the entire sample. Arrows indicate domains where the reaction is complete. The area used for detailed microstructural analysis is outlined by solid black lines.

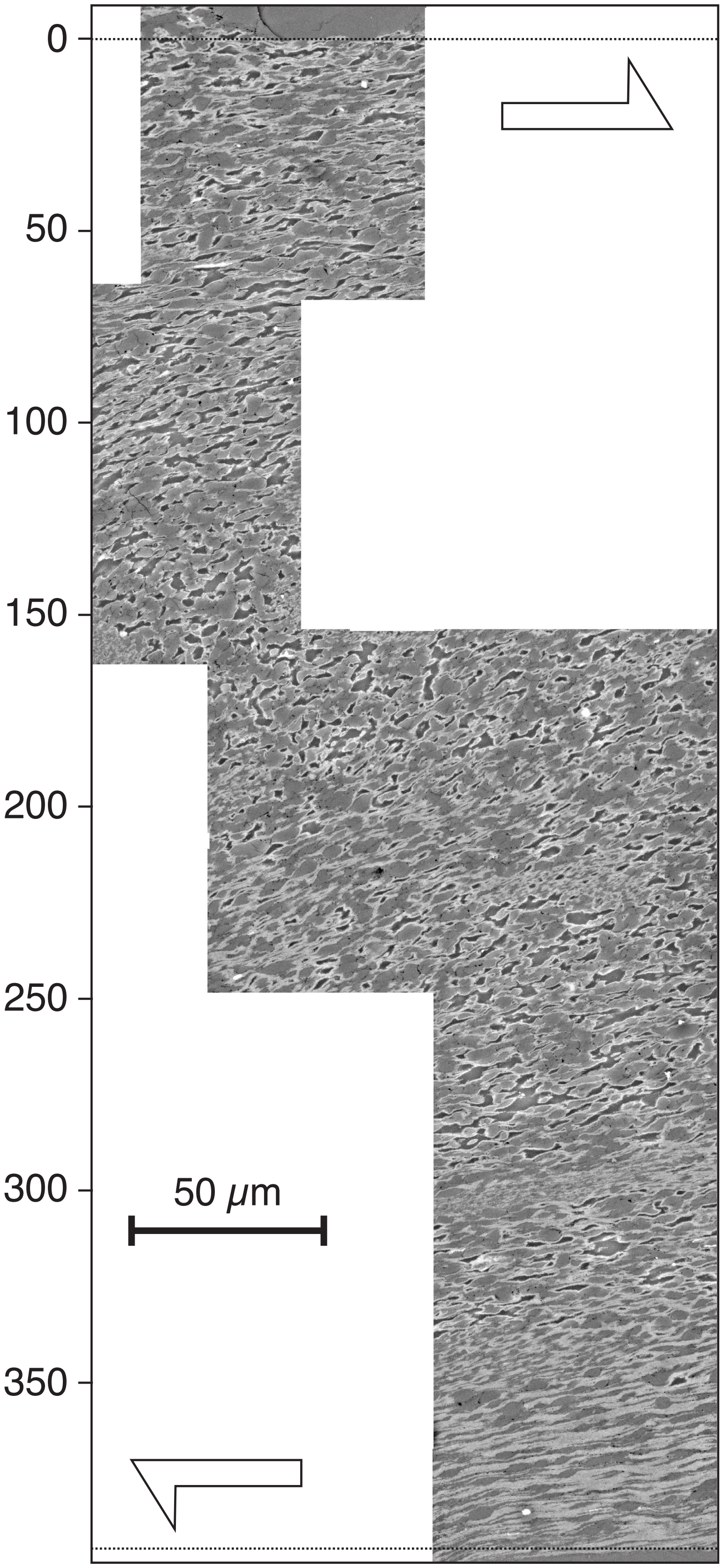

Figure 3.6: SEM backscatter transect across sample 3. The location of the transect in the sample is indicated in Figure 3.5. Minerals: plagioclase (dark), olivine (intermediate grey) and reaction products (light grey). The amount of deformation and of reaction are heterogeneous across the transect. Highly deformed and reacted zone occurs at the bottom of the transect.

pixels, corresponding to 14 x 14 μm. For each square, the ACF is calculated (Fig. 3.7b). For each row, all ACFs are averaged and thresholded (Fig. 3.7c). Assuming no change of microstructure along any given row, the resulting shape is taken to represent the average microstructure or shape fabric of the row. It is quantified by its anisotropy R^* and shape preferred orientation α^* (Fig. 3.7d) and depends only on the distance from the SFBI.

Three phases can be distinguished on the BSEM images (Fig. 3.4), which we can analyse together or separately; plagioclase (PLG) in dark grey, olivine (OL) in intermediate grey and 'reaction products' (RP) in light grey. Figure 3.8 shows how we separate the PLG, OL and RP phases by grey level slicing, creating a binary image for each phase. This procedure allows the individual ACF analysis of all three phases as well as the determination of the area percentages of olivine, plagioclase and reaction products. Based on stereological principles (Underwood, 1970), we can estimate the volume percentage of the phases to be equal to their respective area percentages. In samples 1 and 2, reaction products are absent so that only OL and PLG are present (Figs. 3.3a and 3.4a). In these cases, a separation of phases by grey level slicing (or thresholding) is only useful for volume determinations because the bitmap of OL is the negative of the bitmap of PLG and the ACF of any image and its negative are the same.

We have applied the ACF analysis to samples 1 (Fig. 3.9), 2 (Fig. 3.10) and 3 (Fig. 3.11) in order to determine the fabric of the starting material and to determine local variations of deformation with respect to the reaction progress. The measurements of R^*, α^* and volume percentages of the phases are plotted against distance d from the SFBI. We also determined the average ACFs of samples 1 and 2 by averaging all ACFs within the analysed areas.

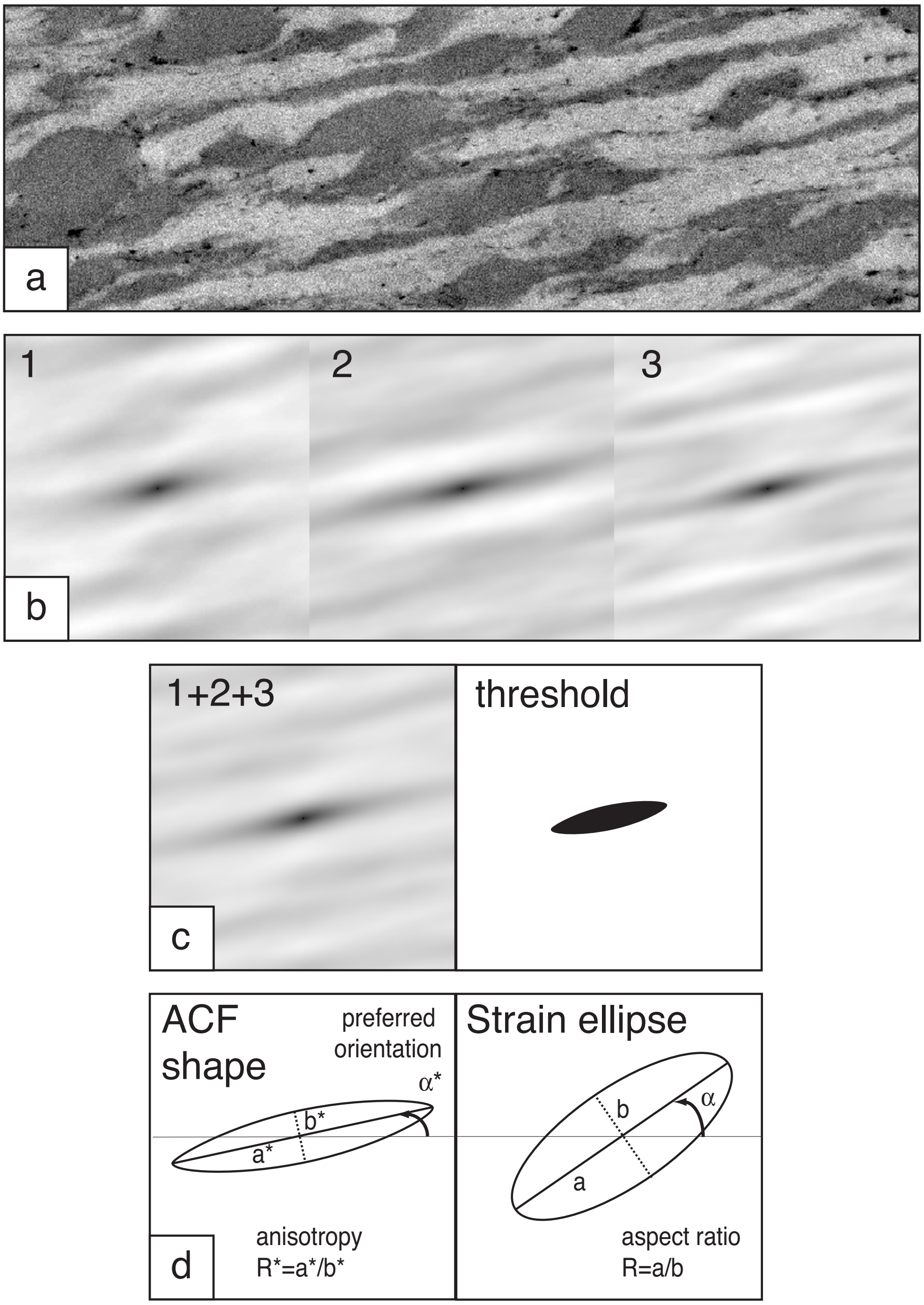

Figure 3.7: Steps in ACF Analysis using 'Lazy ACF Tiles' macro (Heilbronner, 2002). (a) BSEM image of a homogeneous microstructure. Olivine is dark grey, reaction products are light grey. The shear sense is dextral. (b) Three 256x256 pixel ACFs calculated for the area shown in (a). The size of each ACF is 14x14 µm. (c, left) Average ACF of ACFs 1, 2 and 3 in (b). (c, right) Thresholding the ACF (c, left) at a grey level of 39% peak height, yields the characteristic shape of the microstructure. This shape corresponds to the average grain size. (d, left) Fabric parameters derived from the ACF shape: anisotropy R^* and shape preferred orientation α^* (angle of the fabric long axis with a chosen reference line, in this case the SFBI). (d, right) Equivalent parameters of the strain ellipse for simple shear: aspect ratio R and angle α between the long axis of the strain ellipse and the shear direction.

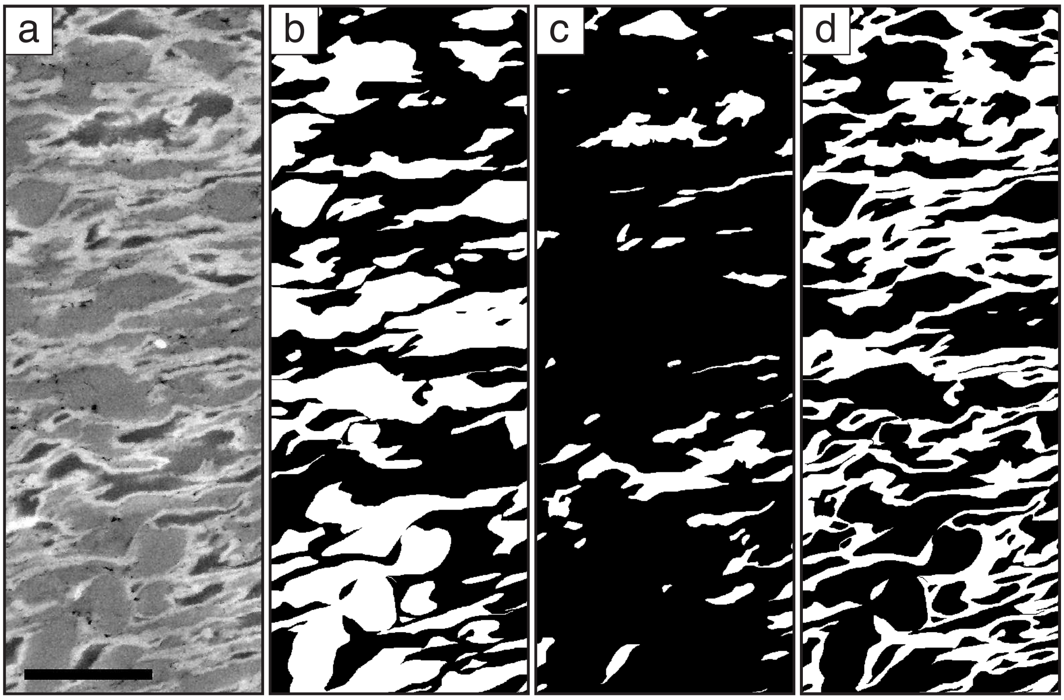

Figure 3.8: Grey level slicing of polyphase BSEM images. (a) Original BSEM image from sample 3 with three phases: plagioclase (dark grey), olivine (intermediate grey) and reaction products (light grey). The scale bar is 10 µm. (b) Binary image of olivine (OL in white). (c) Binary image of plagioclase (PLG in white). (d) Binary image of reaction products (RP in white).

3.4.2 Anisotropy and preferred orientation of the samples

Fabric of the hydrostatic sample

The analysis of the hydrostatic sample (Fig. 3.9) indicates that prior to deformation there is a moderate anisotropy (average R^*=1.56), with a shape preferred orientation (average α^*=6.3) sub parallel to the SFBI. This fabric arises from an alignment of the somewhat elongate initial shapes of the grains probably caused by compaction during hot pressing.

Fabric of the sample deformed without reaction

Across the shear zone of sample 2 (Fig. 3.10), the anisotropy remains constant and is almost identical (average R^*=1.59) to that of hydrostatic sample 1. The preferred orientation of the fabric varies within a slightly larger α^*-range and its average value (α^*=2.6) is shifted closer to the shear plane. In terms of fabric anisotropy, the fabric of sample 2 hardly records any permanent strain. The rotated α^*-values may indicate some shear strain but the larger range of α^*-values argues for a larger error as well.

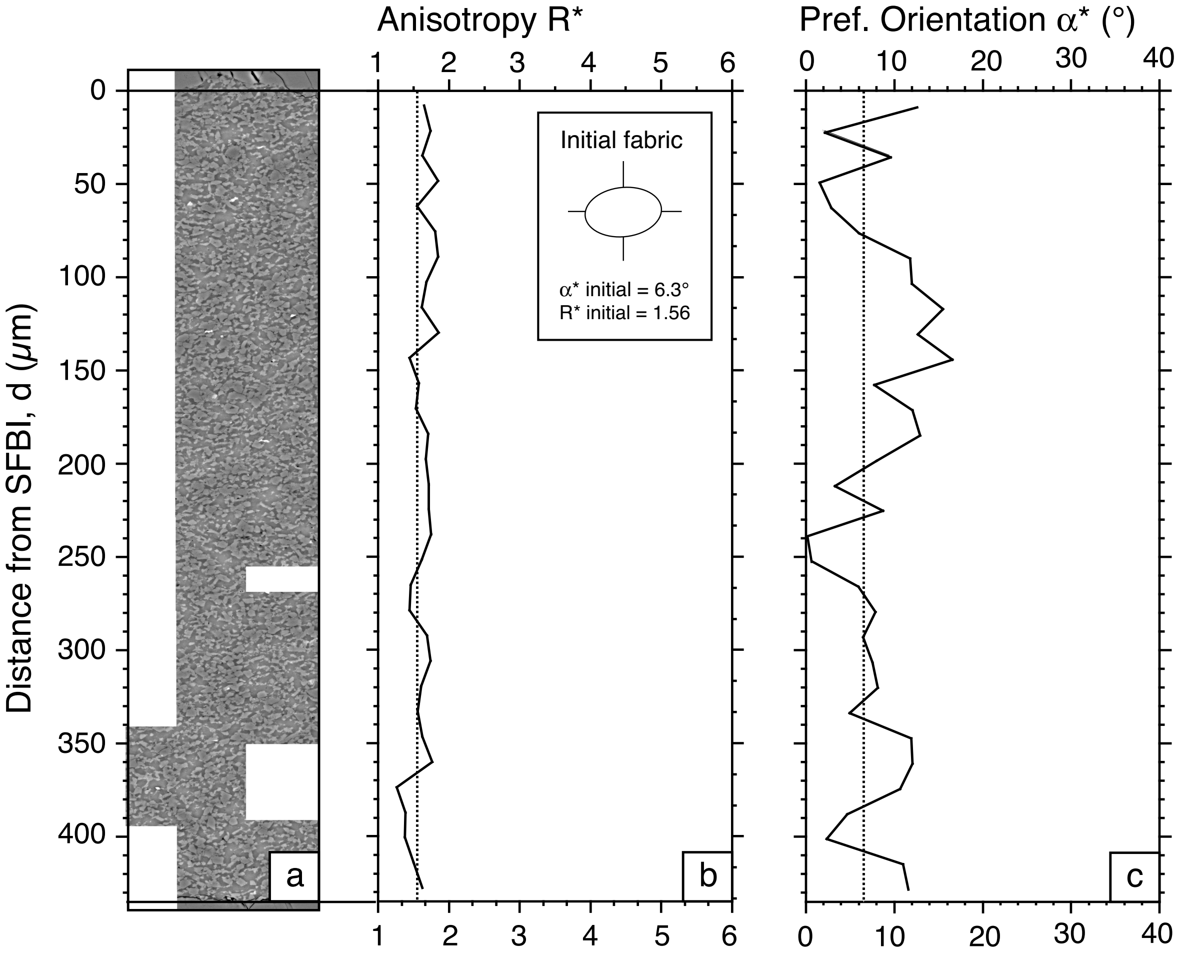

Figure 3.9: ACF analysis of BSEM images of hydrostatic sample 1. (a) Mosaic of BSEM images. (b) Fabric anisotropy R* as a function of distance *d* from the SFBI (solid line) and average R* (dotted line). (c) Shape preferred orientation α^* as a function of distance *d* from the SFBI (solid line) and average α^* (dotted line). The average values for R*=1.56 and α^*=6.3. These values define the initial fabric (inset) and are used in Figures 3.10 and 3.11.

Thus, the permanent strain recorded in the fabric of the labradorite-olivine sample deformed without reaction is negligible.

Fabric of the reacted and deformed sample

For the transect across sample 3 (Figs. 3.6 and 3.11), the three curves for PLG, OL and RP components show that both the fabric anisotropy R* and the fabric preferred orientation α^* vary. Reaction progress and anisotropy are least in the centre of the sample and highest near the SFBI. Near the lower SFBI (Fig. 3.11), the reaction resulted in complete disappearance of anorthite. The aggregate consists of OL+RP only and a single ACF shape fabric is obtained; α^* reaches a minimum value whereas

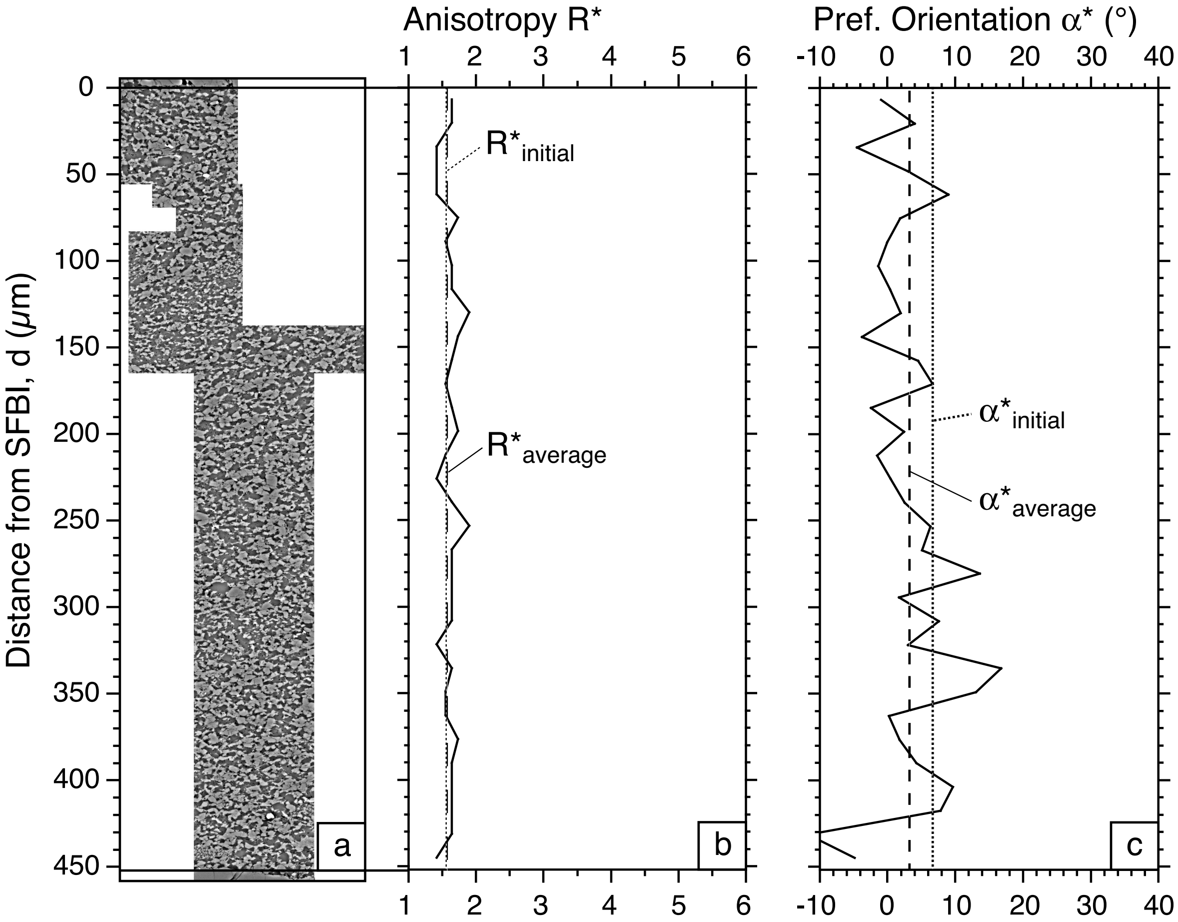

Figure 3.10: ACF analysis of BSEM images of deformed sample 2. (a) Mosaic of BSEM images. (b) Fabric anisotropy R* as a function of distance *d* from the SFBI (solid line) and average R* (dashed line). (c) Shape preferred orientation α^* as a function of distance *d* from the SFBI (solid line) and average α^* (dashed line). The average values for R*=1.59 and α^*=2.6. The initial values of R* and α^* are indicated (dotted lines, values from sample 1, Figure 3.9).

R* and the volume percentage of RP reach maximum values. The values for R* and α^* of the individual components OL, RP and PLG follow the same general trend over the entire width of the sample.

The fabric anisotropy and preferred orientation vary analogous to the ratio R$_f$ and orientation ϕ of the strain ellipse in heterogeneous ductile shear zones (Ramsay and Graham, 1970). In sample 3, the minima of α^* and maxima of R* occur near the sample boundaries. The volume fraction of the reaction products increases with increasing R* and decreasing α^*. The smallest amount of reaction products corresponds to the region of lowest anisotropy and highest angles of preferred orientation. The region in which reaction is complete (bottom part of the sample) corresponds to the region of

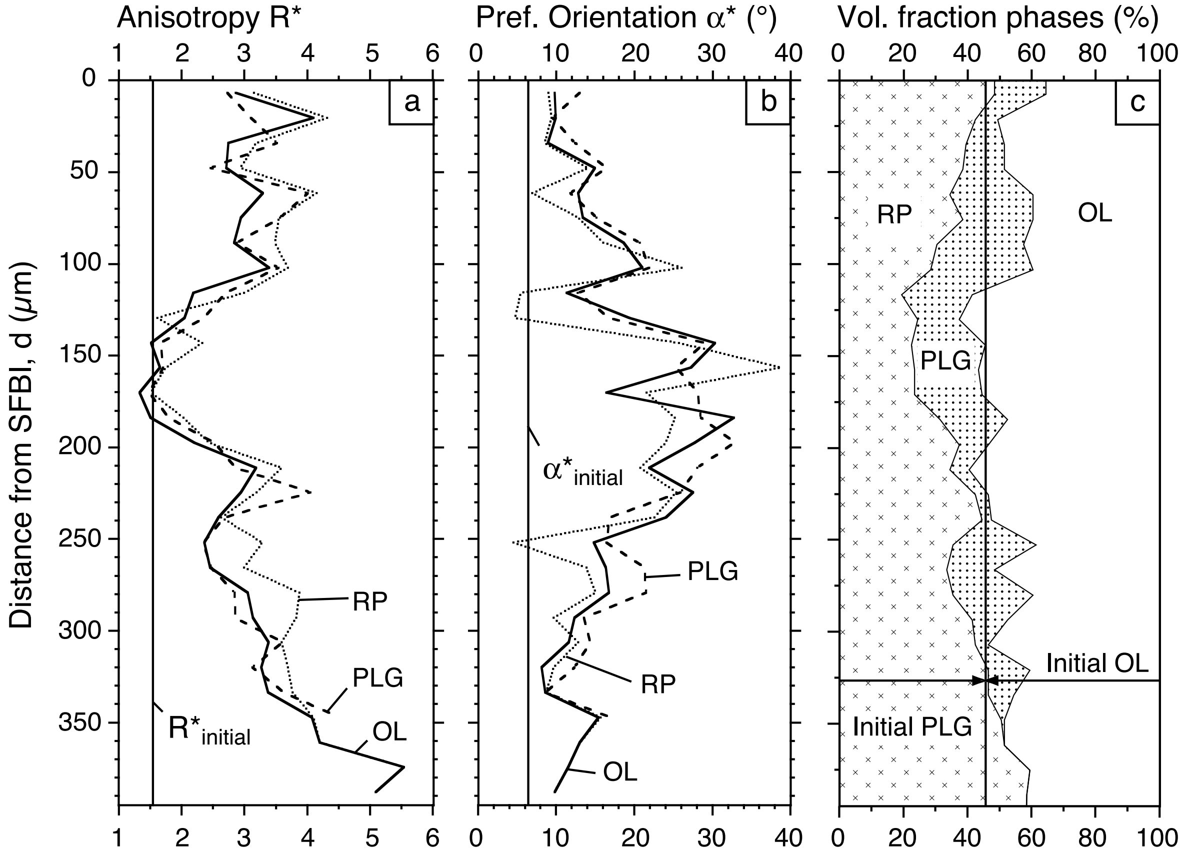

Figure 3.11: Separate ACF analyses of the binary images of OL, PLG and RP of sample 3. Fabric anisotropy R* (a) and preferred orientation α^* (b) as a function of distance d from the SFBI, are given for OL (solid line), PLG (dashed line) and RP (dotted line). (c) Volume fraction of phases. The initial values of R*, α^* and the OL-PLG volume ratio are indicated (values from sample 1). The average values for OL are R*=2.51 and α^*=16.1; for PLG, R*=2.57 and α^*=18.1; for RP, R*=3.23 and α^*=13.7.

highest anisotropy and smallest angles of preferred orientation (Fig. 3.11), i.e. closest parallelism to SFBI. Thus, reaction progress and fabric development are correlated.

3.5 Strain analysis

In the presence of a chemical reaction (as well as in the case of dynamically recrystallised rocks for example), strain markers are absent and a strain analysis in the strict sense is not possible. However, we observe that the development of the shape fabric tracks deformation in a similar way as strain markers would: aspect ratio R* and rotation increase (α^* decreases) for increasing amount of deformation. We therefore use the fabric variation of olivine in sample 3 as an indicator of the shear strain and its spatial variation. In the following sections, we calibrate the quantitative fabric anisotropy for finite strain.

3.5.1 Finite shear strain of the sample

The finite shear strain in sample 3 was determined from (1) the displacement record of the Griggs apparatus, (2) the forcing block displacement on thin section, and (3) the orientation of the fine-grained domains of the sample.

(1). The finite shear strain is calculated from the apparatus displacement record, taking into account the progressive thinning of the sample. The thinning correction assumes that sample shortening normal to the SFBI occurs continuous during the total time of deformation, when sample material is removed from the shearing sample at the forcing blocks ends. Thus, the deformation experiments deviate from an exact simple shear geometry. We consider the total strain of the deformed sample as a combination of simple shear and thinning as described in Ramsay and Huber (1983, p.287).

To the best of our knowledge, the initial thickness of the sample is equal to the thickness of hydrostatic sample 1, because the amount of plagioclase-olivine powder and the sample geometry were kept the same in each experiment. The finite strain calculated from the displacement record using the thinning correction is equal to $\gamma = 4.0$ (Fig. 3.2). Based on the stress-strain curve of sample 2 and the nearly identical fabric data of samples 1 and 2, the total permanent shear strain of sample 2 is zero. The piston displacement up to $\gamma = 1.0$ does not produce permanent strain in the sample. After a shear strain of $\gamma = 1.0$, sample 3 starts to acquire permanent shear strain, leading to a difference in the mechanical records of samples 2 and 3 and a difference in microstructure. The permanent finite shear strain derived from the displacement record $\gamma_{disp} = 3.0$.

(2). Ideally, the total forcing block displacement can be measured in the thin section and, in conjunction with the sample (shear zone) width, could be used to calculate the finite shear strain. Unfortunately however, compaction during hot pressing produces a small but unpredictable initial displacement of the forcing blocks (the forcing block displacement of the deformed sample 2 is smaller than that of the hydrostatic sample 1, Table 3.2). Therefore, measurements of forcing block displacement alone cannot be used for an accurate sample finite shear strain determination.

(3). As an additional estimation of the finite shear strain, we considered the boundaries of the fine-grained domains (Figs. 3.3 and 3.5). We measured the orientation of the long axes of 20 fine-grained domains in the direct neighbourhood of the analysed transect. If their average preferred orientation with respect to the SFBI is considered as the orientation of the long axis of the finite strain ellipse, the calculated shear strain from the angle $\alpha^*_{fgd} = 17°$, is $\gamma_{fgd} = 3.0$. In sum, based on the apparatus displacement data and preferred orientation of fine-grained domains, a bulk finite shear strain of $\gamma \approx 3.0$ is derived for sample 3.

3.5.2 Local shear strain distribution from fabric anisotropy

The changes in measured fabric values R* and α^* are qualitatively similar to those of aspect ratio R and angle α of simple shear geometries (Ramsay and Graham, 1970). A large strain produces strong anisotropies and rotation of the preferred orientation axis into the orientation of the finite strain ellipse (Fig. 3.7d). The variation of the ACF fabric (Fig. 3.11) resembles the variation of shear strain across the sample. Therefore, the fabric anisotropy is taken as a measure of the aspect ratio and the fabric preferred orientation as a measure of the orientation of the long axis of the strain ellipse.

The integration of local shear strains over the width of a shear zone yields the total shear displacement (Ramsay and Huber, 1983, p.34-40). Since the total shear displacement of sample 3 is known, the local strain can be derived if one assumes that the distribution of strain follows the distribution of fabric anisotropies. The measured fabric anisotropy R* is a more robust criterion for shear strain determination than the fabric preferred orientation, mainly because accurate measurements of small angles are difficult. We therefore only use the fabric anisotropy R* for calibration and we only used olivine because olivine remains abundant at all sites in the sample.

As a first step in the calculation, we separate the deformation of the sample into two parts: thinning and simple shear. Thinning implies area loss in a 2-D treatment (the loss occurs at the ends of the sample) and in sample 3 the average sample thickness is reduced by 0.077 mm (∼16% shortening normal to the SFBI, Table 3.2). Whether the thinning is assumed to occur throughout the experiment or at the beginning is difficult to decide. For simplicity, we assume that sample thinning (i.e. area loss) has occurred first, modifying the initial fabric of the starting material (R*=1.56, Fig. 3.9). The anisotropy of the thinned initial fabric, R^*_Δ, is calculated using a Lagrangian position gradient tensor (Ramsay and Huber, 1983, p.55-69). This tensor calculates the change in orientation and aspect ratio of an ellipse after 16% shortening normal to the SFBI. The initial shape and orientation of the ellipse are equal to the average anisotropy (R*=1.56) and preferred orientation (α^*=6.3) of the starting material. The resulting thinned initial fabric anisotropy R^*_Δ has a value of 2.15.

Secondly, the finite shear strain of the sample is $\gamma = 3.0$ and any measured $R^* > R^*_\Delta$

is due to the superimposed shear strain. Using the anisotropy R^* of each ACF row as the aspect ratio R of the shear strain ellipse at that point, an apparent shear strain, γ^*, is calculated (Ramsay and Huber, 1983, p.295,296):

$$\gamma^* = \frac{(R^* - 1)}{\sqrt{(}R^*)}$$

By taking into account initial thinning R^*_Δ, a corrected apparent shear strain γ^*_c is derived:

$$\gamma^*_c = \frac{(R^* - 1)}{\sqrt{(}R^*)} - \frac{(R^*_\Delta - 1)}{\sqrt{(}R^*_\Delta)}$$

In situations where $R^* < R^*_\Delta$, γ^*_c is set to zero.

The total displacement S across the shear zone is equal to the area under the γ-d curve. The total displacement (S = 1.185 mm) is based on the width of the sample in the analysed transect (d = 0.395 mm, Fig. 3.6) and the bulk or average shear strain (γ = 3.0) determined in the previous section. We scaled the area under the γ^*_c-d curve of olivine (S^* = 0.142 mm) to the total displacement S. This allowed us to determine the local shear strain γ, by multiplying the γ^*_c-values by a factor of 8.345 (S/S^*). Finally, the time of deformation in sample 3 was 21.2 hours (Table 3.2). Assuming that the deformation was steady and continuous at all sites d across the transect, we convert the local shear strains to local shear strain rates, $\dot{\gamma}$ (Fig. 3.12a).

3.5.3 Reaction progress

Reaction progress is calculated from the measured volume fractions of plagioclase and reaction products, V_{PLG} and V_{RP}, in each ACF row (Figs. 3.11c and 3.12). For simplicity we assumed that reaction takes place according to the stoichiometric reaction coefficients in the CMAS-system (see Introduction). These molar reaction coefficients correspond to forsterite and anorthite reacting in a 47:53% volume ratio (Fo_{100} = 44.84 cm^3mol^{-1}, An_{100} = 101.15 cm^3mol^{-1}). First, the amount of plagioclase required for the observed V_{RP} per ACF row was calculated: $V_{reacted} = V_{RP}*53/100$. The initial volume of plagioclase per ACF row is $V_{initial} = V_{reacted} + V_{PLG}$. We defined the reaction progress per ACF row as:

$$RP(\%) = 100 * \frac{V_{reacted}}{V_{initial}} = 100 * \frac{V_{initial} - V_{PLG}}{V_{initial}}$$

3.5.4 Distribution of strain and reaction progress

Figure 3.12 illustrates how the local shear strain varies throughout the sample and that positive and negative deviations from the average shear strain of the sample are localised. At the top and bottom part of the sample, the shear strain reaches a maximum value of $\gamma = 9.5$, whereas it approaches zero near the centre of the sample. There is a clear spatial correlation between the reaction progress and shear strain. At peak shear strain locations, the reaction progress is highest. At undeformed locations, reaction progress reaches a maximum of 30-40%.

The partitioning of strain rate in the sample is striking. The zone where most of the strain is accommodated is about 50 μm wide, which is only 12% of the sample thickness. The local shear strain rate in this region is approximately $1.1\text{x}10^{-4}s^{-1}$, which is almost three times the average shear strain rate. About one order of magnitude difference is observed between the strain rate values near the lower sample border and the centre of sample. In the centre of the sample, which is virtually undeformed, the strain rate values approach zero.

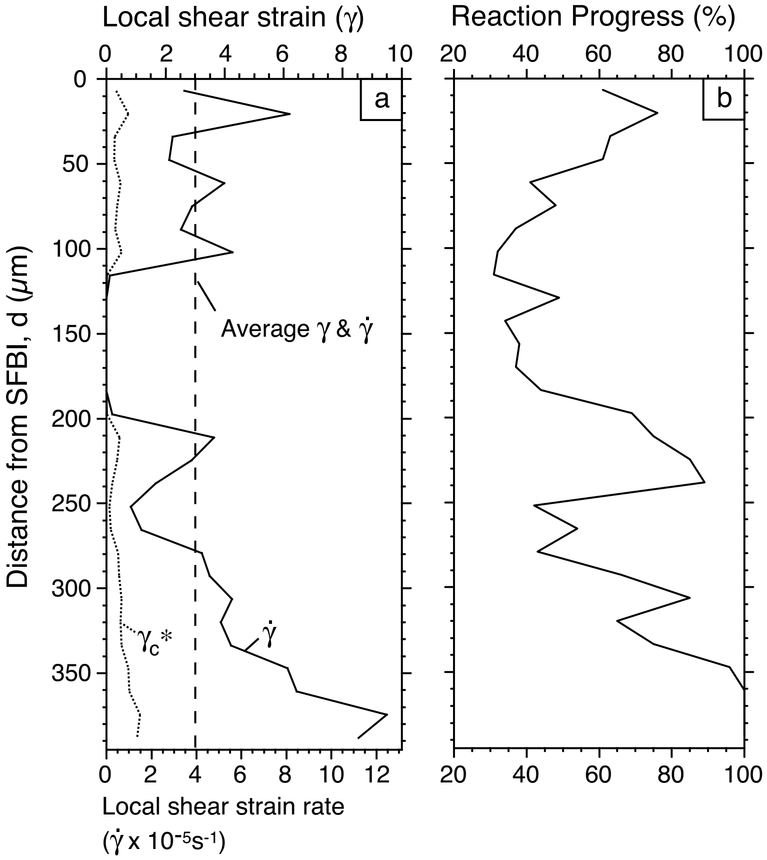

Figure 3.12: Shear strain, strain rate and reaction progress in sample 3. (a) Shear strain rate as a function of distance *d* from the SFBI (solid line) derived from the corrected apparent shear strain (γ_c^*, dotted line). The average shear strain rate is indicated. (b) Local reaction progress as a function of distance from the SFBI, measured by plagioclase breakdown.

3.6 Discussion

Reaction-enhanced weakening and strain partitioning

The shear deformation experiments demonstrate that the syndeformational reaction of plagioclase and olivine significantly weakens the samples. Comparison of the microstructures in Figure 3.4b-d suggests that most of the shear strain is accommodated in layers where the content of reaction products is highest. The original grain size is reduced from 3.4±1.2 µm of the olivine and plagioclase to sub-micron size of the reaction products whose individual phases cannot be resolved in the SEM backscatter images. Thus, the observed weakening is attributed to a switch in deformation mechanism from grain size insensitive creep of the plagioclase-olivine grains to grain size sensitive creep of the fine-grained reaction products (Rubie, 1983; Brodie and Rutter, 1987; Newman et al., 1999). This conclusion is supported by the fact that the bulk sample after reaction is weaker than prior to reaction even though most of the reaction product phases, for example clinopyroxene and orthopyroxene, are mechanically stronger than olivine and plagioclase (Bystricky and Mackwell, 2001; Ji et al., 2001). The grain-scale partitioning of shear deformation into the reaction products layers (Fig. 3.4c, 3.6 and 3.7a) suggests that the reaction products are the mechanically weakest part of the aggregate.

At the scale of the sample (mm-scale), strain localisation occurs during a relatively moderate finite shear strain of $\gamma = 3.0$. Certain parts of the sample are almost undeformed whereas other parts display local shear strains up to $\gamma = 9.5$. Thus, significant strain localisation may occur at small bulk shear strains in polyphase rock experiments. Such thin zones may control the strength of the rock; thus caution is required when extrapolating experimental data to natural conditions. In addition, the partitioning of strain among different plagioclase and olivine has to be considered. Unfortunately, a strain determination using plagioclase in sample 3 is impossible within the fully reacted zone.

Fabric anisotropy and shear strain

Shape changes in recrystallised fabrics may track or mimic strain geometries even in situations, such as dynamically recrystallised rocks, where strain markers are absent (Jensen and Starkey, 1985; Burg et al., 1986; Heilbronner, 2002). Here we use the simple observation that a measured geometry tracks strain without accounting for the physical processes that are involved. This approach is possible if the geometries can be calibrated by independent strain determinations (apparatus displacement record, orientation of fine-grained domains).

A scaling procedure was required in order to fit the total displacement S to the γ_c^* versus distance from the SFBI curve (Fig. 3.12). In order to convert the corrected apparent shear strain and shear strain rate to the values of γ and $\dot{\gamma}$, a rather large conversion factor of 8.345 was needed. This may be explained by the fact that deformation in polycrystalline material can occur both within the grains and along grain boundaries so that individual grains behave as 'harder' inclusions in a 'softer' matrix (Gay, 1968). Therefore the olivine grains deform as more viscous particles in a less viscous matrix which leads to lower fabric anisotropies R^* for olivine and consequently lower γ values.

At sites of complete reaction, the shape anisotropy of residual olivine clasts might not evolve further if all strain is accommodated in the matrix of reaction products and if the clasts act as more or less rigid particles in that matrix. Hence, the analysis of the geometry of plastically deformed rocks in the absence of strain markers is difficult, especially if the contribution of certain physical processes (i.e. reaction) may be limited to a first (transient) stage. The estimation of strain partitioning (spatial and temporal) on the grain-scale remains a key problem in natural dynamically recrystallised and metamorphosed rocks.

We argued that sample 3 has not recorded permanent strain until $\gamma = 1.0$, because in solid-medium deformation experiments it is not possible to interpret the loading part of the stress-strain curve. The ACF fabric analysis may provide useful information for interpreting the mechanical data because it is clear that only permanent deformation of a sample produces a fabric change. Comparison of hydrostatic and deformed samples allows to define the onset of fabric changes so that the understanding of solid media experimental data might benefit from more quantitative fabric studies.

Geological applications

The investigated syndeformational reaction olivine + plagioclase = cpx + opx + spinel (+ grt) has several applications to natural systems. There probably is no direct application to peridotites because the strong pressure increase of the experiments, from the hot-pressing stage where anorthite-olivine aggregates are stable to the deformation stage where they are unstable while deforming, for peridotite or troctolitic rock compositions would tectonically only be realized in subduction zones where the temperatures are much lower at the given pressure range and other reactions are more likely to take place. However, the reversal of the reaction has been observed in natural mylonitic shear zones (Newman et al., 1999; Handy and Stünitz, 2002) and is likely to occur in extensional tectonic settings, where mantle rocks are adiabatically brought up to shallower levels. As a solid-solid reaction during deformation it may serve as a general example for such a reaction, which has also been observed in shear zones in other rock systems (e.g. Rubie, 1983). Weakening by a switch in deformation mechanism has been proposed in natural systems (Rubie, 1983; Stünitz and Fitz Gerald, 1993; Newman et al., 1999). It is demonstrated by the experiments that a pronounced decrease in flow stress occurs during the reaction.

In the reacted sample both strain partitioning and strain localisation have been observed. Strain partitioning occurs into the reaction product layers. Such a partitioning is common and occurs on the grain scale in layers of weak minerals in nature as well (e.g. Handy, 1990). The microstructures of the experimental reaction sample resemble many natural microstructures of quartzo-feldspathic rocks (e.g. Berthé et al., 1979b). The fine-grained reaction products represent such weak layers; their weakness is caused by a switch in the deformation mechanism from dislocation creep to diffusion-accommodated grain boundary sliding.

Strain localisation occurs at a number of scales. At the sample-scale we observe the formation of large strain layers near the SFBI. At a smaller scale we have mentioned layers of large strain between fine-grained domains. At the grain-scale, preferred sites for reaction and deformation (grain boundaries normal to principle stress $\sigma 1$) can be observed. However, the explanation of these strain localisations is beyond the scope of this work and subject of another paper.

For the analysis presented in this study, we merely exploit the fact that the concentration of reaction and deformation are spatially correlated, occurring together in the same locations of the sample. Greater reaction progress in shear zones has been observed frequently in natural systems (e.g. Kerrich et al., 1980; Brodie and Rutter, 1985; Marquer et al., 1985; Keller et al., 2004). The experiments demonstrate that reaction and deformation are concomitant and that reaction progress is not a later event which is concentrated in already deformed zones as proposed as a possibility by Brodie and Rutter (1985).

The concentration of reaction and deformation into certain parts of the sample after relatively small strains of $\gamma = 3.0$ in the experiments shows that the weakening effect of the reaction leads to a considerable increase in strain rate in localised zones, even at fast laboratory strain rates. It is likely that the effect is even more pronounced in natural shear zones because strain rates are slower, whereas the P,T-conditions of the reactions (and thus reaction kinetics) may be similar. Indeed, some reactions in natural rocks only progress significantly in shear zones, whereas the country rock is almost unaffected (Koons et al., 1987).

3.7 Conclusions

In experimentally deformed plagioclase-olivine aggregates at 1500 MPa and 900°C, syndeformational reaction between plagioclase and olivine affects the strength of the rock as well as the distribution of shear strain across the sample. Fabric anisotropy is used to derive local shear strains and shear strain rates. By applying the autocorrelation function to a transect across the sheared samples, a strain analysis of the individual phases was performed.

The following conclusions can be made:

- There is a strong correlation on a sample scale between reaction progress and strain; large shear strain is locally associated with high reaction progress.
- Syndeformational reaction between olivine and anorthite causes a decrease in flow stress. On a grain-scale, fine-grained reaction products accommodate a large part of the shear deformation.
- From variations of fabric anisotropy, local strain variations across the sample can be calculated using measurements of bulk finite strain for calibration.
- Within the studied sample the total range of local shear strain rate from the fastest to the slowest is approximately one order of magnitude.

3.8 Acknowledgements

Dick Yund provided a lot of his excellent laboratory expertise. Bill Collins and Willy Tschudin prepared high quality sections. The Laboratory for Scanning Electron Microscopy of the University of Basel provided assistance and equipment. We thank all of them very much. Michael Stipp and Nils Oesterling helped with useful discussions. Editorial comments of J.-P. Burg and constructive reviews by G. Dresen, M.R. Drury and K. Kanagawa considerably improved this paper. This study was supported by the Swiss National Fond grants 2100-057092.99/1 and 2000-065041.01.

Chapter 4

Reaction-induced weakening of plagioclase-olivine composites [*]

Abstract

The localisation of strain into natural ductile shear zones is often associated with the occurrence of water-deficient metamorphic reactions. In order to study the effects of anhydrous solid-solid mineral reaction on plastic deformation of rocks, we have investigated the shear deformation of plagioclase-olivine composites during the reaction plagioclase + olivine → orthopyroxene + clinopyroxene + spinel (± garnet). Plagioclase-olivine composites were studied after shear deformation experiments in a Griggs apparatus. Experiments were performed on anorthite-forsterite (An-Fo) and labradorite-forsterite (Lab-Fo) composites at 900°C, confining pressures between 1000-1600 MPa and with constant shear strain rates of $\dot{\gamma}$ ~5*$10^{-5}$$s^{-1}$.

In absence of reaction, Lab-Fo composites strain-harden due to the inhibition of extensive recrystallisation by interphase boundaries. Anhydrous reactions induce strain weakening of An-Fo composites by a switch to grain size sensitive deformation mechanisms through the development of fine-grained (size <0.5 μm) polyphase reaction products. Interconnecting layers of reaction products accommodate most of the applied strain by grain size sensitive creep. Recovery processes in the An-Fo composite are pronounced during syndeformational reaction: original anorthite and olivine dynamically recrystallise by subgrain rotation recrystallisation. Presumably the dynamic recrystallisation is caused by reduced stress conditions and partitioning of strain at

---

[*] A.A. de Ronde, H. Stünitz, J. Tullis. To be submitted for publication in *Journal of Geophysical Research*, American Geophysical Union

different rates between the new reaction products and the relict An-Fo grains. The results of our experiments are in good agreement with natural observations of shear localisation in the lower crust and upper mantle, and imply that anhydrous mineral reactions can be important causes for localisation of deformation.

4.1 Introduction

The localisation of strain into natural ductile shear zones is often associated with the occurrence of metamorphic reactions. The relationships between rock deformation and mineral reactions have been the subject of numerous geological and experimental studies over the last decades. Overviews on possible weakening effects that metamorphic reactions may have on the deformation of rocks are given by White et al. (1980), Brodie and Rutter (1985), Brodie and Rutter (1987), Rubie (1990a) and Rutter and Brodie (1995). The most common reaction weakening mechanisms can be summarised as follows:

1. Reactions form fine-grained reaction products which deform by diffusion- accommodated grain boundary sliding (Boullier and Gueguen, 1975; Kerrich et al., 1980; Rubie, 1983, 1990a; Rutter and Brodie, 1988a,b; Stünitz and Fitz Gerald, 1993; Newman et al., 1999; Stünitz and Tullis, 2001)

2. Dehydration reactions lead to (probably transient) weakening due to increased pore pressure (cataclasis) (Murrell and Ismail, 1976; Rutter and Brodie, 1988a; Paterson, 1989; Olgaard et al., 1995)

3. Reactions form new weak phases that deform more easily by crystal plasticity (Mitra, 1978; White and Knipe, 1978; Rubie, 1990a)

4. Solid-state reactions of mineral phases cause weakening by transformation plasticity (Poirier, 1985; Meike, 1993; Schmidt et al., 2003)

Several experimental studies have focused on dehydration (Murrell and Ismail, 1976; Rutter and Brodie, 1988a; Paterson, 1989; Olgaard et al., 1995) and hydration reactions (Rutter et al., 1985; Stünitz and Tullis, 2001). However, the presence of water, both intracrystalline and as a separate phase, has profound effects on the deformation and reaction kinetics of rocks. Water influences the rheological properties of minerals (e.g. Chopra and Paterson, 1984; Karato et al., 1986; Post and Tullis, 1998; Mei and Kohlstedt, 2000) as well as the transport of chemical components during mineral reaction (e.g. Yund and Tullis, 1980; Rubie, 1986; Yund, 1997). In the presence of water it is therefore difficult to distinguish individual deformation processes that occur during concurrent deformation and reaction. Except for deformation studies involving polymorphic phase transitions (Kirby, 1987; Snow and Yund, 1987; Burnley and Green, 1989; Green and Houston, 1995), there have been no experimental studies on anhydrous solid-solid reactions accompanying deformation.

Shear zones in upper mantle peridotites demonstrate that strain localisation associated with retrograde metamorphic reactions during ductile deformation does occur under water limited/deficient conditions. For the Turon de Técouère peridotite in the North Pyrenean Zone, Vissers et al. (1997) and Newman et al. (1999) conclude that strain localisation by reaction-enhanced softening can occur over a wide pressure-temperature space in lithospheric mantle. Handy and Stünitz (2002) describe strain localisation by a combination of fracturing and reaction weakening in spinel lherzolite in the Southern Alps, and infer this process to initiate exhumation of subcontinental mantle beneath rifted margins. Phase-transformations from spinel to plagioclase lherzolite have led to enhanced mylonitisation in lherzolite from the Hidaka metamorphic belt of central Hokkaido, Japan (Furusho and Kanagawa, 1999). These field studies demonstrate that syndeformational metamorphic reactions in garnet and spinel bearing peridotites can play an important role during the exhumation of the upper mantle.

The aim of this study is to examine the effects of nominally dry solid-solid mineral reactions on the plastic behaviour of polyphase rocks. In order to achieve this aim, we have performed shear deformation experiments on dry plagioclase-olivine composites to study the strength and deformation mechanisms during mineral reactions. The results for these plagioclase-olivine experiments have applications to processes in natural peridotitic rocks. Reactions in the peridotite system are important for controlling the deformation of the upper mantle during crustal thinning and the deformation of oceanic crust and upper mantle lithologies during subduction (e.g. Drury et al., 1991; Vissers et al., 1995).

4.2 Peridotite phase transitions

Phase transitions in upper mantle peridotites are largely pressure-dependant. They can be studied in piston cylinder experiments in which confining pressure can be increased within the necessary range (Fig. 4.1). Natural plagioclase-bearing peridotites are stable at low-pressure, high-temperature conditions but when exposed to higher pressures, reactions occur to spinel-, garnet- and pyroxene-bearing mineral assemblages (Fig. 4.1a).

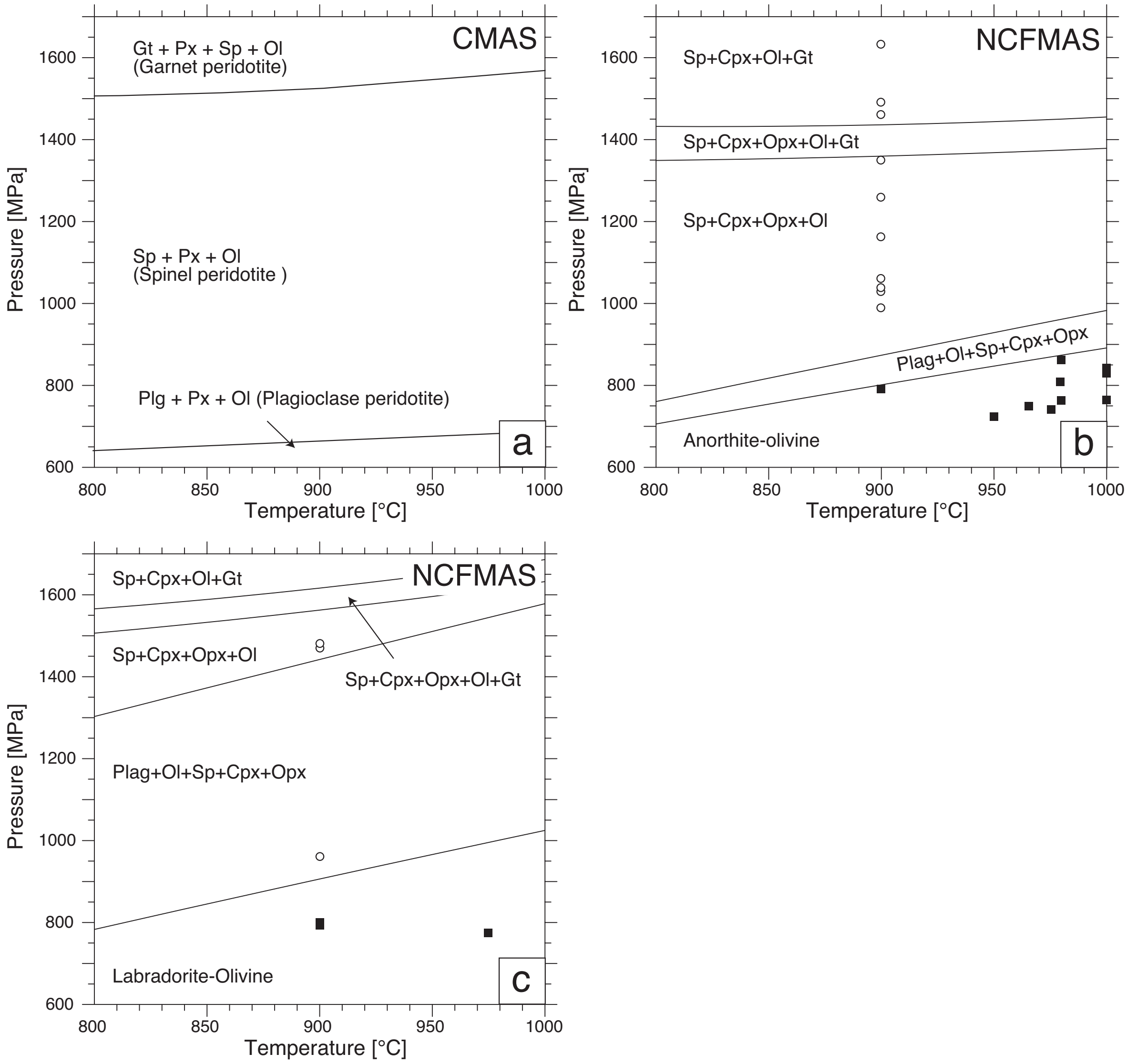

Figure 4.1: Equilibrium phase diagrams for plagioclase, spinel and garnet bearing peridotites. (a) Peridotite phase transitions based on a compilation of experimental data in the CaO-MgO-Al_2O_3-SiO_2-system (Green and Hibberson, 1970; Kushiro and Yoder, 1966; Jenkins and Newton, 1979; O'Neill, 1981; Gasparik, 1984; Herzberg and Gasparik, 1991; Klemme and O'Neill, 2000). (b + c) Equilibrium phase diagrams in the Na_2O-CaO-FeO-MgO-Al_2O_3-SiO_2 system for plagioclase-olivine composites used in this study. The diagrams are calculated by the program DOMINO (de Capitani and Brown, 1987; de Capitani, 1994) using the Berman (1988) database. Solid solution models used: Fuhrman and Lindsley (1988) (plagioclase), Meyre et al. (1997) (clinopyroxene) and Hunziker (2003) (orthopyroxene). Squares indicate P,T conditions of the sample hot pressing. Circles indicate the P,T conditions of the plagioclase-olivine experiments. (b) Phase diagram for anorthite-olivine samples: 1 An_{92} + 2 Fo_{93}. (c) Phase diagram for labradorite-olivine samples: 1 An_{60}+ 2 Fo_{93}.

	Blumone anorthite		Sonoran labradorite		Åheim forsterite	
	wt.% oxides	Ions per 8 O	wt.% oxides	Ions per 8 O	wt.% oxides	Ions per 4 O
SiO_2	45.26	2.090	53.01	2.398	41.18	1.001
Al_2O_3	34.78	1.893	29.83	1.590	0.00	0.000
MnO	0.00	0.001	0.00	0.000	0.05	0.000
FeO	0.56	0.021	0.36	0.013	7.31	0.149
MgO	0.09	0.006	0.00	0.000	50.97	1.847
CaO	18.42	0.912	12.49	0.605	0.07	0.002
Na_2O	0.90	0.080	4.30	0.378	0.01	0.000
K_2O	0.02	0.001	0.30	0.017	0.00	0.000
Total	99.94	5.004	100.29	5.001	99.59	2.999
Normalised mol% of mineral end-members						
		An92		An60		Fo93
		Ab8		Ab38		Fa7
		Or0		Or2		

Table 4.1: Chemical compositions of anorthite, labradorite and olivine starting materials

The peridotite phase transitions strongly vary with the sodium content of plagioclase. Thermodynamic calculations with the program DOMINO (de Capitani and Brown, 1987; de Capitani, 1994) and the Berman (1988) database show that a peridotite containing anorthite-rich plagioclase (An_{92}) at 900°C becomes unstable at pressures above 900 MPa in the Na_2O-CaO-FeO-MgO-Al_2O_3-SiO_2 (NCFMAS)-system (Fig. 4.1b). Plagioclase peridotite composed of intermediate plagioclase (An_{60}) is stable up to a pressure of 1400 MPa (Fig. 4.1c).

By choosing anorthite (An_{92}) and labradorite (An_{60}) compositions (Table 4.1) in our plagioclase-olivine composites, we can study the rheological behaviour of plagioclase-olivine rocks in the presence or absence of reaction, respectively. Anorthite and labradorite have similar strengths (Tullis and Yund, 1999), so the crystal plastic deformation of the plagioclase is not strongly affected by choosing different compositions.

Lab-Fo (An_{60}-Fo_{93}) composites are stable at all confining pressures within the tested range, providing examples of plastic deformation of non-reacting samples. For An-Fo (An_{92}-Fo_{93}) composites in the NCFMAS-system, the applied confining pressures represent different amounts of pressure overstepping (P_o ~200-600 MPa) of the plagioclase peridotite stability field. Using An-Fo composites in the deformation experiments makes it possible to study the effects of mineral reactions on plastic deformation of plagioclase-olivine composites.

4.3 Experimental techniques

4.3.1 Plagioclase-olivine composites

Anorthite-olivine (An-Fo) and labradorite-olivine (Lab-Fo) mixtures were prepared from powders of ground Åheim dunite olivine (Fo_{93}), Blumone gabbro anorthite (An_{92}) and gem-quality Sonoran labradorite (An_{60}; Table 4.1). The minerals were crushed, handpicked and further ground in an alumina mortar. Mineral powders within a 4 to 10 µm grain size range were obtained by a sedimentation method. Distilled water and alcohol were used as the settling fluid for plagioclase and olivine, respectively.

Based on the existing rheological data for both plagioclase (e.g. Rybacki and Dresen, 2000, 2004) and olivine (e.g. Hirth and Kohlstedt, 2003), a starting material with a 4 to 10 µm grain size range was chosen, to ensure that the initial olivine-plagioclase composite would deform by dislocation creep at our experimental conditions (Fig. 4.2). A few grams of olivine and plagioclase powders were combined with a 48.7 to 51.3 wt.% ratio. This weight ratio corresponds to a 2 to 1 molar ratio, in which forsterite (Fo_{100}) and anorthite (An_{100}) ideally react in the CaO-MgO-Al_2O_3-SiO_2-system: 2 forsterite + anorthite = 2 enstatite + diopside + spinel. Plagioclase and olivine powders were mixed in an acetone slurry inside a 5 ml glass beaker within an ultrasonic stirrer. When most acetone was evaporated, the powder slurry was quickly dried in an oven at 110°C after the mixing, which caused rapid evaporation of the acetone. This procedure prevented grain size (density) sorting and mineral segregation. All mineral mixtures were stored continuously at 110°C until processed further.

Forcing block pistons were prepared from 6.3 mm diameter cores of Balsam Gap dunite and Åheim dunite. The dunite cores were cut and ground at 45° to their cylinder axis, which created a flat sample-forcing block interface. In a couple of samples we used dunite forcing blocks with a grooved interface to maintain a good grip on the sample during the experiment. However, the grooves turned out to be unnecessary because the plagioclase-olivine composite bonded well with the dunite forcing blocks during hot pressing.

The Balsam Gap dunite forcing blocks were dried for 24 hours at 980-1000°C in a CO-CO_2 gas mixture. The drying resulted in weight losses up to 0.75% due to the dehydration of small amounts of hydrous minerals like serpentine. The powders were oven-dried at 110°C for at least 72 hours. The oven-dried powders have some absorbed water on the mineral grain boundaries, which was required for sufficient grain growth in the plagioclase-olivine composite during the hot pressing stage of the experiment

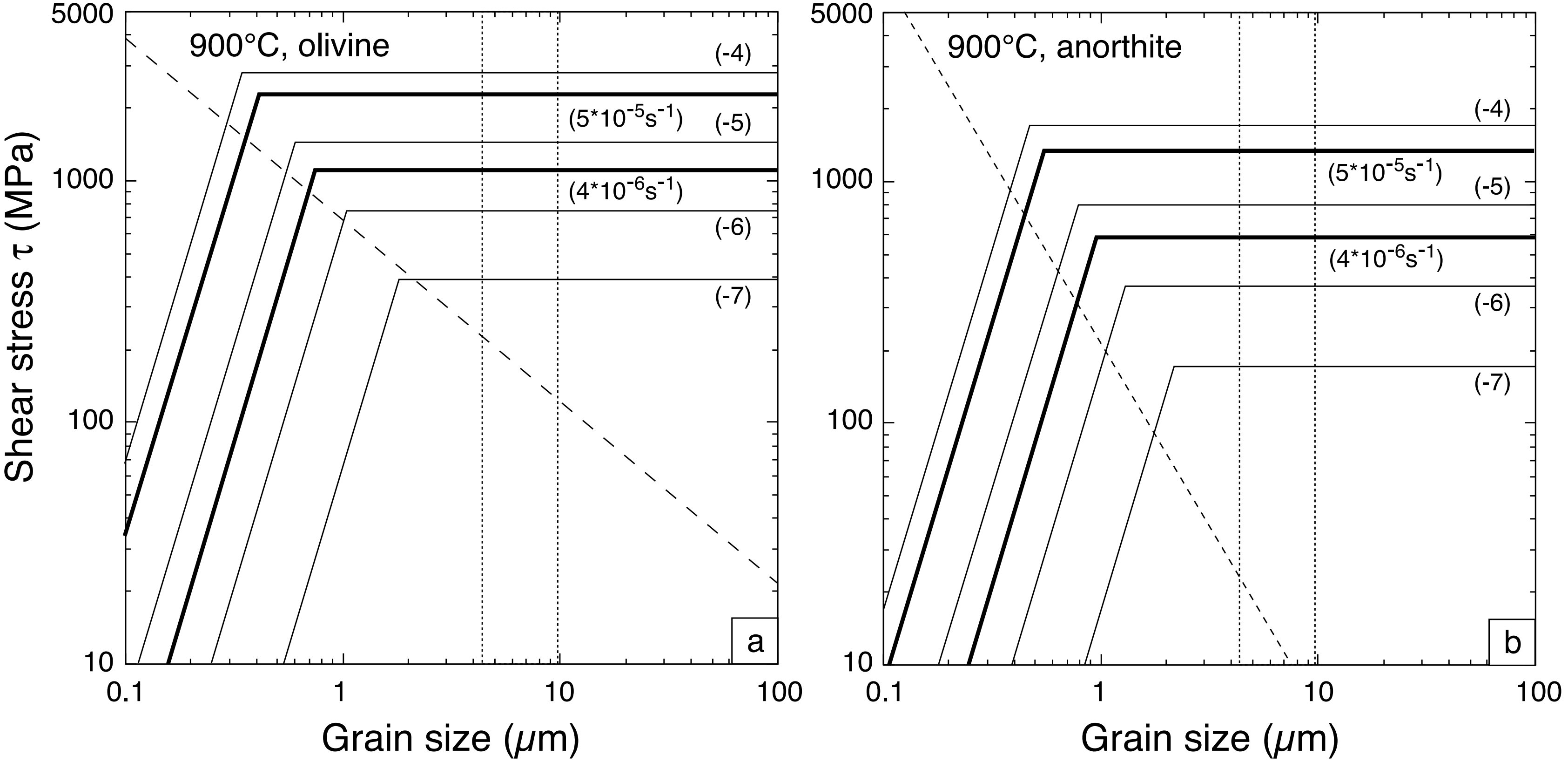

Figure 4.2: Deformation mechanism maps showing the influence of grain size on the flow stress of olivine and anorthite at 900°C. Solid lines indicate constant shear strain rate contours in the dislocation creep regime (grain size insensitive creep; horizontal contours) and the diffusion creep regime (grain size sensitive creep; diagonal contours). The strain rate contours are labelled with the rate-exponent ($10^{exp}s^{-1}$). Thick lines indicate the shear strain rates used in this study. Dotted lines mark the grain size range of the starting material. Striped lines represent recrystallised grain size piezometers. (a) Map for olivine. Diagram is calculated with the olivine (Fo_{90}) flow law parameters of Hirth and Kohlstedt (2003), using a fixed H_2O content of 0.002 wt.%. Piezometer of van der Wal et al. (1993). (b) Map for anorthite. Diagram is calculated with the anorthite (An_{100}) flow law parameters of Rybacki and Dresen (2004), for a fixed H_2O content of 0.004 wt.%. Piezometer of Post and Tullis (1999).

at relatively low temperatures of 970°C (see following section). A different drying procedure was used in the initial stages of this study, in which the powders were dried together with the forcing blocks for 12 hours at 1000°C in a CO-CO_2 gas mixture. As a result, the powders were hot-pressed at temperatures of at least 1050°C to obtain sufficient grain growth of the plagioclase-olivine powder. Unfortunately, the 1050°C hot pressing caused some problems in the execution of the experiments and the procedure was abandoned in subsequent experimental runs.

For each experiment, approximately 78 mg of the olivine-plagioclase powder mixture was placed between the dried dunite forcing blocks inside a nickel-foil jacket. The inner Ni jacket was mechanically sealed around upper and lower Ni foil disks and controls the oxygen fugacity of the sample during the experiment at the Ni-NiO buffer. The inner Ni jacket was placed inside a Pt jacket. The Pt jacket was weld-sealed at its ends and wrapped in extra Ni foil to protect the Pt-jacket from sodium chloride during hot pressing above 900°C.

4.3.2 Hot pressing and deformation

The plagioclase-olivine powders were hot-pressed at high temperature and pressure inside the plagioclase-olivine stability field in order to produce dense and low-porosity plagioclase-olivine rock samples. Hot pressing was performed inside a Griggs solid medium apparatus. Powders dried in CO-CO_2-gas were hot-pressed for 24 hours at 1050°C and P_c ~800 MPa, using an all-sodium chloride sample assembly for molten confining media (Gleason and Tullis, 1995). Oven-dried powders were hot-pressed for 48 hours at ~970°C, using an all-sodium chloride sample assembly for solid confining media (Tullis and Tullis, 1986).

The hot-pressed starting material is a homogeneous mixture of plagioclase and olivine in 49-51±2% volume ratio, with approximately ~2% porosity (Fig.4.3). The mean grain size of the hot-pressed starting material is 6.9±2.6 μm (Fig. 4.3), which was determined from SEM-backscattered images using the program StripStar (Heilbronner, 1998). This grain size applies to olivine grains only, because it was not possible to identify a sufficient number of plagioclase grain boundaries.

The method of sample preparation produces small and sporadic domains of coarse-grained plagioclase and olivine (up to 30 μm). These domains do not change the sample deformation conditions because plagioclase and olivine deform by grain size insensitive creep. Most of the remaining porosity disappeared by additional compaction and annealing at deformation conditions because the apparatus force-piston needs time

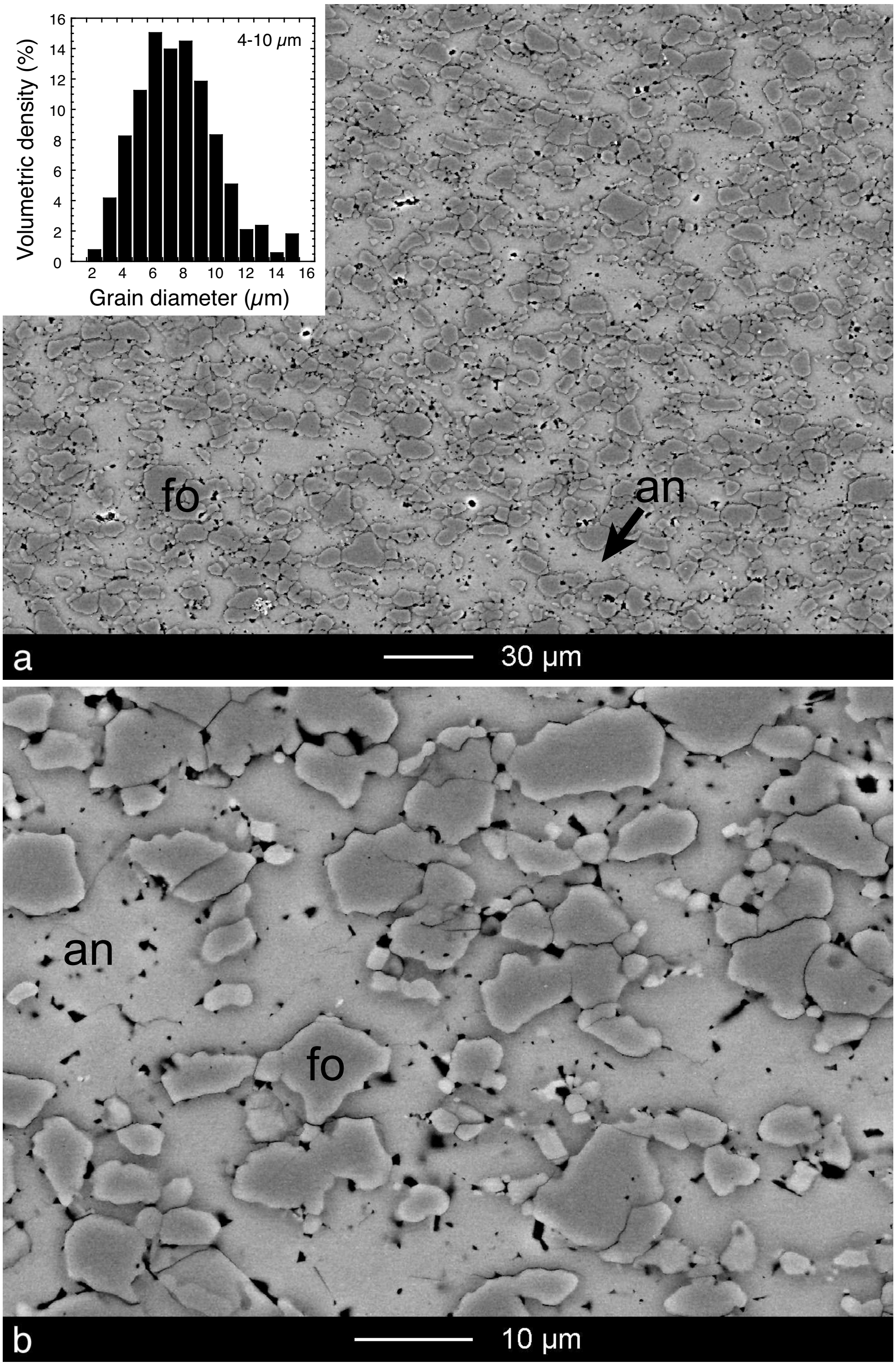

Figure 4.3: Backscattered scanning electron microscope (BSEM) images of plagioclase-olivine starting material (44AA). (a) Magnification 400x. Composite of anorthite (an) and olivine (fo) after annealing powders with 4 to 10 µm grain size at 965°C-750 MPa for 48 hours. The average plagioclase-olivine vol.% ratio is 49-51(±2)%. The histogram shows the volume weighted 3-D grain size distribution of olivine, derived from cross-sectional areas and calculated using the program StripStar (Heilbronner, 1998). The mean grain size of olivine is 6.9±2.6 µm. (b) Magnification 1600x. Black spots indicate sample porosity and holes (vol. ~2%). White rims are due to charging of the sample.

to make contact with the sample ('run-in time' $\leqslant$30 hr at $\dot{\gamma}$=5*10^{-5}s^{-1}).

A couple of samples were prepared from 2 to 6 µm plagioclase and olivine powders by the method of de Ronde et al. (2004). In the hot-pressed 2 to 6 µm starting material, plagioclase and olivine have an initial mean grain size of 3.4±1.2 µm and they are mixed in a 46-54±2% volume ratio.

After the hot pressing, the samples were cooled slowly over two hours to 900°C and P_c=700 MPa. After one hour at these conditions, the confining pressure was increased to the 1000-1600 MPa pressure range (Fig. 4.1b,c). The plagioclase-olivine samples were deformed at a constant shear strain rate of $\dot{\gamma}$ ~5*10^{-5}s^{-1}for varying amounts of shear strain.

Additional deformation experiments were performed on pure olivine and plagioclase samples in order to compare the strength and deformation mechanisms of the composites to those of the plagioclase and olivine end-members. Two hydrostatic experiments were performed, at P_c ~1000 MPa and ~1500 MPa, to determine whether reaction occurred during the run-in time of the deformation experiments. All the samples and the experimental conditions are summarised in Table 4.2.

The Griggs apparatus force and displacement data were processed with a computer program that converts the mechanical data into shear stress and shear strain. The force and displacement data are corrected for: (1) reduction of stressed sample area with progressive shear displacement, (2) internal friction of the assembly and strength of the sample jacket, (3) thinning of the sample with progressive shear displacement and (4) distortion of the apparatus with progressive force. The shear stresses reported here may include a τ±50 MPa piston friction inherent to the solid medium apparatus (Green and Borch, 1989).

4.3.3 Sample characterisation

Thin sections of the samples parallel to the shear direction and forcing block cylinder axis were studied using optical, backscattered scanning electron (BSEM) and transmission electron microscopy (TEM). The identification of the reaction products was carried out by TEM EDS-microanalysis. In order to describe the reaction progress, ξ_{plg}, the area percentages of anorthite were measured in representative high quality BSEM images of the samples (Table 4.2). The area percentages were measured by detailed tracing of interphase boundaries and thresholding mineral phases in a mosaic of four BSEM-images with 1600x magnification. Typical tracing errors are ±1% and the error in the mean of phase area percentages is ±2%. The area percentages are

Table 4.2: Summary of conditions and results of plagioclase-olivine experiments[a]

Run no.	Sample[b]	Grain size (μm)	Forcing blocks [c]		Drying[d]			Hot pressing			Experiment			Stress-strain		ξ_{plg}[f]	Notes
					T (°C)	t (hrs)		t (hrs)	T (°C)	P_c (MPa)	P_c (MPa)	t^e (hrs)	$\dot{\gamma}\cdot 10^{-5}$ (s^{-1})	τ_{peak} (MPa)	γ_{max}	%	
13AA	An-Fo	4-10	BG	pl	1000	24	FB	24	950	730						0	
16AA	An-Fo	4-10	BG	pl	1000	24	FB	24	1000	765						0	
44AA	An-Fo	4-10	BG	pl	980	24	FB	48	965	750						0	
47AA	An-Fo	4-10	BG	pl	980	24	FB	48	975	740	1060	73.3				0	
W1045	An-Fo	2-6	BG	gr	1000	6	all	24	900	790	1490	30.0				<1	
W1028	An-Fo	4-10	AH	gr	1000	13	all	24	1050	780	990	12.5	4.9	397	4.1	8	
33AA	An-Fo	4-10	BG	pl	980	24	FB	48	980	810	1030	22.2	4.3	382	5.8	78	+104 hrs*
55AA	An-Fo	4-10	BG	pl	980	24	FB	48	965	750	1040	49.5	0.4	72	1.7	45	
19AA	An-Fo	4-10	BG	pl	1000	24	FB	24	1000	830	1160	37.0	4.7	321	5.9	65	
25AA	An-Fo	4-10	BG	pl	1000	24	FB	24	1000	840	1350	17.5	7.8	336	5.2	65 (-90)	
32AA	An-Fo	4-10	BG	pl	980	24	FB	48	980	760	1460	22.8	3.8	283	2.2	33	
52AA	An-Fo	4-10	BG	pl	980	24	FB	48	965	730	1480	33.5	3.9	348	2.5	n.a.	
28AA	An-Fo	4-10	BG	pl	1000	24	FB	48	980	860	1630	26.8	4.0	282	4.9	90-100	
W983	Lab-Fo	2-6	BG	gr	1000	6	all	24	900	800	960	14.5	3.8	439	1.7	0	
42AA	Lab-Fo	4-10	BG	pl	980	24	FB	48	975	775	1470	33.0	4.1	786	5.9	0	***
W991	Lab-Fo	2-6	BG	gr	1000	6	all	24	900	790	1480	17.0	4.5	696	4.7	0	
W980	An	2-6	Q	gr	1000	6	all	24	900	790	980	12.2	5.8	179	5.0	amp	
W987	Lab	2-6	Q	gr	1000	6	all	24	900	800	990	11.0	5.5	141	4.6	amp	
43AA	Lab	4-10	BG	pl	980	24	FB	48	970	780	1020	33.0	4.2	96	8.6	amp	
W1027	Fo	4-10	AH	gr	1000	14	all	24	1050	770	1000	8.5	4.5	477	4.0		
50AA	Fo	4-10	BG	pl	980	24	FB	27	960	740	1510	52.6	4.0	349	4.7		***

[a] All experiments were performed at 900°C

[b] An= Anorthite (An_{92}), Lab = Labradorite (An_{60}), Fo = Forsterite (Fo_{93})

[c] AH = Aheim dunite, BG = Balsam Gap dunite, Q = quartz single crystal, gr = grooved surface, pl = plain surface

[d] Drying at atmospheric pressure: all = dried forcing blocks + powder, FB= dried forcing blocks, powders oven-dried at 110°C

[e] Duration of a hydrostatic experiment or the time required to reach sample hitpoint in a deformation experiment.

[f] Extent of reaction in the centre of the sample. amp = nucleation of amphibole

* This sample was kept hydrostatically at P_c=1030 MPa for 104 hours after deformation

*** Brittle fault in forcing block

estimated to represent the volume percentages of phases (Underwood, 1970). Reaction progress ξ_{plg} is defined as

$$\xi_{plg}(\%) = 100 * \frac{V_{initial} - V_{plg}}{V_{initial}} = 100 * \frac{49 - V_{plg}}{49}$$

describing the amount of transformation (or 'disappearance') of anorthite with respect to the starting material.

4.3.4 Water content of the samples

We assume that the oven-dried sample powders contain adsorbed as well as intracrystalline H_2O because vacuum drying at 250°C does not remove all absorbed water from quartz (Gee et al., 1990). In order to determine any differences in H_2O content between the samples, we measured the infrared absorption of hydrogen in olivine of the Åheim and Balsam Gap dunite forcing blocks. At 900°C and P_c=300 MPa, diffusion rates of hydrogen in olivine can range from $10(\pm5)*10^{-11}$ to $10(\pm5)*10^{-12}$ m^2s^{-1} depending on crystal orientation (Mackwell and Kohlstedt, 1990). Using these data, hydrogen is calculated to diffuse 500-3000 µm into the olivine grains for the duration and temperature of the experiments (>24 hr, 900°C). Therefore, the forcing block olivine grains can be used as an internal standard to determine the hydroxyl content of the complete sample (plagioclase-olivine composite and dunite forcing blocks), especially the fine-grained regions, where the grain size is too small to be probed by FTIR.

Analyses of unpolarised hydroxyl adsorption in olivine were made using a Brukner High resolution FTIR spectrometer at the Bayerisches Geoinstitut and at the University of Hannover, Germany. Doubly polished sections were used with a 100-150 µm thickness. Measurements were made at room temperature for a 3000-4000 cm^{-1} wave number range. In all samples with dunite pistons, hydroxyl species were not measured above the detection limit of approximately 490 $H/10^6Si$. This amount of hydroxyl species corresponds a H_2O content of 30 ppm (0.003 wt.%) of olivine (Fo_{90}) and hence the plagioclase-olivine composites.

No intra-crystalline or grain boundary H_2O above the 30 ppm detection limit was measured using FTIR. All samples were treated identically during preparation. No hydrous minerals were detected in the reaction product mineral assemblages of the reacted An-Fo samples (see following sections). Therefore, we suspect that the continuous storage of mineral powders at 110°C has not allowed for substantial adsorption of water to the mineral grain boundaries. During subsequent hot pressing of the powders, the thoroughly dried dunite pistons probably acted as large sinks for any absorbed water within the entire sample.

The plagioclase-olivine composite comprises approximately 6% of the entire sample volume (composite + dunite forcing blocks). Therefore, a 30 ppm H_2O content in the entire sample may imply an initial 0.05 wt.% H_2O content in the oven-dried plagioclase-olivine powders. This value appears to be reasonable because undried ('as-is') Sonoran labradorite powder contains approximately 0.1 wt.% absorbed water (Stünitz and Tullis, 2001). The FTIR analyses indicate that the hot-pressed An-Fo composites can be considered as dry mineral samples.

4.4 Results

4.4.1 Mechanical data

Labradorite-olivine (Lab-Fo) experiments

At 900°C, the Lab-Fo composites are very strong (τ >500 MPa) at all experimental confining pressures (Fig. 4.4a). All deformed samples show strain hardening to the point that the differential stress was similar to the confining pressure of the experiment. It was not possible to obtain flow strengths for Lab-Fo composites at the employed experimental conditions. Brittle faults develop in the dunite forcing block of the Lab-Fo samples deformed at P_c=1470 and 1480 MPa. Olivine grains often show extensive kinking and subgrains (Fig. 4.5a-c). At P_c=1480 MPa, the forcing blocks clearly deformed as shown by the increase in piston diameter near the top of the sample (Fig. 4.5a). The Lab-Fo samples accommodated little to no shear displacement and the measured axial displacement in these experiments is partially accommodated by deformation of the dunite forcing blocks.

The forcing block displacement in the Lab-Fo sample deformed at P_c=1480 MPa is ~0.63 mm (Fig. 4.5a). The Lab-Fo sample shear zone is ~0.5 mm wide, and a shear strain of γ ~1.3 (γ=0.63/0.5) can be inferred as the maximum total shear strain that is accommodated by the Lab-Fo composite. This value suggests that the remaining shear strain of γ ~4.9 (γ=5.9-1.3=4.9; Table 4.2) is accounted for by coaxial deformation of the dunite forcing blocks. Therefore, the total shear strain of the Lab-Fo experiments is probably lower than shown in Figure 4.4. However, the data presentation allows for a relative comparison with the An-Fo experiments. In these experiments, the shear strain values are realistic because the forcing block deformation is lower due to the much lower

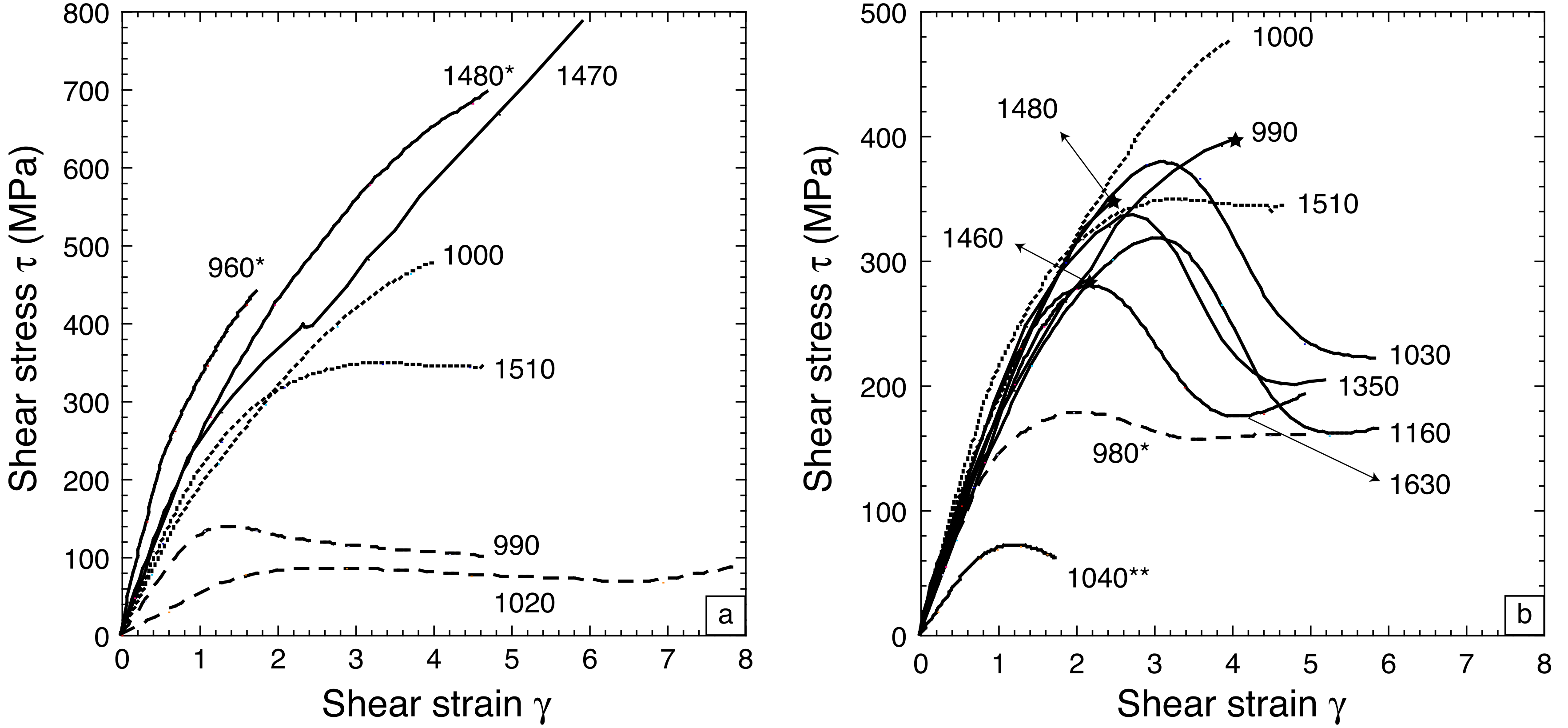

Figure 4.4: Shear stress versus shear strain diagrams for shear deformation experiments on plagioclase-olivine composites at 900°C and $\dot{\gamma}$ ∼5*10^{-5}s^{-1} (Table 4.2). Solid lines are plagioclase-olivine experiments, dotted lines are pure olivine experiments and dashed lines are pure plagioclase experiments. The confining pressure (in MPa) is indicated for each experiment. (*) Samples with 3.4±1.2 µm starting grain size. (a) Lab-Fo samples show strain hardening regardless of the confining pressure. (b) An-Fo samples deformed with mineral reaction show a strain weakening. Note the difference in scale of the shear stress axis with respect to (a). Stars indicate experimental runs stopped at approximately peak stress conditions. (**) An-Fo sample deformed at $\dot{\gamma}$=4*10^{-6}s^{-1}.

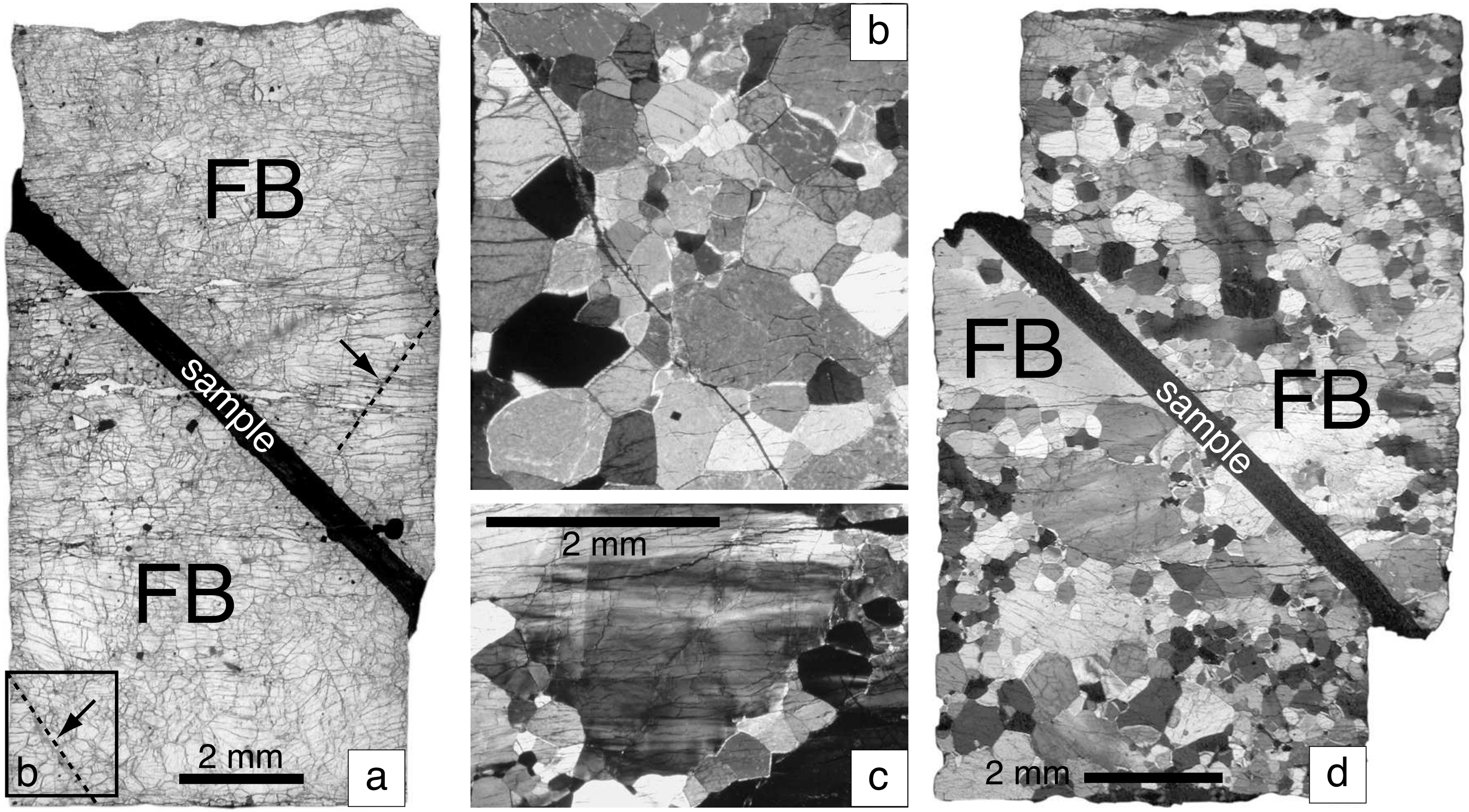

Figure 4.5: Optical micrographs of deformed plagioclase-olivine samples in thin section. Samples are located in the centre, between two dunite forcing blocks (FB). Horizontal cracks in the FBs are due to decompression when retrieving the sample from the apparatus. (a; plain polars) Lab-Fo sample 42AA deformed without reaction at P_c=1470 MPa displays little shear displacement. Arrows indicate diagonal cracks in the upper and lower FB. The upper FB has an increased diameter in the top left, indicating creep. (b: crossed polars) Detail of a brittle fault in (a). (c; crossed polars) Deformed olivine grain in the dunite FB of sample W991. (d; crossed polars) The An-Fo sample 19AA deformed at P_c=1160 MPa with reaction shows significant shear displacement.

flow stress (see next section).

The Lab-Fo composites were stronger than pure olivine and labradorite end-members. At P_c=1510 and 1000 MPa olivine was considerably stronger (τ ~350 MPa) than labradorite (τ ~100 MPa) or anorthite (τ ~160 MPa) at P_c=1000 MPa. The plagioclase end-member experiments illustrate that labradorite and anorthite deform with similar flow stress. Their strengths are similar to that of the pure Sonoran labradorite experiments of Stünitz and Tullis (2001). A small difference in the strength of olivine samples was measured between the P_c=1000 MPa (τ_{max}= 480 MPa) and 1500 MPa (τ=350 MPa) experiments, but steady-state flow was not obtained in the experiment W1027.

Anorthite-olivine (An-Fo) experiments

The mechanical behaviour of An-Fo composites deformed outside the plagioclase peridotite stability field is substantially different from that of the Lab-Fo composites (Fig. 4.4b). The An-Fo samples are initially strong but all samples typically reach a maximum shear stress followed by significant strain weakening. There is a tendency towards a constant shear stress above γ=5.0. The maximum decrease in shear stress is τ ~150-160 MPa in the P_c=1160 and 1030 MPa samples deformed at $\dot{\gamma}$ ~$4.5*10^{-5}s^{-1}$. In all An-Fo experiments most of the axial displacement is accommodated in the An-Fo composite shear zone (Fig. 4.5d). The highest shear stress (τ=400 MPa) is obtained in the sample deformed up to peak stress conditions at P_c=990 MPa. Little shear offset (~0.35 mm) is observed in this sample and, similar to the Lab-Fo experiments, the calculated finite shear strain includes a significant contribution of strain from the dunite forcing blocks.

An-Fo samples deformed at $\dot{\gamma}$ ~$5.0*10^{-5}s^{-1}$ approached a steady state flow stress between τ ~180-220 MPa, which is just above the strength of anorthite deformed at P_c=1000 MPa. Deformation of an An-Fo sample to a shear strain of γ=1.7 at a lower $\dot{\gamma} = 4.0*10^{-6}s^{-1}$ at P_c=1040 MPa occurred at a much lower shear stress of τ ~60 MPa and strain weakening was not observed.

4.4.2 Microstructures and deformation mechanisms

Plagioclase and olivine endmembers

Relict olivine porphyroclasts in the pure olivine sample deformed at P_c=1510 MPa show variable dislocation densities. Dislocation densities can locally be very high (Fig. 4.6a). Some small and isolated dislocation-free new grains (size ~1 µm) occur next to old grains with variable dislocation densities (Fig. 4.6b). There is a large mis-orientation

Figure 4.6: Representative TEM-microstructures of pure olivine sample 50AA deformed to large strain (γ=4.7) at 900°C and P_c=1510 MPa. (a) Olivine grains display variable dislocation densities, with low densities on the left and high densities on the right. The arrow indicates a disordered dislocation array.

between the old and new grains, indicating that the small new grains may be formed by progressive subgrain rotation or by local grain boundary migration mechanisms (e.g. bulging recrystallisation). Well-ordered dislocation walls occur and indicate that some dislocation climb has operated as a recovery mechanism (Fig. 4.6c).

Some elongated arrays of dislocations are disordered with substantial porosity within the dislocation walls (Fig. 4.6d,e). Such porous disordered dislocation walls indicate an origin by micro-cracking. Some cracks are blunted with a few dislocations in their wake. Some of the disordered dislocation wall structures form cells (Fig. 4.6d), whose size (size ∼0.5-1.0 μm) approximately corresponds to that of the new dislocation-free grains. Thus, limited recovery by dislocation climb, presence of micro-cracks and the cell structures with disordered dislocation arrays all indicate low temperature plasticity in the pure olivine sample.

The measured strength of pure plagioclase samples is comparable to that of the plagioclase experiments of Stünitz and Tullis (2001). It is assumed that our pure plagioclase samples deformed by the same deformation mechanisms. At 900°C and P_c=1000 MPa, dislocation creep of labradorite is accommodated by local grain boundary migration recrystallisation, producing relict plagioclase grains with high dislocation densities and small dislocation-free recrystallised grains (size ∼1 μm). In our deformed plagioclase samples some exsolution of amphibole is observed. Experimental deformation of labradorite single crystals (Stünitz et al., 2003) showed that the exsolution and nucleation of amphibole can be triggered by the shear deformation and recrystallisation of plagioclase with a high iron content (Table 4.1).

Labradorite-olivine composites

Little permanent deformation is observed in the BSEM-microstructure of all deformed Lab-Fo composites (Fig. 4.7a). Some plastic deformation has occurred as shown by a weak shape preferred orientation of grains. The microstructural difference with respect to the starting material, however, is small (Fig. 4.3). Occasional cracks in olivine grains parallel to the $\sigma 1$-direction suggest that deformation of olivine at high shear stresses has a component of brittle behaviour. Some brittle behaviour is observed in the coarser olivine grains (size >50 μm) of the forcing blocks as well (Fig. 4.5a-c).

In the deformed Lab-Fo samples, olivine grains have variable dislocation densities, which locally are high (Fig. 4.7b). Dislocations are fairly straight with loops at small inclusions or defects. As in the pure olivine sample, the occurrence of disordered dislocation arrays is often associated with porosity (Fig. 4.7c). Subgrains with ordered

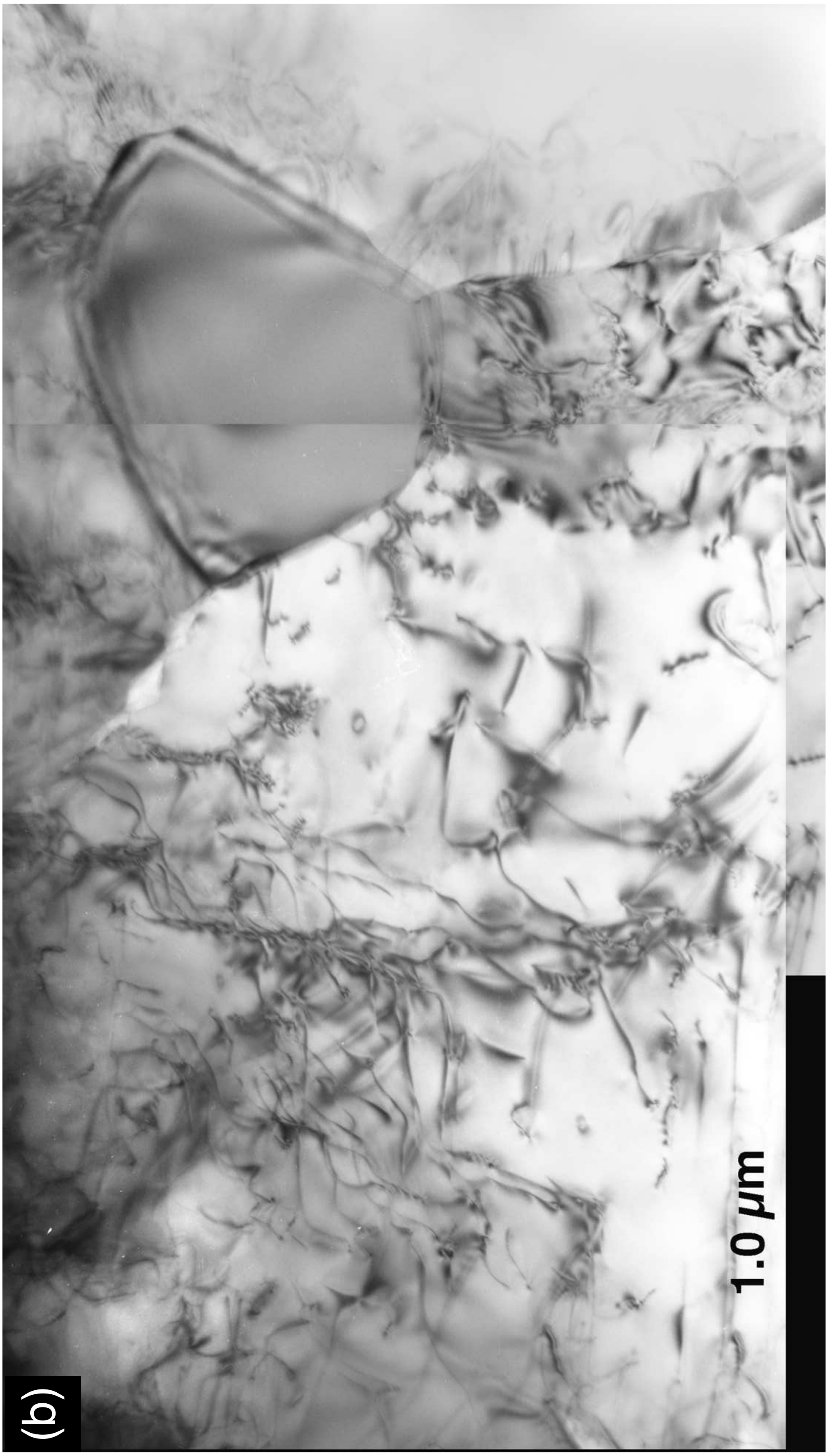

Figure 4.6: (Continued) TEM microstructures of pure olivine sample 50AA (γ=4.7; P$_c$=1510 MPa). (b) A new dislocation-free olivine grain (top right, size ~1 μm) is adjacent to an old grain with a high dislocation density.

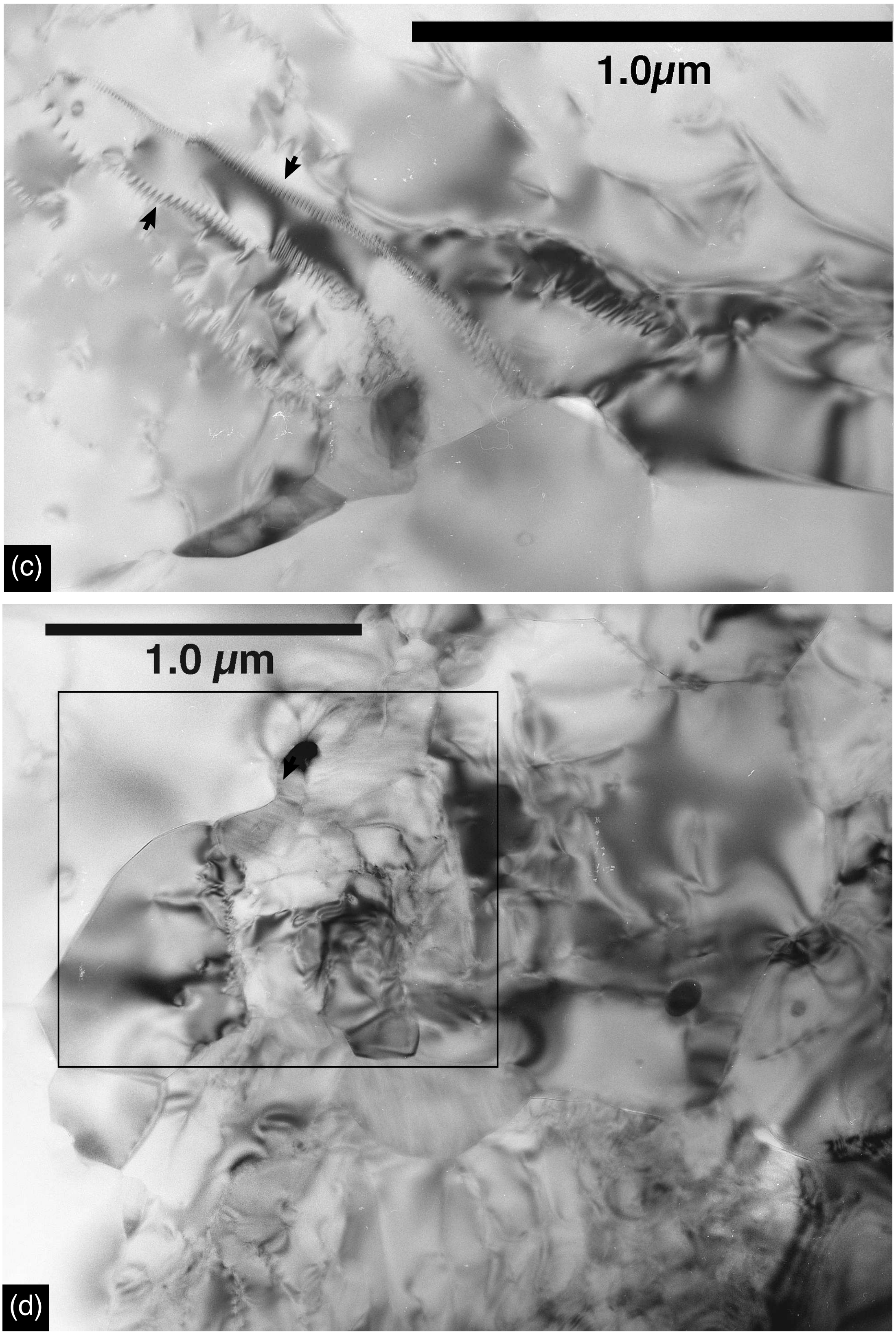

Figure 4.6: (Continued) TEM microstructures of pure olivine sample 50AA (γ=4.7; P_c=1510 MPa). (c) Olivine grains with well-ordered dislocation arrays (arrows). (d) Disordered dislocation substructures in olivine can be associated with porosity, indicating an origin by micro-cracking. The porosity in the marked area is visible when the image is defocused, see (e).

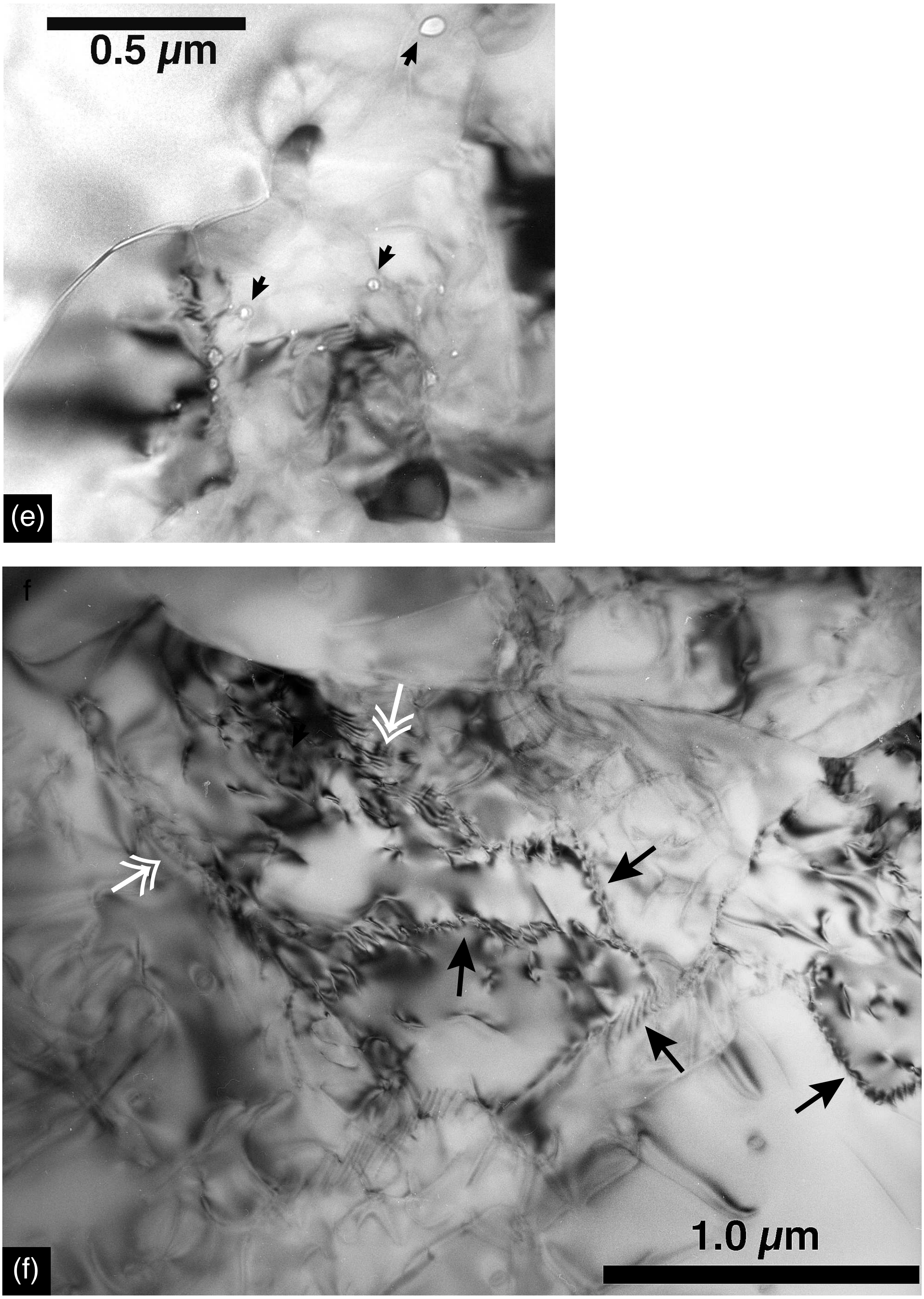

Figure 4.6: (Continued) TEM microstructures of pure olivine sample 50AA (γ=4.7; P_c=1510 MPa). (e) The defocused section corresponding to Fig. 4.6d, to show porosity. Porosity is indicated by arrows and appears as bright spots. (f) Disordered (double arrows) and ordered (single arrows) dislocation walls form a cell structure in olivine.

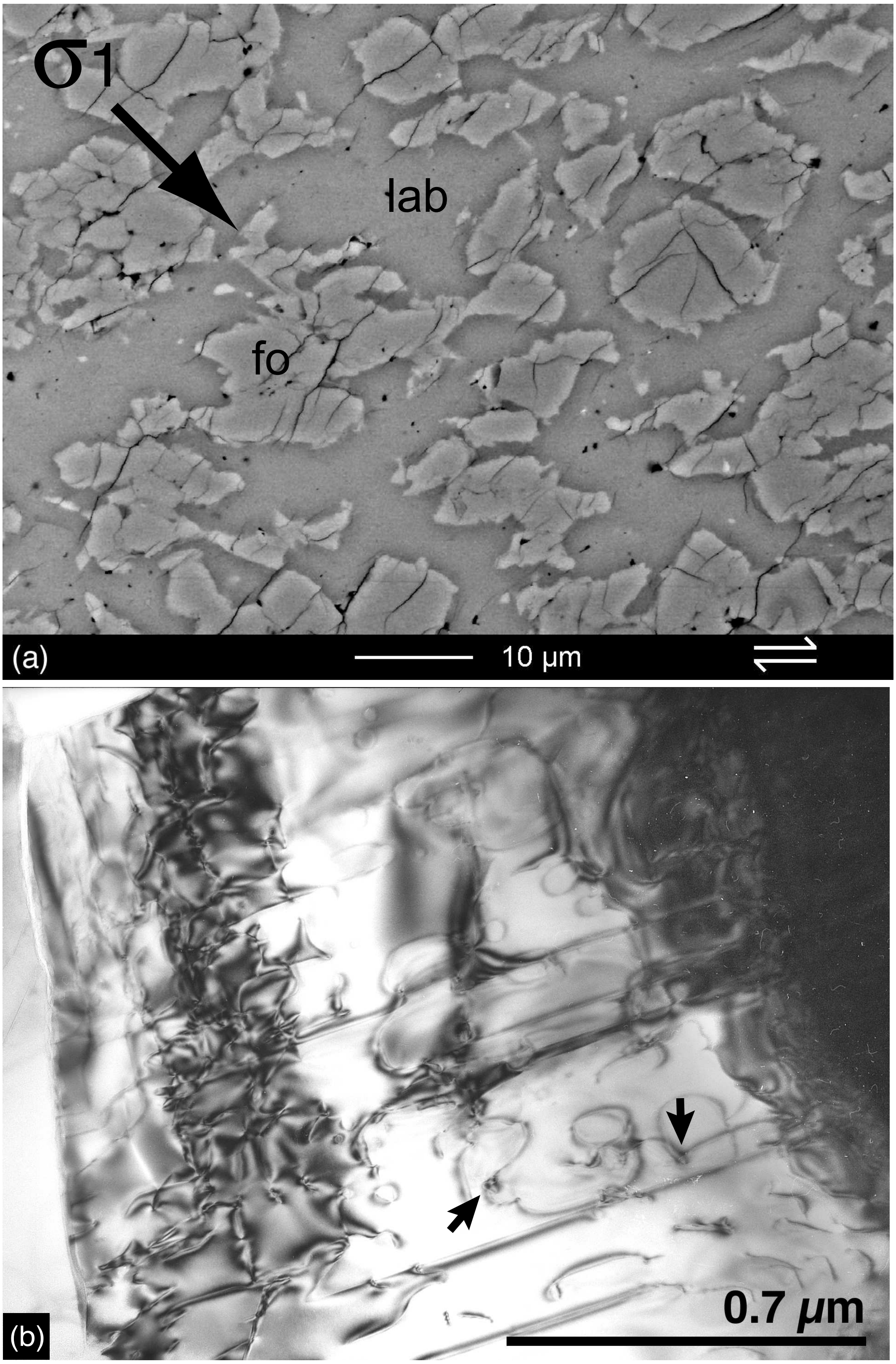

Figure 4.7: Representative microstructures of Lab-Fo composite 42AA deformed at P_c=1470 MPa. (a; BSEM) Labradorite (lab) grains are slightly elongated whereas olivine (fo) grains are rounded. No reaction is observed. Bright rims around olivine result from charging of the sample. Diagonal cracks are due to unloading. (b; TEM) An olivine grain with a high dislocation density. Dislocations are straight and form loops at inclusions and defects (arrows).

dislocation walls and dislocation-free grains are not observed. Thus, it appears that the olivine in the Lab-Fo composite develops fewer recovery features compared to the pure olivine sample (Fig. 4.6).

Labradorite microstructures resemble those of single crystal deformation experiments (Stünitz et al., 2003). Dislocation densities in labradorite are variable but mostly high. Domains with a misorientation of a few degrees are bound by micro-cracks, local high dislocation densities and high elastic strain (cell-like structures; Fig. 4.7d). Such domains occur in regions with high dislocation densities. Micro-twins are often associated with the cell boundaries. Mechanical twinning has been observed to form during fracturing in plagioclase (McLaren and Pryer, 2001; Stünitz et al., 2003), so that some boundaries of the cell structures may be healed micro-cracks. As in olivine, the variable densities of dislocations and the partially micro-crack-induced cell structures in labradorite are indicative of low temperature plagioclase plasticity.

Although the Lab-Fo sample deformed at P_c=1470 MPa only work hardened, few isolated grains of garnet, spinel and orthopyroxene reaction products (size <1 µm) are observed in local regions of high dislocation densities in labradorite grains (Fig. 4.7d). Their occurrence is probably due to some reaction at P_c=1470 MPa, caused by the small pressure overstepping of the labradorite-olivine stability field (Fig. 4.1c).

Anorthite-olivine composites at P_c ~1000 MPa

Syndeformational reaction occurred in all strain weakened An-Fo samples. The weakened An-Fo samples have distinctly different microstructures compared to the strain hardened Lab-Fo samples. In the An-Fo sample deformed to large strain (γ=5.9) at P_c=1160 MPa the extent of reaction is ξ_{plg} ~65% (Fig. 4.8a). Reaction and deformation occurred homogeneously across the sample and decrease towards the undeformed ends of the sample. In BSEM images, the An-Fo reaction is typically characterised by bright aggregates of very fine-grained reaction products (size <1 µm) as well as dark enstatite coronas around the olivine grains (Fig. 4.8b). Reaction products have coalesced and have formed continuous connecting layers across the sample. The reaction products layers define clear C-S-fabrics with well-developed C'-shear bands (Berthé et al., 1979b), consistent with the sense of shear. At P_c=1000 MPa, reaction does not occur under hydrostatic conditions during the time span of the deformation experiments (Table 4.2).

After large strain (γ=5.9), anorthite grains have acquired an elongated shape, with anorthite tails curving into the shear bands. These tails consist of dislocation-free sub-micron sized plagioclase grains (Fig. 4.8c). No compositional differences between

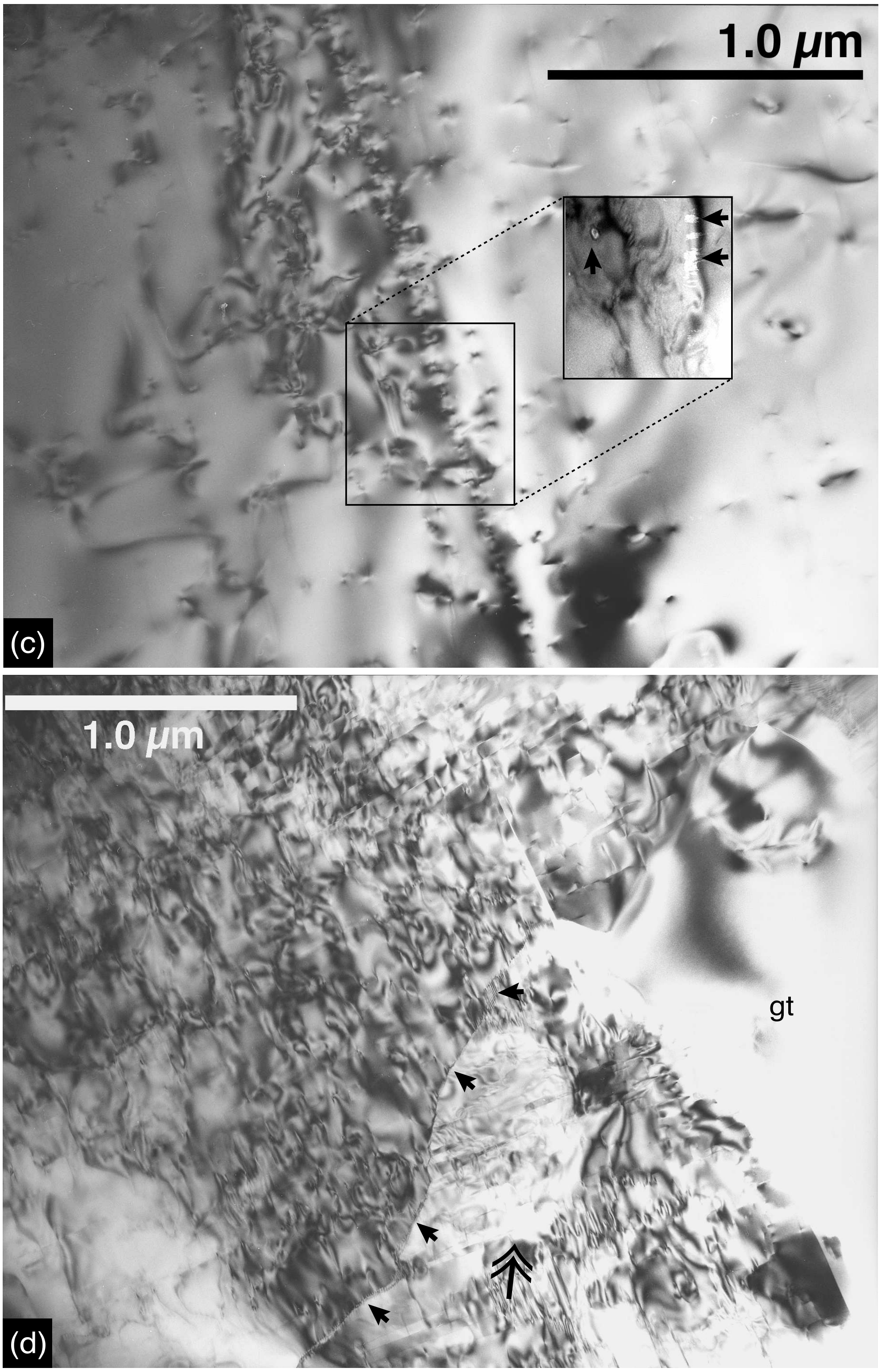

Figure 4.7: (Continued) Representative microstructures of Lab-Fo composite 42AA deformed at P_c=1470 MPa. (c; TEM) A disordered dislocation array in olivine, which is associated with porosity. The inset shows the defocused marked area, in which porosity is visible as bright spots (arrows). (d; TEM) Deformed labradorite grains displaying high dislocation densities. Single arrows indicate a micro-crack with local microtwins. The double arrow indicates a domain bound by micro-cracks and elastically-strained regions. Note a newly formed dislocation-free garnet (gnt) grain on the right.

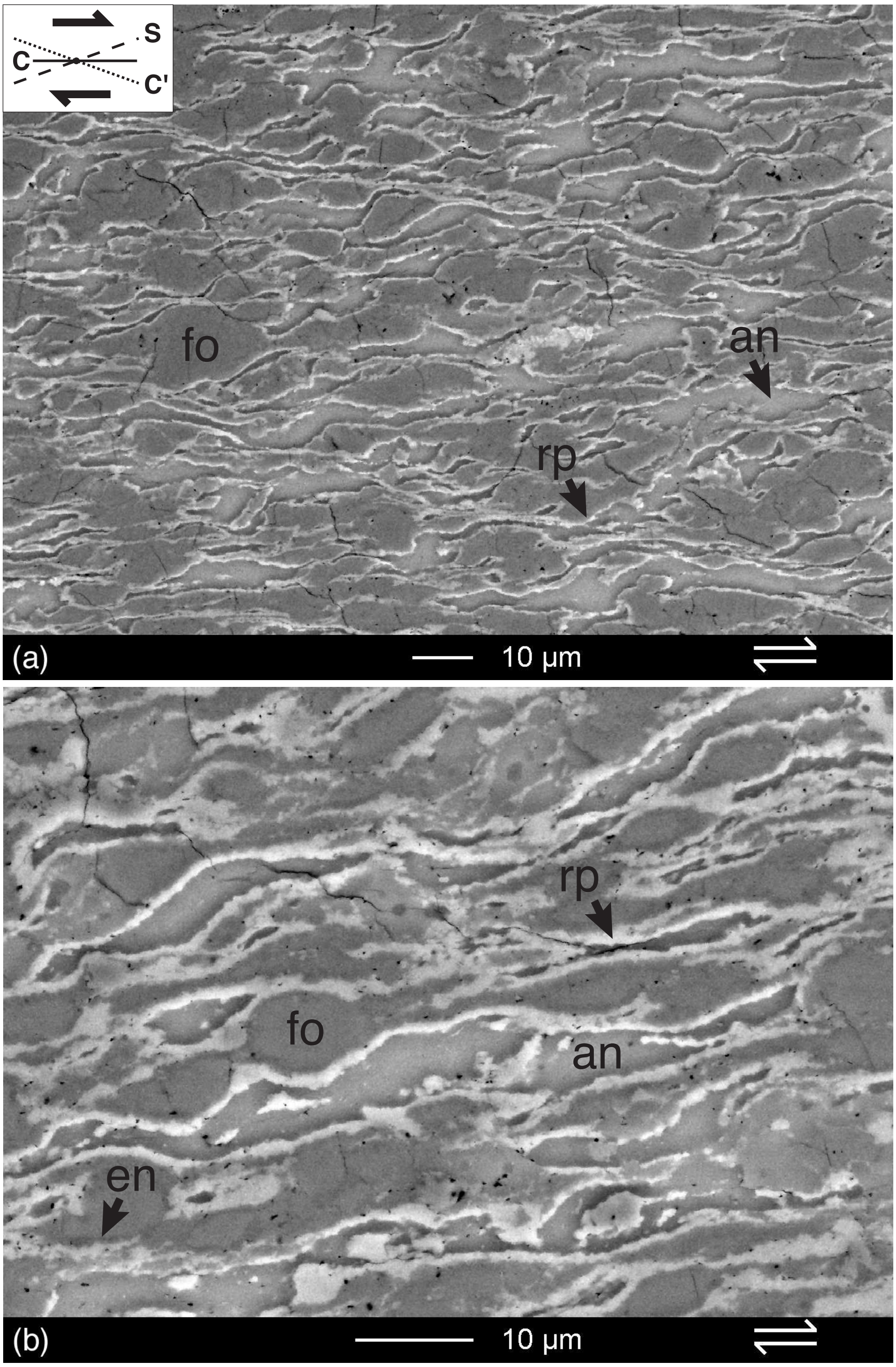

Figure 4.8: Representative microstructures of An-Fo composite 19AA deformed at P_c=1160 MPa. (a = 800x, b = 1600x, BSEM) The An-Fo sample is intensively deformed after large strain (γ=5.9). Olivine (fo), anorthite (an) and fine-grained reaction products (rp; size $<$0.5 µm) define C-S-C' shear bands (see inset, after Berthé et al., 1979a). Reaction products form interconnecting layers in S-foliation orientation. Olivine grains have an enstatite (en) corona.

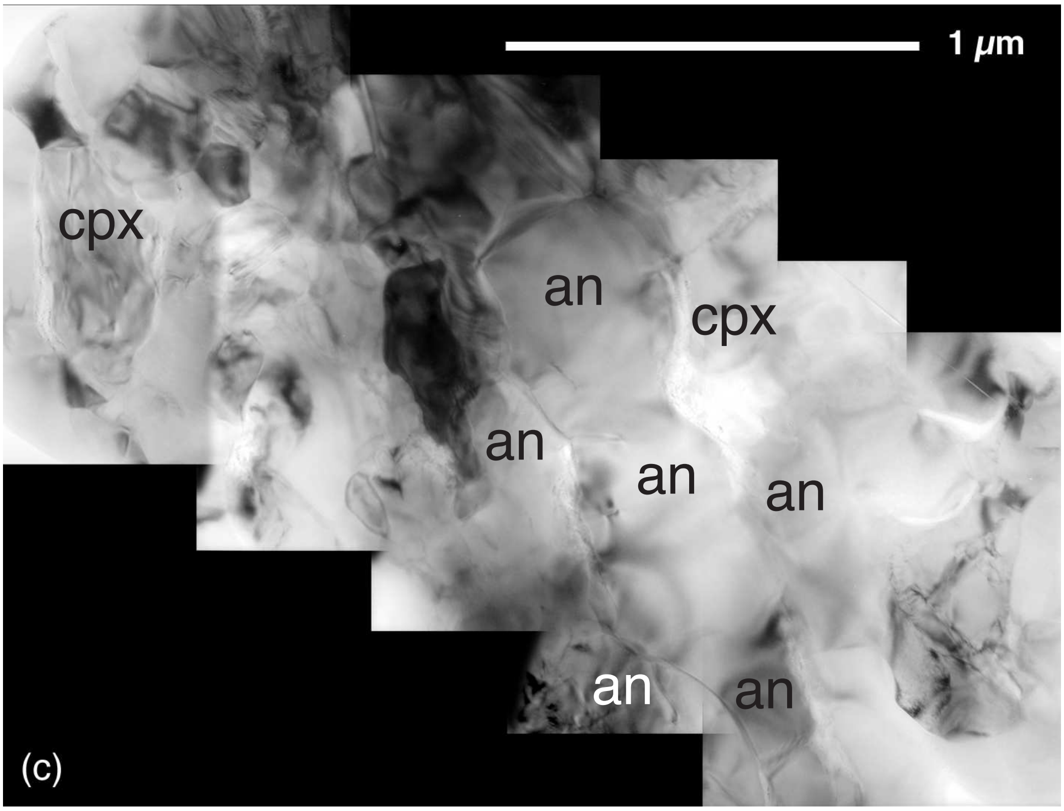

Figure 4.8: (Continued: c; TEM) Small dislocation-free anorthite grains (size ~0.25 μm) occur in the tails of the elongated anorthite grains in (b), indicating dynamic recrystallisation of anorthite.

the sub-micron and relict anorthite grains could be detected by EDS-TEM, indicating dynamic recrystallisation of anorthite. Olivine grains have less elongate shapes and thus appear less deformed than anorthite. Exploratory observations with Electron Backscattered Diffraction (EBSD) microscopy indicate that olivine developed a crystallographic preferred orientation (K. Kunze, pers. comm.). These observations suggest dislocation creep of olivine and more prominent recovery than in the pure olivine and Lab-Fo samples.

Reaction continued to ξ_{plg} ~78% in a sample that was kept for an additional 104 hours at 1030 MPa hydrostatic pressure after large strain deformation (γ=5.8; Fig. 4.9). The coarser microstructure of the reaction product aggregates indicates that reaction products coarsened under hydrostatic conditions, after new phases had nucleated during the deformation stage (Fig. 4.8b). Therefore, it appears that shear deformation during reaction inhibits the coarsening of the reaction products.

The An-Fo composite deformed to peak stress conditions at P_c= 990 MPa only shows incipient formation of very small reaction products in isolated locations at the

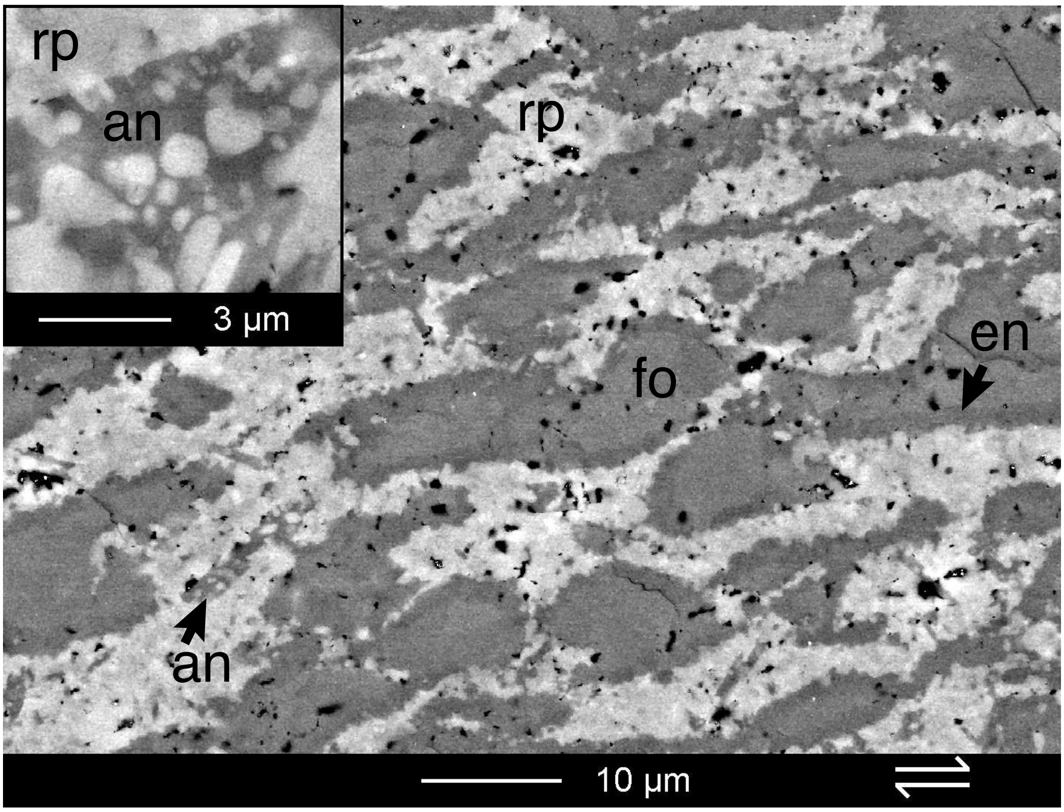

Figure 4.9: Representative microstructures of An-Fo composite 33AA, after a combined deformation and hydrostatic experiment at P$_c$=1030 MPa (BSEM). Large strain (γ=5.8) was followed by an additional 104 hrs at P$_c$=1030 MPa hydrostatic pressure. Reaction progress is $\xi_{plg} \sim 80\%$. The reaction products (rp) have coarsened. Olivine grains (fo) have a well-defined enstatite corona (en). Relict anorthite (an) can only be observed as small patches. The inset shows a detail of an anorthite grain and reaction products.

An-Fo interphase boundaries (ξ_{plg} ~8%; Fig. 4.10). The slightly elongated grain shapes of anorthite as well as the weak alignment of minerals in the shear direction indicate that some plastic flow occurred in the composite.

Deformation to small strain (γ=1.7) at a lower strain rate of $\dot{\gamma}$=4.0*10^{-6}s^{-1} and P$_c$=1040 MPa results in intermediate reaction progress ($\xi_{plg} \sim 45\%$). Reaction products do not form continuous layers after this small amount of strain and C-S fabrics have not developed. As in the P$_c$= 990 MPa sample deformed at $\dot{\gamma}$=5.0*10^{-5}s^{-1}, anorthite and olivine grains display some plastic flow and have a shape preferred orientation in the shear direction (Fig. 4.11).

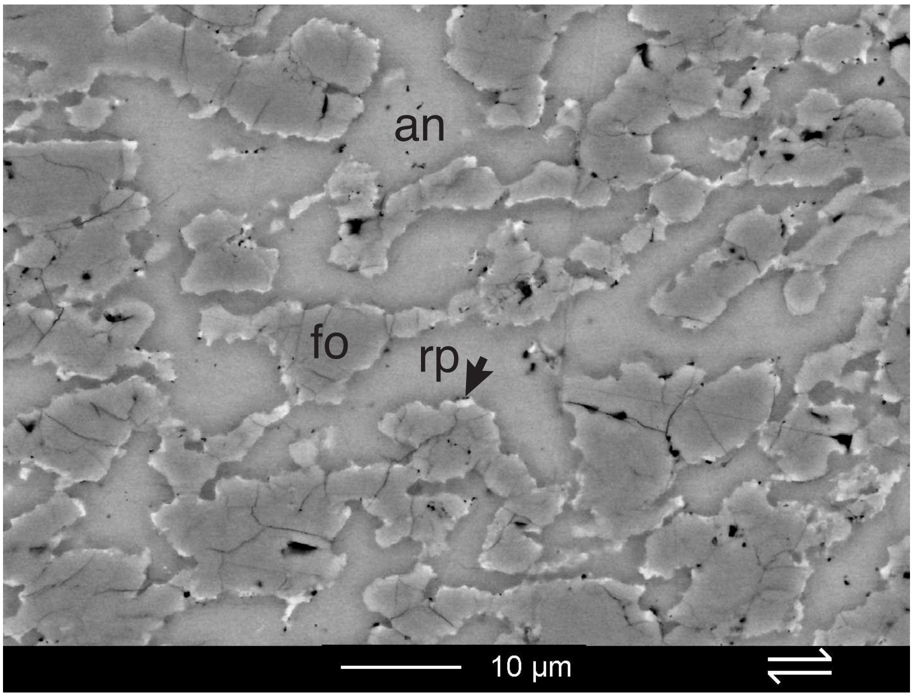

Figure 4.10: Representative microstructures of the An-Fo composite W1028 deformed up to peak stress conditions at P_c=990 MPa (BSEM). Fine-grained reaction products have started to form at the An-Fo interphase boundaries (ξ_{plg} ~8%) before the onset of strain weakening. Enstatite coronas around olivine can not yet be observed.

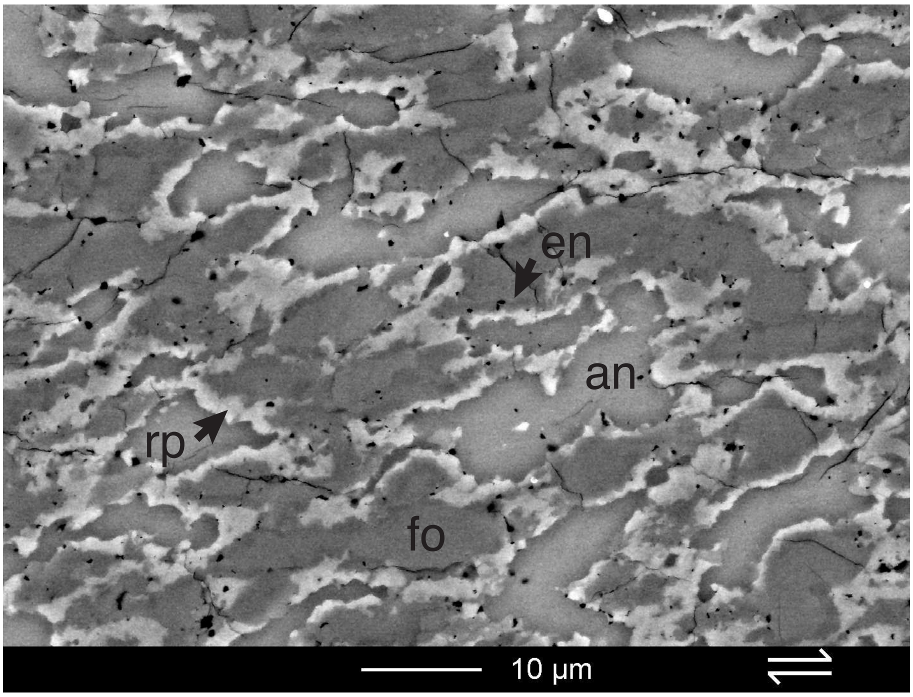

Figure 4.11: Representative microstructures of An-Fo composite 55AA deformed at a shear strain rate of $\dot{\gamma}$=4.0*10^{-6}s^{-1} and P_c=1040 MPa (BSEM). Reaction progressed to $\xi_{plg} \sim 45\%$ in 168 hours. Fine-grained reaction products (rp) and clear enstatite (en) coronas are present. The reaction products have not yet formed interconnecting layers in the sample.

Anorthite-olivine composites at P_c ~1500 MPa

Incipient reaction products in a sample held hydrostatically at P_c=1490 MPa (Table 4.2) indicate that reaction starts under hydrostatic conditions after approximately 30 hrs in experiments with large pressure overstepping (P_c ~1500 MPa). The run-in time of the apparatus force piston to touch the samples and start deformation at $\dot{\gamma} = 5.0*10^{-5}s^{-1}$ takes about the same amount of time in some experiments (e.g. 15-30 hrs). As a consequence, reaction could have started in An-Fo composite samples at the hit-point in experiments with a long run-in time.

In the An-Fo composite deformed to large strain (γ=4.9) at P_c=1630 MPa, approximately 90% of the entire An-Fo composite displays full reaction progress ($\xi_{plg} \sim$ 90-100%), characterised by the near complete disappearance of anorthite from the sample (Fig. 4.12a). C-S-shear bands are present in the sample shear zone, but they are less pronounced than those in samples deformed at lower confining pressures (P_c ~1000 MPa). Relict olivine grains are embedded in a fine-grained reaction product matrix in the P_c=1630 MPa sample (Fig. 4.12b). The An-Fo reaction has formed an enstatite corona around olivine. The corona often grades into the other fine-grained reaction products at the tails of relict olivine porphyroclasts. The enstatite tails give olivine grains a σ-clast character consistent with dextral shear. The σ-clast geometries indicate a strength contrast between less deformed olivine clasts and considerably more deformed matrix of reaction products. The enstatite grains in the corona are fine-grained (size ~0.25-0.5 μm; Fig. 4.12c). Relict olivine grains have a mixture of disordered and ordered dislocation arrays, indicating some recovery of olivine during deformation (Fig. 4.12d).

In the An-Fo sample deformed to small strain and peak shear stress conditions at P_c=1460 MPa (Fig. 4.13a), reaction has progressed further ($\xi_{plg} \sim$ 33%) compared to the small strain sample at P_c=990 MPa($\xi_{plg} <$ 8%). Thin continuous rims of reaction products have formed along all An-Fo interphase boundaries but no true connected layers are observed in the sample. Olivine grains show more ordered dislocation substructures, dislocation-free grains, and only some disordered-dislocation walls associated with porosity, indicative of low temperature plasticity (Fig. 4.13b). Relict anorthite grains have variable dislocation densities (Fig. 4.13c). Local bulging of dislocation-free grains into adjacent regions of high-dislocation density indicates the operation of bulging recrystallisation as a recovery mechanism 4.13d). Compared to the Lab-Fo composites deformed at P_c ~1500 MPa, there is a greater occurrence of dislocation-free grains and well-defined subgrain structures in both anorthite and olivine grains in the

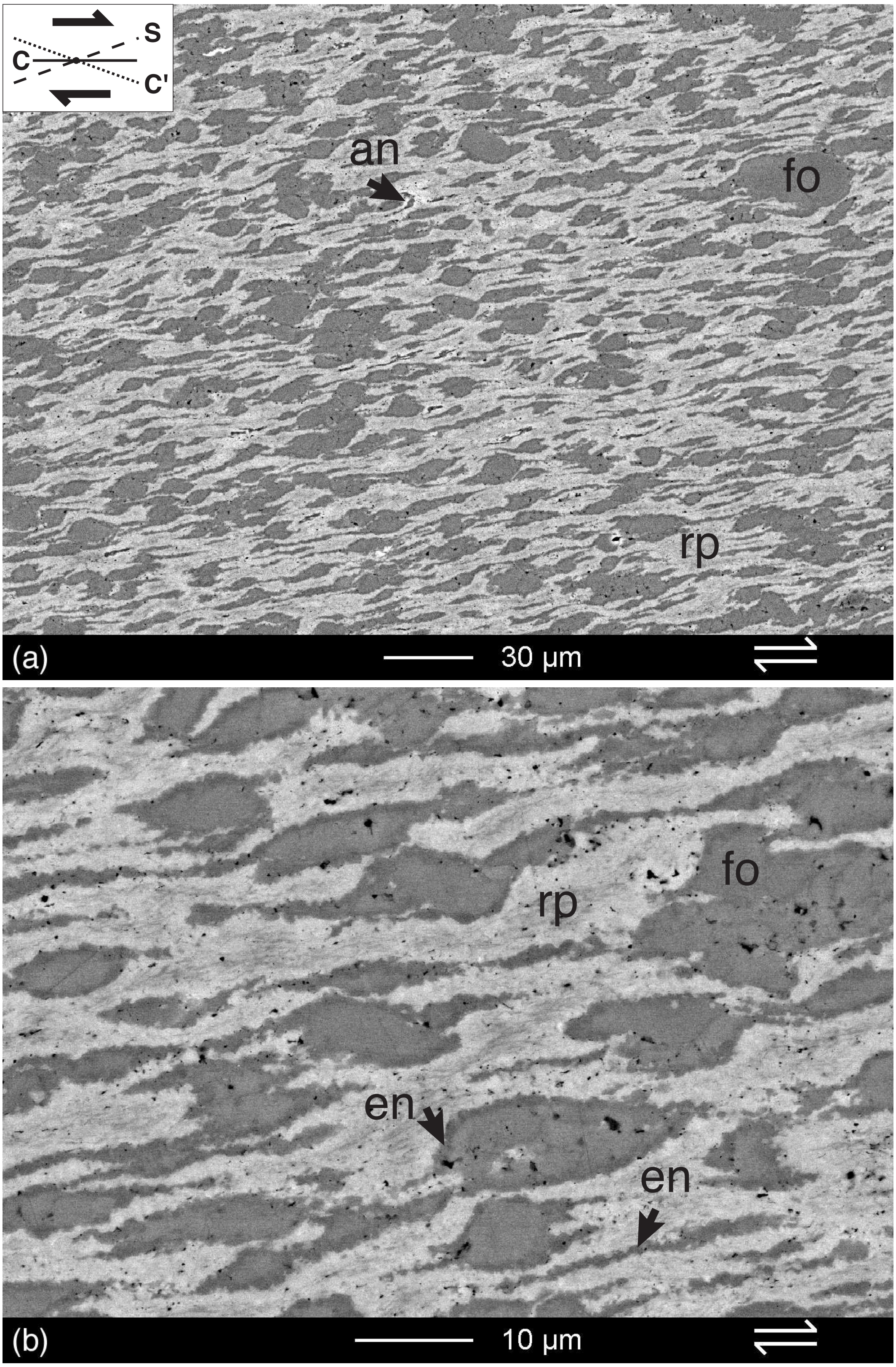

Figure 4.12: Representative microstructures of An-Fo composite 28AA deformed to large strain (γ=4.9) at P_c=1630 MPa. (a; BSEM, 400x) An-Fo reaction is nearly complete ($\xi_{plg} \sim$ 90-100%). The sample 'shear zone' mainly consists of relict olivine (fo) and fine-grained reaction products (rp). Relict anorthite (an) is observed sporadically. The inset shows C-S-C' shear band orientations after (Berthé et al., 1979a).(b; BSEM, 1600x) Tails of enstatite grains (en) extend into the reaction product matrix. Relict olivine grains have σ-clast geometries.

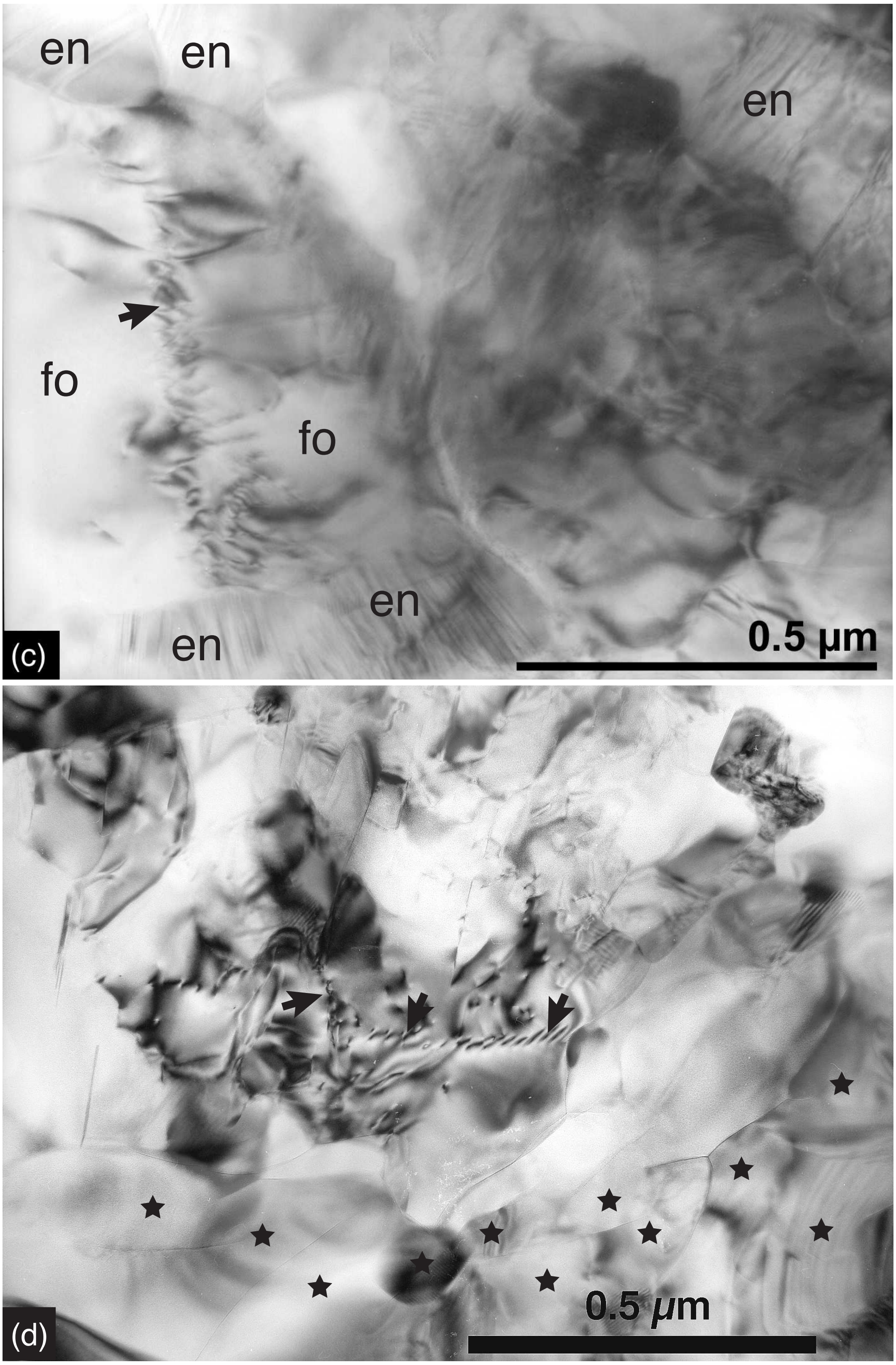

Figure 4.12: (Continued) Bright field TEM microstructures of An-Fo composite 28AA (γ=4.9; P_c=1630 MPa). (c) A relict olivine grain contains a disordered dislocation array and is bounded by small newly-formed enstatite grains (size ~0.25 µm). (d) Relict of olivine grain displaying ordered dislocation walls (arrows). Olivine is surrounded by small grains of reaction products (stars).

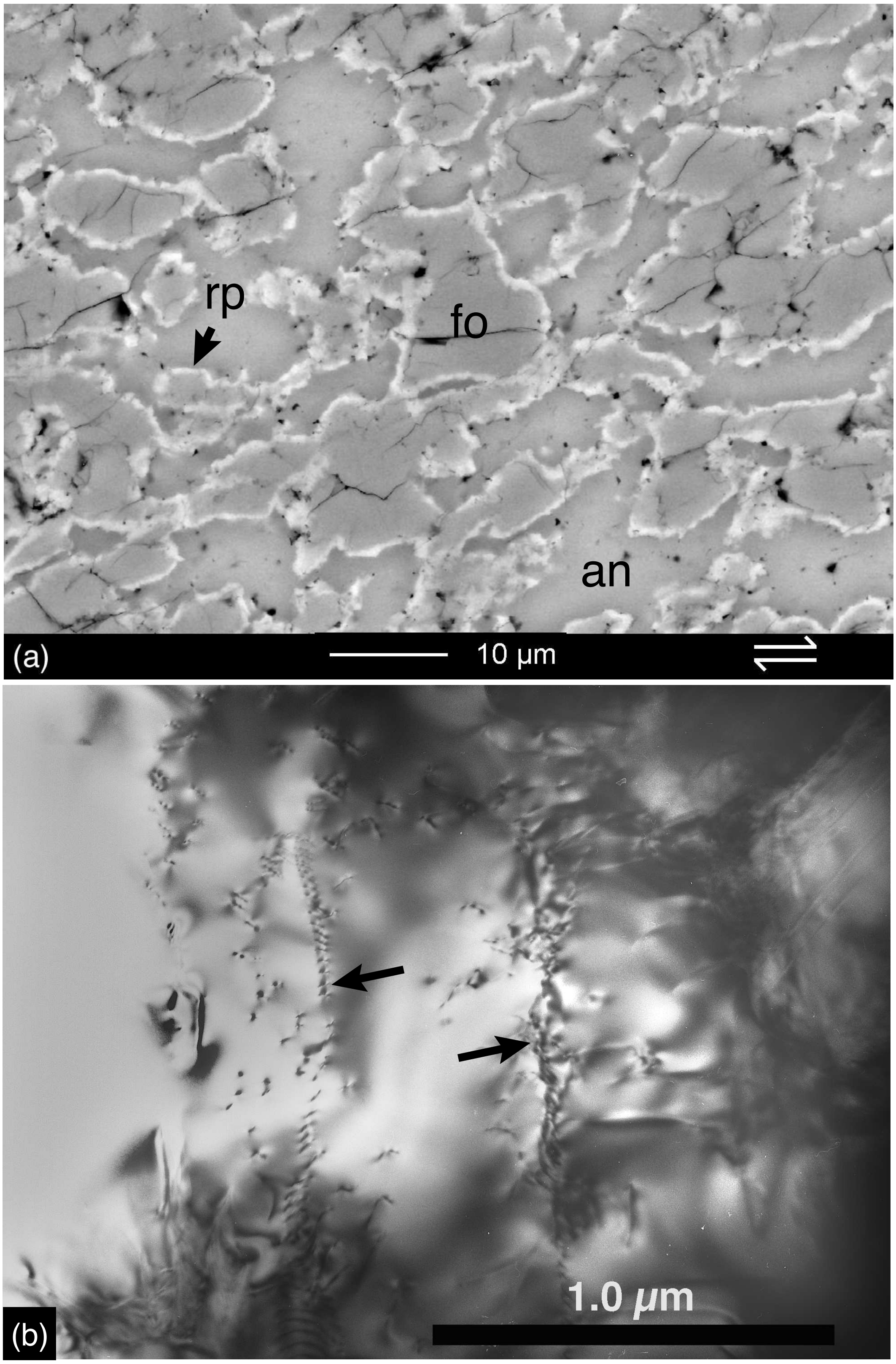

Figure 4.13: Representative microstructures of An-Fo composite 32AA deformed up to peak stress conditions at P_c=1460 MPa. (a; BSEM) Reaction products (rp) occur as a continuous white rim around olivine (fo) and anorthite (an). (b; TEM) Olivine grains have ordered (left arrow) and disordered dislocation arrays (right arrow).

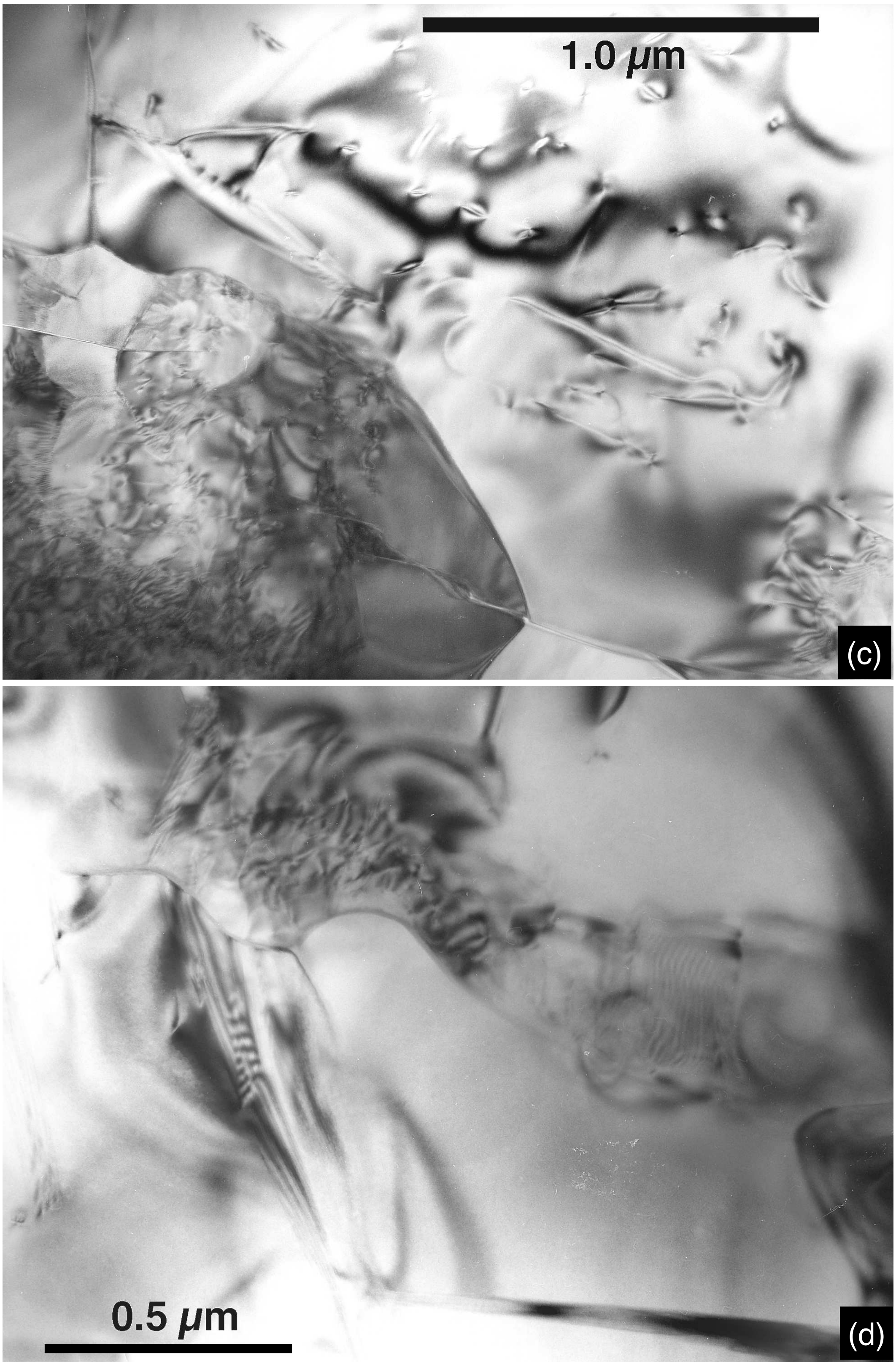

Figure 4.13: (Continued) Bright field TEM microstructures of An-Fo composite 32AA (γ=2.2; P$_c$=1460 MPa). (c) Relict anorthite grains display variable dislocation densities. A high dislocation density is observed in the bottom left, and lower density in the upper right. (d) A dislocation-free anorthite grain bulges into the adjacent anorthite grain where there is a high dislocation density.

reacted sample. Thus, more evidence for recovery is found in the samples deformed with reaction.

Syndeformational reaction products

The reaction products that formed during deformation at P_c=1000 MPa are identified as clinopyroxene, orthopyroxene (enstatite) and spinel (Fig. 4.14a), which corresponds to a spinel peridotite phase assemblage (Fig. 4.1b). Fine-grained (size <0.5 μm) dislocation-free olivine grains often appear intermixed within the reaction products. In all deformed samples, orthopyroxene is mainly observed as a corona around olivine. These corona structures are typical for transport-controlled reactions (e.g. Fisher, 1978). The reaction product aggregates in the P_c ∼1000 MPa samples dominantly consist of clinopyroxene, spinel and orthopyroxene. A mixture of orthopyroxene, clinopyroxene, spinel and garnet (±kyanite) formed during deformation at P_c=1630 MPa (Fig. 4.14b,c).

Most of the polyphase reaction products are very fine-grained (size ∼0.1-0.5 μm) and dominantly free of dislocations (Fig. 4.14a). These small grains have equant grain shapes (Fig. 4.14b). Orthopyroxene grains are often twinned (Fig. 4.14c). The stress concentrations at neighbouring grains caused by twinning may induce dislocations that move away from the stress concentration in these grains, as indicated by slip-traces (Fig. 4.14c).

Orthopyroxene grains with a somewhat larger size (size ∼1 μm) contain arrays of partial dislocations (Fig. 4.14d). The dislocations in orthopyroxene grains are at the tips of (010)-stacking faults. Such faults typically form during deformation-induced transformation via partial dislocations from ortho-enstatite to clino-enstatite (Kirby and Stern, 1993). However, the ubiquitous presence of dislocation-free grains in the reaction product aggregates, their small size (size ∼0.25 μm), equant grain shapes and mixed character, suggest that the polyphase reaction product aggregates do not deform by dislocation creep but by diffusion creep involving grain boundary sliding.

Summarising the mechanical and microstructural observations of plagioclase-olivine experiments, the occurrence of a syndeformational plagioclase-olivine reaction causes strain weakening. At low pressure overstepping (P_c ∼1000 MPa), the onset of weakening is associated with the onset of reaction. At high pressure overstepping (P_c ∼1500 MPa), the start of weakening coincides with the development of reaction product rims. Therefore, the strain weakening of the An-Fo composites is associated with the formation of fine-grained (size ∼0.25 μm) reaction products. The onset of steady-state flow (γ >5) corresponds to microstructures in which fine-grained reaction products form

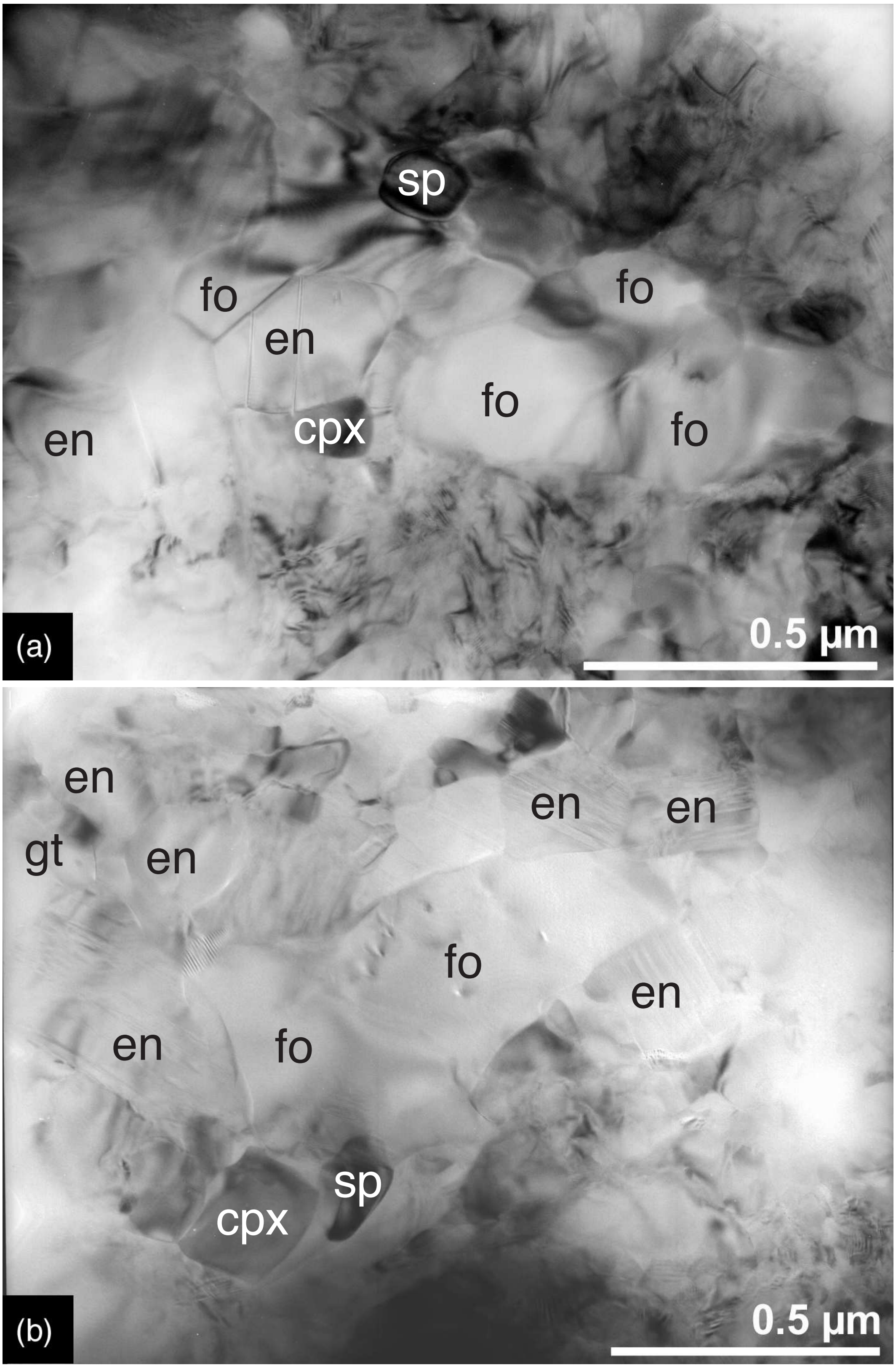

Figure 4.14: Representative TEM microstructures of syndeformational reaction products. (a-b) Fine-grained spinel (sp), orthopyroxene (en), clinopyroxene (cpx) and garnet (gt) reaction products that typically form at (a) P_c ∼1000 MPa and (b) 1500 MPa. The products are <0.5 µm and dislocation-free. Small <0.5 µm forsterite-rich olivine grains (fo) are part of the fine-grained mixture.

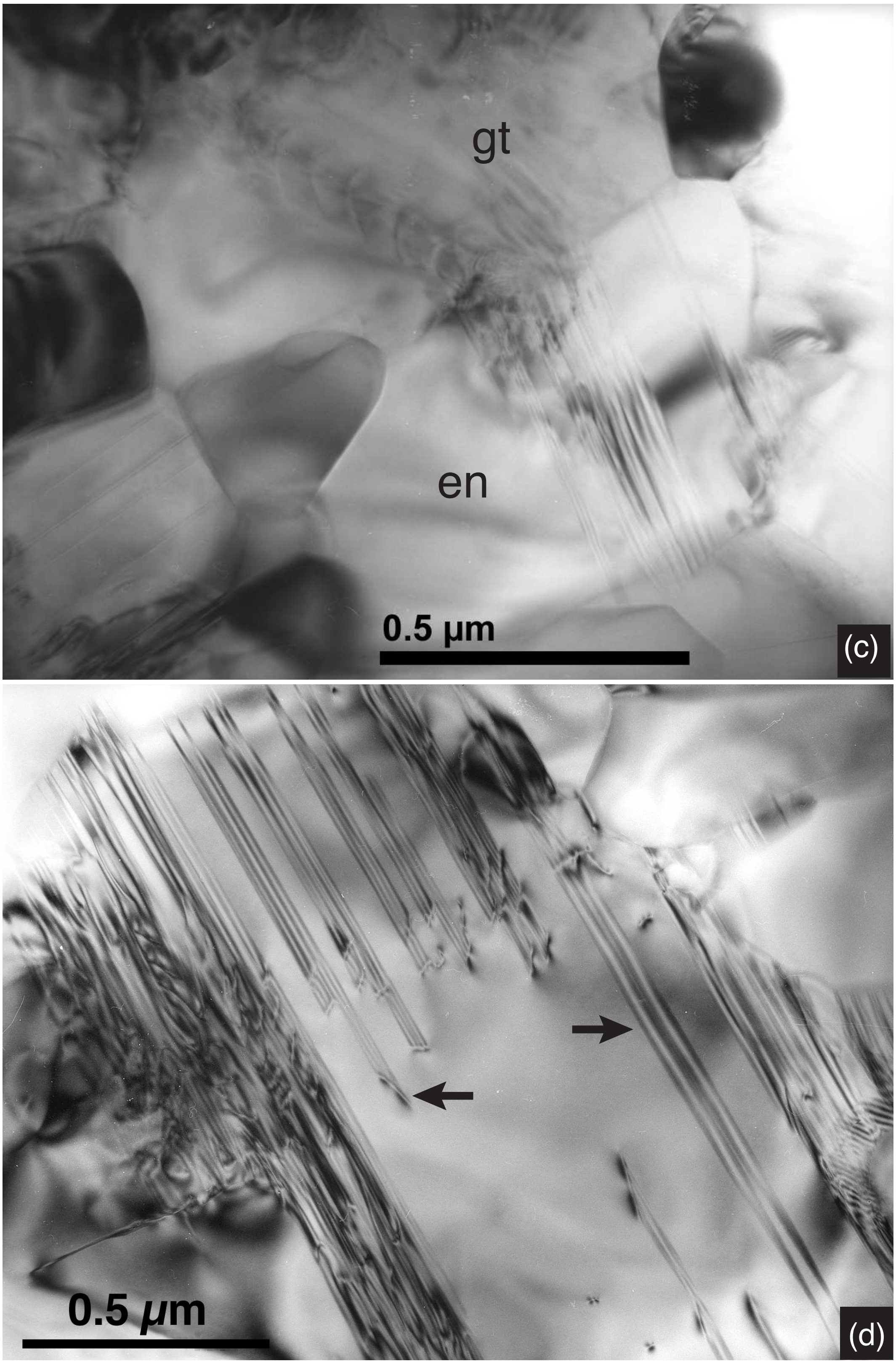

Figure 4.14: (Continued: c) Newly formed orthopyroxene (en) and garnet grains (gt) in sample 28AA (γ=4.9; P_c=1630 MPa). The orthopyroxene grain displays twinning. Stress concentrations in the neighbouring grains caused by the twinning are indicated by slip traces from the centre to the top left. (d) After large strain at P_c=1630 MPa (28AA), newly formed opx grains have been deformed. The dislocations (left arrow) in opx grains are at the tips of stacking faults (right arrow).

interconnecting layers throughout the sample shear zone. In the absence of reaction, plagioclase-olivine composites strain harden until the point of embrittlement.

4.5 Discussion

4.5.1 Strain hardening of Lab-Fo composites

The fact that the deformed Lab-Fo composites are considerably stronger than their olivine and plagioclase end-members indicates that the An-Fo composite strength is not only a function of the strength of its end-members. Two-phase rocks generally obey composite flow laws deduced from end-member flow laws (Tullis et al., 1991; Ji and Zhao, 1994; Ji et al., 2001), if the composite material deforms by identical deformation mechanisms as the monophase material.

Our microstructural observations correspond well to other rheological studies on polyphase rocks with a large strength contrast (e.g. quartz-feldspar: Dell'Angelo and Tullis, 1996, anorthite-quartz: Ji et al., 2000, olivine-basalt: Hirth and Kohlstedt, 1995). These studies indicate that when the stronger phase is volumetrically dominant, strain is primarily accommodated by plastic flow of the weaker phase, while the stronger phase remains rigid or deforms brittlely. Dell'Angelo and Tullis (1996) found that deformation of quartz-feldspar aggregates at 700°C resulted in a strength increase of quartz, which rose above that of feldspar. They inferred that the increased quartz strength was due to the scarcity of quartz-quartz grain boundaries in the aggregate, which limited recovery by grain boundary migration recrystallisation.

Olivine and labradorite in the Lab-Fo composites have a high strength contrast ($\tau_{Fo}/\tau_{Lab,An} \approx 350/100 \approx 3.5$). Dislocation creep processes primarily accommodate deformation in endmember olivine and plagioclase and the dispersion of labradorite and olivine in the composite is good (Fig. 4.7a). Therefore, similar to the quartz-feldspar case of Dell'Angelo and Tullis (1996), a large number of plagioclase-olivine interphase boundaries may have impeded the strain-induced grain boundary migration recrystallisation in the individual phases.

During the low-temperature plasticity that characterises the Lab-Fo samples, the high stresses (τ >500 MPa) cause some grain-scale cracking (Fig. 4.7c). Nevertheless, the temperature is still high enough to allow some recovery in plagioclase (Fig. 4.7d) and olivine (Fig. 4.7b). If plagioclase-olivine interphase boundaries inhibit grain boundary migration, new plagioclase grains can only form by subgrain rotation recrystallisation. However, dislocation climb in plagioclase is limited at 900°C and $\dot{\gamma}$=5.0*10^{-5}s^{-1}

(Stünitz and Tullis, 2001; Stünitz et al., 2003). Thus, the recovery processes in labradorite and in olivine can not keep up with the build-up of dislocation densities. Therefore, labradorite and olivine grains locally fracture during strain hardening by low-temperature plastic deformation (Fig. 4.7c).

4.5.2 Reaction weakening of An-Fo composites

During constant strain rate deformation ($\dot{\gamma}$=5.0*$10^{-5}s^{-1}$) and a reduction of grain size by approximately one order of magnitude (from ~7 μm olivine and plagioclase to ~0.25 μm products), the shear stress decreases because the deformation mechanism changes from grain size insensitive creep (dominantly dislocation creep) to grain size sensitive creep (Fig. 4.2). The strain weakening of An-Fo composites can be explained by a transition in deformation mechanism from dominantly plastic flow of the 'strong' plagioclase-olivine composite to dominantly grain size sensitive deformation of the 'weak' polyphase reaction products and fine-grained recrystallised anorthite and olivine. This transition is supported by the apparent strength decrease between olivine porphyroclasts and the clinopyroxene-rich reaction product matrix (Fig. 4.12b). In deformation experiments on single phase aggregates, clinopyroxene is only found to be weaker than olivine when deforming within the grain size sensitive creep field (Bystricky and Mackwell, 2001; Dimanov et al., 2003).

Because most of the reaction products have an extremely fine grain size (size <1 μm) and they are primarily dislocation free, it is probable that the new phases deform by diffusion-accommodated grain boundary sliding (DAGBS). It is not uncommon, though, that newly formed pyroxene grains contain dislocations (Fig. 4.14d). Therefore some deformation may be accommodated by dislocation-accommodated grain boundary sliding as well.

The implied reaction weakening mechanism, i.e. the formation of fine-grained reaction products that deform by DAGBS, was inferred in other rock deformation studies as well, although always during dehydration (Murrell and Ismail, 1976; Rutter and Brodie, 1988a; Paterson, 1989; Olgaard et al., 1995) and hydration (Rutter et al., 1985; Stünitz and Tullis, 2001) reactions. In the An-Fo composites, the change in deformation mechanism occurs in a dry state during simultaneous anhydrous reaction and plastic deformation.

The onset of strain weakening in P_c ~1000 MPa experiments is associated with the first occurrence of fine-grained reaction products, as documented by experiment W1028 which was stopped at peak stress conditions (Fig. 4.10). Therefore, the observed weakening in the P_c ~1000 MPa experiments is not transient and coincides directly with the onset of the reaction in the composites. In the high pressure overstepping experiments (P_c ~1500 MPa), the reaction starts after approximately 30 hours. This time approximately coincides with the 'run-in' time of the apparatus force piston to reach the hit point. Thus, reaction starts due to the increased chemical driving potential (e.g. due to pressure overstepping) approximately at the hit point. Therefore, reaction products form earlier during An-Fo composite deformation in high pressure overstepping experiments (Fig. 4.13a).

The difference in reaction progress between the high (P_c ~1500 MPa) and low (P_c ~1000 MPa) pressure overstepping experiments can thus be explained by the faster reaction kinetics due to the larger pressure overstepping. As a consequence, the bulk sample strength is reduced and the peak shear stress in some of the high confining pressure experiments can appear lower compared to lower confining pressure experiments (Fig. 4.4b).

Regardless of the amount of pressure overstepping, the onset of steady-state flow in the An-Fo composites is characterised by the coalescence of reaction product layers (Fig. 4.8a), or the formation of a matrix of fine-grained reaction products (Fig. 4.12a). The reaction has not yet gone to completion after large strain (γ=5.9) in the P_c ~1160 MPa experiment. Therefore it appears that steady-state flow is mostly dependent upon the coalescence of the reaction products into continuous layers rather than completion of the reaction. The similar flow stresses at approximate steady-state conditions (τ ~200 MPa; Fig. 4.4b), despite the different reaction progress, suggest that continuous layers of newly-formed phases are the primary control on the composite flow strength.

During syndeformational dehydration of serpentinite (Rutter and Brodie, 1988b) and hydration of plagioclase (Stünitz and Tullis, 2001), the localisation of strain in weak fine-grained reaction products was observed in narrow shear bands. The control of the weakest phase forming continuous layers parallel to the bulk shear plane, on the mechanical strength of two-phase rocks has been studied experimentally by Jordan (1987). This study on the development of a foliation within limestone-halite aggregates shows that the strength of the bulk aggregate decreases as the foliation becomes stronger.

In the An-Fo composites, continuous layers of fine-grained reaction products define the main foliations. Typical C and S shear band structures are observed in all our reacted samples that were deformed to large strain (Figs. 4.8a). Interconnecting layers of reaction products are observed in C-S orientations. The coalescence of reaction product layers becomes stronger with increasing shear strain and with higher reaction progress (compare Figs. 4.13a, 4.8a and 4.12a). The S-oriented layers of reaction products become rotated toward the C-orientation with increasing strain. The C-layers probably are the primary sites of strain accommodation (Jordan, 1987).

C'-planes have also developed, but only after a larger amount of strain (γ >2). They do not develop at the onset of weakening at P_c ~1000 and P_c ~1500 MPa, and may become obliterated with progressive reaction and deformation to large strain (Fig. 4.12a). The C'-bands are defined by curved recrystallised tails of anorthite and olivine (Fig. 4.8b). Strain softening can occur in the C'-structures during dynamic recrystallisation of anorthite in layered quartz-anorthite composites (Ji et al., 2004). It may be inferred that recrystallised grains of anorthite and olivine in the C'-bands have accommodated some strain at these locations.

Strain weakening was not observed in the An-Fo sample deformed at a lower $\dot{\gamma}$=4.0*10^{-6}s^{-1} at P_c =1040 MPa. In this small strain experiment, the fine-grained reaction products have not yet coalesced into continuous layers (Fig. 4.11). This lack of coalescence is probably due to the small shear strain (γ=1.7). Therefore, the question remains open whether a shear stress decrease will be observed after a larger strain at lower strain rates.

Other weakening mechanisms probably have made only small contributions to the weakening of the An-Fo composites. It is difficult to argue for an effect of transformation plasticity (Poirier, 1985; Meike, 1993; Schmidt et al., 2003) because the An-Fo reaction is first of all not a transient phenomenon during deformation and secondly not of a polymorphic reaction type. Some disordered-dislocation substructures associated with porosity have been formed in the An-Fo composite deformed at peak stress conditions at P_c=1460 MPa (Fig. 4.13c). The porosity indicates micro-cracking. Similar dislocation microstructures occur in the strain hardened Lab-Fo composites as well (Fig. 4.7d). Therefore, it is unlikely that grain scale micro-cracking contributed to the observed composite weakening. Water weakening is not important during deformation of plagioclase-olivine composites with a <30 ppm H_2O content.

4.5.3 Recovery processes during reaction

Sub-micron and dislocation-free grains of anorthite (Fig. 4.8c) and olivine (Fig. 4.14a,b) formed in the partially reacted An-Fo composite deformed to large strain at P_c=1160 MPa. Dislocation substructures formed in olivine and plagioclase prior to the strain weakening (Fig. 4.13b). However, elongation of olivine and plagioclase porphyroclasts to large aspect ratios continues after the onset of weakening during progressive shear deformation (Fig. 4.8b and 4.12b). More pronounced recovery features have been observed in olivine in the reacted and weakened samples (Fig. 4.8c, d) compared to unreacted ones (Fig. 4.7b-d). Thus it appears that reaction and deformation of fine-grained reaction product aggregates enhanced recovery of the An-Fo composite grains.

Enhanced recovery during reaction may be explained by the reduction in shear stress, i.e. the strain weakening, that is associated with the formation of new fine-grained phases. In contrast to the strain hardened Lab-Fo composites, recovery processes were able to keep up with the slower rate of deformation of olivine and plagioclase porphyroclasts in the reacted samples because of strain partitioning. The strain rate partitioning between the reaction product aggregates and the relict anorthite and olivine grains has been studied by de Ronde et al. (2004), who have shown that fine-grained opx-cpx-spinel aggregates accommodate a large fraction of the finite strain.

Dynamic recrystallisation of anorthite is not associated with changes in composition in the $P_c \sim 1000$ MPa experiment, although anorthite is metastable. This observation suggests that the driving potential for anorthite recrystallisation is solely due to strain energy stored in the crystals (in the form of dislocations). Such dynamic recrystallisation of metastable phases is only possible if the transport of material is strongly inhibited. In other words, the local chemical equilibrium on a very small scale (~1 µm) suggests a local chemically isolated system. Such a situation is consistent with the dry conditions in the sample.

4.5.4 Application to nature

Our experiments demonstrate reaction-weakening effects that can lead to shear localisation in plagioclase lherzolites during prograde metamorphic reactions to spinel and garnet lherzolites. Shear localization is important in models of mantle denudation during crustal thinning and extension (Lemoine et al., 1987; Drury et al., 1991; Vissers et al., 1995, 1997).

Microstructural studies in peridotites (Furusho and Kanagawa, 1999; Newman et al., 1999; Handy and Stünitz, 2002) suggest that there is a change in the dominant deformation mechanism from dislocation to diffusion creep induced by reactions during the transition from spinel peridotites to plagioclase peridotites, i.e. the reverse of the studied transformation. Striking similarities in microstructures and implied deformation processes are found between the sheared P_c=1500 MPa An-Fo samples (Fig. 4.12b) and plagioclase-bearing ultra-mylonites in the North Pyrenean Zone (Newman et al., 1999; Handy and Stünitz, 2002).

In both cases, the reaction caused a strong reduction in grain size by forming new fine-grained reaction products. Overall strain accommodation in the shear zones occurs in interconnecting layers of new phases, which deform by grain size sensitive creep. The fact that the natural reaction is the reverse of the experimentally studied one is of minor consequence to the underlying processes because it is the small size of reaction products that changes the deformation mechanism and not the type of reaction product itself. In the An-Fo experiments, the weakening is caused by the transition in deformation mechanism from grain size insensitive to grain size sensitive creep, and that transition is also inferred in the natural examples (Newman et al., 1999; Handy and Stünitz, 2002).

The investigated pressure-temperature range is realistic for the upper mantle in extensional tectonic settings. The grain sizes of the reaction products are likely to be somewhat larger in naturally deformed rocks (e.g. sizes <10 µm, Newman et al., 1999); however the occurrence of grain-size sensitive creep shifts to large grain sizes at slower natural strain rates (Fig. 4.2). Despite the fast experimental strain rates, our microstructural results appear to be very similar to the natural cases. Therefore our experiments provide a better understanding of the processes involved in some cases of strain localisation in natural shear zones, and imply similar reaction weakening effects.

In order to obtain grain size sensitive creep (e.g. grain boundary sliding), grain sizes have to be reduced by a significant amount (Brodie and Rutter, 1987). It is obvious from the 0.25-µm reaction product grains that neocrystallisation of new phases is an effective mechanism for grain size reduction. In order to maintain a strain weakened material after grain size reduction, the preservation of small grains is important. Pinning of grain boundaries by different adjacent phases reduces grain growth in polyphase material (Olgaard and Evans, 1988; Olgaard, 1990). Phase boundary pinning is optimised in well-mixed polyphase materials. The dispersion of different phases can be achieved during grain boundary sliding of fine-grained material (Kruse and Stunitz, 1999; Kenkmann and Dresen, 2002).

The An-Fo sample deformed to high strain and subsequently left at P_c=1030 MPa hydrostatic pressure and 900°C for 4 days (Fig. 4.9) shows only limited growth of the new phases that formed during deformation (Fig. 4.8b). Grain growth of existing new phases could have been hindered by either the lack of water, the further nucleation of new phases or significant phase dispersion in the fine-grained aggregates. Well-dispersed, polyphase reaction products appear crucial to the preservation of a reduced grain-size. Therefore the effects of syndeformational reactions that produce polyphase reaction products under anhydrous conditions are expected to be efficient in suppressing grain growth, even during prograde metamorphic conditions. Thus, the strain weakening of plagioclase-olivine composites is not a transient phenomenon because after the weakening, there hardly is an increase in flow stress.

Most importantly, our experiments demonstrate that the localisation of strain by mineral reactions can be achieved under dry, anhydrous conditions. Basement rocks can be dry for long periods of time under metamorphic conditions, with only short and localised periods of fluid infiltration (e.g. Rubie, 1986; Jackson et al., 2004). Also, most rock-forming minerals are solid-solution phases, and their stability is likely to change along any given P,T-path during their tectonic history (e.g. Newman et al., 1999; Stünitz and Tullis, 2001). Therefore, rheological weakening by water-deficient reactions alone is a good candidate for strain localisation in the upper mantle and lower crust, and in other polyphase rocks under a wide range of geological conditions as well.

4.6 Conclusions

In order to study the effects of a solid-solid mineral reaction on the plastic behaviour of rocks, we have performed shear deformation experiments on anhydrous plagioclase-olivine composites at 900°C, confining pressures of 1000-1600 MPa and a constant $\dot{\gamma} \sim 5*10^{-5}s^{-1}$. Good agreement was found with natural observations of strain localisation. Our results point to mineral reactions as important causes for strain localisation in the upper mantle and lower crust. The following conclusions can be made:

1. Under dry conditions, strain localisation in plagioclase-olivine composites can be caused by syndeformational solid-solid metamorphic reactions.

2. At all chosen confining pressures and in absence of reaction, labradorite-olivine composites strain-harden to high stresses, close to the brittle-plastic transition. The strain hardening is probably caused by labradorite-olivine phase boundaries, which prevent recovery processes that require grain boundary migration.

3. Dry syndeformational reaction of anorthite and olivine composites causes a pronounced strain weakening.

4. The reaction weakening mechanism results from grain size reduction by development of fine-grained polyphase reaction products. The polyphase reaction products deform by a grain size sensitive creep mechanism (e.g. grain boundary sliding). As a result, syndeformational reaction causes a change from grain

size insensitive dislocation creep of the anorthite-olivine composite to grain size sensitive creep of reaction products.

5. The onset of the strain weakening coincides with the onset of reaction. The reduction in shear stress and onset of steady-state flow involves the progressive coalescence of fine-grained polyphase reaction product aggregates in interconnecting layers. Most of the applied strain is partitioned into the interconnecting layers of reaction products.

6. Strain partitioning into reaction product layers reduces the strain rate in anorthite and olivine porphyroclasts. As a result, original anorthite and olivine grains deform at lower strain rate conditions as well as lower stress, which enhance dislocation climb.

4.7 Acknowledgements

We thank Dick Yund for his excellent laboratory expertise. Peter Ulmer kindly provided us with Blumone gabbro. We are grateful to Sylvie Demouchy, Steve Mackwell and Harald Behrens for their help with the FITR analysis at Bayreuth and Hannover University. Bill Collins and Willy Tschudin prepared high quality EM sections. Hans-Ruedi Rüegg and Claude Schneider are thanked for their technical assistance in the rock deformation laboratory at Basel. A.A. de Ronde was supported by the Swiss National Fond grants 2100-057092.99 and 2000-065041.01.

Chapter 5

Reaction mechanisms and kinetics during plastic deformation of anorthite-olivine composites *

5.1 Abstract

Although the concentration of metamorphic reactions in ductile shear zones is often attributed to the presence of fluids during deformation, plastic deformation certainly contributes to the reaction progress. We have studied the effects of plastic deformation on the kinetics of the net-transfer reaction anorthite + olivine → orthopyroxene + clinopyroxene + spinel ± garnet. These metamorphic reactions play important roles during shear localisation in the lower crust and upper mantle during crustal thinning and extension.

Hydrostatic and shear deformation experiments were performed on water-deficient anorthite-olivine (An_{92}-Fo_{93}) composites at 900°C and confining pressures between 1000-1600 MPa in a Griggs apparatus. The hydrostatic and deformed samples were compared in terms of phase petrology, reaction progress and mechanisms.

At hydrostatic conditions, the anorthite + olivine reactions are controlled by the transport of chemical components. The slow growth rates of enstatite and pyroxene-spinel-garnet reaction rims imply slow rates of transport and delayed nucleation of new phases at water-deficient conditions, even at pressure overstepping conditions of ~700-900 MPa.

---

[*] A.A. de Ronde, H. Stünitz, J. Tullis. To be submitted for publication in *Contributions to Mineralogy and Petrology*, Springer-Verlag Heidelberg

Despite the water-deficient conditions, plastic deformation enhances mineral reaction in An-Fo composites. Reaction progress as well as the nucleation and growth rate of reaction rims increase during plastic deformation. The transport-controlled syndeformational reaction is enhanced by an increased nucleation rate of new phases, which may be due to the generation of high dislocation densities in the reactant grains by plastic deformation. During shear deformation, the mechanical transport of phases by grain boundary sliding may change the local equilibrium conditions, resulting in the formation of metastable kyanite. The results of our experiments imply that plastic deformation processes can be solely responsible for the initiation and concentration of metamorphic reactions at water-deficient conditions.

5.2 Introduction

Mineral reactions in deforming rocks play an important role in many tectonic environments because of their influence on the mechanical properties of rocks (White and Knipe, 1978; Rubie, 1983; Brodie and Rutter, 1987). For example, eclogitisation of the subducting oceanic crust leads to slab pull, and the metastability of high-pressure rocks is essential for the survival of thick mountain roots (Jackson et al., 2004). Retrograde reactions in the upper mantle are known to cause strain localisation during the exhumation of upper mantle peridotites (Furusho and Kanagawa, 1999; Newman et al., 1999; Handy and Stünitz, 2002). Thus, our understanding of the reaction kinetics and the external processes that trigger and enhance reaction during deformation are important issues in tectonics.

Metamorphic reactions are often localised in shear zones, while the undeformed host rocks only show limited or no reaction progress (e.g. Kerrich et al., 1980; Rubie, 1983; Brodie and Rutter, 1985; Marquer et al., 1985; Austrheim, 1987; Keller et al., 2004). One reason for enhanced reaction kinetics is the presence of fluids during deformation. Fluid infiltration can easily take place in permeable shear zones, for example along for micro-fractures or through fine-grained recrystallised rocks. Hydrous fluid is an extremely effective catalyst in mineral reactions and mass transport (Rubie, 1986).

Although the triggering of metamorphic transformations is often attributed to the infiltration of fluids during ductile deformation (Austrheim, 1987; John and Schenk, 2003), there is a common understanding that plastic deformation may also significantly contribute to metamorphic reaction processes (e.g. Brodie and Rutter, 1985; Stünitz, 1998). For example, Simpson and Wintsch (1989) postulate that stress and strain energy concentrations are the driving force in a K-feldspar replacement reaction between quartz and plagioclase. They suggest that the redundant extra strain energy on high normal stress sites of the grains favours localised reaction at these sites. This strain energy could arise from elastic strain or be associated with tangled dislocations and twin boundaries. However, the evaluation of effects of strain and dislocations on reaction in natural shear zones is difficult to assess because the addition of water may obscure the contribution of strain energy during metamorphic reactions (Rubie and Thompson, 1985). Therefore, the effects of plastic deformation on mineral reactions need to be studied in water-deficient rocks.

Experimental studies on the effects of ductile deformation on reaction processes have primarily focused on kinetics of polymorphic transformations (e.g. Davis and Adams, 1965; Doukhan and Christie, 1982; Snow and Yund, 1987; Burnley and Green, 1989; Kirby and Stern, 1993; Green and Houston, 1995). However, many phase transitions in dry upper mantle and lower crust involve net transfer reactions with multiple reactants. Nucleation of new phases, material transport and growth of reaction products occur during deformation. The mutual effects that reaction and deformation have on each other are still poorly understood in natural rocks.

The effect of a dry solid-solid mineral reaction on plastic deformation of plagioclase-olivine composites has been studied in shear deformation experiments by de Ronde et al. (2004, Chapter 4). In these experiments, prograde syndeformational reactions between anorthite (An_{92}) and olivine (Fo_{93}) at 900°C and 1000-1500 MPa confining pressures cause a strain weakening of the An-Fo composites. It is observed that the onset of observed weakening corresponds to the onset of mineral reaction, and that decreasing shear stress results from the grain size reduction produced by crystallisation of fine-grained (size <0.5 μm) polyphase reaction products.

In the sheared An-Fo composites, the greatest reaction progress correlates with the sites of largest strain (de Ronde et al., 2004), and complete reaction progress occurs within a relatively short laboratory time scale. These experiments indicate that plastic deformation enhances the mineral reaction between anorthite and plagioclase, even under dry conditions. In order to further investigate the potential effect of plastic deformation on the kinetics and mechanisms of a net transfer reaction, we have made a comparison of the experimentally deformed anorthite-olivine composites (Chapter 4) with hydrostatically treated anorthite-olivine composites (i.e. ‘hydrostatic’ samples) at the same P,T-conditions. The two types of experimental samples are compared in terms of phase petrology, reaction progress and reaction mechanisms.

5.3 An-Fo reaction in the NCFMAS-system

Mineral assemblages consisting of anorthite and olivine are typical for low pressure high temperature plagioclase peridotites as well as some gabbros. The plagioclase-olivine phase relationships in the CaO-MgO-Al_2O_3-SiO_2-system (CMAS) are known from experiments (Green and Hibberson, 1970; Kushiro and Yoder, 1966; Jenkins and Newton, 1979; O'Neill, 1981; Gasparik, 1984; Herzberg and Gasparik, 1991; Klemme and O'Neill, 2000). In this study we have to take into account the fayalite and albite components of olivine and plagioclase because natural minerals were used for the study. The equilibrium phase diagram for our An-Fo composites (An_{92}+Fo_{93}, Table 5.1) in the system Na_2O-CaO-FeO-MgO-Al_2O_3-SiO_2 (NCFMAS) is calculated using the DOMINO-THERIAK software (de Capitani and Brown, 1987; de Capitani, 1994). These programs use the Berman (1988) database, the plagioclase solution model of Fuhrman and Lindsley (1988), the omphacite solution model of Meyre et al. (1997) and the orthopyroxene model of Hunziker (2003).

The calculated equilibrium phase diagram of the An-Fo composites is given in Figure 5.1. The applied confining pressures in the experiments (P_c ~1000-1600 MPa) represent different amounts of pressure overstepping of the An-Fo stability field in the NCFMAS-system. At fixed temperature, increasing the pressure corresponds to an expected increased Gibbs free energy of the metastable An-Fo composite and hence an expected increase of the reaction rate. The experiments were performed in the spinel

	Blumone Anorthite		Åheim Forsterite	
	wt.% oxides	Ions per 8 O	wt.% oxides	Ions per 4 O
SiO_2	45.26	2.090	41.18	1.001
Al_2O_3	34.78	1.893	0.00	0.000
MnO	0.00	0.001	0.05	0.000
FeO	0.56	0.021	7.31	0.149
MgO	0.09	0.006	50.97	1.847
CaO	18.42	0.912	0.07	0.002
Na_2O	0.90	0.080	0.01	0.000
K_2O	0.02	0.001	0.00	0.000
Total	99.94	5.004	99.59	2.999
Normalised mol% of mineral end-members				
		An92		Fo93
		Ab8		Fa7
		Or0		

Table 5.1: Electron microprobe analyses of Blumone gabbro anorthite and Åheim dunite olivine. Analyses represent an average of 10 measurements.

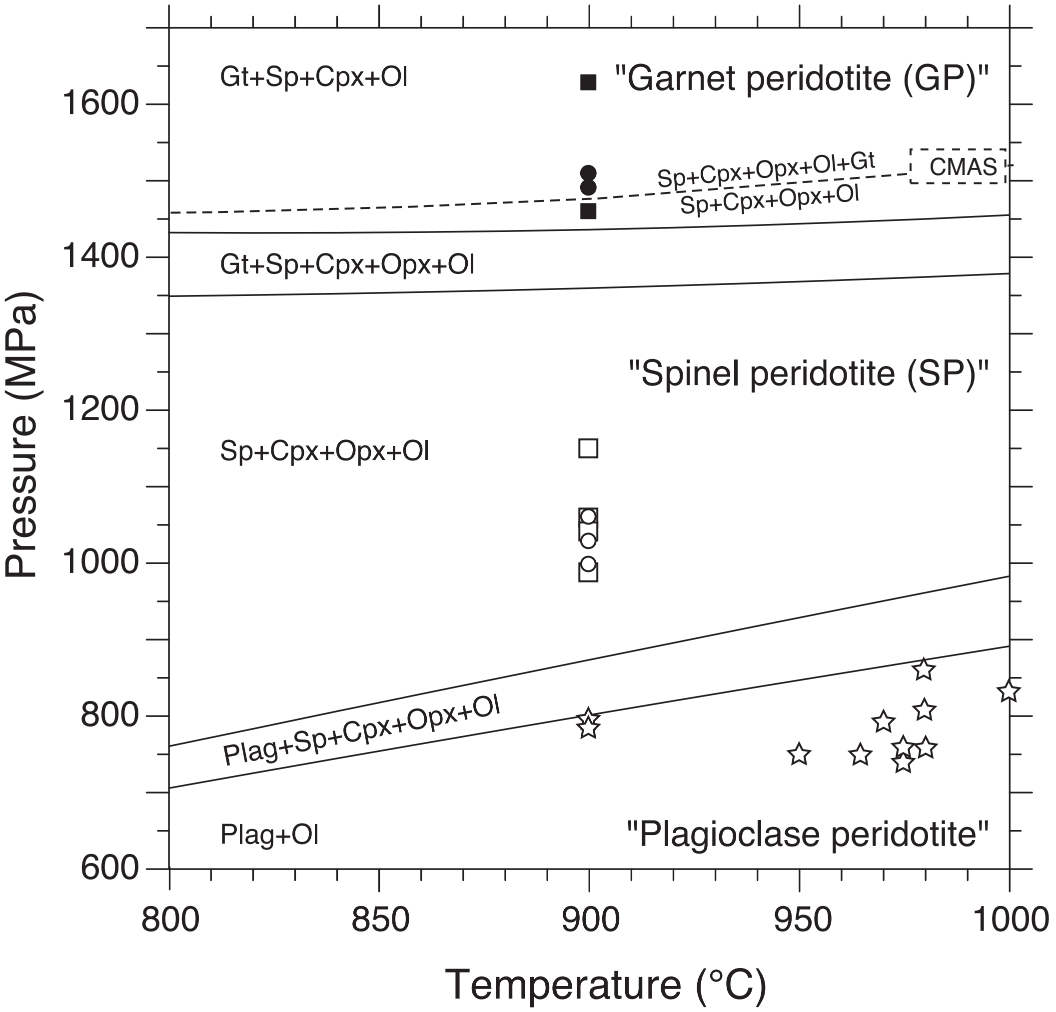

Figure 5.1: Phase diagram for plagioclase, spinel and garnet bearing peridotites in the NCFMAS-system. The diagrams are calculated for a 0.48 An_{92} + 1.16 Fo_{93} bulk composition (49-51 vol.% An-Fo composite) using the program DOMINO (de Capitani and Brown, 1987; de Capitani, 1994) and the Berman (1988) database. Solid solution models used: Fuhrman and Lindsley (1988) (plagioclase), Meyre et al. (1997) (clinopyroxene) and Hunziker (2003) (orthopyroxene). Stars: hot pressing conditions inside the An-Fo stability field. Circles: hydrostatic experiments. Squares: shear deformation experiments. Open symbols: experiments in the spinel peridotite (SP) field. Solid symbols: experiments in the garnet peridotite (GP) field. Dashed line: compilation of experimental data of the SP-GP transition in the CMAS (Green and Hibberson, 1970; Kushiro and Yoder, 1966; Jenkins and Newton, 1979; O'Neill, 1981; Gasparik, 1984; Herzberg and Gasparik, 1991; Klemme and O'Neill, 2000).

peridotite (SP) and garnet-spinel (GP) peridotite fields. In these fields, anorthite (an) and olivine (ol) react to spinel (sp), clinopyroxene (omphacite; cpx), orthopyroxene (opx) and garnet (gt) bearing mineral assemblages. The theoretical mineral reactions marking the change in the equilibrium assemblages as depicted in (Fig. 5.1) are given by

$$1.2\,\mathrm{ol} + 0.49\,\mathrm{an} \rightarrow 0.49\,\mathrm{opx} + 0.49\,\mathrm{cpx} + 0.28\,\mathrm{ol} + 0.39\,\mathrm{sp} \tag{5.1}$$

for the spinel peridotite field (P_c ~1000 MPa) and

$$1.2\,\mathrm{ol} + 0.49\,\mathrm{an} \rightarrow 0.32\,\mathrm{gt} + 0.34\,\mathrm{cpx} + 0.55\,\mathrm{ol} + 0.13\,\mathrm{sp} \tag{5.2}$$

for the garnet-spinel peridotite field (P_c ~1500 MPa) respectively. As shown by de Ronde et al. (2004), these reactions typically form a rim of enstatite (en) around olivine porphyroclasts as well as a fine-grained reaction rim of polyphase reaction products (primarily cpx, opx, sp, ±gt) in these experiments. We will refer to the first as the 'enstatite rim' and the latter as the 'SP'-rim or 'GP'-rim, referring to the peridotite field in which reaction occurs.

Reactions 5.1 and 5.2 indicate that olivine is part of the reaction products mineral assemblage. Hence, full reaction progress is characterised by the complete disappearance of anorthite from the rock whereas some olivine remains. Therefore, reaction progress is defined by the amount of anorthite transformation, ξ_{An},

$$\xi_{An} = 1 - \frac{V_{An_{residual}}}{V_{An_{initial}}} = 1 - \frac{V_{An_{residual}}}{49}$$

which describes the volume fraction of transformed anorthite with respect to the initial An-Fo composite (see following sections).

5.4 Experimental procedures

The experimental procedure for preparing the An-Fo (An_{92}-Fo_{93}) composites is given in Chapter 4 and the reader is referred to that work for a more detailed description. The experiments have been performed in a Griggs piston cylinder apparatus using an all NaCl-confining medium sample assembly (Fig. 5.2a). In this kind of assembly, the An-Fo composite sample is orientated in a shear geometry between two dunite forcing blocks. The temperature of the experiment is measured directly at the centre of the sample (Fig. 5.2b). Considering the central part of the sample, only a small temperature gradient is assumed across the sample.

The dunite forcing block pistons are 6.3 mm diameter cores of Balsam Gap dunite and Åheim dunite, which are cut and ground at 45° to their cylinder axis. The dunite forcing blocks were thoroughly dried for 12 to 24 hours at 980-1000°C in a CO-CO_2

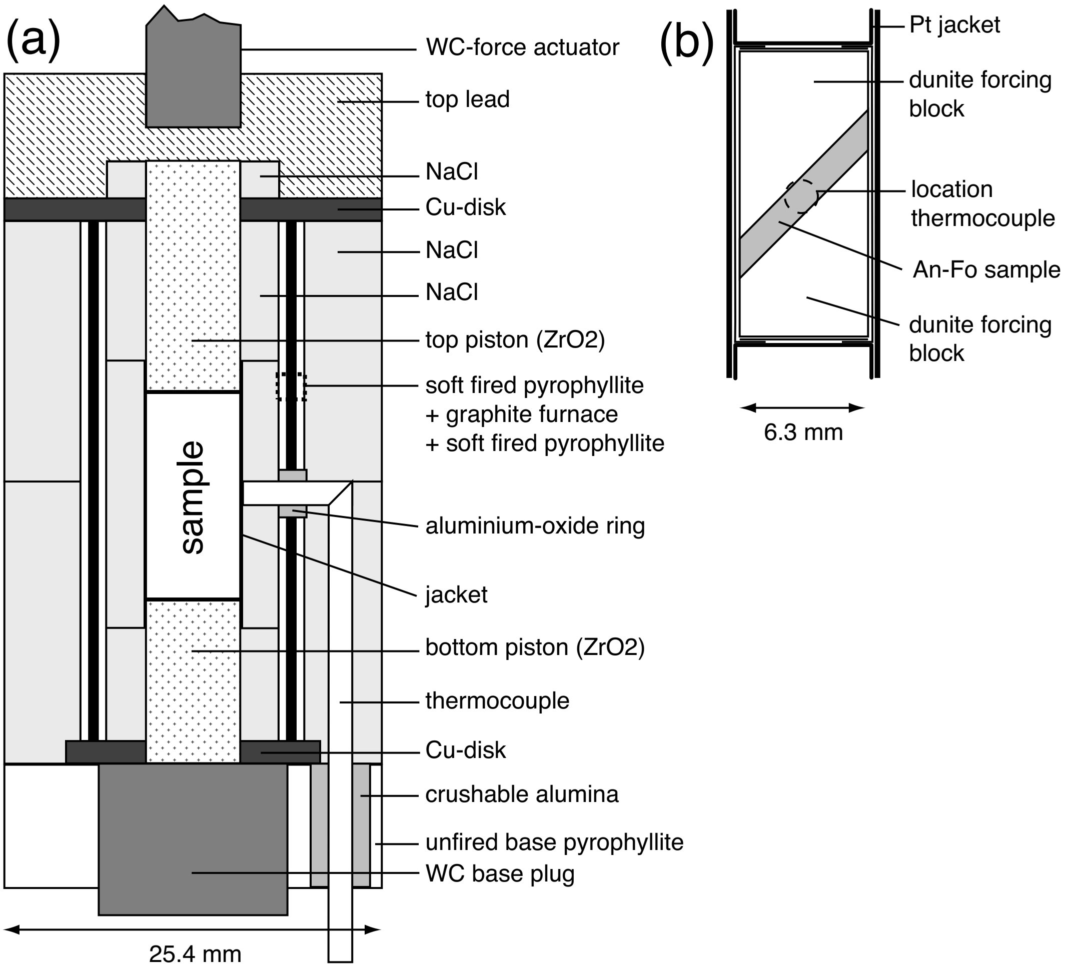

Figure 5.2: Schematic diagram of the sample assembly used in the experiments. (a) Sample assembly with a solid NaCl-confining medium. (b) An-Fo sample between two dunite forcing blocks, which are cut at 45° to their vertical axis. The sample + forcing block jacket consists of mechanically-sealed inner Ni-foil and outer weld-sealed Pt tubing.

gas mixture (Table 5.2). The drying resulted in weight losses up to 0.75% due to the dehydration of small amounts of hydrous minerals like serpentine. Anorthite-olivine (An-Fo) mixtures were prepared from powders with a 4 to 10 µm grain size of Åheim dunite olivine (Fo_{93}) and Blumone gabbro anorthite (An_{92}). The powders were stored in an oven at 110°C for at least 72 hours ('oven-dried'). The oven-dried powders have some absorbed water on the mineral grain boundaries, which was required for sufficient grain growth in the plagioclase-olivine composite during the hot pressing stage of the experiment at the relatively low temperatures of 970°C.

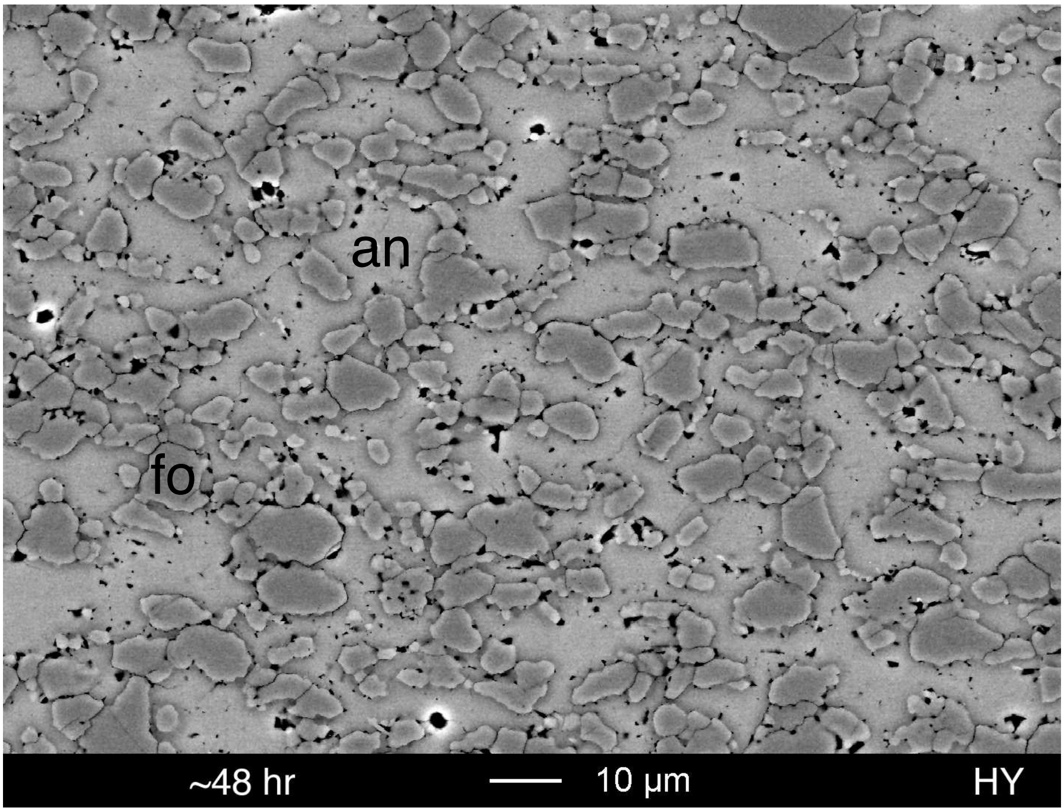

Figure 5.3: Backscattered scanning electron microscope (BSEM) image of An-Fo composite 44AA after 48 hr annealing at 965°C and 750 MPa. Phases: anorthite (an= An_{92}, light grey, low relief), olivine (fo = Fo_{93}, dark grey, high relief). Average An-Fo vol.% ratio = 49-51 (±2)%. The initial mean grain size of olivine and presumably plagioclase is 6.9±2.6 µm. Sample porosity and holes ~2% (black). White rims are due to charging of the sample.

5.4.1 An-Fo composite starting material

Dense An-Fo composites were obtained by isostatic hot pressing of the anorthite-olivine powder mixtures for 24-48 hours at high temperatures of 900-1050°C and pressures P_c=740-860 MPa (Fig. 5.1 and 5.3). These conditions were chosen to keep the assemblage in its stability field during the hot pressing. After hot pressing, anorthite and olivine have a mean initial grain size of 7±2.6 µm and are mixed in a 49-51(±2) volume percent ratio (0.8-2.0 An-Fo molar ratio). No new phases were observed after 48 hours of annealing. No microscopic reaction products were added to the starting material (i.e. 'unseeded' samples).

In order to determine the H_2O-content of the hot pressed samples, we have measured the infrared absorption of hydrogen in the olivine of the dunite forcing blocks. At 900°C and P_c=300 MPa, diffusion rates of hydrogen in olivine can range from $10(\pm5)*10^{-11}$ to $10(\pm5)*10^{-12}$ m^2s^{-1} depending on crystal orientation (Mackwell and Kohlstedt, 1990).

Using these data, hydrogen is calculated to diffuse 500-3000 μm into the olivine grains at the duration and temperature of the experiments (>24 hr, 900°C). Therefore, the large (size >100 μm) olivine grains in the forcing blocks can be used as an internal standard to determine the hydroxyl content of the complete sample (plagioclase-olivine composite and dunite forcing blocks), especially the fine-grained regions, where the grain size is too small to be probed by FTIR.

Analyses of unpolarised hydroxyl adsorption in olivine were made using a Brukner high resolution FTIR spectrometer at the Bayerisches Geoinstitut and at the University of Hannover, Germany. Doubly polished sections were used with a 100-150 μm thickness. Measurements were made at room temperature for a 3000-4000 cm^{-1} wave number range. Hydroxyl species were not measured above the detection limit of approximately 490 $H/10^6Si$ in all samples with dunite pistons. This amount of hydroxyl corresponds to an H_2O-content of $\leqslant$30 ppm (0.003 wt.%) for the olivine (Fo_{90}) pistons and hence for the plagioclase-olivine composites.

No intra-crystalline or grain boundary H_2O above the 30 ppm detection limit was measured using FTIR. Because all samples were treated identically during preparation, we suspect that the continuous storage of mineral powders at 110°C has not allowed for substantial adsorption of water to the mineral grain boundaries. During subsequent hot pressing of the powders, the thoroughly dried dunite pistons probably acted as large sinks for any absorbed water within the entire sample. The FTIR analyses indicate that the hot pressed An-Fo composites can be considered as dry mineral samples.

5.4.2 Hydrostatic and shear deformation experiments

All experiments were performed at 900°C and confining pressures P_c of 1000-1600 MPa (Fig. 5.1). The An-Fo composites were deformed with constant shear strain rates ($\dot{\gamma}$) to variable amounts of strain (γ) or left at hydrostatic pressure for a certain amount of time. Table 5.2 lists the experiments used in this study. The pressure inside the sample assembly is maintained by a top lead piece sealing off the assembly. No initial contact exists between the deformation actuator and the top zirconia piston above the jacketed sample (Fig. 5.2a). In order to start the sample deformation, the force piston first has to travel through the lead until it reaches the ‘touch-point’ with the top piston and sample. Therefore, the total duration of deformation experiments consists of two parts: (1) a hydrostatic part in which the force piston advances towards the sample touch-point and (2) the part of actual sample deformation. Because both parts occur at a pressure outside the An-Fo stability field, the total time of hydrostatic experiments

Table 5.2: Summary of anorthite-forsterite experiments[a].

Run	Drying			hot pressing			Hydrostatic[c]		Shear deformation[d]				Vol. phases (%)[e]				
No.	T (°C)	t (hr)		t (hr)	T (°C)	P_c (MPa)	P_c (MPa)	t_{hy} (hr)	$\dot{\gamma} \cdot 10^{-5}$ (s^{-1})	γ	t_{de} (hr)	t_{total} (hr)	An	Fo	En	SP GP	ξ
44AA	980	24	FB	48	965	750							49	51			0.00
W1046	1000	12	all	24	1050	760	1000	19				19.0	51	49			0.00
36AA	980	24	FB	48	970	790	1030	168				168.0	43	47	←	10	0.12
47AA	980	24	FB	48	975	740	1060	73.3				73.3	45	55			0.00
W1045[f]	1000	6	all	24	900	790	1490	30				30.0	46	54			<0.01
49AA	980	24	FB	48	975	760	1510	59				59.0	36	49	←	15	0.27
34AA	980	24	FB	48	950	750	1510	167.5				167.5	13	31	21	35	0.73
W1028[g]	1000	13	all	24	1050	780	990	12.5	4.9	4.1	23.3	35.8	45	48	←	7	0.08
33AA[h]	980	24	FB	48	980	810	1030	22.2	4.3	5.8	37.7	163.9	11	19	22	48	0.78
19AA	1000	24	FB	24	1000	830	1160	37	4.7	5.9	35.0	72.0	17	21	19	43	0.65
32AA	980	24	FB	48	980	760	1460	22.8	3.8	2.2	15.9	38.7	33	48	←	19	0.33
28AA	1000	24	FB	48	980	860	1630	26.8	4.0	4.9	34.0	60.8	2	21	25	54	0.96
55AA	980	24	FB	48	965	750	1040	49.5	0.4	1.7	115.4	164.9	27	28	19	26	0.45

[a] All experiments were performed at 900°C

[b] Drying in CO-CO_2-gas at atmospheric pressure: all = dried powder + forcing blocks,
FB= dried forcing blocks + oven-dried powders (110°C, >72 hrs)

[c] t_{hy}: duration at hydrostatic confining pressure

[d] t_{de}: duration of 'sample deformation'; $t_{total} = t_{de} + t_{hy}$

[e] Estimated volume percentages of phases and reaction rims. Arrows (←) indicate that the enstatite rim was not observed, but might be part of the measured olivine volume.

[f] Sample with 3.4±1.2 μm starting grain size (de Ronde et al., 2004)

[g] The shear strain value is smaller than calculated due to forcing block deformation

[h] This sample was kept hydrostatically at P_c=1040 MPa for 104 hrs after deformation

was chosen to be equal to the total time of the deformation experiments. This allowed a direct comparison of the potential reaction period in hydrostatic and deformed samples. Unfortunately, some deviations exist between sets of hydrostatic and deformed samples, due to difficulties in reproducing identical confining pressures. The comparison of the deformation and hydrostatic experiments in terms of time, shear strain, forcing block offset and microstructures is illustrated in Figure 5.4a. The mechanical data of the general shear experiments as shear stress (τ) versus shear strain (γ) are given in Figure 5.4b.

5.4.3 Sample characterisation

Thin sections were prepared normal to the sample-forcing block interface and parallel to the shear direction. The samples were studied in backscattered imaging mode (BSEM) using an EDS-equipped Phillips XL 30 Field Emission scanning electron microscope. A transmission electron microscope (TEM) equipped with an energy-dispersive system (EDS) was used to identify the mineral assemblages of sub-micron sized reaction products and to obtain information on grain sizes and dislocation microstructures of all phases.

The volume percentages of anorthite, olivine and reaction product phases were estimated from their area percentages in thin section (Underwood, 1970). The area percentages of the phases were obtained by detailed tracing of phase boundaries as well as thresholding of phases in representative high quality mosaics of four BSEM-images of the samples with 1600x magnification. Errors in the estimated volume percentages due to tracing are in the order ±1% and the error in the mean volume percentages is ±2%.

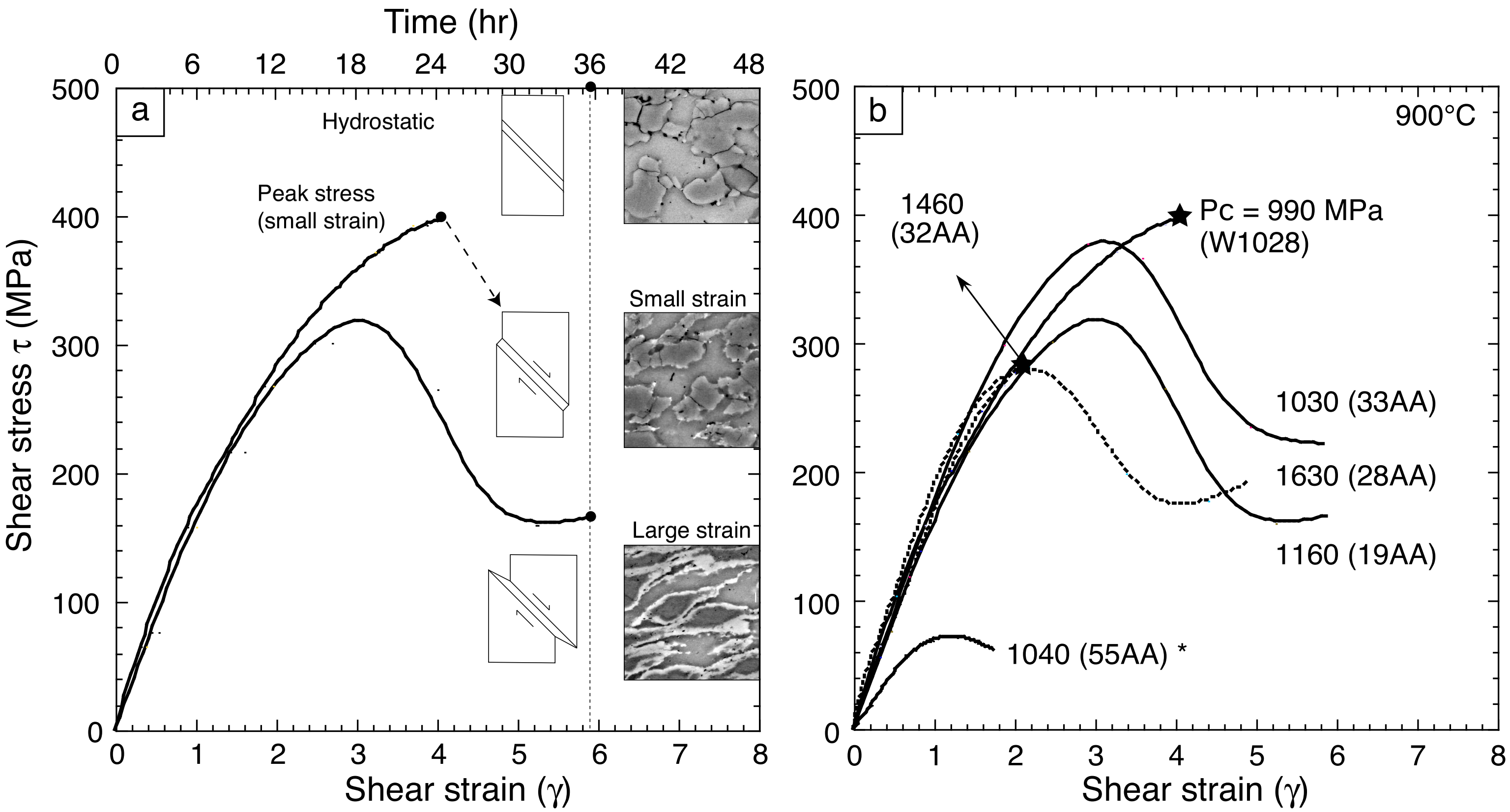

Figure 5.4: Shear stress versus shear strain diagrams for shear deformation experiments on An-Fo composites at 900°C using $\dot{\gamma}$ ~5x10^{-5}s^{-1} (Table 5.2). (a) Typical example of a set of hydrostatic and deformation experiments. After a small strain deformation experiment (top curve + middle inset), the forcing block offset is small. Very few reaction products are observed in the sample (white spots). After large strain (bottom curve + inset), the forcing block offset is large. The An-Fo composite is extensively deformed and has reacted (white rims). The forcing blocks show no offset after a hydrostatic experiment for the same duration as the large strain experiment (top inset). Reaction does not occur at hydrostatic conditions. (b) Mechanical data for experiments in the spinel peridotite (solid lines) and the garnet peridotite (dashed lines) field (Chapter 4). Labels indicate the sample number and the applied confining pressure. Stars indicate experimental runs stopped at approximate peak stress conditions. Deformation of An-Fo composites results in strain weakening (e.g. shear stress decrease) and an onset of constant shear stress at γ ~5.0. The peak shear stress decreased with confining pressure, e.g. with larger pressure overstepping. (*) An-Fo sample 55AA deformed in the SP-field with $\dot{\gamma}$=4x10^{-6}s^{-1}.

5.5 Microstructures

5.5.1 Experiments in the spinel peridotite (SP) field

At hydrostatic conditions and P_c=1060 MPa (~300 MPa pressure overstepping), the An-Fo reaction in the SP-field does not take place in the time span of deformation experiments (t_{total}=73 hr, Fig. 5.5a). The only clear reaction products in the SP-field have been observed in the hydrostatic sample kept at P_c=1030 MPa for 168 hr (Fig. 5.5b). Small patches of fine-grained products occur quite homogeneously throughout the sample (ξ=0.12.). However no continuous SP-rims form, which indicates that the nucleation of new phases in the dry samples is difficult and does not occur at all interphase boundaries. An enstatite rim was not observed below ξ=0.10. The time required for nucleation of new phases under hydrostatic conditions in the SP-field is not well constrained in the data presented here.

Deformation to peak stress conditions at P_c=990 MPa resulted in a reaction progress of ξ=0.08 (t_{total}=36 hr, Fig. 5.5c). The slightly elongated grain shapes of anorthite as well as the weak alignment of minerals in the shear direction indicate some plastic flow. The observed reaction progress is similar to that for the 168 hr hydrostatic sample at P_c=1030 MPa (Fig. 5.5b), which suggests that the rate of reaction is higher during deformation. The nucleation of product phases must be triggered by shear deformation as well, because the reaction does not start under hydrostatic conditions after 36 hours (Fig. 5.5a).

Deformation of An-Fo composites to large strains (γ >3) is characterised by a strain weakening (Fig. 5.4). Plastic deformation of anorthite and olivine to a shear strain of γ=5.9 at P_c=1160 MPa (t_{total}=72 hr) is partially accommodated by dynamic ('syntectonic') recrystallisation of olivine and anorthite and deformation of reaction products (Chapter 4). During dynamic recrystallisation, dislocations in anorthite and olivine grains are arranged into dislocation walls (formation of subgrains). Subgrain rotation as well as migration of grain boundaries (grain boundary bulging) produces new recrystallised grains. As a result, the deformed anorthite and olivine grains are elongated and have fine-grained recrystallised tails (Fig. 5.5d and 5.6a).

Deformation to large strain (γ=5.9) at P_c=1160 MPa results in extensive reaction (ξ=0.65; t_{total}72 hrs; Fig. 5.5d). It is striking that the reaction progress is more than five times higher than that of the hydrostatic sample at P_c=1030 MPa for 168 hr (ξ=0.12). The syndeformational reaction is characterised by a continuous rim (SP-rim, width ~0.8 µm) of fine-grained (size < 1 µm) reaction products around anorthite grains

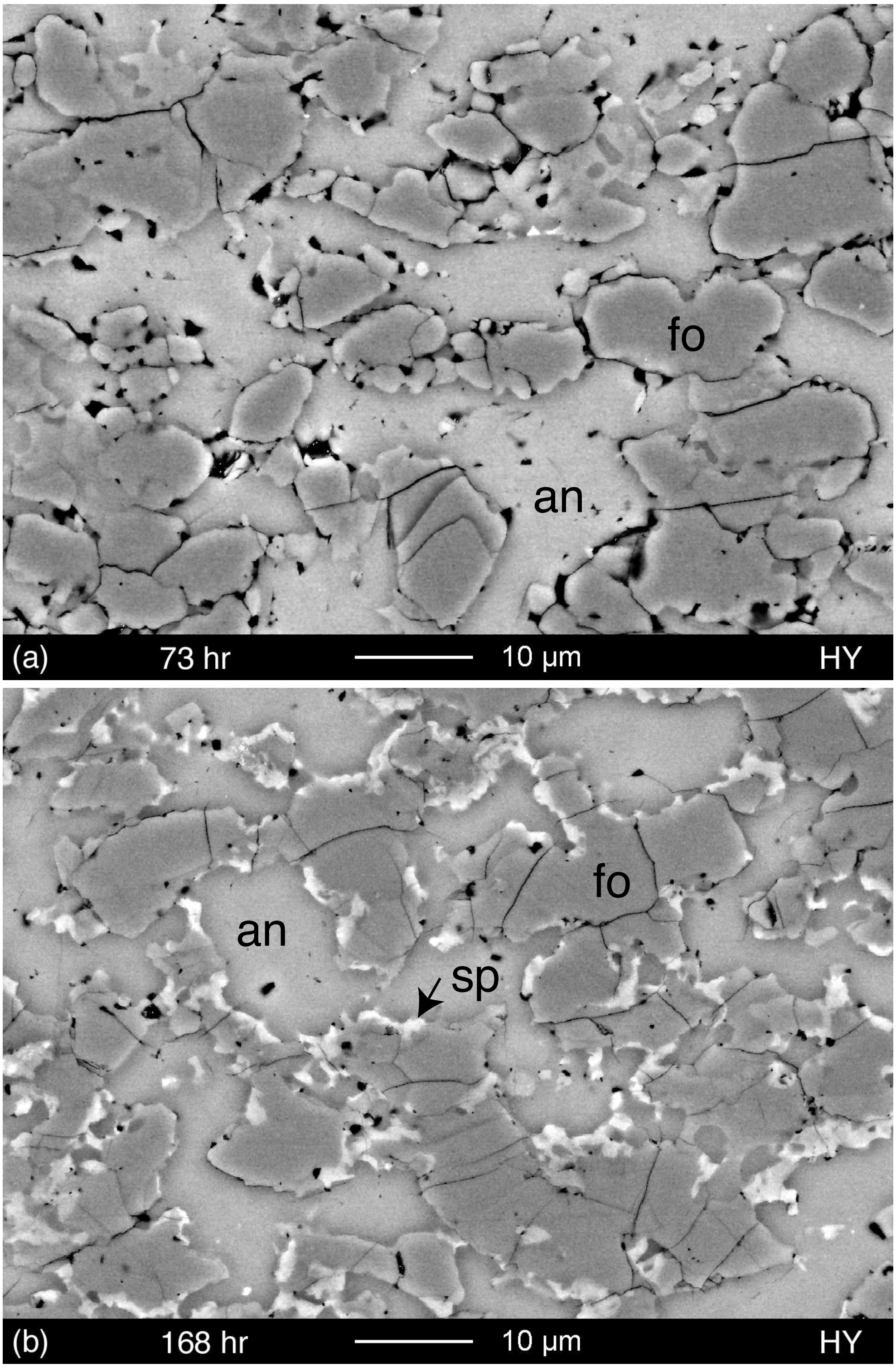

Figure 5.5: Representative microstructures of An-Fo composites in the SP-field (BSEM). Phases: fo (olivine), an (anorthite), sp (opx+cpx+spinel), en (enstatite rim). (a) Hydrostatic sample 47AA at P_c=1060 MPa for 73.3 hour. An-Fo reaction has not occurred (ξ=0.0). (b) Hydrostatic sample 36AA at P_c=1030 MPa for 168 hour. Small patches of products formed at anorthite-olivine interfaces (ξ=0.12).

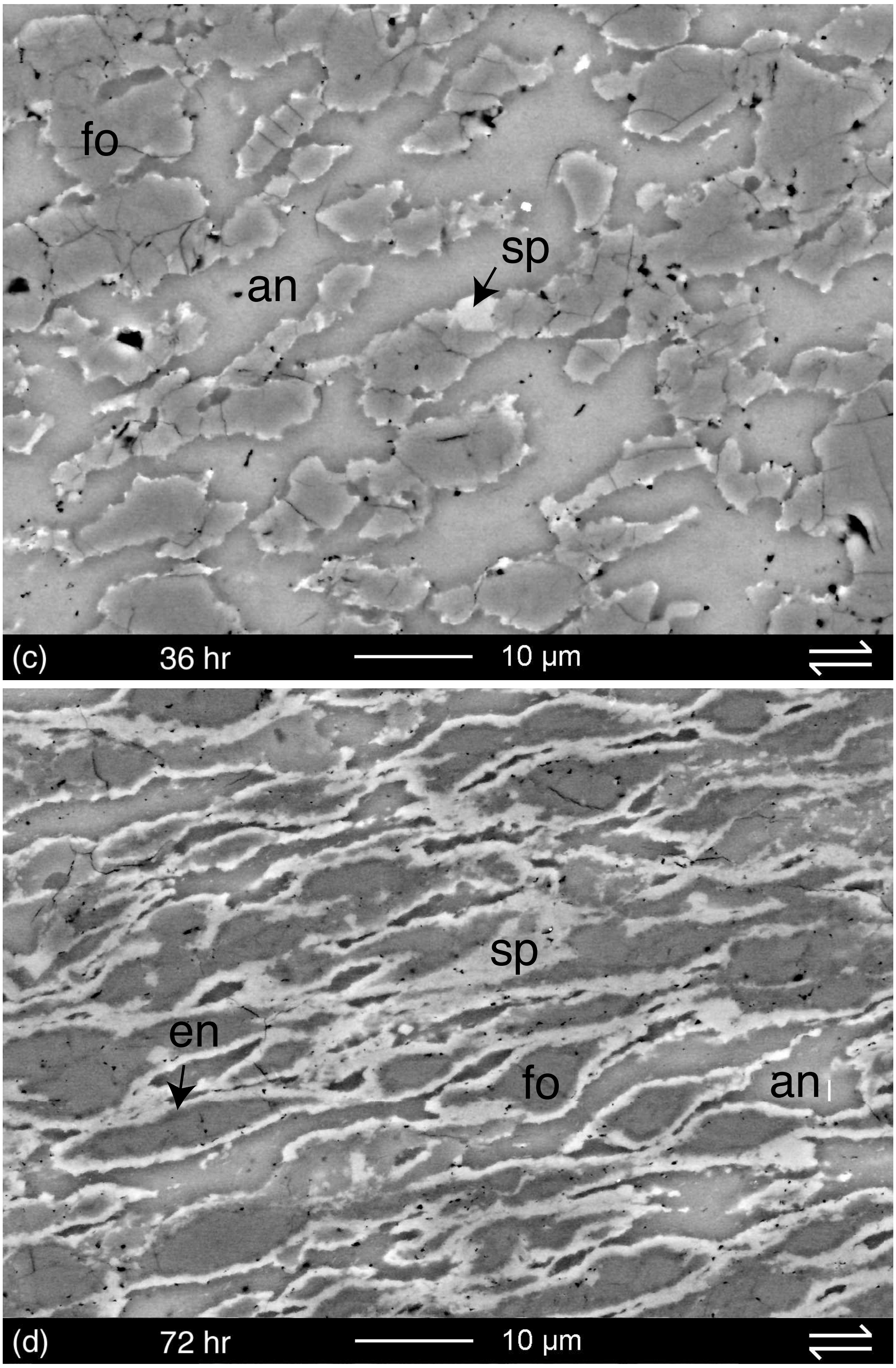

Figure 5.5: (Continued: c) At P_c=990 MPa, syndeformational products formed in sample W1028 after 35.8 hours of deformation to peak stress conditions (ξ=0.08). (d) Sample 19AA deformed to large strain at P_c=1160 MPa (t_{total}=72 hr, γ=5.9) is characterised by strongly deformed anorthite and olivine grains and extensive reaction (ξ=0.65). Fine-grained SP-reaction products have coalesced and form layers across the sample. Olivine grains have an enstatite rim.

as well a thin (width ∼0.6 μm) enstatite rim around olivine grains (Fig. 5.5d). Shear displacement of the reaction products causes them to coalesce, forming interconnecting layers across the sample. As a result, the original geometry of the SP-rims is somewhat obscured in the deformed sample. The reaction products have accommodated most of the shear displacement in the interconnecting layers by non-frictional grain boundary sliding (Chapter 4), which allows small grains to slide past each other (Ashby and Verrall, 1973; Boullier and Gueguen, 1975).

The enstatite rim of olivine grains does not extend into the tails of olivine porphyroclasts (Fig. 5.5d). The smooth interface between the enstatite rim and olivine indicates that the reaction between anorthite and olivine is possibly transport-controlled, because well-developed mineral zones with sharp zone boundaries are characteristic structures for transport controlled reactions (Fisher, 1978).

The syndeformational reaction products that formed in the spinel peridotite field samples have been identified as orthopyroxene (opx), clinopyroxene (cpx) and spinel (Fig. 5.6b). The new phases are fine-grained (size <0.5 μm) and dislocation-free. Small olivine grains, originating from dynamic recrystallisation, as well as opx appear dispersed in the SP-rim. Small ∼0.25 μm grains of metastable anorthite occur in recrystallised anorthite aggregates (Fig. 5.6a). The presence of such metastable anorthite grains adjacent to newly formed reaction products indicates that local equilibrium may be preserved on a very small scale (∼1 μm).

When an An-Fo sample is deformed to large strain (γ=5.8) at P_c=1030 MPa and subsequently subjected to hydrostatic treatment for 104 hours, coarser-grained reaction products (size up to 1 μm) and thicker enstatite rims (width ∼2 μm) develop around olivine (Fig. 5.7a). The coarsening of reaction products in this sample is indicated by their more granular microstructure (Fig. 5.7a) compared to the sample that was only deformed to large strain (γ=5.9; Fig. 5.5d). Probably, some growth occurs of the very small minerals (size <0.25 μm) that formed during the preceding period of deformation (Fig. 5.5d and 5.6b). However, even after the additional 104 hours of hydrostatic treatment, full transformation of anorthite was not achieved (ξ=0.78) and fine-grained remnants (size ∼2 μm) of plastically deformed anorthite are still observed throughout the sample (Fig. 5.7b).

Sample deformation to small strain (γ=1.7) at a lower strain rate of $\dot{\gamma} = 4.0{*}10^{-6}\mathrm{s}^{-1}$ and P_c=1040 MPa (Fig. 5.8) takes place at a much lower shear stress (τ=60 MPa). Comparison of this sample to the sample deformed to large strain (γ=5.9) at high shear stress (τ >150 MPa) and $\dot{\gamma}$=5.0*$10^{-5}\mathrm{s}^{-1}$ (ξ=0.65, Fig. 5.5d), indicates that

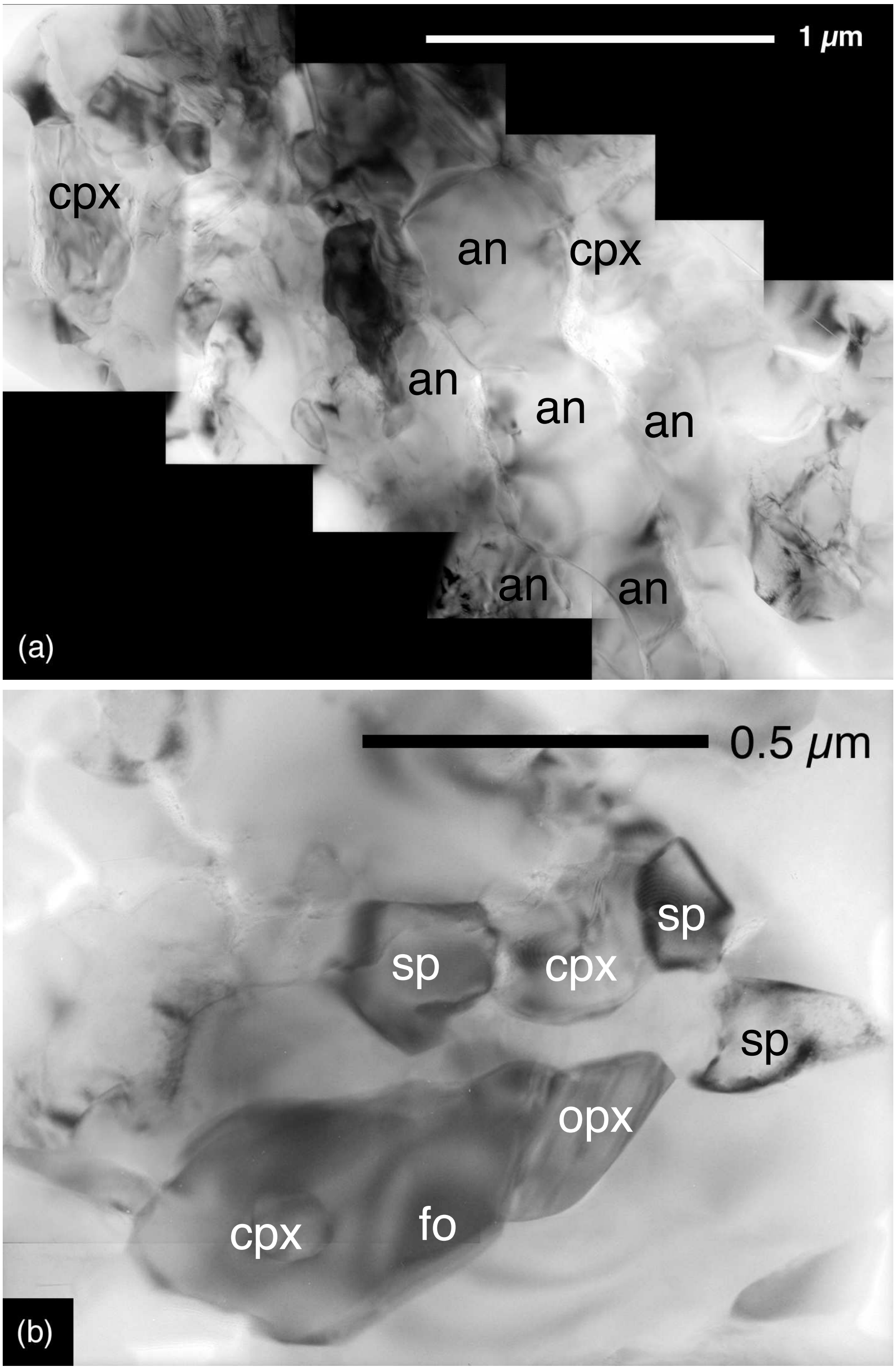

Figure 5.6: Representative microstructures of deformed An-Fo composites in the SP-field (bright-field TEM). (a) Small dislocation-free anorthite (an) grains (size ∼0.25 µm) make up the tails of the elongated anorthite grains in Fig. 5.5d. These small metastable anorthite grains occur directly adjacent to newly formed cpx. (b) Detail of fine-grained (size ∼0.25 µm) syndeformational reaction products at $P_c \sim 1000$ MPa (Fig. 5.5d). The mineral assemblage consists of clinopyroxene (cpx), orthopyroxene (opx) and spinel (sp). The products are dominantly dislocation-free.

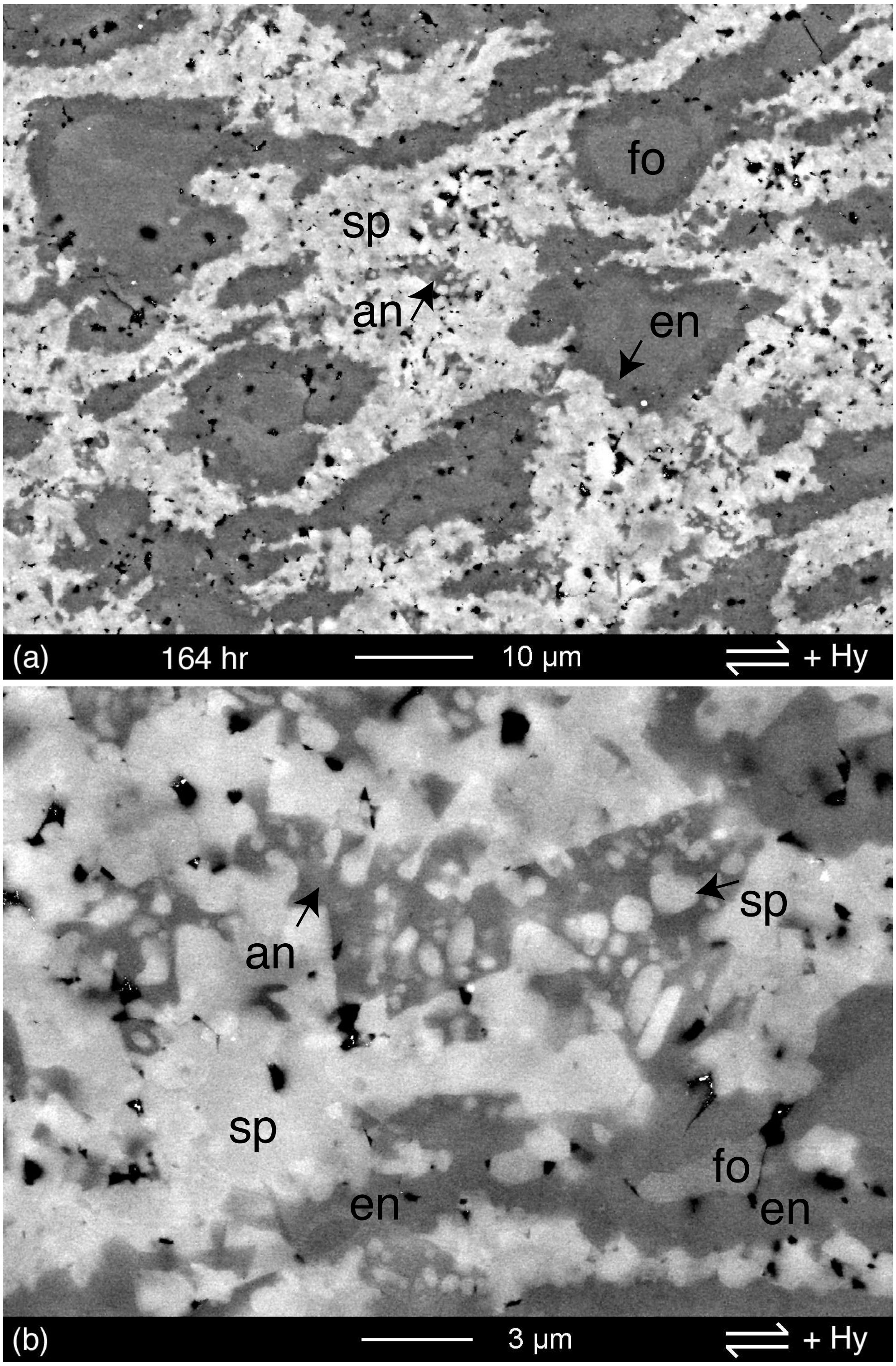

Figure 5.7: Representative microstructures of An-Fo composite 33AA after a combined deformation and hydrostatic experiment at P_c=1030 MPa (BSEM). Large strain (γ=5.8) was followed by an additional 104 hour at hydrostatic pressure (t_{total}=163.9 hr; ξ=0.78). Phases: fo (olivine), an (anorthite), sp (opx+cpx+spinel), en (enstatite rim). (a) Thick ~1-2 µm enstatite rims formed. The SP-reaction product matrix has a granular texture. SP-rim structures are obliterated. (b) Detail of the bright SP-reaction product matrix. New phases appear coarser-grained (sizes up to ~1.5 µm) and grew into the plastically deformed anorthite grains (Fig. 5.5d).

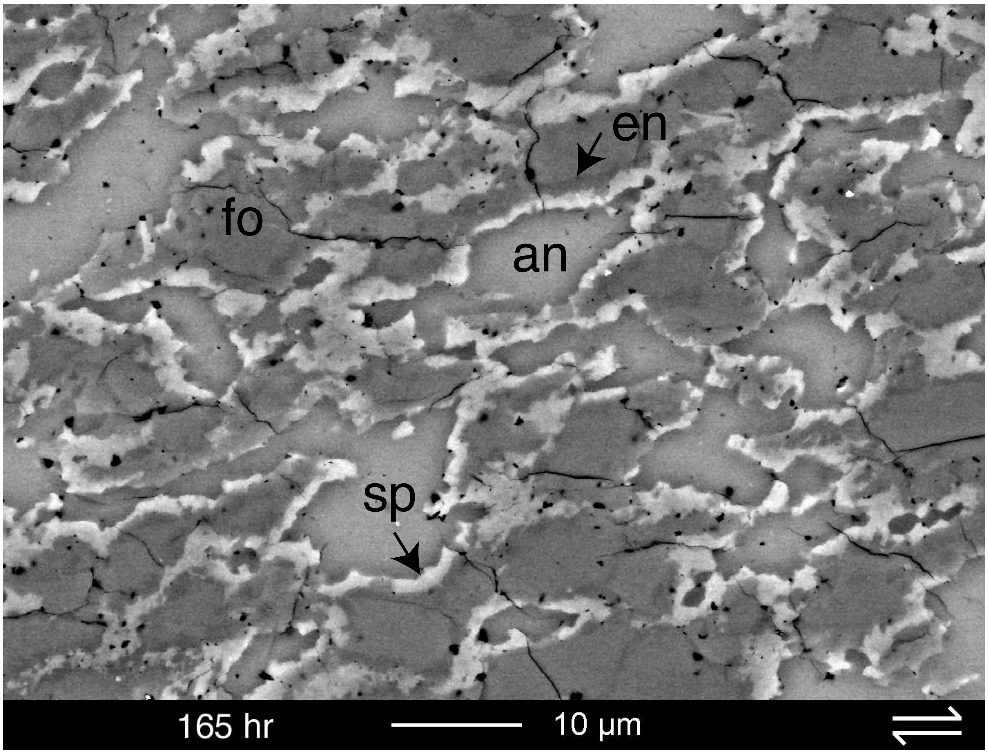

Figure 5.8: Representative microstructures (BSEM) of An-Fo composite 55AA deformed at a shear strain rate of $\dot{\gamma}$=4x10^{-6}s^{-1} and P$_c$=1040 MPa (t$_{total}$=165 hr, γ=1.7; ξ=0.45). Phases: fo (olivine), an (anorthite), sp (opx+cpx+spinel), en (enstatite rim). A shape preferred orientation toward the shear direction developed after a small strain. Olivine grains have clear enstatite rims. SP-reaction products form a continuous rim around anorthite grains.

the lower stress conditions caused a smaller reaction progress (ξ=0.45). However, the reaction progress is still considerably larger after slow strain rate deformation than at hydrostatic conditions (ξ=0.12; Fig. 5.5b). Hence it appears that even small amounts of shear strain, in this case γ=1.7, enhance the reaction progress.

The experiments in the spinel peridotite field suggest that the extent of reaction is dependent on the amount of shear strain and the shear strain rate. The reaction progress decreases with shear strain for a fixed strain rate (Fig. 5.5d, 5.5c and 5.5a). The reaction progress decreases with decreasing shear strain rate, i.e. during deformation at lower shear stress conditions, for a fixed shear strain (Fig. 5.5d, 5.8 and 5.5b).

5.5.2 Experiments in the garnet-spinel peridotite (GP) field

At hydrostatic conditions, reaction in the GP-field starts after shorter duration than that in the SP-field, probably due to the greater pressure overstepping (700-900 MPa). A continuous GP-rim forms (width ~0.8 µm) at the An-Fo interphase boundaries after 59 hours at P_c=1510 MPa (ξ=0.27, Fig. 5.9a). Reaction progressed to ξ=0.73 after 168 hrs (Fig. 5.9b) and can be almost complete at rare sample locations (ξ >0.90, Fig. 5.9c). As in the SP-field, enstatite rims are pronounced at this high amount of reaction.

In the An-Fo sample deformed to small strain (γ=2.2) and peak shear stress conditions at P_c=1460 MPa (Fig. 5.9d), reaction has progressed further (ξ=0.33) compared to the P_c=990 MPa sample in the SP-field (ξ=0.08, Fig. 5.5c). Thin continuous GP-rims of reaction products (width ~1 µm) form along all An-Fo interphase boundaries. The original anorthite and olivine grains are only slightly deformed and have a weak shape preferred orientation.

After large strain at P_c=1630 MPa (γ=4.9), approximately 90% of the sample consists of relict olivine grains embedded in a fine-grained reaction product matrix (Fig. 5.9e). This near complete reaction during shear deformation is achieved after only

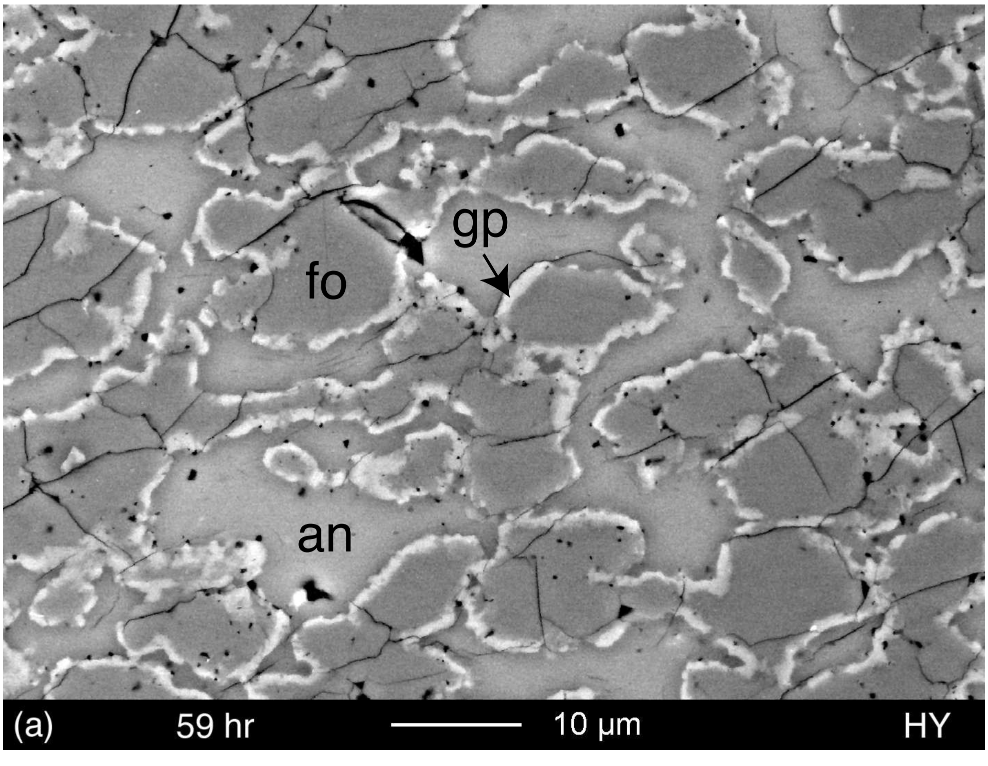

Figure 5.9: Representative microstructures of An-Fo composites in the GP-field (BSEM). Phases: fo (olivine), an (anorthite), gp (opx + cpx + spinel + garnet ±kyanite), en (enstatite rim). (a) Hydrostatic sample 49AA at P_c=1510 MPa for 59 hours (ξ=0.27).

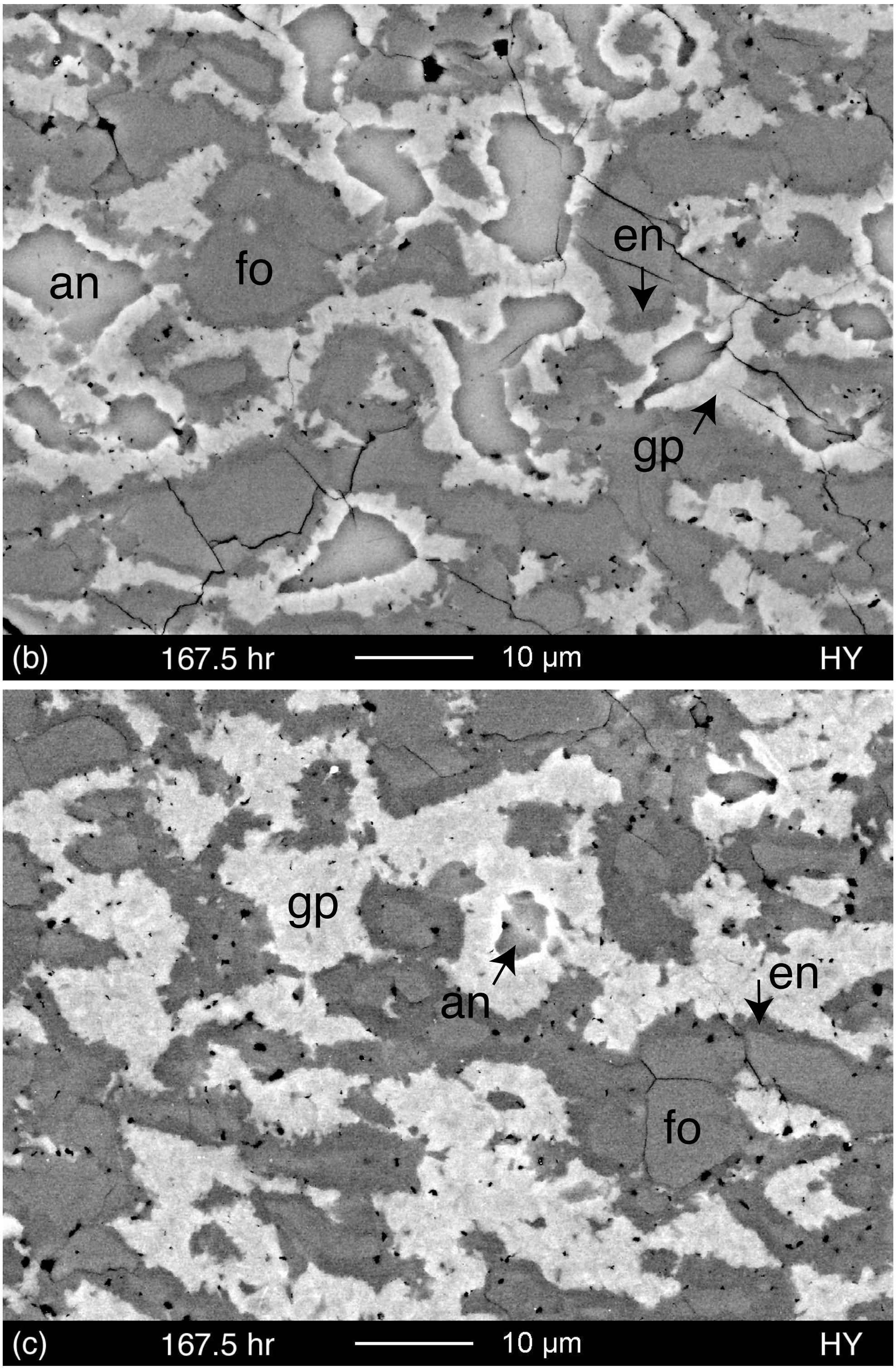

Figure 5.9: (Continued: b) Hydrostatic sample 34AA at P_c=1510 MPa for 167.5 hours (ξ=0.73). Enstatite and GP-reaction products form pronounced rims and indicate a transport-controlled reaction. (c) Different location in sample 34AA, where reaction is almost complete (ξ >0.90).

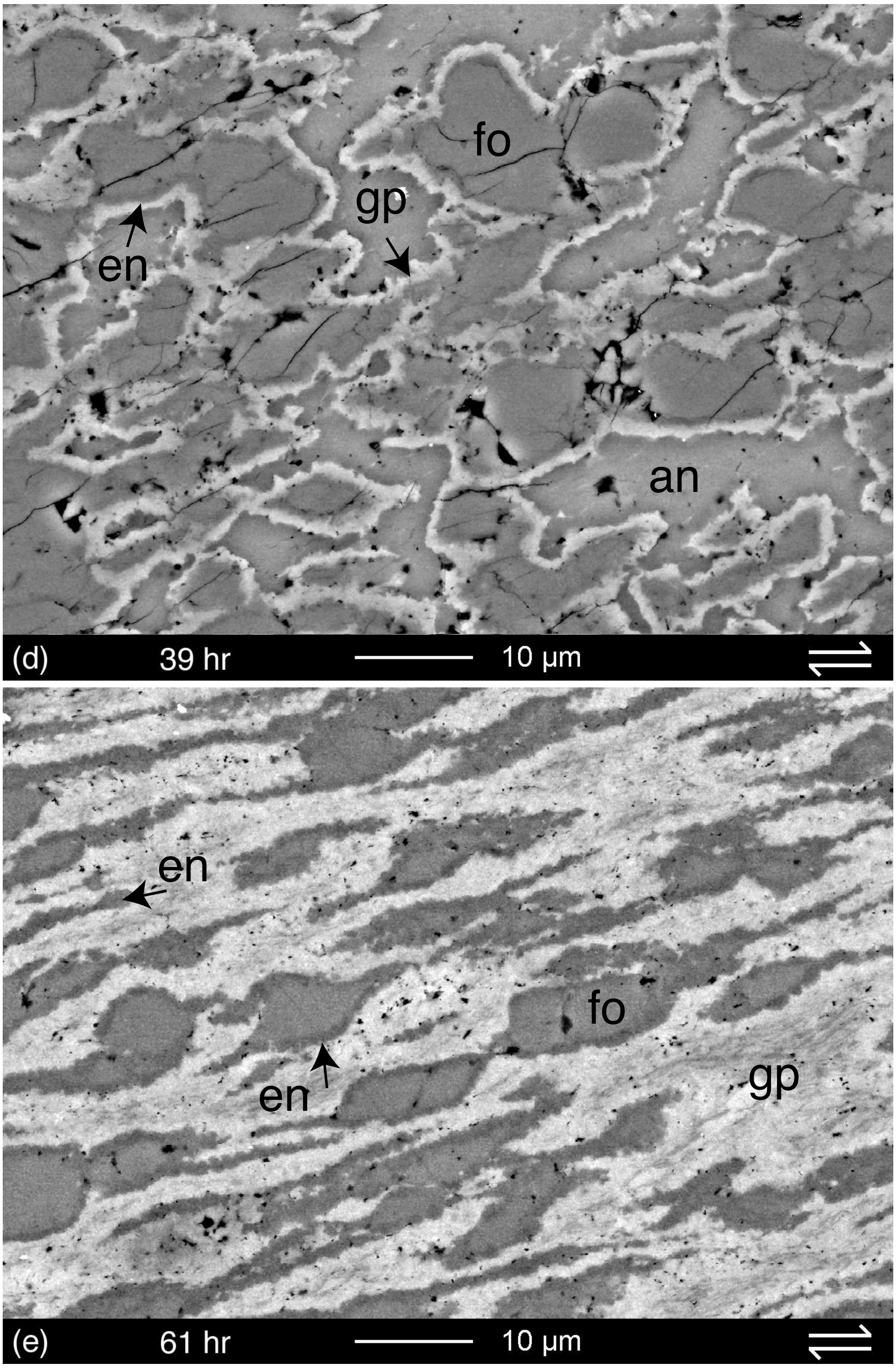

Figure 5.9: (Continued: d) Sample 32AA deformed to peak stress conditions at P_c=1460 MPa (t_{total}=38.7 hr, γ=2.2, ξ=0.33). A shape preferred orientation toward the shear direction developed. Olivine grains have a thin (width ∼1.0 µm) enstatite rim. GP-reaction products form a continuous rim around anorthite. (e) Sample 28AA deformed to large strain at P_c=1630 MPa (t_{total}=60.8 hr, γ=4.9). The An-Fo reaction is near complete in the centre of the sample shear zone (image displays ξ=1.00). Relict olivine grains are embedded in a bright matrix of GP-reaction products. GP-rim structures are obliterated. Olivine grains have rims and tails of fine-grained enstatite.

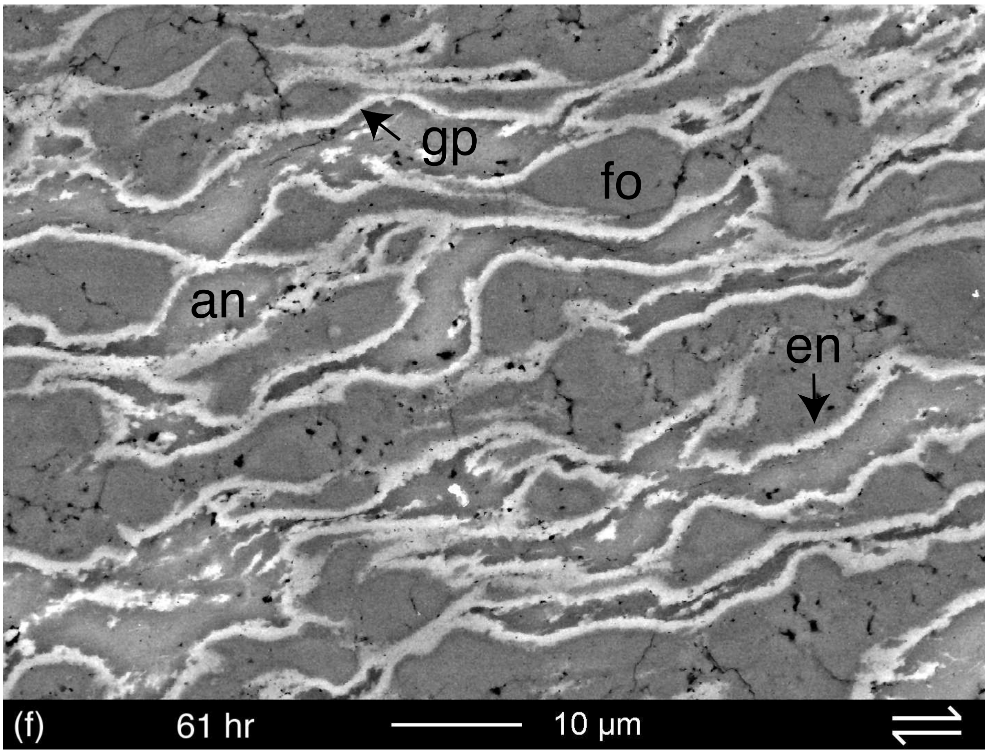

Figure 5.9: (Continued: f) Details of the shear zone ends of sample 28AA (P_c=1630 MPa; t_{total}=60.8 hr). The An-Fo composite is considerably less deformed than the centre (e). Here anorthite grains endured but are strongly deformed and a have clear continuous GP-rim ($\xi \sim$0.60).

61 hours (ξ=0.96), whereas only thin continuous rims developed at hydrostatic pressure after 167.9 hours (Fig. 5.9a). Residual anorthite mainly persists near the much less deformed ends of the sample (Fig. 5.9f). Fine-grained enstatite rims form tails on relict olivine porphyroclasts inside the other fine-grained reaction products (Fig. 5.9e).

Distinctive reaction product microstructures form at high reaction progress in both the deformed and hydrostatic samples in the GP-field. Hydrostatic growth of products at P_c=1510 MPa results in relatively coarse-grained phases in the GP-rim. The reaction product grains often appear as both blocky and fibrous (Fig. 5.10a). The interface between the enstatite rim and olivine is relatively smooth, which suggests, like in the SP-field experiments, that the reaction of olivine and anorthite in the garnet peridotite field is transport-controlled (Fisher, 1978; Joesten, 1986).

The enstatite rims in the large strain sample at P_c=1630 MPa have more irregular and lobate shapes (Fig. 5.10b), suggesting that enstatite is removed from the growing enstatite rim during shear deformation by grain boundary sliding. The reaction product matrix between the relict olivine clasts is finer-grained than that in the P_c=1510 MPa hydrostatic sample (compare Fig. 5.10a and 5.10b), suggesting that new phases have

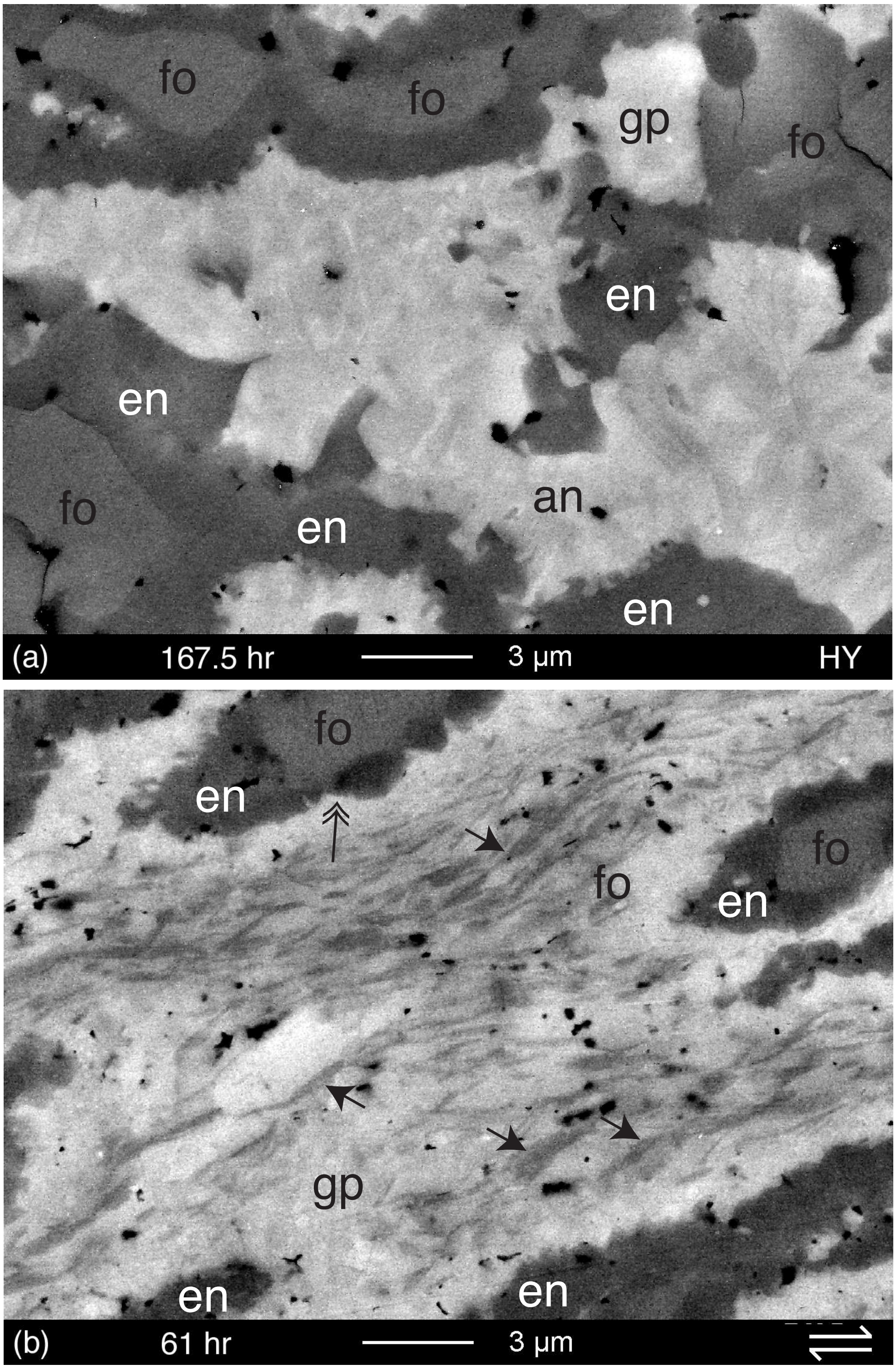

Figure 5.10: Representative microstructures of reaction products in the GP-field (BSEM). Phases: fo (olivine), gp (opx + cpx + spinel + garnet ±kyanite), en (enstatite rim). (a) The bright hydrostatic reaction product matrix appears coarse-grained and has a needle-like texture after 167.5 hours at P_c=1510 MPa (Fig. 5.9b; 34AA). enstatite rims are pronounced. The en-fo interface is smooth. (b) The matrix of syndeformational GP-product contains dark elongate minerals (single arrows), presumably kyanite. Enstatite rims around olivine are continuous but have an irregular, lobate appearance (double arrows).

remained small while syndeformational reaction progressed. Elongated and needle-shaped phases occur in the internal parts of the reaction product matrix and are absent in a ∼1.5 μm wide zone directly adjacent to the enstatite rims (Fig. 5.10b).

The fine-grained reaction products (size = 0.1-0.5 μm) after large strain at P_c=1630 MPa have been identified as opx, cpx, spinel, garnet (gt) and kyanite (Fig. 5.11). This phase assemblage deviates strongly from the theoretically calculated equilibrium assemblage of garnet peridotites in the NCFMAS-system (Eq. 5.2; Fig. 5.1). The new phases appear heterogeneously mixed and are dislocation-free (Fig. 5.11a).

The TEM size of the needle-shaped kyanite grains (size ∼1 μm, Fig. 5.11b) approximately corresponds to the size of needle-shaped phases observed in the BSEM images (Fig. 5.10b), which suggests that kyanite primarily occurs in the central parts of the fine-grained reaction product matrix. The enstatite rims are characterised by fine-grained (size <0.5 μm) opx grains directly adjacent to relict olivine. Olivine grains frequently display dislocation walls, indicating dislocation creep (Fig. 5.11c). Dislocation arrays in newly formed pyroxene grains with a somewhat larger grain size of ∼0.5 μm indicate some deformation by dislocation creep processes.

In the small strain sample deformed to peak stress conditions at P_c=1460 MPa (γ=2.2; Fig. 5.9d), opx, spinel and garnet are typically observed as clusters of small grains (0.1 to 0.5 micron in size) at sites of high dislocation densities in relict grains (Fig. 5.11d). Relict anorthite and olivine grains contain local high dislocation densities and poorly organised dislocation walls typical for low temperature plasticity (Chapter 4). Kyanite is not observed in low strain samples, only at larger shear strain ($\gamma > 2$) and higher reaction extent (ξ >0.33).

5.5.3 Reaction rates

In summary, it is evident from the microstructural observations that plastic deformation of An-Fo composites enhances the reaction between anorthite and olivine. Plotting the amount of anorthite transformation versus time indicates that hydrostatic reaction progress at P_c ∼1500 MPa follows an exponential relationship with time (Fig. 5.12), similar to other commonly observed reaction rates based on the Avrami equation (Avrami, 1939; Rubie and Thompson, 1985).

The amount of anorthite transformation in deformed samples in the GP-field is much higher and appears linear with time for a fixed shear strain rate of $\dot{\gamma}$ ∼$4.0{*}10^{-5}s^{-1}$ (Fig. 5.12). Nearly complete reaction is obtained after less than 35 hours of shear deformation ($\dot{\gamma}$=$5.0{*}10^{-5}s^{-1}$) in the garnet-spinel peridotite field, indicating a transformation rate

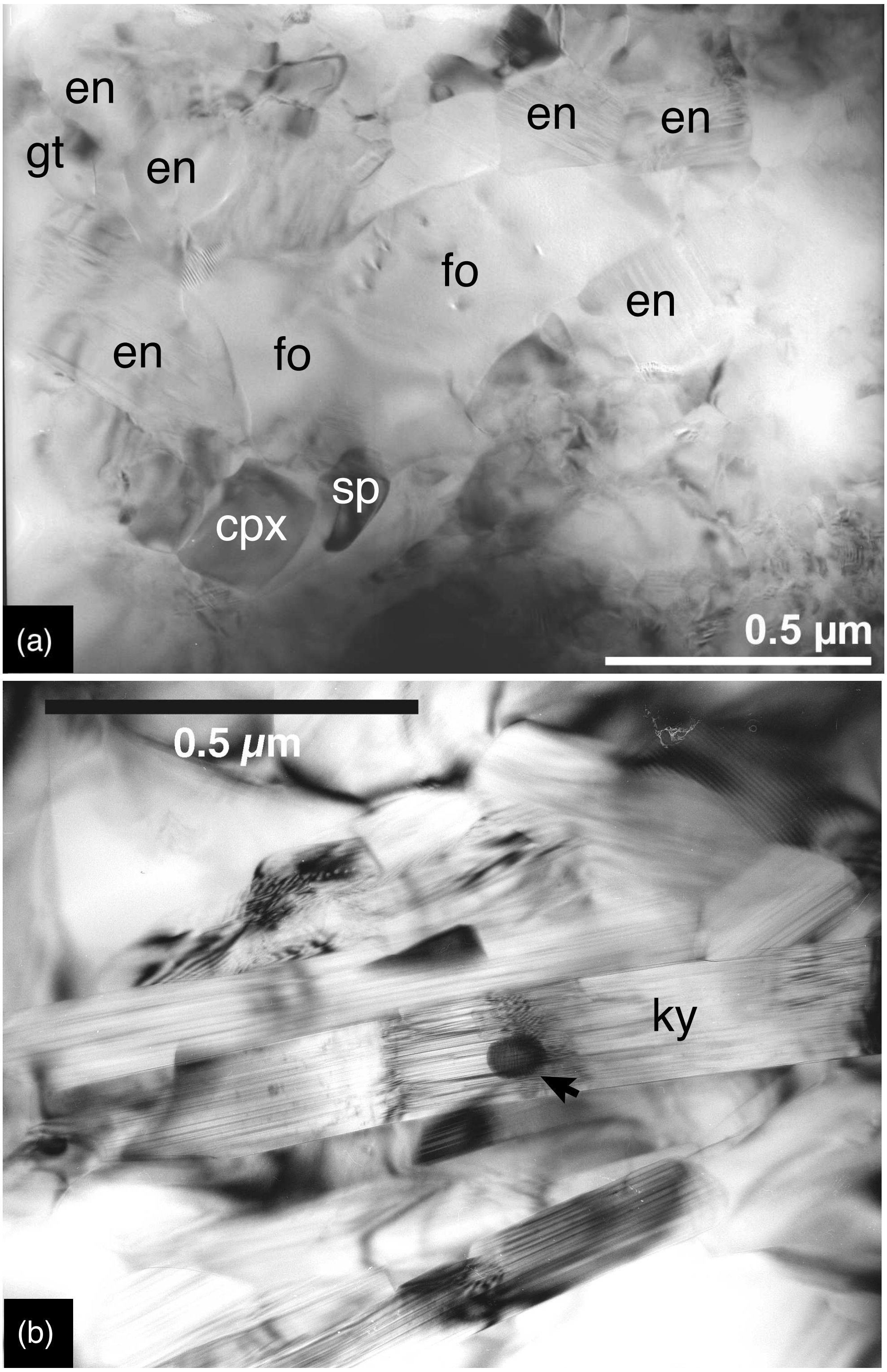

Figure 5.11: Representative microstructures of syndeformational reaction products in the GP-field (bright field TEM). (a) Typical syndeformational reaction products at P_c ∼1500 MPa: spinel (sp), orthopyroxene (en), clinopyroxene (cpx) and garnet (gt) together with small <0.5 µm forsterite-rich olivine grains (fo). The products are dominantly dislocation-free. (b) Needle-shaped kyanite (ky) formed after large strain (γ=4.9) at P_c=1630 MPa (28AA). The dark spot inside the grain indicates the size of an EDS analysis.

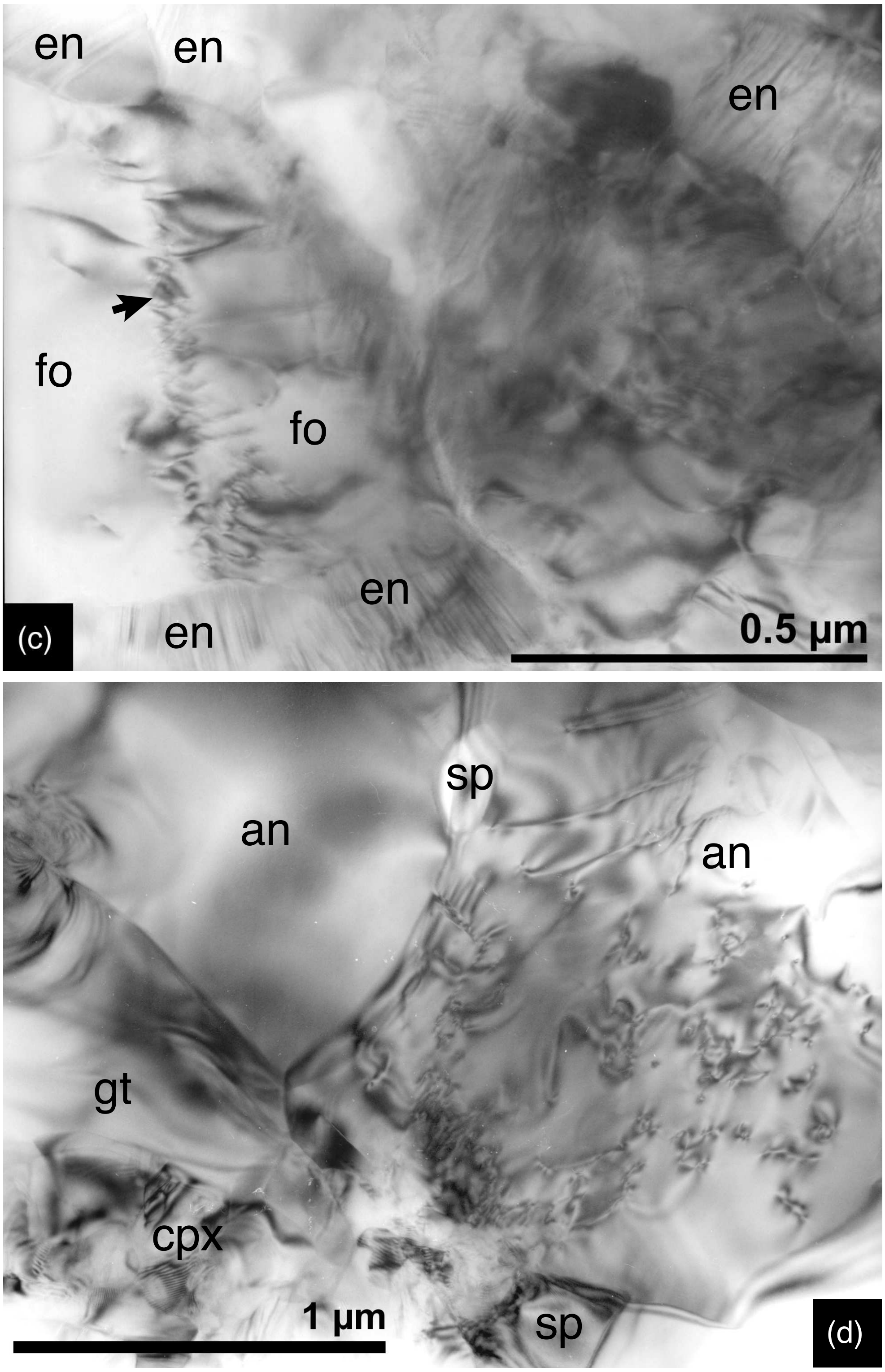

Figure 5.11: (Continued: c) Detail of 0.25 µm orthopyroxene grains (en) adjacent to a small relict olivine grain (fo) after large strain at P_c ∼1500 MPa. The olivine grain contains a disordered dislocation wall (arrow). (d) Garnet (gt), spinel (sp) and clinopyroxene (cpx) formed adjacent to an anorthite grain (an) with a high dislocation density after small strain (γ=2.2) at P_c ∼1460 MPa (32AA). Note also a dislocation-free anorthite grain in the top left.

of $\dot{\xi}$ ~0.03 $\xi \mathrm{hr}^{-1}$. This rate is lower in the samples deformed in the SP-field and varies between the individual experimental runs. The rate varies from $\dot{\xi}$ ~0.02 $\xi \mathrm{hr}^{-1}$ for the P_c=1160 MPa sample to $\dot{\xi}$ ~0.003 $\xi \mathrm{hr}^{-1}$ for the P_c=990 MPa sample. In the SP-field the relationship of reaction progress with time is unknown. Assuming a comparable reaction progress after γ=5.8 and P_c=1030 MPa, $\dot{\xi}$ decreases from 0.02 to 0.001 $\xi \mathrm{hr}^{-1}$ when reaction was continued under hydrostatic conditions after shear deformation. Thus, it appears that ongoing (active) deformation processes enhance the reaction rate.

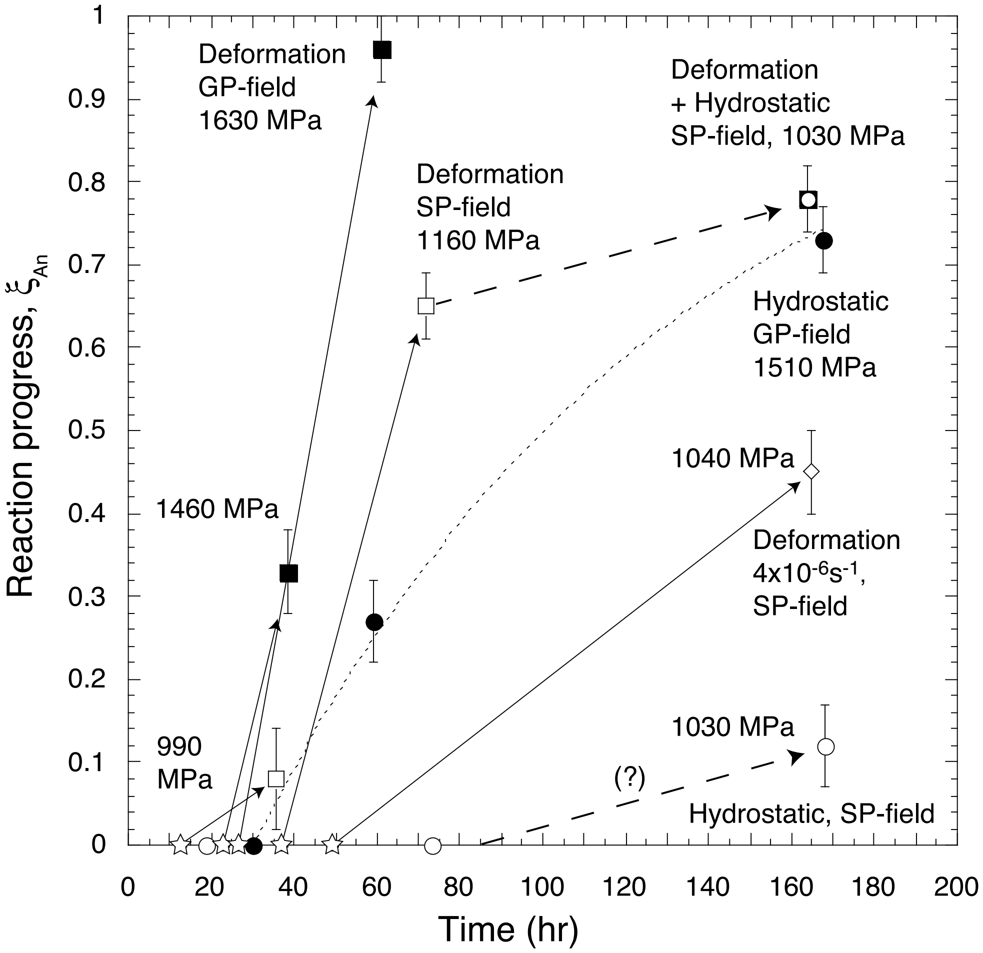

Figure 5.12: Reaction progress ξ_{An} versus time. Circles: hydrostatic experiments. Squares: shear deformation experiments. Open symbols: experiments in the spinel peridotite (SP) field. Solid symbols: experiments in the garnet peridotite (GP) field. Stars: the 'hit point time' of deformation experiments (Table 5.2). Error bars are the standard error in mean vol.% of the initial An-Fo volume ratio. The dashed line is an exponential curve fit of ξ_{An} with time for hydrostatic reaction in the GP-field ($\xi = 1 - \exp(0.01 \cdot (30 - t))$). Solid arrows indicate the ξ_{An} obtained during deformation. Dashed arrows indicate how reaction continued hydrostatically after a shear strain of γ ~5.8 (top) and the unknown onset of hydrostatic reaction in the SP-field (bottom).

5.6 Quantitative analysis of reaction

5.6.1 Theoretical mineral reactions

Spinel peridotite reaction. Despite the differences in reaction progress and the conditions at which reactions occur, hydrostatic and syndeformational reactions in the spinel peridotite field result in fairly similar mineral assemblages. No differences are observed between the final phase assemblages of hydrostatic and deformed samples at P_c ~1000 MPa.

The small grain size of the new phases makes it difficult to fully balance the mineral reactions because of the lack of quantitative analysis of the phases. As mentioned earlier, a further difficulty is the fact that the ratio of olivine + anorthite in the starting material does not correspond to the stoichiometry of the reactions. Some olivine is always left, whereas anorthite can be completely consumed (Fig. 5.7). In order to balance the reactions, we have tried to use a theoretical equilibrium mineral assemblage from thermodynamic calculations to fit the relative proportions of the phases.

The program THERIAK (de Capitani and Brown, 1987; de Capitani, 1994) is used to calculate the theoretical equilibrium mineral assemblage for a 49-51 An-Fo vol.% bulk sample and actual anorthite and olivine mineral compositions at the PT-conditions of the experiments. THERIAK describes a mineral assemblage in terms of its stoichiometric coefficients of compositions of stable phases, their molar volumes and relative volume percentages. The theoretical equilibrium mineral assemblage for the An-Fo composites in the spinel peridotite field at 900°C is independent of pressure and volumetrically consists of 14% olivine (fo_{92}+fa_8), 34% orthopyroxene (en_{80}+Al-Fe-Mg-opx_{10}), 35% omphacite (di_{89}+jd_8+hd_3) and 17% spinel (sp_{85}+hc_{15}). Because olivine is stable before and after reaction (Eq. 5.1), i.e. no olivine forms during the net reaction, the theoretical bulk composition of all reaction products in the SP-field consists of 39% opx + 41% cpx + 20% spinel (Table 5.3).

In a chemically closed system, the bulk composition of reaction products should be equal to the sum of anorthite and olivine that are transformed by reaction. The anorthite and olivine starting compositions are known (Table 5.1) and the estimated volume percentages of anorthite, olivine and reaction rims in the BSEM-images (Table 5.2) are used to determine a bulk composition of reaction products.

The bulk composition of reaction products from image analysis is calculated by subtracting the measured (final) An-Fo volume fractions (Table 5.2) from the 49-51 An-Fo vol.% starting material. The resulting 'consumed' An-Fo volume fraction is

Theoretical equilibrium mineral assemblages:									
*based on 49-51 An-Fo vol.%						*based on image analysis			
						19AA	33AA	55AA	36AA
Stable minerals					Products	1160	1030	1040	1030
Name	N	V/mol	V(ccm)	V(%)	V(%)	V(%)	V(%)	V(%)	V(%)
Opx	0.486	64	31	34	**39**	36	**38**	34	**37**
Omph	0.484	67	33	35	**41**	37	**40**	35	**40**
Ol	0.284	45	13	14		8	**3**	14	**3**
Sp	0.392	41	16	17	**20**	18	**19**	17	**19**
*based on 51-49 An-Fo vol.%						*based on image analysis			
Opx	0.508	64	32	35	**39**	**38**	**38**	**37**	23
Omph	0.504	67	34	37	**41**	**40**	**40**	**39**	24
Ol	0.198	45	9	10		**2**		**5**	
Sp	0.408	41	17	18	**20**	**20**	**19**	**19**	12
Plg							**3**		40

Table 5.3: Theoretical mineral assemblages at 900°C in the spinel peridotite field. Calculations are made with the program THERIAK and the Berman (1988) database (see Fig. 5.1 for the applied solid solution models). The assemblages are calculated from the bulk compositions of all reaction products (see text for details). Good agreement between the theoretical mineral assemblages and those based on image analysis is indicated in **bold**. Confining pressures of the experiments are indicated in MPa.

rewritten to moles ($An_{92} = 101.23\ cm^3mol^{-1}$, $Fo_{93} = 45.02\ cm^3mol^{-1}$) and used as a THERIAK input. The theoretical mineral assemblages were calculated for four SP-field experiments and are described in terms of volume percentages of new minerals (Table 5.3). In order to account for variations in the bulk composition of the An-Fo starting material, calculations were repeated using a 51-49 An-Fo vol.% bulk composition.

Although the volume ratios of phases in the fine-grained mixtures are unknown due to their small size, the analysis indicates that the bulk composition of reaction products estimated from the BSEM images corresponds quite well to a stable spinel peridotite mineral assemblage (Table 5.3). It appears that opx is primarily partitioned in the enstatite rim (~22% in sample 33AA) and little in the SP-rim (~1% in sample 33AA), which reflects BSEM observations (Figs. 5.5d and 5.7a). Considering the error in volume percent measurements (±2%) and the occurrence of some olivine within the reaction products matrix (Fig. 5.6a) the agreement with theoretical phase petrology is excellent. The applied solid solution models proved to be suitable for the plagioclase-spinel peridotite transition (Fig.5.1).

The resulting net stoichiometric reaction in the SP-field that corresponds to the relative proportions of phases in the microstructures is given by

$$0.47\,\mathrm{an} + 0.85\,\mathrm{ol} \rightarrow 0.47\,\mathrm{opx} + 0.47\,\mathrm{cpx} + 0.38\,\mathrm{sp}$$

It is interesting to note that the product assemblages in the analysed samples were obtained by different pathways: unstrained at hydrostatic conditions (Fig. 5.5b), large strain at high strain rate (γ=5.9; $\dot{\gamma}$=4.7x10^{-5}; Fig. 5.5d), small strain at low strain rate (γ=1.7; $\dot{\gamma}$=4.0x10^{-6}; Fig. 5.8) and large strain followed by hydrostatic pressure (γ=5.8; Fig. 5.7). Therefore, the final mineral assemblage of the reaction products in the spinel peridotite field (P_c ~1000 MPa) seems to be independent of the amount of strain and the applied strain rates.

Garnet peridotite reaction. The correlation of theoretical equilibrium assemblages and the observed reaction product assemblage in the GP-field experiments was not possible. Orthopyroxene is not calculated for anorthite-olivine assemblage at 900°C and P_c=1630 MPa using THERIAK with the Berman (1988) database (Eq. 5.1; Fig. 5.1). However enstatite rims formed during hydrostatic and syndeformational reactions (Fig. 5.9c and 5.9f). Better agreement is found with the mineral assemblage of the P_c=1400 MPa garnet-spinel field or the experimental CMAS-data (Fig. 5.1), in which opx is part of the stable garnet peridotite assemblage. The reason for the discrepancy between the calculated and observed assemblages is probably due to the garnet solid solution model in the NCFMAS-system.

The THERIAK software calculates a theoretical equilibrium assemblage at 900°C and P_c=1630 MPa which volumetrically contains a lot of garnet (43%; Table 5.4). Although garnet is identified in the samples, it appears to make up far less than ~40 vol.% of the reaction product assemblage (Fig. 5.11a). A volumetric (i.e. molar) reduction of pyrope-rich garnet in the calculated mineral assemblage would provide more magnesium to form additional opx and spinel. However, incorporating such a modification in the calculations here is beyond the scope of this study and should be addressed in future work.

The formation of kyanite grains during deformation cannot be explained by assuming bulk equilibrium conditions in the samples. The presence of kyanite is due to local disequilibrium. For example, reaction may have occurred between anorthite and adjacent reaction products. In order to examine to formation of syndeformational kyanite in the GP-rims, THERIAK was used to calculate the theoretical reactions from bulk compositions that represent a deviation from the initial 0.8-2.0 An-Fo molar ratio. The results of the calculations are summarised in Table 5.4.

Two potential reactions were identified to explain the occurrence of kyanite during deformation at P_c=1630 MPa. (1) Kyanite (17 vol.%) and an intermediate plagioclase (12 vol.% An_{74}) form when anorthite and olivine react in a 2:1 molar ratio instead of a 0.8:2 molar ratio. (2) Kyanite (34 vol.%) forms with some quartz (2 vol.%) during reaction of anorthite with enstatite. It seems unlikely that reaction (1) occurred because intermediate plagioclase was not observed using TEM in the P_c ~1500 MPa samples. Reaction (2) is likely to occur once the enstatite rims have formed around olivine. The small amount of quartz may have remained undetected in the TEM samples. The occurrence of this reaction suggests that transport in the fine-grained aggregates is very limited and local equilibria may persist on a small scale.

Bulk	Molar coefficients of stable phases, N							
composition	Omph	Gt	Ol	Sp	Ky	Plg	Cor	Qtz
0.8 An+2 Fo	0.312	0.329	0.559	0.117				
An+3 Fo	0.641	0.680	1.760	0.240				
An+0.5 Fo	0.365	0.400			0.381	0.119	0.051	
An+ En	0.984	0.038			0.883			0.118
An+2 En	0.804	0.491			0.429			0.571
	Volume percentages (%)							
	Omph	Gt	Ol	Sp	Ky	Plg	Cor	Qtz
49 An+51 Fo	23	43	28	5				
43 An+57 Fo	20	38	37	5				
82 An+18 Fo	24	47			17	12	1	
50 An+40 En	59	4			35			2
43 An+57 En	38	40			13			9
	Solid solution end members (%)							
	Omph	Gt	Ol	Sp	Ky	Plg	Cor	Qtz
0.8 An+2 Fo	$di_{86}jd_{12}hd_2$	$py_{75}gr_{17}al_8$	$fo_{94}fa_6$	$sp_{89}hc_{11}$				
An+3 Fo	$di_{86}jd_{12}hd_2$	$py_{74}gr_{18}al8$	$fo_{94}fa_6$	$sp_{88}hc_{12}$				
An+0.5 Fo	$di_{85}jd_{13}hd_2$	$py_{52}gr_{43}al_5$			ky	$an_{74}ab_{26}$	cor	
An+En	$di_{92}jd_8$	$py_{86}gr_{14}$			ky			qtz
An+2 En	$di_{90}jd_{10}$	$py_{87}gr_{13}$			ky			qtz

Table 5.4: Theoretical mineral assemblages at 900°C and P_c=1630 MPa. Calculations are made with the program THERIAK and the Berman (1988) database (see Fig. 5.1 for the applied solid solution models). The applied bulk compositions represent the original An-Fo composite (0.8 An+2 Fo), local olivine enrichment (An+3 Fo) and depletion (An+0.5 Fo) and anorthite-enstatite reaction (An+1 En, An+2 En). An = An_{92}, Fo = Fo_{93}. Kyanite (ky), corundum (cor) and quartz (qtz) form when olivine is depleted or when anorthite reacts with enstatite.

5.6.2 Nucleation and growth of reaction rims

The rims in the deformed and hydrostatic An-Fo composites are quite similar in terms of their microstructures and reaction rim sequence at all applied confining pressures. The general structure of the double reaction rim can be denoted as:

$$An|Cpx+Fo+Opx+Sp|En|Fo \qquad \text{and} \qquad An|Cpx+Fo\pm Ky+Gt+Opx+Sp|En|Fo$$

in the SP-field and in the GP-field, respectively. Similar rim structures were studied experimentally by Liu et al. (1997), who used the polymineralic rim growth rate k to quantitatively compare bulk diffusion rates between dry and water-added anorthite-olivine samples. The formation of an enstatite rim around olivine has been attributed to transport-controlled mineral growth between anorthite and olivine (Joesten, 1978; Mongkoltip and Ashworth, 1983) and olivine and quartz (Yund, 1997; Milke et al., 2001) as well. The rims formed by the syndeformational and hydrostatic An-Fo reactions in our samples are considered to be transport-controlled at a first level of interpretation.

Analogous to Liu et al. (1997), we measured the thickness of the enstatite, SP- and GP-rims in order to make a quantitative comparison of rim growth rates between the deformed and hydrostatic samples. Due to the complexity of the reactions, the enstatite rim thickness is the most reliable measure to use in comparing all samples. Unfortunately, the enstatite rim is not visible in BSEM-images after low reaction progress (ξ <0.10). Therefore the SP and GP rim thickness are needed for the comparison as well.

The geometry of the reaction rims in the deformed samples can be somewhat obscure due to the coalescence of reaction products into S-oriented layers (Fig. 5.5d). Therefore, rims were only measured at locations with a clear 'An|rim|Fo' sequence perpendicular to olivine and anorthite grain surfaces. Because the width of the rims can be rather thin (width ~1 μm), more than 50 measurements have been made in high quality 1600x and 6400x magnification BSEM images at two different locations in the centres of the samples. The GP-rim thickness in the large strain P_c=1630 MPa sample (Fig. 5.9e) was measured near the ends of the sample shear zone, where a GP-rim structure can still be observed (Fig. 5.9f). Laterally discontinuous rims are included (Fig. 5.5b,c), which require some caution in interpretation because they are attributed to slow nucleation instead of diffusion (Liu et al., 1997).

Transport-controlled rim growth is parabolic with time ($X^2 \propto k * t$; Fisher, 1978), thus thickness squared (X^2 in μm^2) of the enstatite, SP and GP rims is plotted versus the total time, t_{total}, of the experiments (Fig. 5.13). All samples show Gaussian distributions of rim widths. The mean rim thickness can be used to quantitatively compare the rim growth rate k between hydrostatic and deformed samples.

The enhancement of nucleation rate by shear deformation is shown by the intercepts of the linear growth rate on the time axis. The onset of nucleation of phases in hydrostatic experiments in the SP-field is rather delayed and does not occur before 70 hour at P_c=1030 MPa (Fig. 5.12 and 5.13a). The nucleation time is reduced to 29 hours in shear deformation experiments, which indicates that plastic deformation causes a faster nucleation rate of new phases.

The hydrostatic nucleation time also decreases when the pressure overstepping is increased into the GP-field (Fig. 5.13b). These results are in accord with an increase of the rate of nucleation (Rubie, 1998) by a larger Gibbs free energy difference of the An-Fo assemblage and the equilibrium assemblage. The start of the hydrostatic reaction happens to coincide with the run-in time of the fast strain rate ($\dot{\gamma}$=5.0*$10^{-5}s^{-1}$) deformation experiments before the touch-point. Therefore, it can be assumed that the onset of sample deformation in the GP-field occurred simultaneously with reaction.

The parabolic growth of GP- and enstatite rims in the hydrostatic samples indicates that the hydrostatic reaction is indeed transport-controlled (Fig. 5.13b). Although the nucleation time of phases in hydrostatic SP-field experiments is unknown, the growth rate k in the GP-field appears higher than in the SP-field, i.e. k ~0.02 $\mu m^2 hr^{-1}$ for the GP-rim and k ~0.01 $\mu m^2 hr^{-1}$ for the enstatite rim.

Shear deformation has a pronounced effect on the growth rate. Taking into account the hit point time of the deformation experiments, the GP-rim growth during deformation appears parabolic with time (Fig. 5.13b). The syndeformational GP-rim growth rate (k ~0.05 $\mu m^2 hr^{-1}$) is more than twice as high as the hydrostatic growth rate. The enstatite rim thickness is not parabolic with time, because shear displacement most probably leads to progressive thinning of the rim when opx grains move from the rim into tails (Fig. 5.9d).

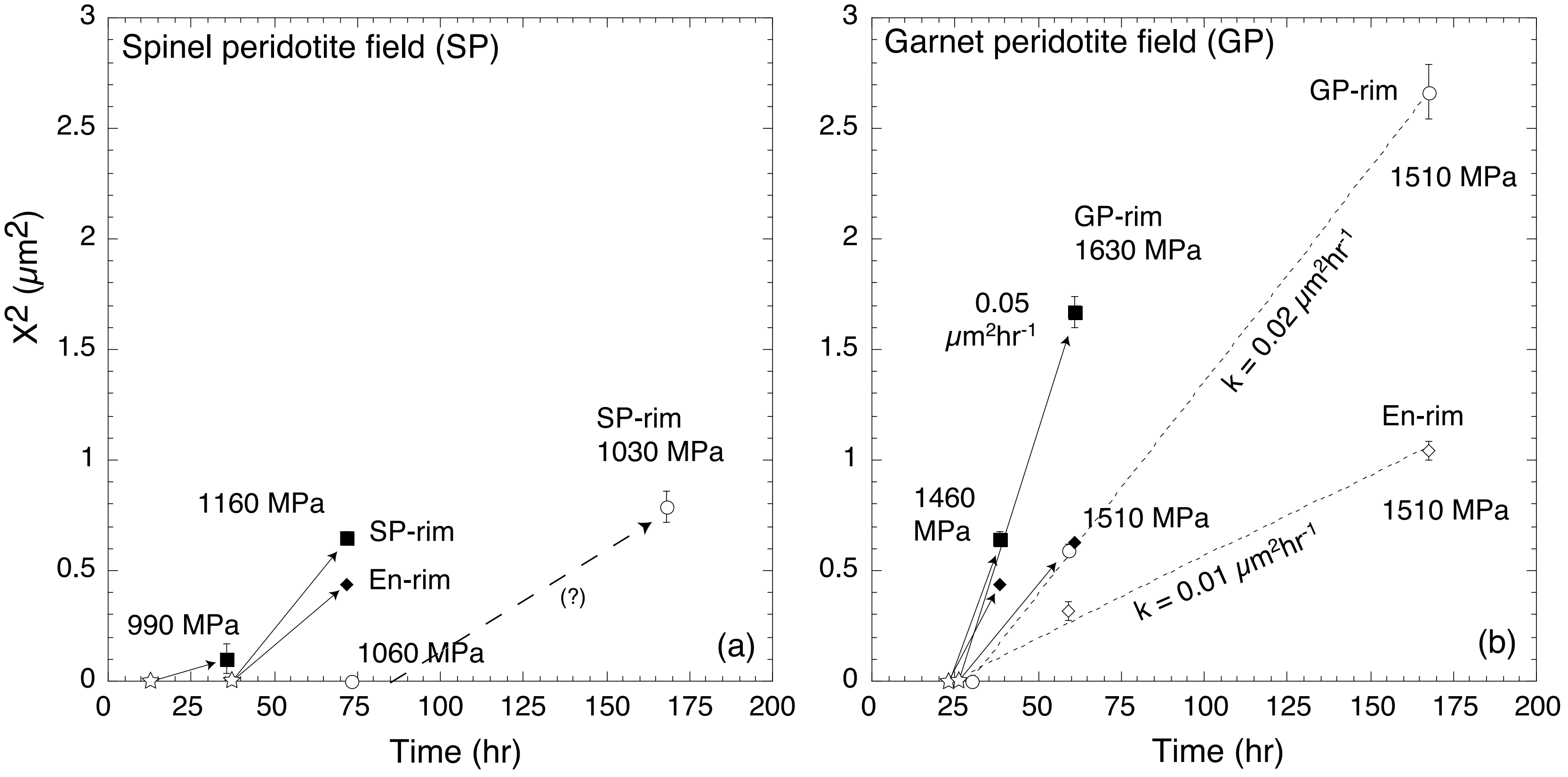

Figure 5.13: Rim width squared, X^2 (μm^2), versus time. Circles: hydrostatic experiments. Squares: shear deformation experiments. Open diamonds: enstatite rims in hydrostatic samples. Solid diamonds: enstatite rims in deformed samples. Stars: the 'hit point time' of deformation experiments (Table 5.2). Solid arrows indicate the syndeformational rim growth. Error bars are the standard errors in the mean X. (a) Experiments in the spinel peridotite field. A $X^2 \sim 0.75$ μm^2 is obtained within a much shorter duration during deformation compared to reaction under hydrostatic conditions. The dashed arrow indicates the unknown onset of hydrostatic rim growth in the SP-field. (b) Experiments in the garnet peridotite field. The dashed lines indicate first order linear curve fits for the hydrostatic growth of rims. The time-intercepts for syndeformational and hydrostatic reaction almost coincide. The syndeformational rim growth in the GP-field is faster than in the SP-field.

5.7 Discussion

5.7.1 Hydrostatic reaction mechanisms

Hydrostatic An-Fo reactions in the spinel and garnet peridotite field display a delayed nucleation of new phases before the onset of reaction rim growth (Fig. 5.13). At P_c ~1000 MPa, no new phases are observed after ~75 hours and at P_c ~1500 MPa, the first reaction products nucleate after ~30 hours. The difficulty of nucleation of phases is demonstrated by the formation of discontinuous reaction rims after 168 hours at P_c=1030 MPa (Fig. 5.5b). The onset of hydrostatic nucleation occurred earlier in the GP-field than in the SP-field because the rate of nucleation increases exponentially with the difference in Gibbs free energy (Christian, 1975), and therefore with the amount of pressure overstepping for pressure-sensitive reactions.

A 'late' onset of nucleation is common in laboratory studies on polymorphic phase transformations, in which equilibrium boundaries need to be overstepped by at least 200 to 400 MPa before new phases nucleate experimentally (Rubie, 1998). A nucleation barrier can be caused, for example, by the large dissimilarities between the structures of the reactants and products (Rubie, 1998) or the slow transport rate to assemble the chemical components.

The parabolic growth rate of hydrostatic reaction rims in the GP-field as well as the strong microstructural analogy of the samples with other kinetic studies (Liu et al., 1997; Milke et al., 2001) suggest that after the formation of the first new phases, growth of the reaction rim under hydrostatic conditions is controlled by transport of chemical components through a growing layer of reaction products. It is difficult to determine the transport rate controlling components in our samples because the observed rim structures do not represent a steady-state configuration (Joesten, 1978; Liu et al., 1997). However, the observed growth rates can be used to compare the results to other studies.

The overall hydrostatic growth rate of the double reaction rim in the GP-field is k ~0.03 $\mu m^2 hr^{-1}$ at P_c=1630 MPa. Liu et al. (1997) found a parabolic rate constant of k ~0.25 $\mu m^2 hr^{-1}$ at 1000°C and P_c=700 MPa in vacuum dried (250°C) olivine-anorthite samples. Also, they measured a X^2 ~30 μm after approximately 140 hours at these P,T conditions. Our hydrostatic SP-samples, however, display a X^2 <1 μm after 168 hours at P_c=1000 MPa and 900°C. The difference of one order of magnitude in growth rate as well as the large difference in X^2 suggests that it is not only the 100°C lower temperature, but also the much lower water content of our samples which are responsible for the limited rim growth. Hence, the hydrostatic samples indicate that the transport of chemical components is very slow due to the extremely small water content of our samples. In the light of the fine-grained nature of the reaction products and the reactants, it is likely that the transport mechanism is grain boundary diffusion.

Unfortunately, the rate of rim growth is unknown in hydrostatic SP-samples. Therefore a direct comparison with the GP-samples is not possible. Yund (1997) showed that the bulk transport rates through enstatite rims are independent of pressure in forsterite-quartz experiments at P_c=210-1400 MPa and 950-1100°C, which suggests that similar rim growth rates can be inferred for the SP- and GP-rims. However, it is observed that discontinuous and continuous rims form after 168 hours at P_c=1000 MPa and P_c=1510 MPa, respectively.

It difficult to argue for an effect of H_2O on the rim growth rates with increasing pressure because reactions have taken place at water-deficient conditions. Therefore it appears that the rates of transport at anhydrous conditions are not the same at different overstepping pressures. The discontinuous SP-rims indicate that limited nucleation of phases is important during the reaction at hydrostatic conditions. Hence, the higher reaction progress at higher pressure overstepping is inferred to reflect the exponential increase of nucleation with the difference in Gibbs free energy.

In summary, the hydrostatic reaction between anorthite and olivine can be described as primarily transport-controlled at all our experimental conditions. However, the rates of transport are extremely slow due to the anhydrous conditions of the samples. Therefore, the progress of reaction strongly depends on the slow nucleation of new phases as well. As the nucleation rate increases with the difference in Gibbs-free energy, higher reaction rates are observed at larger pressure overstepping conditions.

5.7.2 Syndeformational reaction mechanisms

The enhancement of reaction in the deformed samples is most clearly expressed by the earlier onset of reaction (formation of new phases, Fig. 5.13a) and the greater increase in reaction progress with time, compared to the hydrostatic samples (Figs. 5.12 and 5.13b). The fact that the reaction rate is higher during deformation is indicated by the decrease in reaction rate when plastic deformation processes are stopped at P_c ~1000 MPa (Fig. 5.12): although the transport-controlled reaction continues under hydrostatic conditions, the rate of reaction decreases (Fig. 5.12).

The very low transport rate in the samples is indicated by the dynamic recrystallisation of anorthite (Fig. 5.6b). Dynamic recrystallisation of anorthite is not associated with changes in composition in the P_c ~1000 MPa experiment, although anorthite is metastable. This observation suggests that the driving potential for anorthite recrystallisation is solely due to deformational energy stored in the crystals (in the form of dislocations). Such dynamic recrystallisation of metastable phases is only possible if the transport of the components needed for reaction is strongly inhibited. In other words, the chemical equilibrium on a very local scale ($\sim$1 μm) suggests a local chemically isolated system. Such a situation is consistent with the dry conditions in the sample.

Due to the water-deficient conditions in the samples, and the corresponding slow rates of transport, it is difficult to argue that transport of chemical components is mainly controlling the rate of reaction during deformation. As described in the previous section, the nucleation rate of reaction products is slow under hydrostatic conditions. An increase in nucleation sites during the reaction may reduce the distances for the transport of material. A smaller transport distance may cause new phases to nucleate earlier and faster. Deformation-induced dislocations can enhance the nucleation rate, which was demonstrated by experiments on the calcite-aragonite transformation during ductile deformation Snow and Yund (1987).

In order to explain the effect of plastic deformation on reaction in our samples, the microstructural development of the An-Fo composites with progressive deformation must be considered. To do so, two categories of deformation processes are distinguished and discussed: (1) the effects of small scale plastic deformation processes on the nucleation of new phases and (2) the effects of shear displacement on the distribution of new phases in the sample.

Effects of plastic deformation processes

Recovery processes in grains of anorthite and olivine, i.e. strain-induced grain boundary migration, are initially inhibited by the presence of anorthite-olivine phase boundaries (Chapter 4). As a result, the dislocation density increases continuously in anorthite and olivine grains while deforming the samples to peak stress conditions. Dislocations in anorthite and olivine, both individual dislocations and those in ordered and disordered walls, increase the stored strain energy of the minerals and raise their Gibbs free energy (e.g. Wintsch and Dunning, 1985; Stünitz, 1998).

The nucleation of new phases is energetically favourable at higher dislocation densities because dislocations contribute to the energy difference that reduces the critical nucleus size (Cahn, 1957; Rubie and Thompson, 1985; Lasaga, 1998). Thus, dislocations act as 'nucleating agents', which decrease the free energy barrier needed for reaction. The first macroscopic observations of heterogeneously distributed reaction products at

P_c=990 MPa are made near peak stress conditions (Fig. 5.5c), which indicates that nucleation assisted by dislocations may actually occur.

At hydrostatic conditions, the reaction starts approximately after 30 hours in the P_c ~1500 MPa experiments (Fig. 5.13b). This time approximately coincides with the 'run-in' time of the apparatus force piston to reach the hit point. Hence, reaction in the P_c ~1500 MPa deformation experiments may have started due to the increased chemical driving potential approximately at the hit point. Nevertheless, a reaction progress of ξ ~0.30 is achieved in shorter duration during deformation to peak stress conditions (t_{tot}=39 hrs; Fig. 5.9d) than by reaction at hydrostatic conditions (t_{tot}=59 hrs; Fig. 5.9a). The higher rate of reaction while loading the deformation experiments to peak stress conditions suggests that the build-up of dislocations in anorthite and olivine grains enhances the already nucleating mineral reaction.

After the onset of strain weakening, as the samples achieve large strains and high reaction extent, progressive plastic deformation of the composites in the SP-field is accompanied by low-temperature plasticity and some dynamic recrystallisation of both the anorthite and the olivine (Chapter 4). Therefore, the strain energy resulting from dislocations is expected to continuously contribute to the Gibbs free energy of the minerals, although the decreasing stress should result in decreased dislocation densities. The high dislocation densities and formation of dislocation walls continuously enhance the nucleation of reaction products (Fig. 5.11c,d).

The net effect of dislocation-assisted reaction is reflected in the An-Fo composite deformed at a low shear strain rate (Fig. 5.8). At $\dot{\gamma}$ ~4x10^{-6}s^{-1}, the An-Fo composite deformation takes place at lower stress conditions (τ ~60 MPa) than that at a strain rate of $\dot{\gamma}$ ~5x10^{-5}s^{-1} (Fig. 5.4b). Anorthite and olivine grains deform to a small strain by dislocation and possibly diffusion creep mechanisms (see Fig. 4.2, Chapter 4). Recovery processes will be able to keep up with the build-up of dislocations at the lower stress conditions. As a consequence, the anorthite and olivine grains display lower dislocation densities. Therefore, the deformation-enhanced nucleation rate is reduced and a lower rate of reaction is observed ($\dot{\xi}$ ~0.004 ξhr^{-1}; Fig. 5.12) compared to that in the composites deformed at $\dot{\gamma}$ ~5x10^{-5}s^{-1} ($\dot{\xi}$ ~0.02 ξhr^{-1}).

A reaction mechanism in which a transport-controlled reaction is aided by increased nucleation due to dislocations also explains why a slower reaction rate is observed at hydrostatic conditions in the SP-field (Fig. 5.12). The reaction rate decreases from $\dot{\xi}$ ~ 0.02 to 0.001 ξhr^{-1} when plastic deformation is stopped at P_c ~1000 MPa, and the transport-controlled reaction continues under hydrostatic conditions. No new dislocations form in the reacting minerals in the absence of plastic deformation. Therefore, the rate of nucleation decreases and consequently the rate of reaction as well. As a consequence, the reaction product grains coarsen during the hydrostatic treatment and the resulting microstructure has a more granular appearance then the deformation experiments (compare Figs. 5.5 and 5.7).

Another important aspect is the overall reduction of grain size during syndeformational reaction. Dislocation creep in anorthite and olivine produced some dynamically recrystallised grains with sub-micron sizes (size <0.5 μm; Figs. 5.6b). New phases can form at the boundaries of such small metastable anorthite grains (Fig. 5.7b) because they have a large surface area, which enhances the dissolution rate of material as well as the nucleation of reaction products. Grain boundaries in general are known to be very influential during reaction because they serve as primary pathways for diffusion of chemical species (Farver and Yund, 1991). Experimental studies on plagioclase and K-feldspar suggest that moving grain boundaries (and perhaps moving dislocations) enhance the diffusion of chemical components through the minerals (Yund and Tullis, 1980, 1991). Static dislocations have no effects on the bulk diffusion (Yund et al., 1989).

Effects of shear displacement

The syndeformational reaction products accommodated displacement by grain boundary sliding and remained fine-grained in comparison to hydrostatic products (Fig. 5.10). The coarser microstructure of the products that formed at hydrostatic pressure suggests grain coarsening of minerals by transport-controlled growth after initial nucleation (Fig. 5.7a and 5.10a). It is known from studies on natural shear zones that shear deformation by grain boundary sliding leads to an increased dispersion of phases in the shear zone (Kruse and Stunitz, 1999; Kenkmann and Dresen, 2002). A well-dispersed polyphase nature of products hinders mineral grain growth by grain boundary pinning (Olgaard and Evans, 1988; Olgaard, 1990). Therefore the shear displacement can suppress grain growth of fine-grained reaction products. As a consequence, new reaction products must nucleate continuously in order to achieve a higher reaction progress during deformation.

During progressive shear displacement at P_c= 1630 MPa, the reactants anorthite and olivine literally become separated by the reaction product rims. Enstatite in the tails of relict olivine grains extend into the fine-grained reaction product aggregates (Fig. 5.9e). The transport of enstatite into different parts of the sample by grain boundary sliding may change the local chemical system, and therefore affect the course of mineral reactions on a local scale. Also, because the rate of transport is so slow under these dry conditions, the local equilibrium conditions that anorthite grains ‘perceive’ in their direct environment may deviate from the initial 0.83 An_{92} + 2.00 Fo_{93} bulk composition. Therefore, it is likely that a kyanite-forming reaction occurred between anorthite and enstatite (Table 5.4), due to the limited transport and the changes in local equilibrium. Such additional reactions must have contributed to the total reaction progress as well.

In summary, the effect of plastic deformation of An-Fo composites on the reaction kinetics under water-deficient conditions appears to be two-fold. First, the high dislocation densities that form by plastic deformation processes enhance the nucleation rate of reaction products. The enhanced nucleation during deformation assists the transport-controlled reaction under water-deficient conditions. Secondly, the combination of fast nucleation, slow transport and the ‘mechanical’ transport of material through the sample by shear displacement affects the local equilibrium conditions. This local equilibrium allows new mineral reactions. Higher reaction progress is achieved during deformation as a net result.

Other effects of deformation on the reaction of anorthite and olivine might include the distribution of stress in the sample. The initial stages of the shear deformation experiments involve a pressurisation of the An-Fo composite up to shear strain of $\gamma \sim 1$, which in rock deformation studies using a solid-medium apparatus is most commonly interpreted as elastic strain (de Ronde et al., 2004). However, such pressurisation may cause internal stresses and if these are not overcome by viscoelastic relaxation, the elastic strain in the minerals will contribute to the nucleation rate (Rubie, 1998).

There is also a possible effect of the higher mean stress on the reaction progress in the deformed samples. The range of mean stress σ_m between peak stress conditions and steady-state flow ranges from σ_m= 1200-1280 MPa and σ_m= 1740-1820 MPa, for the P_c=1030 MPa (33AA) and P_c=1630 MPa (28AA) deformation experiments, respectively. If the mean stress on a sample scale is comparable to a confining pressure, then the deformation experiments have a greater pressure overstepping than the hydrostatic experiments. Therefore it can be suggested that, due to a greater overstepping, deformed samples display a higher reaction progress than the hydrostatic samples. However, we infer that the increased mean stress on a sample scale during deformation is likely to have only a small contribution to the enhancement of reaction. Large variations in dislocation densities are observed in the olivine and anorthite grains, which suggest that an uneven distribution of mean stress on the grain scale is more important.

An accelerated nucleation might have been triggered by nonhydrostatic stress on the grain-scale. Experiments on the olivine-spinel transition demonstrated anisotropic growth of spinel nuclei during nonhydrostatic stress (Vaughan et al., 1984). Also, higher pressures strongly influenced the nucleation rate of enstatite during forsterite-quartz reaction (Yund, 1997). The mean stress acting on the An-Fo phase boundaries during deformation was higher than the hydrostatic pressure. This may lead to anisotropic growth of reaction products in, for example, the $\sigma 1$-direction (Shimizu, 1992). Unfortunately, no clear relationships of the location of new phases in planes perpendicular to $\sigma 1$ have been observed (Fig. 5.5c). Therefore, it is suggested that the main enhancement of nucleation and growth during deformation at P_c ~1000 MPa is caused by the dislocation-associated substructures in the minerals. Local stress concentrations are probably important for these processes (Fig. 4.14, Chapter 4).

5.7.3 Geological relevance

The anorthite-olivine deformation experiments point to several implications for concurrent deformation and reaction in natural systems in general. The spinel peridotite field experiments demonstrate that onset of reaction and shear deformation are concurrent. This implies that the development of high reaction progress in shear zones is not necessarily a later event that concentrates in fine-grained ductile shear zones (e.g. Brodie and Rutter, 1985).

Also, the high reaction progress during ductile deformation of An-Fo composites is obtained at anhydrous conditions. Hence, a significant infiltration of water into ductile shear zones does not seem to be a prerequisite for the localisation of metamorphic reactions in shear zones. A similar conclusion was made by Kerrich et al. (1980), who studied chemical transformations during ductile deformation of granite in the Miéville shear zone. They observed that the localisation of reaction in the mylonite was not associated with high fluid fluxes. Therefore there can be an increase in the reaction rate by plastic deformation itself, and possibly not necessarily by fluid infiltration.

Rubie (1998) pointed out that metastable phases may form when reactions occur at conditions of large overstepping due to a delayed nucleation. The similarity in reaction products and rim structures of the hydrostatic and deformed SP-samples indicate that reaction progress at fixed pressure-temperature conditions was independent of the degree and the rate of ductile deformation. No metastable phases are formed during shear deformation of An-Fo composites at ~300 MPa pressure overstepping; however, a full reaction progress was not reached in these experiments. Kyanite formed during shear deformation to large strain at P_c=1630 MPa, as a consequence of local equilibrium due to the slow transport rate of components. Therefore, it appears that the enhancement of nucleation by plastic deformation can cause the growth of phases that are not part of the bulk equilibrium assemblage. However, this situation does not constitute metastability but local equilibrium, caused by water-poor conditions with very limited transport rates of chemical components.

The reversal of the investigated reaction is often observed in dry natural mylonitic shear zones in extensional tectonic settings, where mantle rocks are adiabatically brought up to shallower levels in the crust and become chemically unstable (Furusho and Kanagawa, 1999; Newman et al., 1999; Handy and Stünitz, 2002). The investigated pressure-temperature range in the experiments is realistic for such upper mantle shear zones. Natural deformation takes place at slower strain rates ($\dot{\epsilon} \sim 10^{-14} \mathrm{s}^{-1}$) and stresses. Although natural strain rates are slower, the deformation of upper mantle rock can take place by dislocation creep mechanisms due to the larger grain sizes (for example, sizes >100 µm in peridotite proto-mylonites, Newman et al., 1999; Handy and Stünitz, 2002).

As described in the previous sections, the deformation-enhanced nucleation rate is reduced during deformation at lower strain rate, because there is a lower build-up of dislocations in reactant minerals due to the lower shear stress. Therefore it is expected that the enhancement of reaction by plastic deformation (by the contribution of dislocations to the nucleation of new phases) will occur to a lesser extent in naturally deformed rocks. However, grain-scale stress concentrations in minerals deforming by dislocation creep, leading to a local increase of dislocation densities, probably occur in naturally deformed polyphase rocks as well. Therefore the results of our experiments do apply to natural cases of syndeformational reaction, and contribute to the understanding of the processes that are involved in the concentration of metamorphosed rocks during plastic deformation at water-deficient conditions in natural shear zones.

Retrograde reactions in the upper mantle are known to cause strain localisation during the exhumation of upper mantle peridotites (Furusho and Kanagawa, 1999; Newman et al., 1999; Handy and Stünitz, 2002). A metamorphic grain size reduction by the crystallisation of fine-grained phases causes the deformation mechanism to change to grain size sensitive diffusion creep. Basement rocks can be dry for long periods of time under metamorphic conditions, with only short and localised periods of fluid infiltration (Rubie, 1986; Jackson et al., 2004). Therefore, the enhancement of reaction by plastic processes during high stress deformation is important for the initiation and continuation of strain localisation in the dry lower crust and upper mantle during crustal thinning and extension.

5.8 Conclusions

We studied the effects of plastic shear deformation on the kinetics of a transport-controlled net transfer reaction between anorthite and olivine at water-deficient conditions. For this purpose, we performed shear deformation and hydrostatic experiments on anhydrous plagioclase-olivine composites at 900°C and confining pressures of 1000-1600 MPa. The principal conclusions of this study are as follows:

- Plastic deformation enhances mineral reaction in An-Fo composites at water-deficient conditions. This enhancement is reflected by the increase of reaction progress as well as the increase of the nucleation and growth rate of reaction rims during deformation.

- At hydrostatic conditions, the formation of an enstatite rim around olivine with a sharp enstatite-olivine interface, indicates that the reaction between anorthite and olivine is controlled by the transport of chemical components. Comparison of the growth rates of enstatite and pyroxene-spinel-garnet reaction rims to other kinetic studies, implies that the water-deficient conditions in the studied samples result in slow transport rates of chemical components. The studied reactions display a delayed nucleation of new phases, even at pressure overstepping conditions of ∼700-900 MPa.

- During plastic deformation, the transport-controlled reaction between anorthite and olivine is mainly enhanced by an increased nucleation rate of new phases. The increased nucleation rate may be due to high dislocation densities in the reactant grains.

- The mechanical transport of phases by grain boundary sliding may change the local equilibrium conditions. Due to the limited transport of chemical species in the sample, changes in the local equilibrium result in additional reactions and the formation of metastable phases like kyanite. These reactions can contribute to the overall reaction progress.

- The amount of pressure overstepping in the experiments affects the reaction progress in the An-Fo composites, because the rate of nucleation increases exponentially with the Gibbs free energy of reaction and therefore with the amount of pressure overstepping for pressure-sensitive reactions.

5.9 Acknowledgements

We thank Ralph Milke and Rainer Abart for useful discussions on reaction kinetics. Christian di Capitani and Phillipe Hunziker are thanked for their help with the petrological calculations and providing the aluminium-pyroxene solid solution model. A.A. de Ronde was supported by the Swiss National Fond grants 2100-057092.99 and 2000-065041.01.

Chapter 6

Conclusions and recommendations for future work

The aim of this thesis is to investigate the relationships between the processes of plastic deformation and mineral reactions in plagioclase-olivine composites. This chapter summarises the principal conclusions of this thesis, in relation to the research aims stated in Chapter 1. Additionally, recommendations and ideas are given for future work on plagioclase-olivine rocks as well as for the general study on concurrent deformation and mineral reaction in rocks.

6.1 Conclusions

Shear deformation and hydrostatic experiments performed on water-deficient plagioclase-olivine composites at 900°C, within a confining pressure range of 1000-1600 MPa and at shear strain rates of $5\text{x}10^{-5}\text{s}^{-1}$, show fundamental interrelationships of plastic deformation and reaction processes. The main conclusions of the thesis are described below.

Relation between the distribution of strain and metamorphic reactions in plagioclase-olivine composites

Deformation and reaction in the deformed samples are localised within 0.5-mm wide shear zones. When analysing the reacting minerals for their fabric anisotropy (fabric elongation) and shape preferred orientation (fabric angle with the shear plane) using the autocorrelation function (ACF), a strong correlation between reaction progress and deformation is demonstrated on a sample scale.

The fabric anisotropy can be calibrated to quantify strain variations across the sheared samples. There is a strong correlation on a sample scale between reaction progress and strain; large shear strain is locally associated with high reaction progress. Using the variations of fabric anisotropy, local strain variations across the sample can be calculated using measurements of bulk finite strain for calibration. The total range of local shear strain rate from the fastest to the slowest rate is approximately one order of magnitude.

Effect of mineral reactions on the strength, deformation mechanisms and microstructures plagioclase-olivine composites

Chemically stable labradorite-olivine composites strain-harden and are extremely strong during shear deformation, regardless of the confining pressure. The strain hardening is probably caused by labradorite-olivine interphase boundaries. These boundaries inhibit recovery processes that rely on grain boundary migration processes. This low temperature plasticity deformation results in plagioclase and olivine grains with high dislocation densities. Deformation takes place at high stresses and close to the brittle-plastic transition.

Chemically unstable anorthite-olivine composites display a pronounced strain weakening, i.e. a decrease in shear stress, during shear deformation at all chosen confining pressures. The onset of the strain weakening coincides with the formation of fine-grained polyphase reaction products (size ~0.25-1.0 µm). The polyphase reaction products deform by a grain size sensitive creep mechanism (probably diffusion-accommodated grain boundary sliding).

The onset of steady-state flow is associated with the coalescence of fine-grained polyphase reaction product aggregates in interconnecting layers. On a grain-scale the applied strain is localised and accommodated in these interconnecting layers of reaction products. Strain partitioning into reaction product layers reduces the strain rate in anorthite and olivine porphyroclasts. As a result, original anorthite and olivine grains deform at lower strain rate conditions as well as lower stress, which enhance dislocation climb.

The reaction weakening mechanism in anorthite-olivine composites is grain size reduction by crystallisation of fine-grained polyphase reaction products, which deform by grain size sensitive creep. As a result, the mineral reaction causes a change in deformation mechanism from grain size insensitive creep of the anorthite-olivine composite to grain size sensitive creep of the reaction products. The measured reduction of shear stress at a constant strain rate confirms that this transition is the dominant deformation mechanism of the samples.

Effect of ductile shear deformation on the reaction kinetics, mechanisms and microstructures plagioclase-olivine composites

At hydrostatic and water-deficient conditions, the formation of an enstatite-rim around olivine with a sharp enstatite-olivine interface, indicates that the reaction between anorthite and olivine is controlled by the transport of chemical components. Comparison of the growth rates of enstatite and pyroxene-spinel-garnet reaction rims to other kinetic studies, implies that the water-deficient conditions in the studied samples result in slow transport rates of chemical components. The studied reactions display a delayed nucleation of new phases (30 to ∼80 hrs), even at pressure overstepping conditions of ∼700-900 MPa.

Plastic deformation of An-Fo composites enhances the studied mineral reactions at water-deficient conditions. This enhancement is demonstrated by the increase of reaction progress through an increase of the nucleation rate of products and of the growth rates of reaction rims during deformation. The transport-controlled reaction between anorthite and olivine is enhanced by an increase in the nucleation rate of new phases. The increased nucleation rate may be caused by high dislocation densities in the reactant grains that form during the low-temperature plasticity deformation.

The mechanical transport of reaction products by grain boundary sliding may change the local equilibrium conditions. Due to the limited diffusion in the sample, changes in the local equilibrium result in additional mineral reactions and the formation of metastable phases. These reactions contribute to the overall reaction progress.

The amount of pressure overstepping in the experiments affects the reaction progress in the An-Fo composites, because the rate of nucleation increases exponentially with the Gibbs free energy of reaction and therefore with the amount of pressure overstepping for pressure-sensitive reactions.

6.2 Geological applications

The relationships between plastic deformation and mineral reactions in plagioclase-olivine composites have several applications to natural systems. Reactions between olivine and plagioclase occur in high-pressure granulite-facies meta-troctolites and meta-gabbros (e.g. Mongkoltip and Ashworth, 1983; Joesten, 1986; Lang et al., 2004). There probably is no direct correlation to these natural systems because the reaction would tectonically only be realised in subduction zones where the temperatures are much lower at the studied pressure range and other reactions are more likely to take place. However, the reversal of the investigated reaction is often observed in dry natural mylonitic shear zones (Furusho and Kanagawa, 1999; Newman et al., 1999; Handy and Stünitz, 2002), when mantle rocks become unstable during adiabatic decompression into shallower levels in the crust. As solid-solid minerals reactions during deformation, the studied minerals reactions may serve as a general example for such reactions.

The investigated pressure-temperature range is realistic for upper mantle shear zones. Natural deformation takes place at lower strain rates ($\dot{\epsilon}$ ~10^{-14}s^{-1}) and stresses. The grain sizes of the reaction products are likely to be somewhat larger in naturally deformed rocks (e.g. sizes <10 μm, Newman et al., 1999), however grain-size sensitive creep is obtained at larger grain sizes and slower natural strain rates (Fig. 4.2). Deformation of upper mantle rock often takes place by dislocation creep mechanisms as well due to the larger grain size in nature (for example, sizes >200 μm in peridotite proto-mylonites, Newman et al., 1999; Handy and Stünitz, 2002).

There are striking similarities in microstructures and inferred deformation processes between the experimentally deformed plagioclase-olivine composites and plagioclase-bearing ultra-mylonites in the North Pyrenean Zone (Newman et al., 1999; Handy and Stünitz, 2002). These studies on peridotite shear zones proposed that the decompression reactions from garnet and spinel to plagioclase-bearing peridotites caused the localisation of deformation in interconnecting layers and aggregates of fine-grained reaction products. It is inferred that the reaction products deform at a higher strain rate and accommodate deformation by grain size sensitive creep. Therefore, most studies suggest that the metamorphic grain size reduction induces a change in the deformation mechanism from grain size insensitive dislocation creep of the reactants to grain size sensitive diffusion creep of the products.

The plagioclase-olivine experiments indicate that the processes inferred above may occur during concurrent deformation and reaction. The pronounced decrease in flow stress during mineral reaction at water-deficient conditions confirms that the change in deformation mechanism is directly linked to the occurrence of the metamorphic grain size reduction. The fact that the natural reaction is the reverse of the experimentally studied one is of minor consequence of the underlying processes. It is the small size of reaction products that changes the transition in deformation mechanism and not the type of reaction product itself. Despite the fast experimental strain rates, our microstructural results appear to correspond very well to the examples of strain localisation in upper mantle shear zones. Therefore the experiments presented here provide a better understanding of the processes involved in some cases of strain localisation as a consequence of reactions in natural shear zones.

The inhibition of grain growth plays a major role during deformation because a reduced grain size is required to preserve a strain-weakened material after grain size reduction. Significant grain growth of the reaction products would cause the deformation mechanism to change back to grain size insensitive dislocation creep. As a consequence, the stress will increase. In the reacted plagioclase-olivine composites, only limited grain growth of the reaction product phases is observed after high strain (sizes <1.0μm), and there is almost no increase flow stress after the strain weakening. This indicates that grain growth of the reaction products was hindered during deformation. A well-dispersed and polyphase nature of reaction products is crucial to the preservation of a reduced grain-size. Therefore the effects of syndeformational net-transfer reaction under anhydrous conditions are expected to be efficient in suppressing grain growth, even during prograde metamorphic conditions. The preservation of a strain-weakened material is important for stable deformation and therefore the continuation of localised strain.

Greater reaction progress in shear zones is observed frequently in natural systems (e.g. Kerrich et al., 1980; Brodie and Rutter, 1985; Marquer et al., 1985; Keller et al., 2004), which is often attributed to the infiltration of water because a hydrous fluid is an extremely effective catalyst in mineral reaction and mass transport (e.g. Rubie, 1986). However, the enhanced reaction progress during shear deformation of An-Fo composites is obtained at water-absent conditions. Therefore, a significant infiltration of water into ductile shear zones does not seem to be a prerequisite for the localisation of metamorphic reactions in shear zones.

The onset of reaction and shear deformation are simultaneous in plagioclase-olivine experiments in spinel peridotite field. This implies that the development of high reaction progress in shear zones is not necessarily a later event that concentrates in already deformed fine-grained ductile shear zones (e.g. Brodie and Rutter, 1985). Instead there can be an increase in reaction rate due to plastic deformation itself, even in the absence of fluids.

The dislocation creep of the An-Fo composite at a strain rate of $\dot{\gamma}$ ~4x10^{-6}s^{-1} takes place at lower stress conditions (τ= 50 MPa) than at a strain rate of $\dot{\gamma} \sim 5x10^{-5}$s^{-1} (Chapter 5). At lower stress conditions, recovery processes will be able to keep up with the build-up of dislocations, which will lead to smaller dislocation densities in anorthite and olivine grains. As a result, the nucleation rate of new phases during plastic deformation is reduced and the rate of reaction decreases. Because natural rocks are deformed at even lower strain rates and stresses, it is expected that the enhancement of reaction by plastic deformation will occur to a lesser extent in natural deformed rocks. However, grain-scale stress concentrations in minerals deforming by dislocation creep, leading to a local increase of dislocation densities, are likely to occur in coarser grained natural deformed polyphase rocks as well. Thus, the results of this study contribute to the understanding of the processes that are involved in the concentration of metamorphosed rocks during plastic deformation at water-deficient conditions in natural shear zones.

In summary, this study demonstrates the possibility of the localisation of deformation and reaction progress at water-deficient conditions. The fact that such conditions can be reached at dry metamorphic conditions, is important for the occurrence of localisation of deformation in the upper mantle and lower crust (Lemoine et al., 1987; Drury et al., 1991; Vissers et al., 1995, 1997). Basement rocks can be dry for long periods of time under metamorphic conditions, with only short and localised periods of fluid infiltration (Rubie, 1986; Jackson et al., 2004). Also, most rock-forming minerals are solid-solution phases and their stability is likely to change along any given pressure-temperature path during their tectonic history (e.g. Newman et al., 1999; Stünitz and Tullis, 2001). Therefore, the enhancement of reaction by plastic processes at high stress deformation conditions is important for the initiation of reaction in metastable lithologies and consequently for the localisation of deformation over a large pressure-temperature range in the Earth's crust and upper mantle.

6.3 Recommendations for future work

This thesis demonstrates that the study of concurrent plastic deformation and mineral reaction processes is highly interdisciplinary, and many new questions arose from the experiments. This section proposes some recommendations for the extension and improvements of this study.

1. The steady-state flow of chemically stable labradorite-olivine composites is unknown from the data presented here. This work can be improved by experiments that investigate (1) whether steady-state can be achieved in chemically stable plagioclase-olivine composites at either higher temperatures or lower strain rates,

and consequently (2) if the composite strain weakens by dynamic recrystallisation of plagioclase and olivine grains, when recovery processes are not inhibited by interphase boundaries and low-temperature plasticity. The flow stress of chemically stable plagioclase-olivine composites should than be compared to the strength of reaction-weakened plagioclase-olivine composites.

2. The preservation of small grains plays a major role in maintaining a weak material after reaction weakening. This study suggests that the well-dispersed and polyphase nature of reaction products is crucial to the preservation of a reduced grain-size. A future study should quantify the spatial distribution and grain growth of minerals in fine-grained polyphase reaction product aggregates that are produced during shear deformation and at hydrostatic conditions. This would test the preservation of weak material after reaction weakening.

3. Experiments on polymorphic phase transitions (e.g. Vaughan et al., 1984) as well as theoretical studies point out that anisotropic growth of reaction products can occur during non-hydrostatic stress. The direction of growth may be into the direction of the highest mean stress (e.g. Shimizu, 1992; Wheeler, 1992). Such effects are difficult to investigate by simple shear deformation. Coaxial experiments could be performed in order to assess the influence of the mean stress on the development of reaction, because of the constant direction of the principal stresses.

4. The reversal of the reactions studied here is often observed during the exhumation of natural garnet peridotites. So far, there are few experimental data on the deformation behaviour of garnet and spinel or on metastable garnet-spinel-olivine rocks at low pressures. This thesis points out that strong olivine-bearing rocks can be deformed under chemical disequilibrium. Pioneering experiments at high temperature (T >1000°C) and low pressure (P_c <500 MPa) conditions should be performed on garnet-olivine or spinel-olivine composites to test if the present study can be applied to those rock types as well.

5. This thesis points out that plastic deformation enhances reaction progress, probably because dislocations in minerals may contribute to the nucleation of new phases. It is known that dislocations contribute to the stored strain energy of the minerals and raise their Gibbs free energy (e.g. Wintsch and Dunning, 1985; Stünitz, 1998). Although the theory to describe these effects does exist, there are

very few experimental studies that are aimed at accurately determining the contribution of dislocations to the free energy of reaction (Liu et al., 1995). Rock deformation experiments just below or at the actual phase transitions could provide information on how much additional strain energy is required for reaction to nucleate. Such an investigation would require a very good control on the location of the phase transition in pressure and temperature space and well-known thermodynamic and rheological data for the reacting minerals.

6. Further quantification of the relation between strain and mineral fabrics in recrystallised rocks is important. It was demonstrated in Chapter 3 that rock deformation experiments are ideal for studying the relation between strain and recrystallised mineral fabrics in shear zones, because the total amount of the shear displacement is a known parameter. The possibility to deform rocks to very high amounts of strain in laboratory experiments (up to $\gamma \sim 50$ in torsion experiments) is of great advantage. Systematic calibration of grain shapes (fabrics) at varying amounts of strain would provide relations between rocks fabrics and the amount of strain. Such an investigation would enable better quantification of the distribution of strain in natural shear zones, in which the total displacement is often unknown.

7. Chapter 5 describes how reaction rims developed during deformation and at hydrostatic conditions. During deformation at P_c=1630 MPa, kyanite formed as the result of the limited diffusion in the samples and changes in the local equilibrium. The interpretations in this thesis might benefit from an extended quantification and balancing of the observed reactions using the mineral compositions of the reaction products. The mineral compositions of these fine-grained (size <1 μm) minerals could be obtained by calibrating the TEM-EDS micro-analyses with EDS-SEM and Electron Microprobe data. If the balanced reactions are known, it might be possible to study the diffusion of species in the deformed and undeformed anorthite-olivine samples in more detail.

8. The deformation experiments presented in this thesis may serve as an alternative for seeded hydrostatic experiments close to equilibrium. The plagioclase-olivine deformation experiments at P_c=1000 MPa demonstrate that deformation close to equilibrium conditions results in stable equilibrium phase assemblages in short laboratory time-scales, irrespective of the amount and rate of deformation. The syndeformational phase assemblages may be applied to provide feedback to exist-

ing thermodynamic models and petrological phase relationships.

Bibliography

Ashby, M. F., Verrall, R. A., 1973. Diffusion-accommodated flow and superplasticity. Acta Metal. 21 (2), 149–163.

Austrheim, H., 1987. Eclogitization of lower crustal granulites by fluid migration through shear zones. Earth. Planet. Sc. Lett. 81 (2-3), 221–232.

Avrami, M., 1939. Kinetics of phase change. J. Chem. Phys. 7, 1103–1112.

Berman, R. G., 1988. Internally-consistent thermodynamic data for minerals in the system Na_2O-K_2O-CaO-MgO-FeO-Fe_2O_3-Al_2O_3-SiO_2-TiO_2-H_2O-CO_2. J. Petrol. 29 (2), 445–522.

Berthé, D., Choukroune, P., Gapais, D., 1979a. Orientations préférentielles du quartz et orthogneissification progressive en régime cisaillant; l'exemple du cisaillement sud-armoricain. B. Mineral. 102 (2-3), 265–272.

Berthé, D., Choukroune, P., Jegouzo, P., 1979b. Orthogneiss, mylonite and non-coaxial deformation of granites: the example of the South Armorican shear zone. J. Struct. Geol. 1 (1), 31–42.

Boullier, A. M., Gueguen, Y., 1975. SP-mylonites: origin of some mylonites by superplastic flow. Contrib. Mineral. Petr. 50 (2), 93–104.

Boyd, F. R., England, J. L., 1960. Apparatus for phase-equilibrium measurements at pressures up to 50 kilobars and temperatures up to 1750°C. J. Geophys. Res. 65 (2), 741–748.

Brewer, J. A., Matthews, D. H., Warner, M. R., Hall, J., Smythe, D. K., Whittington, R. J., 1983. BIRPS deep seismic reflection studies of the British Caledonides. Nature 305, 206–210.

Brodie, K. H., 1980. Variations in mineral chemistry across a shear zone in phlogopite peridotite. J. Struct. Geol. 2 (1-2), 265–272.

Brodie, K. H., Rutter, E. H., 1985. On the relationship between deformation and metamorphism, with special reference to the behaviour of basic rocks. In: Thompson, A. B., Rubie, D. C. (Eds.), Metamorphic Reactions: Kinetics, Textures and Deformation. Springer-Verlag, New York, pp. 138–179.

Brodie, K. H., Rutter, E. H., 1987. The role of transiently fine-grained reaction products in syntectonic metamorphism: natural and experimental examples. Can. J. Earth Sci. 24, 556–564.

Burg, J. P., Wilson, C. J. L., Mitchell, J. C., 1986. Dynamic recrystallization and fabric development during the simple shear deformation of ice. J. Struct. Geol. 8 (8), 857–870.

Burnley, P. C., Green, H. W., 1989. Stress dependence of the mechanism of the olivine-spinel transformation. Nature 338 (6218), 753–756.

Bystricky, M., Mackwell, S., 2001. Creep of dry clinopyroxene aggregates. J. Geophys. Res. 106 (7), 13443–13454.

Cahn, J. W., 1957. Nucleation on dislocations. Acta Met. 5, 169–172.

Chopra, P. N., Paterson, M. S., 1981. The experimental deformation of dunite. Tectonophysics 78 (1-4), 453–473.

Chopra, P. N., Paterson, M. S., 1984. The role of water in the deformation of dunite. J. Geophys. Res. 89 (9), 7861–7876.

Christian, J. W., 1975. The Theory and Transformation In Metals and Alloys. Pergamon Press, Oxford.

Clark, S. P., 1959. Effect of pressure on the melting point of eight alkali halides. J. Chem. Phys. 31, 1526–1531.

Davidson, C., Rosenberg, C., Schmid, S. M., 1996. Synmagmatic folding of the base of the Bergell pluton, Central Alps. Tectonophysics 265 (3-4), 213–238.

Davis, B. L., Adams, L. H., 1965. Kinetics of the calcite-aragonite transformation. J. Geophys. Res. 70 (2), 433–441.

de Bresser, J. H. P., Ter Heege, J. H., Spiers, C. J., 2001. Grain size reduction by dynamic recrystallization: Can it result in major rheological weakening? Int. J. Earth Sci. 90 (1), 28–45.

de Capitani, C., 1994. Gleichgewichtsphasendiagramme: Theorie und software. Eur. J. Mineral. 6, 48–50.

de Capitani, C., Brown, T. H., 1987. The computation of chemical equilibrium in complex systems containing non-ideal solutions. Geochim. Cosmochim. Ac. 51 (10), 2639–2652.

de Ronde, A. A., Heilbronner, R., Stünitz, H., Tullis, J., 2004. Spatial distribution of deformation and mineral reaction in experimentally deformed plagioclase-olivine aggregates. Tectonophysics 389 (1-2), 93–109.

Dell'Angelo, L. N., Tullis, J., 1996. Textural and mechanical evolution with progressive strain in experimentally deformed aplite. Tectonophysics 256 (1-4), 57–82.

Dimanov, A., Lavie, M. P., Dresen, G., Ingrin, J., Jaoul, O., 2003. Creep of polycrystalline anorthite and diopside. J. Geophys. Res. 108 (1), 2061.

Doukhan, J. C., Christie, J. M., 1982. Plastic deformation of sillimanite Al_2SiO_5 single crystals under confining pressure and TEM investigation of the induced defect structure. B. Mineral. 105 (6), 583–589.

Drury, M. R., Vissers, R. L. M., Van der Wal, D., Hoogerduijn Strating, E. H., 1991. Shear localisation in upper mantle peridotites. Pure App. Geophys. 137 (4), 439–460.

Evans, B., Renner, J., Hirth, G., 2001. A few remarks on the kinetics of static grain growth in rocks. Int. J. Earth Sci. 90 (1), 88–103.

Farver, J. R., Yund, R. A., 1991. Measurement of oxygen grain boundary diffusion in natural, fine-grained, quartz aggregates. Geochim. Cosmochim. Ac. 55 (6), 1597–1607.

Fisher, G. W., 1978. Rate laws in metamorphism. Geochim. Cosmochim. Ac. 42 (7), 1035–1050.

Fitz Gerald, J. D., Stünitz, H., 1993. Deformation of granitoids at low metamorphic grade. 1. Reactions and grain-size reduction. Tectonophysics 221 (3-4), 269–297.

Fuhrman, M. L., Lindsley, D. H., 1988. Ternary-feldspar modelling and thermometry. Am. Mineral. 73, 201–215.

Furusho, M., Kanagawa, K., 1999. Transformation-induced strain localization in a lherzolite mylonite from the Hidaka metamorphic belt of central Hokkaido, Japan. Tectonophysics 313 (4), 411–432.

Gasparik, T., 1984. Two-pyroxene thermobarometry with new experimental data in the system CaO-MgO-Al_2O_3-SiO_2. Contrib. Mineral. Petr. 87 (1), 87–97.

Gay, N. C., 1968. Pure shear and simple shear deformation of inhomogenous viscous fluids. 1. Theory. Tectonophysics 5 (3), 211–234.

Gee, M. L., Healy, T. W., White, L. R., 1990. Hydrophobicity effects in the condensation of water films on quartz. J. Colloid. Interf. Sc. 140, 450–465.

Gleason, G. C., Tullis, J., 1993. Improving flow laws and piezometers for quartz and feldspar aggregates. Geophys. Res. Lett. 20 (19), 2111–2114.

Gleason, G. C., Tullis, J., 1995. A flow law for dislocation creep of quartz aggregates determined with the molten salt cell. Tectonophysics 247 (1-4), 1–23.

Goldsmith, J. R., 1982. Plagioclase stability at elevated temperatures and water pressure. Am. Mineral. 67, 653–675.

Green, D. H., Hibberson, W., 1970. The instability of plagioclase in peridotite at high pressure. Lithos 3, 209–221.

Green, H. W., Borch, R. S., 1989. A new molten salt cell for precision stress measurements at high pressure. Eur. J. Mineral. 1, 213–219.

Green, H. W., Houston, H., 1995. The mechanics of deep earthquakes. Annu. Rev. Earth. Pl. Sc. 23, 169–213.

Griggs, D. T., 1967. Hydrolitic weakening of quartz and other silicates. Geophys. J. R. Astr. Soc. 14, 19–31.

Handy, M. R., 1989. Deformation regimes and the rheological evolution of fault zones in the lithosphere; the effects of pressure, temperature, grainsize and time. Tectonophysics 163 (1-2), 119–152.

Handy, M. R., 1990. The solid-state flow of polymineralic rocks. J. Geophys. Res. 95 (6), 8647–8661.

Handy, M. R., Stünitz, H., 2002. Strain localization by fracturing and reaction weakening - a mechanism for initiating exhumation of subcontinental mantle beneath rifted margins. In: de Meer, S., Drury, M. R., de Besser, J. H. P., Pennock, G. M. (Eds.), Deformation Mechanisms, Rheology and Tectonics: Current Status and Future Perspectives. Vol. 200. Geol. Soc., Spec. Pub., London, pp. 387–407.

Heilbronner, R., 1998. StripStar, public domain program for the calculation of 3-D grain size distributions from histograms of 2-D sections. University of Basel. http://www.unibas.ch/earth/micro/software/index.html.

Heilbronner, R., 2002. Analysis of bulk fabrics and microstructure variations using tesselations of autocorrelation functions. Comp. Geosci. 28, 447–455.

Herzberg, C., Gasparik, T., 1991. Garnet and pyroxenes in the mantle; a test of the majorite fractionation hypothesis. J. Geophys. Res. 96 (10), 16.263–16.274.

Hirth, G., Kohlstedt, D. L., 1995. Experimental constraints on the dynamics of the partially molten upper mantle: Deformation in the diffusion creep regime. J. Geophys. Res. 100 (2), 1981–2001.

Hirth, G., Kohlstedt, D. L., 2003. Rheology of the upper mantle and the mantle wedge: a view from the experimentalists. In: Eiler, J. (Ed.), The Subduction Factory, Geophys. Monogr. Vol. 138. A.G.U., Washington DC, pp. 83–105.

Hobbs, B. E., Muhlhaus, H. B., Ord, A., 1990. Instability, softening and localization of deformation. In: Knipe, R. J., Rutter, E. H. (Eds.), Deformation Mechanisms, Rheology and Tectonics. Vol. 54. Geol. Soc., Spec. Pub., London, pp. 143–166.

Hunziker, P., 2003. The stability of tri-octrahedral Fe^{2+}-Mg-Al chlorite. a combined experimental and theoretical study. Ph.D. thesis, University Basel.

Hutchison, C. S., 1974. Laboratory Handbook of Petrographic Techniques. John Wiley & Sons Inc, New York.

Jackson, I., Paterson, M. S., Fitz Gerald, J. D., 1992. Seismic-wave dispersion and attenuation in Åheim dunite - an experimental study. Geophys. J. Int. 108 (2), 517–534.

Jackson, J. A., Austrheim, H., McKenzie, D., Priestley, K., 2004. Metastability, mechanical strength, and the support of mountain belts. Geology 32 (7), 625–628.

Jenkins, D. M., Newton, R. C., 1979. Experimental determination of the spinel peridotite to garnet peridotite inversion at 900°C and 1000°C in the system CaO-MgO-Al_2O_3-SiO_2, and at 900°C with natural garnet and olivine. Contrib. Mineral. Petr. 68 (4), 407–419.

Jensen, L. N., Starkey, J., 1985. Plagioclase microfabrics in a ductile shear zone from the Jotun Nappe, Norway. J. Struct. Geol. 7 (5), 527–539.

Ji, S., Jiang, Z., Rybacki, E., Wirth, R., Prior, D., Xia, B., 2004. Strain softening and microstructural evolution of anorthite aggregates and quartz-anorthite layered composites deformed in torsion. Earth. Planet. Sc. Lett. 222, 377–390.

Ji, S., Wang, Z., Wirth, R., 2001. Bulk flow strength of forsterite-enstatite composites as a function of forsterite content. Tectonophysics 341 (1-4), 69–93.

Ji, S., Wirth, R., Rybacki, E., Jiang, Z., Prior, D., Wheeler, J., 2000. High temperature deformation of quartz-plagioclase multilayers by layer-normal compression. J. Geophys. Res. 105 (7), 16651–16664.

Ji, S., Zhao, P., 1994. Strength of two-phase rocks: a model based on fiber-loading theory. J. Struct. Geol. 16 (2), 253–262.

Joesten, R., 1978. Diffusion-controlled growth of pyroxene-spinel coronas between forsterite and anorthite in the system CaO-MgO-Al_2O_3-SiO_2. Geol. Soc. Am. Abstr. Program. 10, 429.

Joesten, R., 1986. The role of magmatic reaction, diffusion and annealing in the evolution of coronitic microstructure in troctolitic gabbro from Risör, Norway. Min. Mag. 50, 441–467.

John, B. E., Stuenitz, H., 1997. Evidence for magmatic fracturing and small-scale melt segregation during pluton emplacement. In: Bouchez, J. L., Clemens, J. (Eds.), Processes of Melt Segregation. Kluwer Press, Amsterdam, pp. 55–74.

John, T., Schenk, V., 2003. Partial eclogitisation of gabbroic rocks in a late Precambrian subduction zone (Zambia); prograde metamorphism triggered by fluid infiltration. Contrib. Mineral. Petr. 146 (2), 174–191.

Jordan, P. G., 1987. The deformational behavior of bimineralic limestone halite aggregates. Tectonophysics 135 (1-3), 185–197.

Karato, S., 1989. Grain growth kinetics in olivine aggregates. Tectonophysics 168 (4), 255–273.

Karato, S., Paterson, M. S., Fitz Gerald, J. D., 1986. Rheology of synthetic olivine aggregates: Influence of grain size and water. J. Geophys. Res. 91 (8), 8151–8176.

Keller, L. M., Abart, R., Stuenitz, H., de Capitani, C., 2004. Deformation, mass transfer and mineral reactions in an eclogite facies shear zone in a polymetamorphic metapelite (Monte Rosa Nappe, Western Alps). J. Metamorph. Geol. 22 (2), 97–118.

Kenkmann, T., Dresen, G., 2002. Dislocation microstructure and phase distribution in a lower crustal shear zone - an example from the Ivrea-Zone, Italy. Int. J. Earth Sci. 91 (3), 445–458.

Kerrich, R., Allison, J., Barnett, R. L., Moss, S., Starkey, J., 1980. Microstructural and chemical transformations accompanying deformation of granite in a shear zone at Miéville, Switzerland; with implications for stress corrosion cracking and superplastic flow. Contrib. Mineral. Petr. 73 (3), 221–242.

Kirby, S. H., 1987. Localized polymorphic phase-transformations in high-pressure faults and applications to the physical mechanisms of deep earthquakes. J. Geophys. Res. 92 (13), 789–800.

Kirby, S. H., Stern, L. A., 1993. Experimental dynamic metamorphism of mineral single crystals. J. Struct. Geol. 15 (9-10), 1223–1240.

Klaper, E. M., 1990. Reaction-enhanced formation of eclogite-facies shear zones in granulite-facies anorthosites. In: Knipe, R. J., Rutter, E. H. (Eds.), Deformation Mechanisms, Rheology and Tectonics. Vol. 54. Geol. Soc., Spec. Pub., London, pp. 167–173.

Klemme, S., O'Neill, H. S. C., 2000. The near-solidus transition from garnet lherzolite to spinel lherzolite. Contrib. Mineral. Petr. 138 (3), 237–248.

Koons, P. O., Rubie, D. C., Frueh-Green, G., 1987. The effects of disequilibrium and deformation on the mineralogical evolution of quartz diorite during metamorphism in the eclogite facies. J. Petrol. 28 (4), 679–700.

Kruse, R., Stunitz, H., 1999. Deformation mechanisms and phase distribution in mafic high- temperature mylonites from the Jotun Nappe, southern Norway. Tectonophysics 303 (1-4), 223–249.

Kushiro, I., Yoder, H. S., 1966. Anorthite-forsterite and anorthite-enstatite reactions and their bearing on the basalt-eclogite transformation. J. Petrol. 7 (3), 337–362.

Lang, H. M., Wachter, A. J., Peterson, V. L., Ryan, J. G., 2004. Coexisting clinopyroxene/spinel and amphibole/spinel symplectites in metatroctolites from the Buck Creek ultramafic body, North Carolina Blue Ridge. Am. Mineral. 89, 20–30.

Lasaga, A. C., 1998. Kinetic Theory in the Earth Sciences. Princeton University Press, New Jersey.

Lemoine, M., Tricart, P., Boillot, G., 1987. Ultramafic and gabbroic ocean floor of the Ligurian Tethys (Alps, Corsica, Apennines); in search of a genetic model. Geology 15 (7), 622–625.

Liu, M., Peterson, J. C., Yund, R. A., 1997. Diffusion-controlled growth of albite and pyroxene reaction rims. Contrib. Mineral. Petr. 126 (3), 217–223.

Liu, M., Yund, R. A., Tullis, J., Topor, L., Navrotsky, A., 1995. Energy associated with dislocations: a calorimetric study using synthetic quartz. Phys. Chem. Minerals 22, 67–73.

Mackwell, S. J., Kohlstedt, D. L., 1990. Diffusion of hydrogen in olivine - implications for water in the mantle. J. Geophys. Res. 95 (4), 5079–5088.

Marquer, D., Gapais, D., Capdevila, R., 1985. Comportement chimique et orthogneissification d'une granodiorite en facies schistes verts (Massif de l'Aar, Alpes Centrales). B. Mineral. 108 (2), 209–221.

McLaren, A. C., Pryer, L. L., 2001. Microstructural investigation of the interaction and interdependence of cataclastic and plastic mechanisms in feldspar crystals deformed in the semi-brittle field. Tectonophysics 335 (1-2), 1–15.

Mei, S., Kohlstedt, D. L., 2000. Influence of water on plastic deformation of olivine aggregates 2. dislocation creep regime. J. Geophys. Res. 105 (9), 21.471–21.481.

Meike, A., 1993. A critical review of investigations into transformation plasticity. In: Boland, J. N., Fitz Gerald, J. D. (Eds.), Defects and Processes in the Solid State:

Geoscience Applications (The McLaren Volume). Vol. 14. Elsevier, Amsterdam, pp. 5–25.

Meyre, C., de Capitani, C., Partzsch, J. H., 1997. A ternary solid solution model for omphacite and its application to geothermobarometry of eclogites from the Middle Adula Nappe (Central Alps, Switzerland). J. Metamorph. Geol. 21 (8), 813–829.

Milke, R., Wiedenbeck, M., Heinrich, W., 2001. Grain boundary diffusion of Si, Mg, and O in enstatite reaction rims: a SIMS study using isotopically doped reactants. Contrib. Mineral. Petr. 142 (1), 15–26.

Mitra, G., 1978. Ductile deformation zones and mylonites: the mechanical processes involved in the deformation of crystalline basement rocks. Am. J. Sci. 278, 1057–1084.

Mongkoltip, P., Ashworth, J. R., 1983. Quantitative estimation of an open-system symplectite-forming reaction: restricted diffusion of Al and Si in coronas around olivine. J. Petrol. 24 (4), 635–661.

Murrell, S. A. F., Ismail, I. A. H., 1976. The effect of the decomposition of hydrous minerals on the mechanical properties of rocks at high pressures and temperatures. Tectonophysics 31 (3-4), 207–235.

Newman, J., Lamb, W. M., Drury, M. R., Vissers, R. L. M., 1999. Deformation processes in a peridotite shear zone: reaction-softening by an H_2O-deficient, continuous net transfer reaction. Tectonophysics 303 (1-4), 193–222.

Olgaard, D. L., 1990. The role of second phase in localizing deformation. In: Knipe, R. J., Rutter, E. H. (Eds.), Deformation Mechanisms, Rheology and Tectonics. Vol. 54. Geol. Soc., Spec. Pub., London, pp. 175–181.

Olgaard, D. L., Evans, B., 1988. Grain growth in synthetic marbles with added mica and water. Contrib. Mineral. Petr. 100 (2), 246–260.

Olgaard, D. L., Ko, S. C., Wong, T. F., 1995. Deformation and pore pressure in dehydrating gypsum under transiently drained conditions. Tectonophysics 245 (3-4), 237–248.

O'Neill, H. S. C., 1981. The transition between spinel lherzolite and garnet lherzolite, and its use as a barometer. Contrib. Mineral. Petr. 77 (2), 185–194.

Panozzo Heilbronner, R., 1992. The autocorrelation function: an image processing tool for fabric analysis. Tectonophysics 212 (3-4), 351–370.

Panozzo Heilbronner, R., 1993. Controlling the spatial distribution of deformation in experimentally deformed and dehydrated gypsum. In: Boland, J. N., Fitz Gerald, J. D. (Eds.), Defects and Processes in the Solid State: Geoscience Applications (The McLaren Volume). Vol. 14. Elsevier, pp. 169–194.

Paterson, M. S., 1989. The interaction of water with quartz and its influence in dislocation flow - an overview. In: Karato, S. I., Toriumi, M. (Eds.), Rheology of Solids and the Earth. Oxford Univ. Press, New York, pp. 107–142.

Pfleiderer, S., Ball, D. G. A., Bailey, R. C., 1993. AUTO: a computer program for the determination of the two-dimensional autocorrelation function of digital images. Comp. Geosci. 19 (6), 825–829.

Poirier, J. P., 1980. Shear localization and shear instability in materials in the ductile field. J. Struct. Geol. 2 (1-2), 135–142.

Poirier, J. P., 1985. Creep of Crystals: High-temperature Deformation Processes in Metals, Ceramics and Minerals. Cambridge University Press, Cambridge.

Post, A., Tullis, J., 1998. The rate of water penetration in experimentally deformed quartzite, implications for hydrolytic weakening. Tectonophysics 295 (1-2), 117–137.

Post, A., Tullis, J., 1999. A recrystallized grain size piezometer for experimentally deformed feldspar aggregates. Tectonophysics 303 (1-4), 159–173.

Raleigh, C. B., Paterson, M. S., 1965. Experimental deformation of serpentinite and its tectonic implications. J. Geophys. Res. 70 (16), 3965–3985.

Ramsay, J. G., Graham, R. H., 1970. Strain variation in shear belts. Can. J. Earth Sci. 7, 786–813.

Ramsay, J. G., Huber, M. I., 1983. The Techniques of Modern Structural Geology, Strain Analysis. Vol. 1. Academic Press, London.

Rubie, D. C., 1983. Reaction-enhanced ductility: the role of solid-solid univariant reaction in deformation of the crust and mantle. Tectonophysics 96 (3-4), 331–352.

Rubie, D. C., 1986. The catalysis of mineral reactions by water and restrictions on the presence of aqueous fluid during metamorphism. Min. Mag. 50, 399–415.

Rubie, D. C., 1990a. Mechanisms of reaction-enhanced deformability in minerals and rocks. In: Barber, D. J., Meredith, P. G. (Eds.), Deformation Processes in Minerals, Ceramics and Rocks. Unwin Hyman, London, pp. 262–295.

Rubie, D. C., 1990b. Role of kinetics in the formation and preservation of eclogites. In: Carswell, D. A. (Ed.), Eclogite Facies Rocks. Blackie, Glasgow, pp. 111–140.

Rubie, D. C., 1998. Disequilibrium during metamorphism: the role of nucleation kinetics. In: Treloar, P. J., O'Brien, P. J. (Eds.), What Drives Metamorphism and Metamorphic Reactions. Vol. 138. Geol. Soc., Spec. Pub., London, pp. 199–214.

Rubie, D. C., Thompson, A. B., 1985. Kinetics of metamorphic reactions at elevated temperatures and pressures: An appraisal of available experimental data. In: Thompson, A. B., Rubie, D. C. (Eds.), Metamorphic Reactions: Kinetics, Textures and Deformation. Springer-Verlag, New York, pp. 27–79.

Rutter, E. H., Brodie, K. H., 1988a. Experimental "syntectonic" dehydration of serpentinite under conditions of controlled pore water pressure. J. Geophys. Res. 93 (5), 4907–4932.

Rutter, E. H., Brodie, K. H., 1988b. The role of tectonic grain size reduction in the rheological stratification of the lithosphere. Geol. Rundsch. 77, 295–308.

Rutter, E. H., Brodie, K. H., 1995. Mechanistic interactions between deformation and metamorphism. Geol. J. 30, 227–240.

Rutter, E. H., Peach, C. J., White, S. H., Johnston, D., 1985. Experimental 'syntectonic' hydration of basalt. J. Struct. Geol. 7 (2), 251–266.

Rybacki, E., Dresen, G., 2000. Dislocation and diffusion creep of synthetic anorthite aggregates. J. Geophys. Res. 105 (11), 26017–26036.

Rybacki, E., Dresen, G., 2004. Deformation mechanism maps for feldspar rocks. Tectonophysics 382 (3-4), 173–187.

Schmidt, C., Bruhn, D., Wirth, R., 2003. Experimental evidence of transformation plasticity in silicates: minimum of creep strength in quartz. Earth. Planet. Sc. Lett. 205, 273–280.

Shimizu, I., 1992. Nonhydrostatic and nonequilibrium thermodynamics of deformable materials. J. Geophys. Res. 97 (4), 4587–4597.

Simpson, C., Wintsch, R. P., 1989. Evidence for deformation-induced K-feldspar replacement by myrmekite. J. Metamorph. Geol. 7 (2), 261–275.

Snow, E., Yund, R. A., 1987. The effect of ductile deformation on the kinetics and mechanisms of the aragonite-calcite transformation. J. Metamorph. Geol. 5 (2), 141–153.

Spry, A., 1969. Metamorphic Textures. Pergamon Press, Oxford.

Steffen, K., Selverstone, J., Brearley, A., 2001. Episodic weakening and strengthening during synmetamorphic deformation in a deep-crustal shear zone in the Alps. In: Holdsworth, R., Strachan, R., Magloughlin, J., Knipe, R. (Eds.), The Nature and Tectonic Significance of Fault Zone Weakening. Vol. 186. Geol. Soc. Spec. Publ., London, pp. 141–156.

Stünitz, H., 1998. Syndeformational recrystallisation: dynamic or compositionally induced? Contrib. Mineral. Petr. 131 (2-3), 219–236.

Stünitz, H., Fitz Gerald, J. D., 1993. Deformation of granitoids at low metamorphic grade. 2. Granular flow in albite-rich mylonites. Tectonophysics 221 (3-4), 299–324.

Stünitz, H., Fitz Gerald, J. D., Tullis, J., 2003. Dislocation generation, slip systems, and dynamic recrystallization in experimentally deformed plagioclase single crystals. Tectonophysics 372 (3-4), 215–233.

Stünitz, H., Tullis, J., 2001. Weakening and strain localization produced by syndeformational reaction of plagioclase. Int. J. Earth Sci. 90 (1), 136–148.

Teall, J. J. H., 1885. The metamorphosis of dolerite into hornblende-schist. Quart. J. Geol. Soc. London 41, 133–145.

Tsurumi, J., Hosonuma, H., Kanagawa, K., 2003. Strain localization due to a positive feedback of deformation and myrmekite-forming reaction in granite and aplite mylonites along the Hatagawa Shear Zone of NE Japan. J. Struct. Geol. 25 (4), 557–574.

Tullis, J., Yund, R. A., 1982. Grain growth of quartz and calcite aggregates. J. Geol. 90, 301–318.

Tullis, J., Yund, R. A., 1985. Dynamic recrystallization of feldspar: a mechanism for ductile shear zone formation. Geology 13, 238–241.

Tullis, J., Yund, R. A., 1999. Shear deformation of plagioclase aggregates; effects of composition and water. Eos. Trans. A.G.U. 80 (40), 1054.

Tullis, T. E., Horowitz, F. G., Tullis, J., 1991. Flow laws of polyphase aggregates from end-member flow laws. J. Geophys. Res. 96 (5), 8081–8096.

Tullis, T. E., Tullis, J., 1986. Experimental rock deformation techniques. In: Hobbs, B. E., Heard, H. C. (Eds.), Mineral and Rock Deformation Laboratory Studies, The Paterson Volume. Vol. 36. A.G.U. Geophys. Mon., pp. 297–324.

Underwood, E. E., 1970. Quantitative Stereology. Addison-Wesley Publishing Company, Reading, Mass.

van der Wal, D., Chopra, P. N., Drury, M. R., Fitz Gerald, J. D., 1993. Relationships between dynamically recrystallised grain size and deformation conditions in experimentally deformed olivine rocks. Geophys. Res. Lett. 20 (14), 1479–1482.

Vaughan, P. J., Green, H. W., Coe, R. S., 1984. Anisotropic growth in the olivine-spinel transformation of Mg_2GeO_4 under nonhydrostatic stress. Tectonophysics 108 (3-4), 299–322.

Vernon, R. H., 1977. Relationships between microstructures and metamorphic assemblages. Tectonophysics 39 (1-3), 439–452.

Vissers, R. L. M., Drury, M. R., Hoogerduijn Strating, E. H., Spiers, C. J., van der Wal, D., 1995. Mantle shear zones and their effect on lithosphere strength during continental breakup. Tectonophysics 249 (3-4), 155–171.

Vissers, R. L. M., Drury, M. R., Hoogerduijn Strating, E. H., van der Wal, D., 1991. Shear zones in the upper mantle; a case study in an Alpine lherzolite massif. Geology 19 (10), 990–993.

Vissers, R. L. M., Drury, M. R., Newman, J., Fliervoet, T. F., 1997. Mylonitic deformation in upper mantle peridotites of the North Pyrenean Zone (France): implications for strength and strain localization in the lithosphere. Tectonophysics 279 (1-4), 303–325.

Wheeler, J., 1987. The significance of grain-scale stresses in the kinetics of metamorphism. Contrib. Mineral. Petr. 97 (3), 397–404.

Wheeler, J., 1992. Importance of pressure solution and Coble creep in the deformation of polymineralic rocks. J. Geophys. Res. 97 (4), 4579–4586.

White, S. H., 1979. Grain and sub-grain size variations across a mylonite zone. Contrib. Mineral. Petr. 70 (2), 193–202.

White, S. H., Burrows, S. E., Carreras, J., Shaw, N. D., Humphreys, F. J., 1980. On mylonites in ductile shear zones. J. Struct. Geol. 2 (1-2), 175–187.

White, S. H., Knipe, R. J., 1978. Transformation- and reaction enhanced ductility in rocks. J. Geol. Soc. London 135, 513–516.

Wintsch, R. P., 1975. Feldspathization as a result of deformation. Geol. Soc. Am. Bul. 86 (1), 35–38.

Wintsch, R. P., 1985. The possible effects of deformation on chemical processes in metamorphic fault zones. In: Thompson, A. B., Rubie, D. C. (Eds.), Metamorphic Reactions: Kinetics, Textures and Deformation. Springer-Verlag, New York, pp. 251–268.

Wintsch, R. P., Dunning, J., 1985. The effect of dislocation density on the aqueous solubility of quartz and some geologic implications: a theoretical approach. J. Geophys. Res. 90 (5), 3649–3657.

Yund, R. A., 1997. Rates of grain boundary diffusion through enstatite and forsterite reaction rims. Contrib. Mineral. Petr. 126 (3), 224–236.

Yund, R. A., Quigley, J., Tullis, J., 1989. The effect of dislocations on bulk diffusion in feldspars during metamorphism. J. Metamorph. Geol. 7 (3), 337–341.

Yund, R. A., Tullis, J., 1980. The effect of water, pressure, and strain on Al/Si order-disorder kinetics in feldspar. Contrib. Mineral. Petr. 72 (3), 297–302.

Yund, R. A., Tullis, J., 1991. Compositional changes of minerals associated with dynamic recrystallisation. Contrib. Mineral. Petr. 108 (3), 346–355.

Zwart, H. J., 1963. Some examples of the relations between deformation and metamorphism from the central Pyrenees. Geol. Mijnbouw 42 (5), 143–154.

Appendix A

List of experiments

This Appendix summarises the details of the experiments. All experiments were performed at 900°C. Symbols and abbreviations:

Title	Subtitle	Explanation
Experiment	Location	Brown University (BR), Basel University (BSL), Apparatus (Rig)
Sample	Type	An = Anorthite (An_{92}), Lab = Labradorite (An_{60})
		Fo = Forsterite (Fo_{93}), BG = Balsam Gap dunite
	GZ, M	Powder grain size range (μm), Weight (mg) sample powder
	Th	Thickness sample (mm), measured after experiment
Forcing blocks	Type	AH = Aheim dunite, BG = Balsam Gap dunite
		Q = quartz single crystal, SC = San Carlos single crystal
	A(°)	Angle of the sample to the compression direction
	S	Forcing block surface: with grooves (gr), plain (pl)
Drying		Drying at atmospheric pressure: all = dried pistons and powder
		FB = forcing block only + 'as-is' powder (>72 hrs, oven dried 110°C)
Cell		Sample assemblies: 'molten salt' (MS) or 'all salt' (AS)
		CrAl: used chromel-aluminium thermocouple instead of Pt-PtRh
Deformation	HP(h)	Duration at run conditions before the sample hit point.
Reaction		Indication of amount mineral reaction: ++ (significant), + (partial),
		± (little), - (sporadic nuclei), (≠) none, amp (nucleation of amphibole)
Strain trend		Indication of mechanical trend, strain hardening and weakening
Comments		Failed experiments (†), HP = hot pressing, Def = deformation
		TC = thermocouple, FB = forcing block

Table A.1: Hydrostatic experiments.

Experiment		Sample	GZ	M	Th	Forcing block			Jacket	CO-CO$_2$ Drying			Cell
No.	Location	Type	(µm)	(mg)	(mm)	Type	A(°)	S		T(°C)	t(h)		
W975	BR,R2	An-Fo	2-6	77.0	0.552	BG	45	gr	Ni-Ni	1000	6	all	AS
W1015	BR,R3	An-Fo	4-10	75.0	0.528	AH	45	gr	Ni-Ni	1000	12	all	AS
W1026	BR,R2	An-Fo	4-10	77.0	0.426	AH	45	gr	Ni-Pt	1000	12	all	MS
W1039	BR,R2	An-Fo	4-10	78.0	n.a.	AH	45	gr	Ni-Pt	1000	13	all	MS
W1045	BR,R2	An-Fo	2-6	77.0	0.491	BG	45	gr	Ni-Ni	1000	6	all	AS
W1046	BR,R2	An-Fo	4-10	75.0	0.492	AH	45	gr	Ni-Pt-Ni	1000	12	all	MS
W1047	BR,R3	An-Fo	4-10	77.0	n.a.	AH	45	gr	Ni-Pt-Ni	1000	12	all	MS
3AA	BSL,R1	An-Fo	4-10	78.0	0.759	BG	90	pl	Ni-Pt	1000	24	all	AS
5AA	BSL,R1	An-Fo	4-10	77.9	0.722	BG	90	pl	Ni-Pt	1000	24	all	AS
7AA	BSL,R1	An-Fo	4-10	77.5	n.a.	AH	45	gr	Ni-Pt-Ni	1000	24	all	AS
13AA	BSL,R1	An-Fo	4-10	78.0	0.722	BG	90	pl	Ni-Pt	1000	24	FB	AS
16AA	BSL,R1	An-Fo	4-10	78.0	0.473	BG	45	pl	Ni-Pt-Ni	1000	24	FB	AS
18AA	BSL,R1	An-Fo	4-10	78.0	n.a.	BG	45	pl	Ni-Pt-Ni	1000	24	FB	AS
24AA	BSL,R1	An-Fo	4-10	76.0	n.a.	BG	90	pl	Ni-Pt-Ni	1000	24	all	AS
26AA	BSL,R1	An-Fo	4-10	76.0	n.a.	BG	90	pl	Ni-Pt-Ni	1000	24	all	AS
34AA	BSL,R1	An-Fo	4-10	77.8	0.469	BG	45	pl	Ni-Pt-Ni	980	24	FB	AS
36AA	BSL,R1	An-Fo	4-10	77.9	0.497	BG	45	pl	Ni-Pt-Ni	980	24	FB	AS
44AA	BSL,R1	An-Fo	4-10	77.8	0.485	BG	45	pl	Ni-Pt-Ni	980	24	FB	AS
47AA	BSL,R1	An-Fo	4-10	77.7	0.553	BG	45	pl	Ni-Pt-Ni	980	24	FB	AS
49AA	BSL,R1	An-Fo	4-10	77.8	0.475	BG	45	pl	Ni-Pt-Ni	980	24	FB	AS
W1042	BR,R3	Lab-Fo	4-10	77.0	n.a.	AH	45	gr	Ni-Pt	1000	13	all	MS
40AA	BSL,R1	Lab-Fo	4-10	77.4	0.514	BG	45	pl	Ni-Pt-Ni	980	24	FB	AS
20AA	BSL,R1	BG	>10			coaxial			Ni-Pt-Ni	1000	24	all	AS-CrAl
21AA	BSL,R1	BG	>10			coaxial			Ni-Pt-Ni	1000	24	all	AS-CrAl
22AA	BSL,R1	BG	>10			coaxial			Ni-Pt-Ni	1000	24	all	AS

Table A.1: Hydrostatic experiments, continued.

	Hot pressing			Hydrostatic		Reaction	Comments
No.	t(h)	T(°C)	Pc (MPa)	t(h)	Pc (MPa)		
W975	1	900	800			≠	† HP: TC
W1015	24	900	600			≠	
W1026	24	1050±7	750			≠	
W1039						≠	† 700°C: TC-elbow
W1045	24	900	790	30.0	1490	≠	
W1046	24	1050±3	760	19.0	1000	≠	
W1047	24	1050±2	790			≠	† post-HP: TC-sleeves
3AA	48	900	740±20			≠	
5AA	24	1000	775±15			≠	
7AA	24	1000	790			≠	† post-HP, TC-inner NaCl- sleeves
13AA	24	950	730			≠	
16AA	24	1000	765			≠	
18AA	24	1000	789			≠	† post-HP: TC-sleeves
24AA	3	975	805			≠	† HP: no water flow
26AA	8	1000±25	730			≠	† HP: TC-sleeves
34AA	48	950	750	167.5	1510	+/++	unstable: 980±20°C
36AA	48	970±1	790	168.0	1030	±	
44AA	48	965	750			≠	unstable: 980°C
47AA	48	975	740	73.3	1060	-	
49AA	48	975	760	59.0	1510	+	
W1042	2	1050	810			≠	† HP: TC-sleeves
40AA	48	975±1	760	12.0	1610	≠	† Def: TC-Cu disk
20AA	3	1000	778				† HP: no water flow
21AA	7	1000±2	806				† HP: TC-tubing
22AA							† 900°C: TC-Cu disk

Table A.2: Deformation experiments.

Experiment		Sample	GZ	M	Th	Forcing block			Jacket	CO-CO$_2$ Drying			Cell	Hot pressing		
No.	Location	Type	(µm)	(mg)	(mm)	Type	A(°)	S		T(°C)	t(h)			t(h)	T(°C)	P$_c$(MPa)
W976	BR,R3	An-Fo	2-6	77.0	0.437	BG	45	gr	Ni-Ni	1000	6	all	AS	24	900	775
W978	BR,R3	An-Fo	2-6	78.0	0.415	BG	45	gr	Ni-Ni	1000	6	all	AS	24	900	825
W1028	BR,R3	An-Fo	4-10	77.8	0.455	AH	45	gr	Ni-Pt	1000	13	all	MS	24	1050±2	780
W1040	BR,R2	An-Fo	4-10	77.0	0.478	AH	45	gr	Ni-Pt	1000	13	all	MS	24	1050±5	750
W1041	BR,R3	An-Fo	4-10	77.0	0.351	AH	45	gr	Ni-Pt	1000	12	all	MS	24	1050±3	770
W1043	BR,R1	An-Fo	4-10	77.0	0.383	AH	45	gr	Ni-Pt	1000	12	all	MS	25	1050±5	760
17AA	BSL,R1	An-Fo	4-10	78.0	0.420	SC	45	gr	Ni-Pt-Ni				AS	24	1000	771
19AA	BSL,R1	An-Fo	4-10	77.8	0.459	BG	45	pl	Ni-Pt-Ni	1000	24	FB	AS	24	1000±1	830
25AA	BSL,R1	An-Fo	4-10	77.7	0.466	BG	45	pl	Ni-Pt-Ni	1000	24	FB	AS	24	1000±3	840
28AA	BSL,R1	An-Fo	4-10	77.9	0.479	BG	45	pl	Ni-Pt-Ni	1000	24	FB	AS	48	980	860
32AA	BSL,R1	An-Fo	4-10	77.8	0.520	BG	45	pl	Ni-Pt-Ni	980	24	FB	AS	48	980	760
33AA	BSL,R1	An-Fo	4-10	78.0	0.464	BG	45	pl	Ni-Pt-Ni	980	24	FB	AS	48	980	810
52AA	BSL,R1	An-Fo	4-10	77.8	0.498	BG	45	pl	Ni-Pt-Ni	980	24	FB	AS	48	965	730
55AA	BSL,R1	An-Fo	4-10	77.9	0.467	BG	45	pl	Ni-Pt-Ni	980	24	FB	AS	48	965	750
W983	BR,R3	Lab-Fo	2-6	77.0	0.429	BG	45	gr	Ni-Ni	1000	6	all	AS	24	900	800
W986	BR,R3	Lab-Fo	2-6	77.0	0.444	BG	45	gr	Ni-Ni	1000	6	all	AS	24	900	800
W991	BR,R3	Lab-Fo	2-6	77.0	0.479	BG	45	gr	Ni-Ni	1000	6	all	AS	24	900	790
W1044	BR,R1	Lab-Fo	4-10	77.0	0.437	AH	45	gr	Ni-Pt-Ni	1000	12	all	MS	24	1050±1	790
42AA	BSL,R1	Lab-Fo	4-10	77.2	0.452	BG	45	pl	Ni-Pt-Ni	980	24	FB	AS	48	975	775
W980	BR,R3	An	2-6	71.0	0.383	Q	45	gr	Ni-Ni	1000	6	all air	AS	24	900	790
W987	BR,R3	Lab	2-6	77.2	0.435	Q	45	gr	Ni-Ni	1000	6	all air	AS	24	900	800
43AA	BSL,R1	Lab	4-10	70.0	0.505	BG	45	pl	Ni-Pt-Ni	980	24	FB	AS	48	970±5	780
W989	BR,R3	Fo	2-6	85.4	0.450	BG	45	gr	Ni-Ni	1000	6	all	AS	24	900	800
W1027	BR,R3	Fo	4-10	85.0	0.509	AH	45	gr	Ni-Pt	1000	14	all	MS	24	1050±5	770
50AA	BSL,R1	Fo	4-10	85.2	0.498	BG	45	pl	Ni-Pt-Ni	980	24	FB	AS	27	960±2	740

Table A.2: Deformation experiments, continued.

No.	Deformation P$_c$ (MPa)	HP(h)	Strain rate $\dot{\gamma}\cdot 10^{-5}$s^{-1}	Max stress τ (MPa)	Max strain γ	Reaction	Strain trend	Comments
W976	950	12.5	5.4	196	4.9	+	weakening	
W978	1500	30.5	5.3	349	4.0	+/++	weakening	some asymmetric shearing
W1028	990	12.5	4.9	397	4.1	-/±	hardening	† peak stress
W1040	1460	23.3	3.9	820	3.0	-	hardening	extensive twins in FB-olivine
W1041	1030	19.5	6.3	282	6.8	+	weakening	some oblique shearing
W1043	1260	15.6	6.0	97	5.8	++	weak	
17AA	1435	35.3	4.6	359	4.5	++	weakening	FB cracked before peak stress
19AA	1160	37.0	4.7	321	5.9	+	weakening	
25AA	1350	17.5	7.8	336	5.2	+/++	weakening	σ3 piston cracked
28AA	1630	26.8	4.0	282	4.9	++	weakening	gears disrupted, unstable: 1000±20°C
32AA	1460	22.8	3.8	283	2.2	+	hardening	
33AA	1030	22.2	4.3	382	5.8	++	weakening	+ 104 hrs hydrostatically at 1030 MPa
52AA	1480	33.5	3.9	348	2.5	+/++	hardening	+ 343 hrs hydrostatically at 1470 MPa
55AA	1040	49.5	0.4	72	1.7	+	weakening	
W983	960	14.5	3.8	439	1.7	≠	hardening	TC 90° off, † during Def. but restarted
W986	1480	18.2	3.7	449	1.6	≠	hardening	
W991	1480	17.0	4.5	696	4.7	≠	hardening	
W1044	1460	27.7	5.1	478	5.3	≠	hardening	FB buckled
42AA	1470	33.0	4.1	786	5.9	≠	hardening	crack FB
W980	980	12.2	5.8	179	5.0	amp	weakening	
W987	990	11.0	5.5	141	4.6	amp	weakening	
43AA	1020	33.0	4.2	96	8.6	amp	weak	
W989	975	11.7	5.0	307	4.0		hardening	
W1027	1000	8.5	4.5	477	4.0		hardening	oblique shearing, FB buckled
50AA	1510	52.6	4.0	349	4.7		hardening	ZrO$_2$-piston cracked

Appendix B

Mechanical data

This Appendix summarises the mechanical data of the general shear deformation experiments in terms of axial load (N) versus axial displacement (mm) and shear stress τ (MPa) versus shear strain γ. First the data are given for pure anorthite (An = An_{92}), labradorite (Lab = An_{60}) and forsterite (Fo = Fo_{93}) samples, followed by the data for the Lab-Fo and An-Fo composites. Details of all the experimental runs are given in Table A.2.

The shear stress and shear strain data were calculated using the program RigS (Version 2.0). The source code of this program as well as an example input and output file are given at the end of this Appendix. All data were corrected for apparatus distortion: Brown experiments by $8.42*10^{-6}$ mmN^{-1} ($1.05*10^{-3}$ inch kb^{-1}, determined by T. Tullis in 1976) and Basel experiments by $3.316*10^{-6}$ mmN^{-1} (determined by H. Stünitz in 2004). All shear stress and shear strain data include a friction correction of 922.65 Nmm^{-1} (determined by R.A. Yund at Brown University, in experiment W997 for a 10^{-6} gear train) and a thinning correction. The initial plagioclase-olivine composite thickness used in the thinning correction is an average thickness of hydrostatic samples. Basel experiments: 0.506 mm (samples 16AA, 36AA, 44AA, 47AA and 32AA). Brown experiments: 0.491 mm (samples W1045 and W1046).

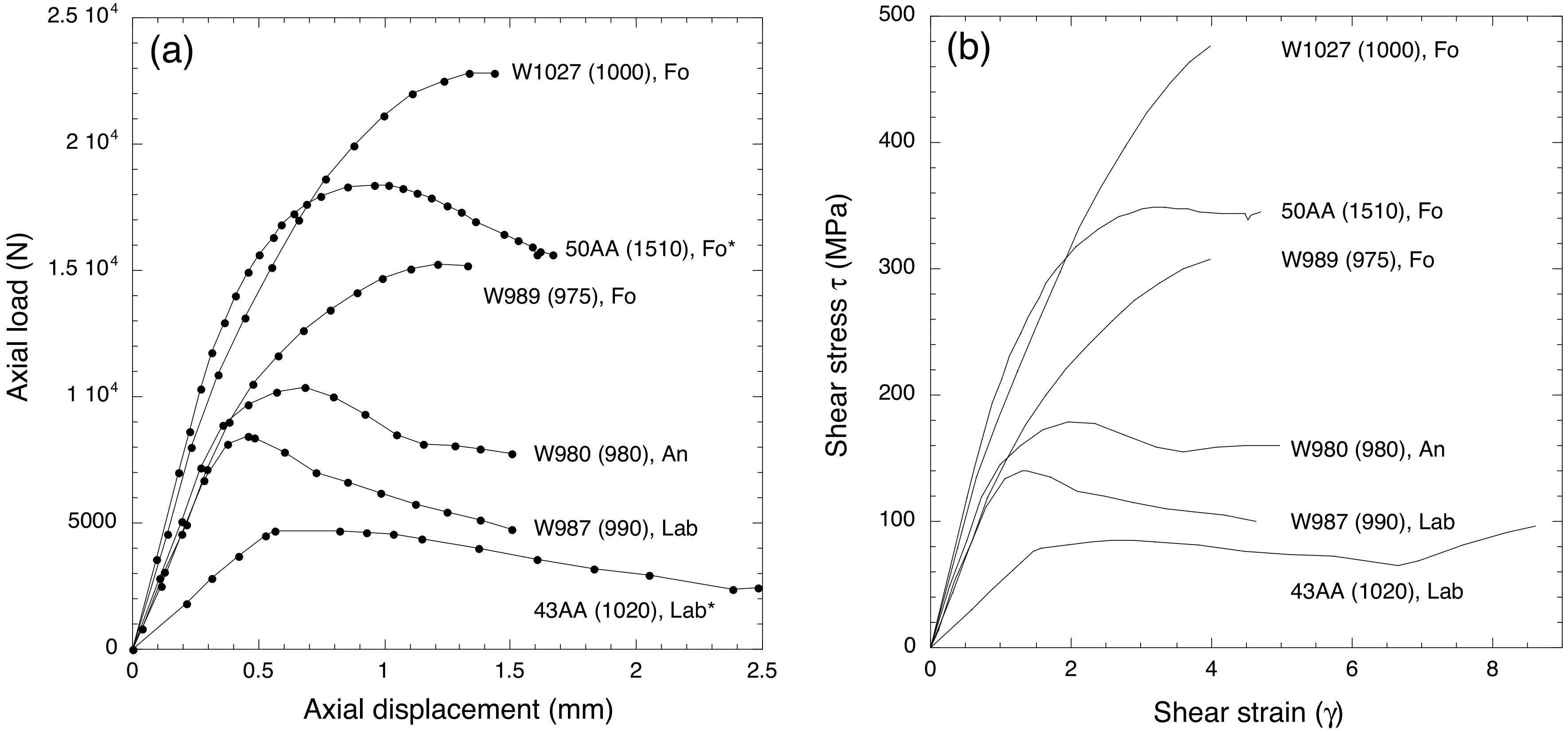

Figure B.1: Mechanical data for shear deformation experiments on pure anorthite (An), labradorite (Lab) and forsterite (Fo) samples at 900°C. The run number and confining pressure (MPa in brackets) of the experiment is indicated for each curve. 'As-is' samples are indicated with an asterisk (*). Strength of the samples as a function of (a) axial load (N) and axial displacement (mm) and (b) shear stress (MPa) and shear strain (γ). The late apparent strain hardening of experiment 43AA may be due to an increase in strain rate when a thinned sample is deformed at a constant shear displacement.

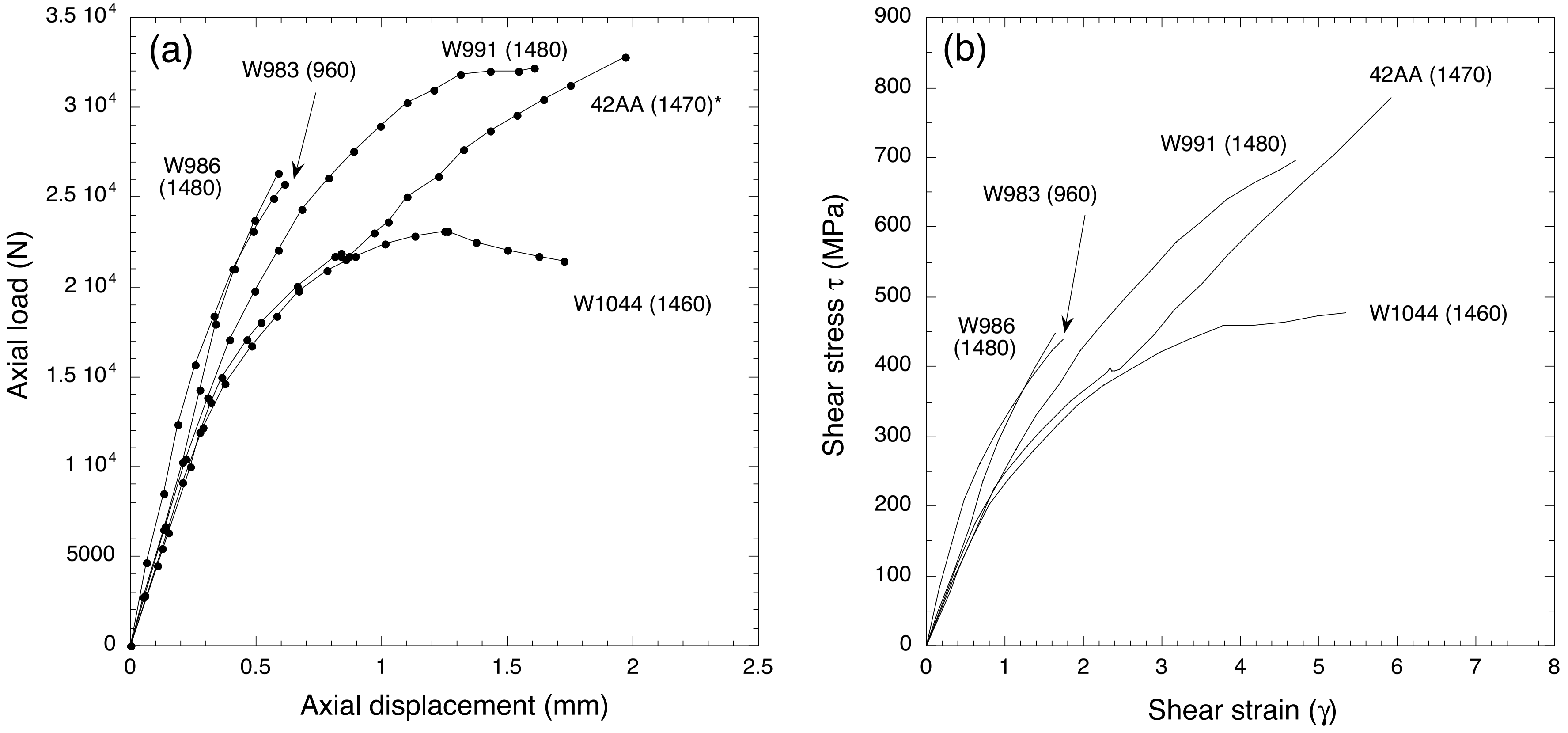

Figure B.2: Mechanical data of shear deformation experiments on labradorite-forsterite composites at 900°C. The run number and confining pressure (MPa in brackets) of the experiment is indicated for each curve. ‘As-is’ samples are indicated with an asterisk (*). Strength of the samples as a function of (a) axial load (N) and axial displacement (mm) and (b) shear stress (MPa) and shear strain (γ).

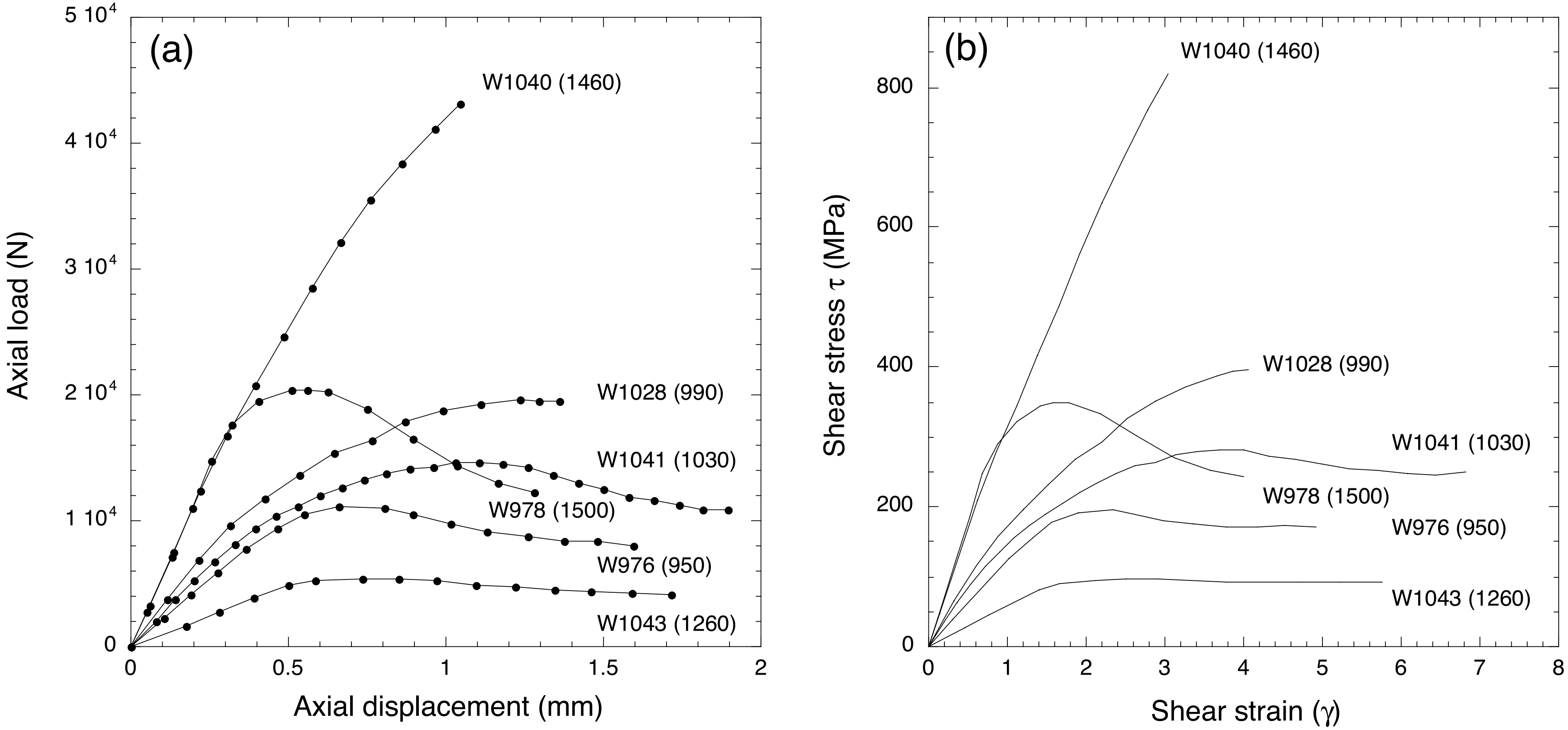

Figure B.3: Mechanical data of shear deformation experiments on dried anorthite-forsterite composites at 900°C. The run number and confining pressure (MPa in brackets) of the experiment is indicated for each curve. Strength of the samples as a function of (a) axial load (N) and axial displacement (mm) and (b) shear stress (MPa) and shear strain (γ). The late apparent strain hardening of experiment W1041 may be due to an increase in strain rate when a thinned sample is deformed at a constant shear displacement.

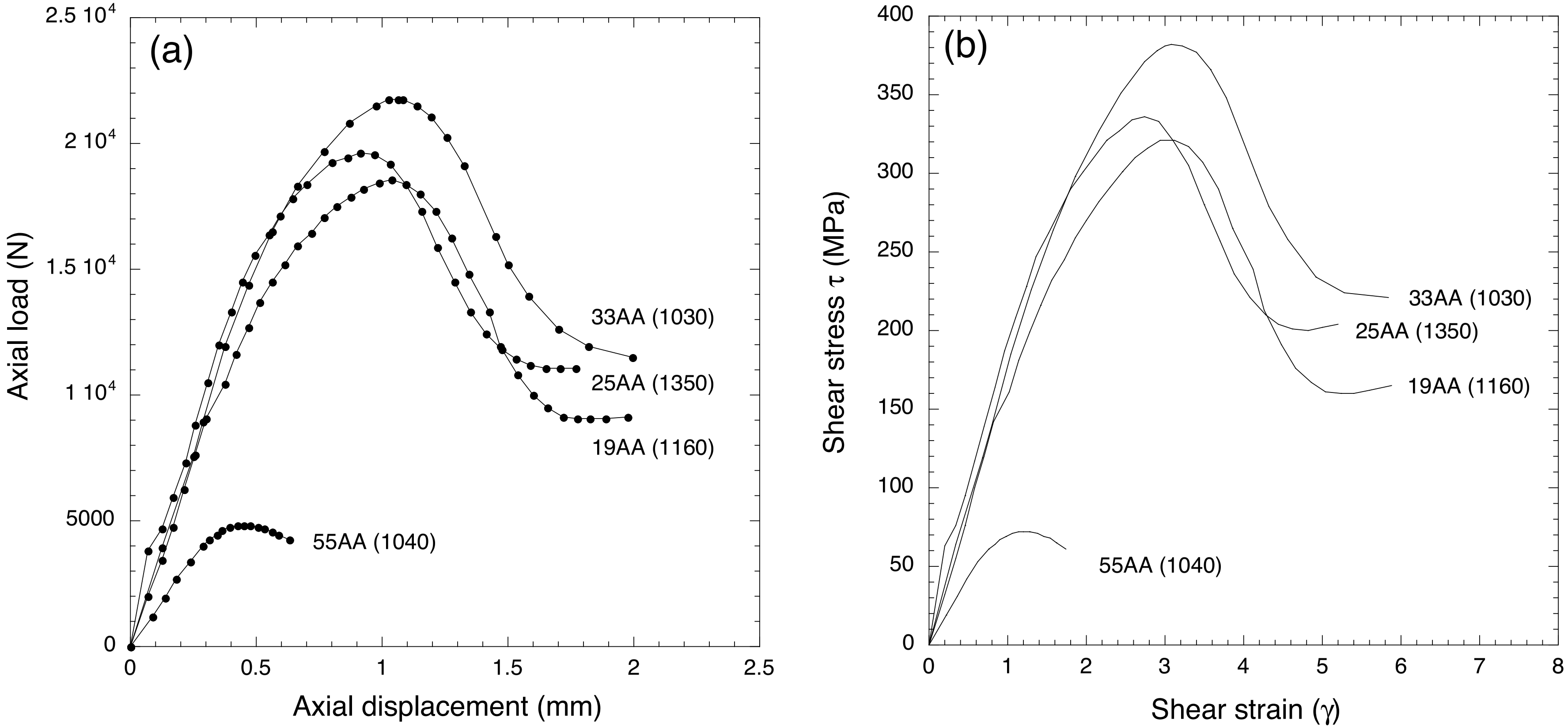

Figure B.4: Mechanical data of shear deformation experiments on ‘as-is’ anorthite-forsterite composites at 900°C and confining pressures of P_c=1030 to 1350 MPa. The run number and confining pressure (MPa in brackets) of the experiment is indicated for each curve. Strength of the samples as a function of (a) axial load (N) and axial displacement (mm) and (b) shear stress (MPa) and shear strain (γ). The late apparent strain hardening of experiments 19AA and 25AA may be due to an increase in strain rate when a thinned sample is deformed at a constant shear displacement.

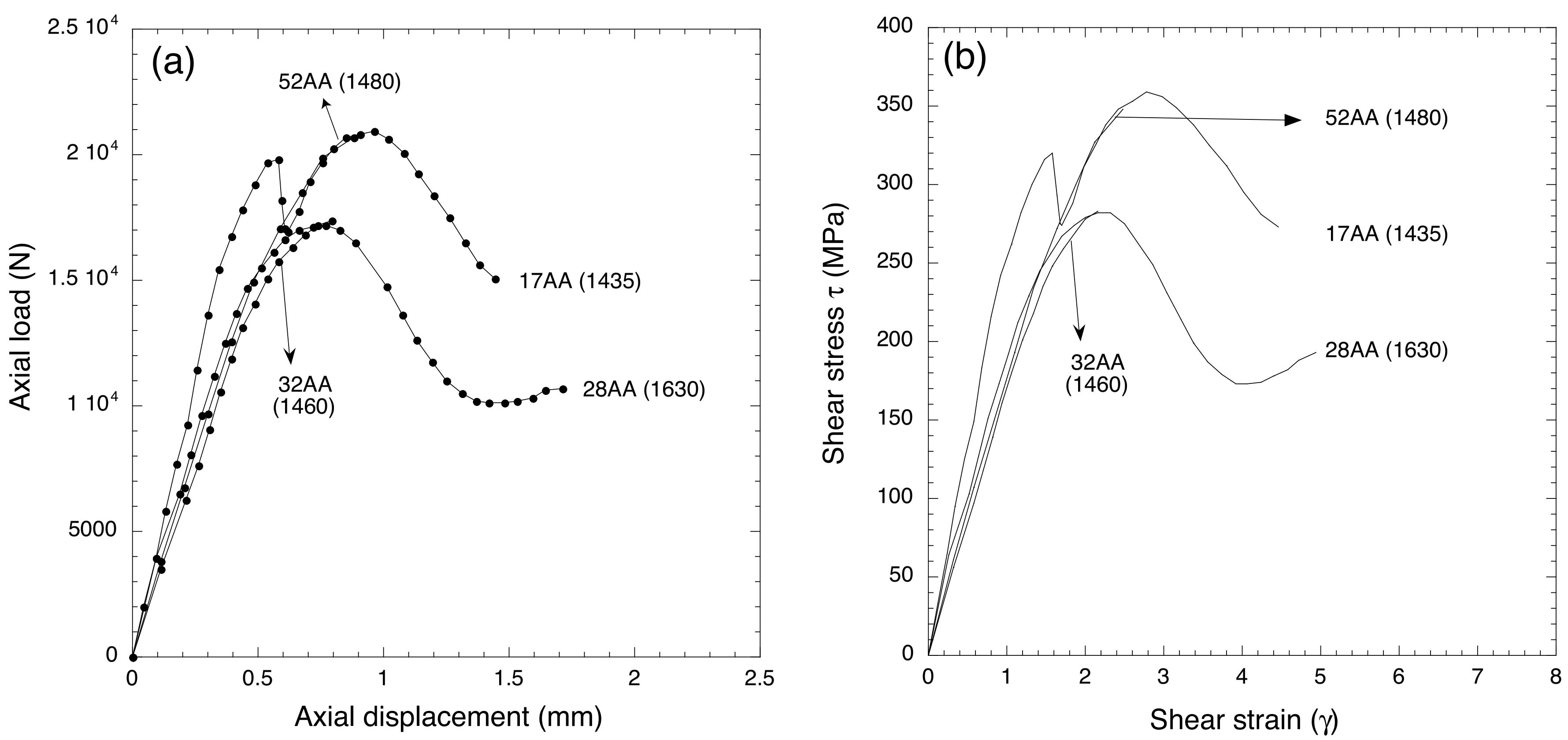

Figure B.5: Mechanical data of shear deformation experiments on ‘as-is’ anorthite-forsterite composites at 900°C and confining pressures of P_c=1435-1630 MPa. The run number and confining pressure (MPa in brackets) of the experiment is indicated for each curve. Strength of the samples as a function of (a) axial load (N) and axial displacement (mm) and (b) shear stress (MPa) and shear strain (γ). The late apparent strain hardening of experiment 28AA may be due to an increase in strain rate when a thinned sample is deformed at a constant shear displacement.

Fortran 77 source code for program RigS (Version 2.0)

```
C Program rigS2 (Standard Fortran 77 for MacOSX / Linux)
C
C The idea of this program is to read from a pre-existing input file:
C   ALL the sample specifications
C   ALL the necessary conversion factors and rig settings
C   ALL the calibrations
C   N, the number of (digitized) data points, and
C   F(N), D(N) = load and displacement in chart units
C
C   T(N) is calculated from D(N) on the basis that the displacement
C   rate is constant, i.e. D(N) is linear function of time.
C
C If the input file does not exist, it has to be generated using
C e.g., Edit II or and text editor.
C This input file is meant to be explicit, no implicit
C conversions or assumptions are "hidden" in the program.
C Upon reading, the chart units are converted to
C real t(n), f(n) and d(n), where t is in seconds,
C f is in Newtons and d is in millimeters

C 1. the displacement is corrected (rig stiffness); this correction can be zero.
C 2. the load is corrected (friction); this correction can be zero.
C   there is no separate jacket correction.
C 3. the differential stress is calculated for constant piston diameter
C   assuming constant cross-sectional area for the forcing blocks.
C 4. across the shear zones, the flattening strain, is calculated,
C   parallel to the shear zone, displacement and gamma, are calculated.
C 5. between consecutive points, flattening strain rate and shear strain rate
C   are calculated.
C 6. the shear stress is corrected using a contact area correction, taking into
C   account the decreasing area of contact between the forcing blocks.
C---> rigS assumes that the active contact area is the projection of the ellipse
C   parallel to the sample axis => max.contact at start of experiment.
C---> rigS2 assumes that the active contact area is the projection of the ellipse
C   normal to the shearzone => max.contact after slip equals shear zone thickness

C The output file contains a list of
C    t(n)  time (s)
C    fc(n)  load, after friction correction  (N)
C    dc(n)  displacement, after rig stiffness correction (mm)
C    s(n)  1/2 of differential stress (MPa)
C    v(n)  shear stress, after contact correction
C    o(n)  flattening strain across shear zone dth/th0 (%)
C    om(n)  magnitude of flattening strain across shear zone
C    ot(n)  rate of flattening strain magnitude (multiples of 10-6 s-1)
C    g(n)  shear strain gamma
C    gm(n)  strain magnitude from shear strain
C    gt(n)  shear strain rate (multiples of 10-6 s-1)
C From this file various plots can be generated e.g., using Kaleidagraph
C
C This program has been developed from a previous version of rigC,
C which has been compiled (copied and pasted) from a number of
C precursor programs (such as RIGCX etc.) written for the Griggs
C apparatus at Brown Univ. and from another program (RIG) written for
C the Heard apparatus at ETH Zürich.
C
C Brown, August 2001  RH
C adapted for MacOSX November 2003
C new thinning correction August 2004


      program rigS2
*     creates stress-strain curves from digitzed coordinates
*     of load-time and dislacement-time records

```

```
*---from input file
*---sample identification
*   samplename   name of sample (text)

*---sample geometry
*   sdia       sample diameter (mm)
*   alfa       angle of precut with axis
*   th0        initial thickness of shear zone
*   thf        final thickness of shear zone

*---starting points (hit points)
*   d0,f0      starting values of displacment and load in chart units

*---conversion factors
*   gspeed     gear speed (displacement rate)
*   convd      chart units -> displacement (mm)
*   convf      chart units -> load (N)

*---calibrations
*   distor     distortion of rig mm / N
*   friction   friction correction N / mm

*---no.of data points
*   n  number of d/f data points

*---data points
*   F  load (y coordinate) in chart units
*   D  displacement (y coordinate) in chart units
*   NOTE !!!  F and D have to be defined for the same T values

*---variable names and factors after read & conversion

*   t  time (x coordinate), true time (s)
*   f  load (y coordinate), uncorrected (kN)
*   d  displacement (y coordinate), uncorrected (mm)

* variables used
      dimension t(200), f(200), d(200), fc(200), dc(200)
      dimension s(200), a(200), g(200), gt(200), v(200)
      dimension o(200), om(200), ot(200),gm(200)
      dimension dz1(200), dz2(200), th(200), ds(200)
      character*80 header, dummy
      character*40 infile, outfile

      data nmax / 200/
      data pi / 3.14159/
      slipcorr = 1

*   ask file names
      write(6,*) ' filename of input file:'
      read(5,'(a)') infile
      write(6,*) ' filename of output file:'
      read(5,'(a)') outfile

*  header for output file
      write(6,'(a)') ' header for output file > '
      read (5, '(a)') header

*   open file
      open(unit=1,file=infile, status='OLD',
     .    form='formatted', access='sequential')
      read(1,'(a)') dummy               ! "filename"
      read(1,'(a)') dummy               ! "sdia, alfa, th0, thf"
      read(1,*)    sdia, alfa, th0, thf
      write(6,*)    sdia, alfa, th0, thf
```

```
  read(1,'(a)') dummy              ! "d0,f0"
  read(1,*)    d0,f0
  write(6,*)    d0,f0
  read(1,'(a)') dummy              ! "gspeed, convd, convf"
  read(1,*)    gspeed, convd, convf    ! 1.834E-05 mm/s !  10-6 gear
  write(6,*)    gspeed, convd, convf
  read(1,'(a)') dummy              ! "distor, friction"
  read(1,*)    distor, friction       ! 8.42E-06 mm/N !  1.05E-03 "/kbar (1976 T.Tullis)
  write(6,*)    distor, friction       ! 922.65 N/mm !  .01848 slope (w997)
  read(1,'(a)') dummy              ! "n"
  read(1,*)    n
  write(6,*)    n
  read(1,'(a)') dummy              ! "d(i), f(i)"
  do i=1,n
    read(1,*) d(i), f(i)
    write(6,*) d(i), f(i)
  enddo

*  close file
  close (unit=1)
  if (n.ge.200) write(6,'(a)') ' file is too long, max.no. = 200'
  if (n.ge.200) go to 9999

*  conversions
  do k=1,n
    i=n+1-k
    d(i+1)= (d(i)-d0)*convd
    f(i+1)= (f(i)-f0)*convf
    t(i+1)=  d(i+1)/gspeed
  enddo

  t(1)=0.
  f(1)=0.
  d(1)=0.
  n=n+1

  write(6,'(a)') ' t(i) sec, d(i) mm, f(i) N'
  do i=1,n
    write(6,*) t(i), d(i), f(i)
  enddo

*  convert
*1---- rig distortion: d -> dc
  do i=1,n
    dc(i) = d(i)-f(i)*distor
  enddo

*2---- friction: f -> fc (using uncorrected d)
  do i = 1,n
    fc(i) = f(i)-d(i)*friction
  enddo

*3---- load to differential stress: fc -> s
  r = 0.5 * sdia
  area = 3.14159 * r * r  !   r in mm2
*    N/mm2 = MPa   since  N/m2 = Pa
  do i=1,n
    s(i) = fc(i) / area
  enddo

*4---- strain calculations
*4a--- thickness correction for shear zone

* final (total) values for dz1, dz2, dr
  do i=1,n
```

```
        th(i)=th0
     enddo
     alfa = alfa * pi/180.
     sinalfa = sin (alfa)
     cosalfa = cos (alfa)
     tanalfa = sinalfa/cosalfa

*  find proportion (dz1(i) : dc(i)) from final (dz1tot : dc(n))
     dz1tot = (th0-thf) / sinalfa
     proportion = dz1tot / dc(n)
     do i=1,n
        dz1(i) = proportion * dc(i)
        dz2(i) = dc(i) - dz1(i)
        th(i)  = th0 - dz1(i) * sinalfa
        ds(i)  = dz2(i) / cosalfa
        g(i)   = ds(i) / th(i)
     enddo


*4b--- flattening strain
     do i=1,n
        o(i) = (th0-th(i))/th0
     enddo

*4c--- total strain magnitude
     write(6,*) ' dz1(i),th(i),dslip(i),g(i),s(i),o(i),om(i),gm(i)'
     do i=1,n
        om(i) = smag(o(i))
        gm(i) = smags(g(i))
        write(6,'(8f10.4)')
     . dz1(i),th(i),ds(i),g(i),s(i),o(i),om(i),gm(i)
     enddo

*5--- strain rate between two consecutive points
     ot(1) = 0.
     gt(1) = 0.
     do i=1,n-1
        j=i+1
        tdif=t(j)-t(i)
        if(tdif.ne.0.) ot(j) = (o(j)-o(i))/tdif
        if(tdif.ne.0.) gt(j) = (g(j)-g(i))/tdif
     enddo

*6--- slip correction (="area" correction) for reduced piston overlap
*    assuming max. overlap occurs after slip = 1*thickness of sample (if 45°)
*    or else slip necessary to oppose corresponding edges at right angle
*    (after suggestion by Terry Tullis 19.8.2004)
     if (slipcorr.eq.0) go to 1010
     do i=1,n
        slip = th(i)/tanalfa
        contact = (ds(i) - slip)/ (sdia / sinalfa)
        v(i) = 0.5 * s(i) / ACF(contact)
C    write(6,*) ' th, slip, contact, acf ', th(i), slip, contact, ACF(contact)
     enddo

1010 continue

*  write output file
     open(unit=1, file=outfile, status='new',
     .    form='formatted', access='sequential')

*  time - displacement - force - sigma - tau
*  flattening strain (%) - fl. strain magnitude
*  gamma - flat rate - gamma rate
*  last two (*1000)  times thousand = parts per thousand "ppt"
```

```
*  and (*1'000'000)  times million = parts per million "ppm"

   write(1,'(1x,a)') outfile
   write(1,'(1x,a)') header
   write(1,3000)
3000 format(' t(s)',t10,'d(mm)',t20,'F(N)',t30,'sig(MPa)',
    . t40,'tau(MPa)',t50,'flat(%)',
    . t60,'fl_mag()',t70,'gamma()',t80,'g_mag()',
    . t90,'fl_rate(-6s-1)',t105,'g_rate(-3s-1)'/)

   do i=1,n
      o(i)=o(i)*100
      ot(i)=ot(i)*1000000
      gt(i)=gt(i)*1000
      write(1,'(11e12.5)')
    .  t(i),dc(i),fc(i),s(i),v(i),o(i),om(i),g(i),gm(i),ot(i),gt(i)
   enddo
   close(unit=1)
9999 continue

   end

*  function smag strain mag from shortening strain delta_l/l0
   function smag(del)
   smag = 0.
   if(del.le.0.0) go to 100
   e    = 1.-del
   e1   = alog(e)
   e2   = alog(sqrt(1./e))
   e3   = e2
   e1e2 = e1-e2
   e2e3 = e2-e3
   e3e1 = e3-e1
   oct  = (e1e2*e1e2)+(e2e3*e2e3)+(e3e1*e3e1)
   smag= 0.57735*sqrt(oct)
100   return
   end

*  function smags  strain mags from gamma of simple shear
   function smags(g)
   smags = 0.
   if(g.le.0.0) go to 100
   qe   = 0.5*(g*g+2.+g*sqrt(g*g+4.))
   e    = sqrt(qe)
   e1   = alog(e)
   e2   = alog(1./e)
   e3   = 0.
   e1e2 = e1-e2
   e2e3 = e2-e3
   e3e1 = e3-e1
   oct  = (e1e2*e1e2)+(e2e3*e2e3)+(e3e1*e3e1)
   smags= 0.57735*sqrt(oct)
100   return
   end

*  function ACF
*  3rd order polynomial fit to plot profile of ACF of circle (NIHImage)
*  modified to calculate ACF of negative x   20.8.04
   function ACF(x)
   if(x.lt.0.) x=-x
   acf= 1.00 - 1.2082*x - 0.19134*x*x + 0.39461*x*x*x
   return
   end

```

Input template for program RigS (Version 2.0)

```
[samplename]
sdia (mm)                     alpha (°)                     thick0 (mm)          thickfinal (mm)
[sample diameter]             [shear angle]                 [initial thickness]  [final thickness]
d0 (chartdiv)                 f0 (chartdiv)
[displacement at hitpoint]    [force at hitpoint]
gearspeed (mm/s)              convd (mm/chartdiv)           convf (N/chartdiv)
[gearspeed]                   [conversion displacement]     [conversion force]
distortion (mm/N)             friction (N/mm)
[distortion]                  [friction]
n
[number of data points from chart record]
d(i)      f(i)
[list datapoints, displacement force]
[displacement force]
[displacement force]
[displacement force]
```

Input example for program RigS (Version 2.0)

```
W978
sdia (mm)                     alpha (°)                     thick0 (mm)          thickfinal (mm)
6.231                         45.0                          0.491                0.415
d0 (chartdiv)                 f0 (chartdiv)
21.50                         32.60
gearspeed (mm/s)              convd (mm/chartdiv)           convf (N/chartdiv)
1.834E-05                     0.0254                        395.87
distortion (mm/N)             friction (N/mm)
8.42E-06                      992.65
n
14
d(i)      f(i)
25.00     41.00
29.00     51.10
32.90     61.00
36.50     71.00
40.10     78.30
44.10     83.40
48.50     85.90
50.50     86.10
53.00     85.80
57.50     82.50
62.50     77.00
67.40     72.00
72.10     68.70
76.50     67.00
```

Output example of program RigS (Version 2.0)

```
    W978
    t(s)  d(mm)       F(N)  sig(MPa)  tau(MPa)    flat(%)   fl_mag()   gamma()    g_mag() fl_rate(-6s-1) g_rate(-3s-1)

    0.00   0.00       0.00      0.00      0.00       0.00       0.00      0.00       0.00           0.00          0.00
 4847.30   0.06    3237.10    106.16     56.25       0.74       0.01      0.16       0.11           1.52          0.03
10387.00   0.13    7134.50    233.97    122.32       1.56       0.02      0.35       0.24           1.48          0.03
15788.00   0.19   10955.00    359.27    185.43       2.35       0.03      0.53       0.37           1.48          0.03
20774.00   0.25   14823.00    486.11    248.11       3.05       0.04      0.69       0.48           1.41          0.03
25760.00   0.32   17622.00    577.91    291.24       3.86       0.05      0.88       0.60           1.62          0.04
31300.00   0.40   19540.00    640.81    322.95       4.89       0.06      1.12       0.76           1.84          0.04
37394.00   0.51   20419.00    669.63    344.16       6.13       0.08      1.43       0.94           2.05          0.05
40164.00   0.56   20448.00    670.57    348.01       6.74       0.09      1.58       1.02           2.18          0.05
43626.00   0.62   20266.00    664.61    349.30       7.52       0.10      1.78       1.13           2.25          0.06
49858.00   0.75   18846.00    618.04    333.09       9.03       0.12      2.17       1.33           2.43          0.06
56783.00   0.89   16543.00    542.51    301.30      10.78       0.14      2.64       1.54           2.53          0.07
63569.00   1.03   14440.00    473.55    271.06      12.49       0.16      3.12       1.74           2.51          0.07
70079.00   1.16   13015.00    426.82    251.44      14.06       0.19      3.58       1.90           2.42          0.07
76172.00   1.28   12231.00    401.11    242.69      15.48       0.21      4.00       2.04           2.33          0.07
```

Appendix C

Analytical data

C.1 Electron Microprobe

This section contains the compositions of Blumone gabbro anorthite and Åheim dunite olivine. All measurements were obtained with a JEOL JXA-8600 Electron Microprobe, 15 kV acceleration voltage and the PROZA Correction. Standardisation for anorthite analyses was made using a defocused beam. Anorthite was analysed in a thin section of the Blumone gabbro hand sample that was used as the source rock for the anorthite in this study. Åheim dunite olivine was measured in the forcing blocks (FB) and sample shear zone (SZ) of samples W1028, W1040 and W978.

Table C.1: Composition of Blumone gabbro anorthite

Sample	Blumone gabbro hand specimen										
Weight per cent oxides											**Average**
SiO_2	45.11	44.96	45.36	45.39	45.49	45.57	44.77	45.52	45.09	45.30	**45.26**
FeO	0.45	0.77	0.47	0.72	0.52	0.65	0.38	0.41	0.86	0.32	**0.56**
CaO	18.46	18.38	18.58	18.67	18.44	18.38	18.47	18.63	17.64	18.59	**18.42**
MgO	0.03	0.04	0.05	0.03	0.04	0.02	0.03	0.04	0.64	0.02	**0.09**
Na_2O	0.62	0.93	0.93	0.92	1.03	1.01	0.83	0.91	0.99	0.81	**0.90**
K_2O	0.00	0.04	0.02	0.00	0.01	0.02	0.02	0.01	0.04	0.01	**0.02**
Al_2O_3	35.18	34.26	34.43	34.64	34.71	34.58	34.86	35.27	34.57	35.25	**34.78**
MnO	0.03	0.00	0.03	0.08	0.00	0.00	0.00	0.00	0.01	0.00	**0.02**
Total	99.88	99.38	99.87	100.45	100.24	100.23	99.36	100.79	99.84	100.30	**100.03**
Numbers of ions based on the basis of 8O											
Si	2.083	2.093	2.099	2.091	2.096	2.101	2.081	2.085	2.087	2.084	**2.090**
Fe	0.017	0.030	0.018	0.028	0.020	0.025	0.015	0.016	0.033	0.012	**0.021**
Ca	0.913	0.917	0.921	0.922	0.910	0.908	0.920	0.914	0.875	0.916	**0.912**
Mg	0.002	0.003	0.003	0.002	0.003	0.001	0.002	0.003	0.044	0.001	**0.006**
Na	0.056	0.084	0.083	0.082	0.092	0.090	0.075	0.081	0.089	0.072	**0.080**
K	0.000	0.002	0.001	0.000	0.001	0.001	0.001	0.001	0.002	0.001	**0.001**
Al	1.915	1.880	1.878	1.881	1.885	1.879	1.909	1.904	1.886	1.911	**1.893**
Mn	0.001	0.000	0.001	0.003	0.000	0.000	0.000	0.000	0.000	0.000	**0.001**
Total	4.987	5.010	5.005	5.009	5.007	5.005	5.003	5.003	5.016	4.997	**5.004**
Normalised mol per cent plagioclase end members											
An	94	91	92	92	91	91	92	92	91	93	**92**
Ab	6	8	8	8	9	9	8	8	9	7	**8**
Or	0	0	0	0	0	0	0	0	0	0	**0**

Table C.2: Composition of Åheim dunite olivine

Sample	W1040 SZ	W1040 FB	W1028 FB	W1028 FB	W1028 FB	W1028 FB	W1028 SZ	W978 SZ	W978 SZ	W978 SZ	
Weight per cent oxides											**Average**
SiO_2	41.01	41.36	41.46	40.96	41.00	41.33	41.55	40.94	40.90	41.24	**41.18**
FeO	6.71	7.58	7.11	7.49	7.63	7.29	7.34	7.37	6.99	7.55	**7.31**
CaO	0.06	0.01	0.00	0.04	0.04	0.00	0.16	0.09	0.13	0.14	**0.07**
MgO	50.99	51.30	51.28	50.77	50.60	51.22	51.06	50.78	51.11	50.56	**50.97**
Na_2O	0.00	0.00	0.00	0.03	0.01	0.01	0.00	0.00	0.00	0.01	**0.01**
K_2O	0.00	0.01	0.00	0.00	0.00	0.00	0.00	0.00	0.00	0.01	**0.00**
Al_2O_3	0.00	0.00	0.00	0.00	0.00	0.00	0.00	0.00	0.00	0.00	**0.00**
MnO	0.09	0.00									**0.05**
Total	98.86	100.26	99.85	99.29	99.28	99.85	100.11	99.18	99.13	99.51	**99.57**
Numbers of ions based on the basis of 4O											
Si	1.002	0.999	1.003	0.999	1.001	1.001	1.004	1.000	0.998	1.004	**1.001**
Fe	0.137	0.153	0.144	0.153	0.156	0.148	0.148	0.150	0.143	0.154	**0.149**
Ca	0.002	0.000	0.000	0.001	0.001	0.000	0.004	0.002	0.003	0.004	**0.002**
Mg	1.856	1.848	1.850	1.847	1.841	1.850	1.839	1.848	1.859	1.835	**1.847**
Na	0.000	0.000	0.000	0.001	0.000	0.000	0.000	0.000	0.000	0.000	**0.000**
K	0.000	0.000	0.000	0.000	0.000	0.000	0.000	0.000	0.000	0.000	**0.000**
Al	0.000	0.000	0.000	0.000	0.000	0.000	0.000	0.000	0.000	0.000	**0.000**
Mn	0.002	0.000	0.000	0.000	0.000	0.000	0.000	0.000	0.000	0.000	**0.000**
Total	2.998	3.001	2.997	3.001	2.999	2.999	2.996	3.000	3.002	2.997	**2.999**
Normalised mol per cent olivine end members											
Fo	93	92	93	92	92	93	93	92	93	92	**93**
Fa	7	8	7	8	8	7	7	8	7	8	**7**

C.2 FTIR Spectrometry

This section contains unprocessed infrared adsorption measurements of hydroxyl in olivine of Åheim and Balsam Gap dunite forcing blocks. These measurements were used to determine the relative differences in water content between the samples. Measurements were made in a 1000-4000 cm^{-1} wave number range at room temperature using a Brukner High Resolution FTIR spectrometer at the Bayerisches Geoinstitut (Germany). Doubly polished sections of ~0.1 mm in thickness were used with aperture 50-100 µm and 100 scans. A poly-chlortrifluor-ethylen oil was applied to increase the thickness around the sample. Sample 34AA was analysed at the Institute of Mineralogy, University of Hannover (Germany), using a ~0.1-0.2 mm thick section, 50 scans and an aperture of 60*60 µm.

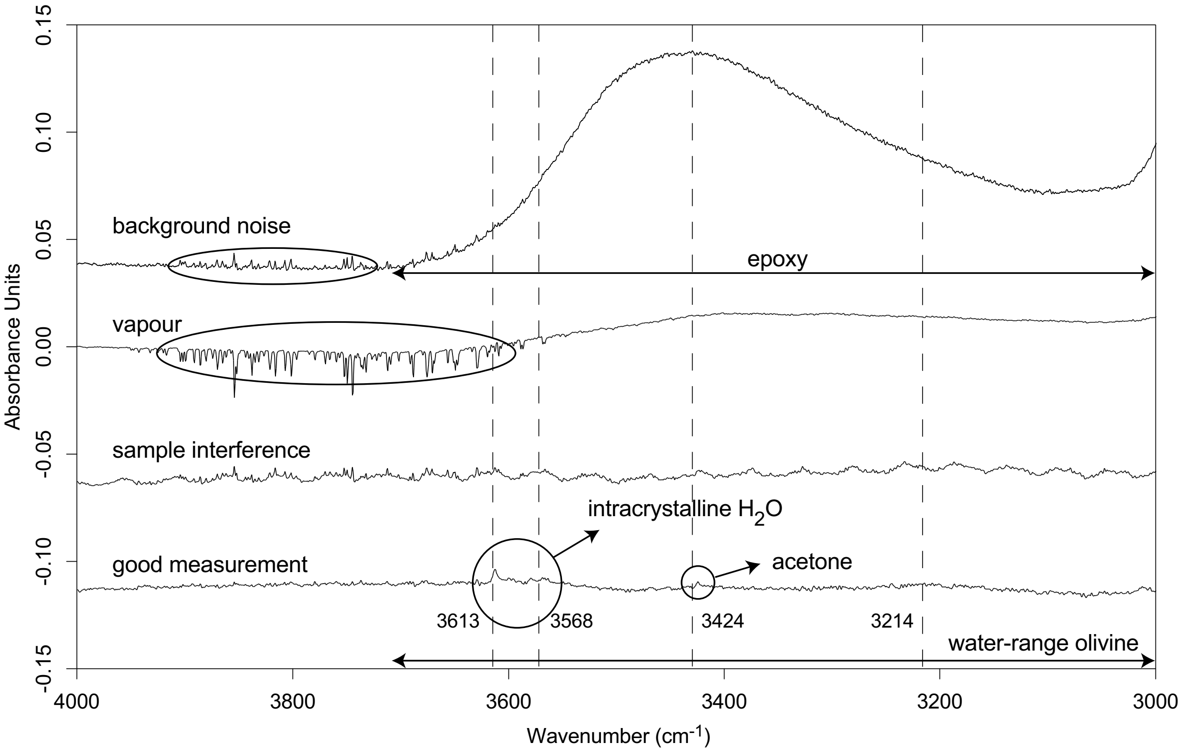

Figure C.1: General features to the FTIR spectra in the 3000-4000cm^{-1} wave number range.

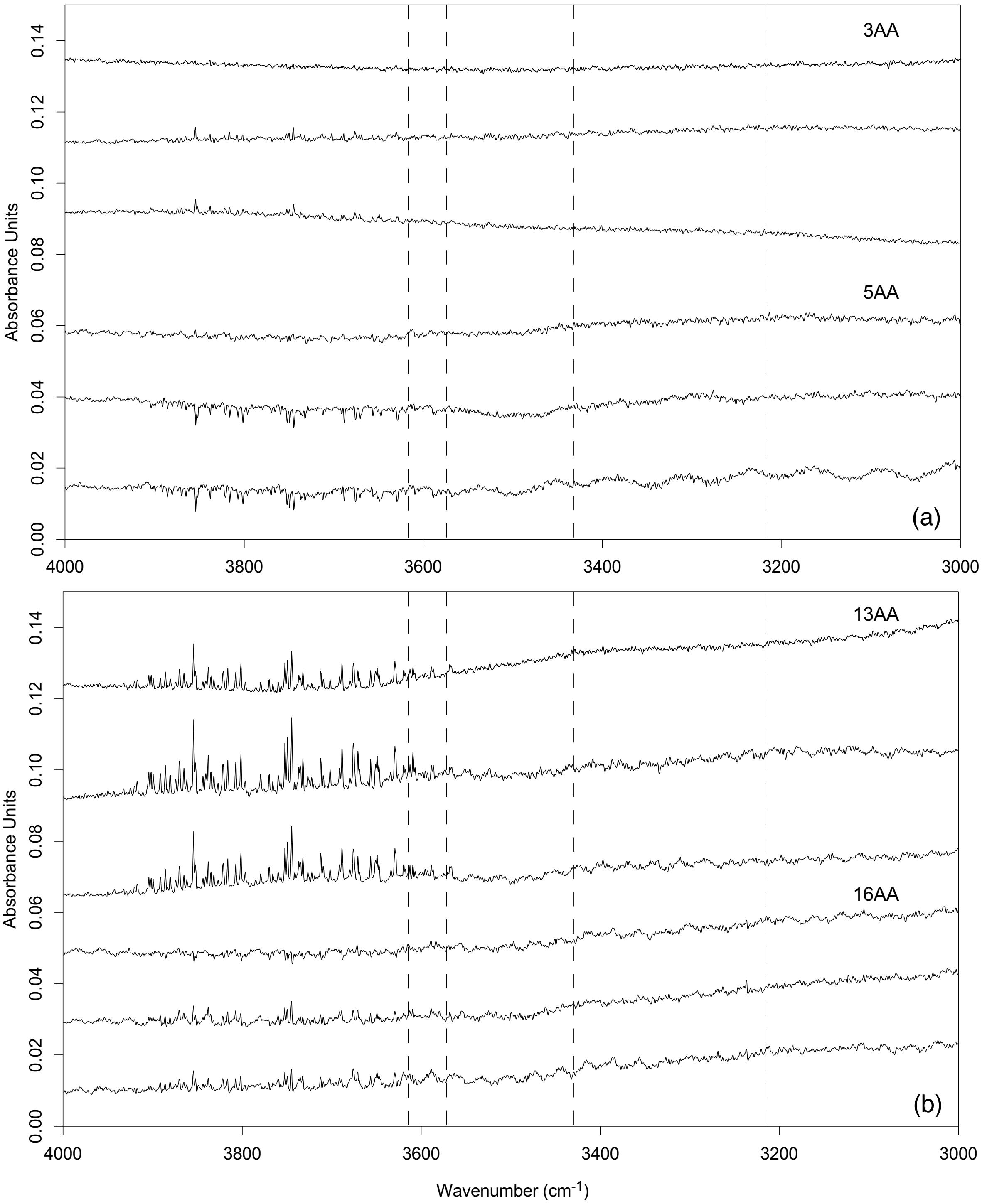

Figure C.2: FTIR spectra of hot pressed An-Fo samples with Balsam Gap forcing blocks. (a) Dried samples and forcing blocks (6 hrs, 1000°C). (b) As-is samples (>72 hrs, oven dried 110°C) and dried forcing blocks (24 hrs, 1000°C).

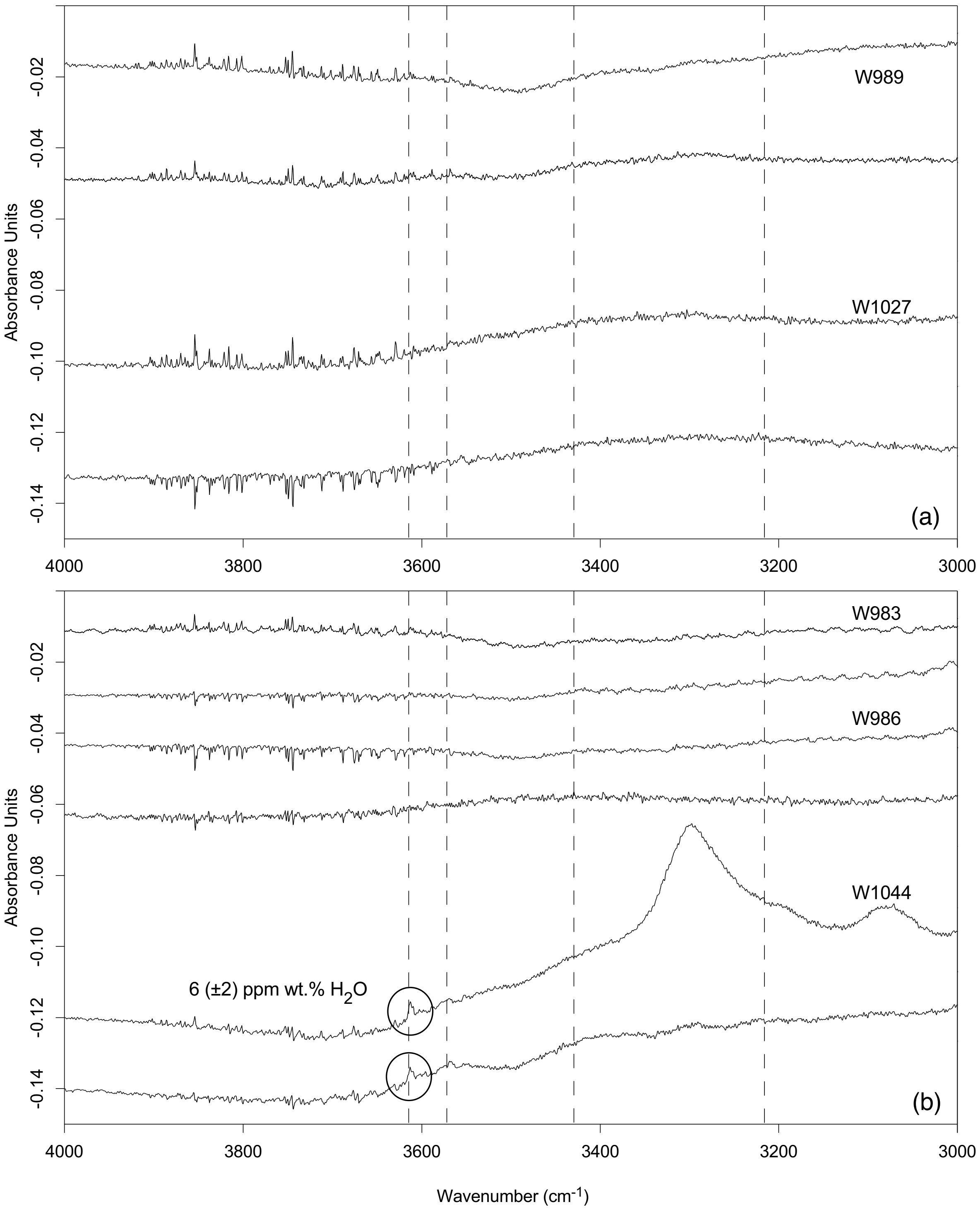

Figure C.3: FTIR spectra of deformed samples. (a) Pure olivine experiments with dried samples and forcing blocks (6-14 hrs, 1000°C). (b) Lab-Fo experiments with dried samples and forcing blocks (6-12 hrs at 1000°C).

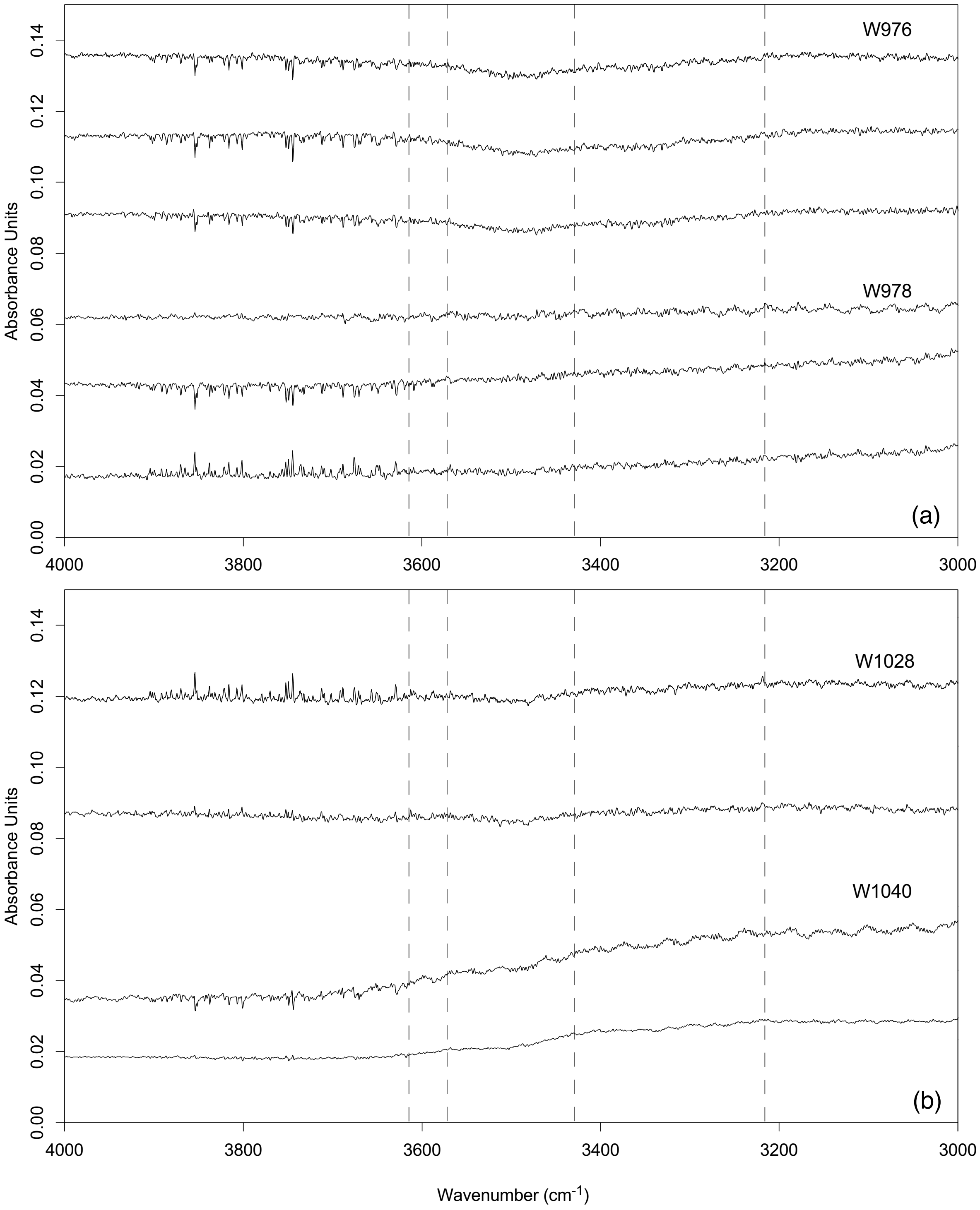

Figure C.4: FTIR spectra of deformed An-Fo samples. (a) Dried samples and Balsam Gap forcing blocks (6 hrs, 1000°C). (b) Dried samples and Åheim forcing blocks (12 hrs, 1000°C).

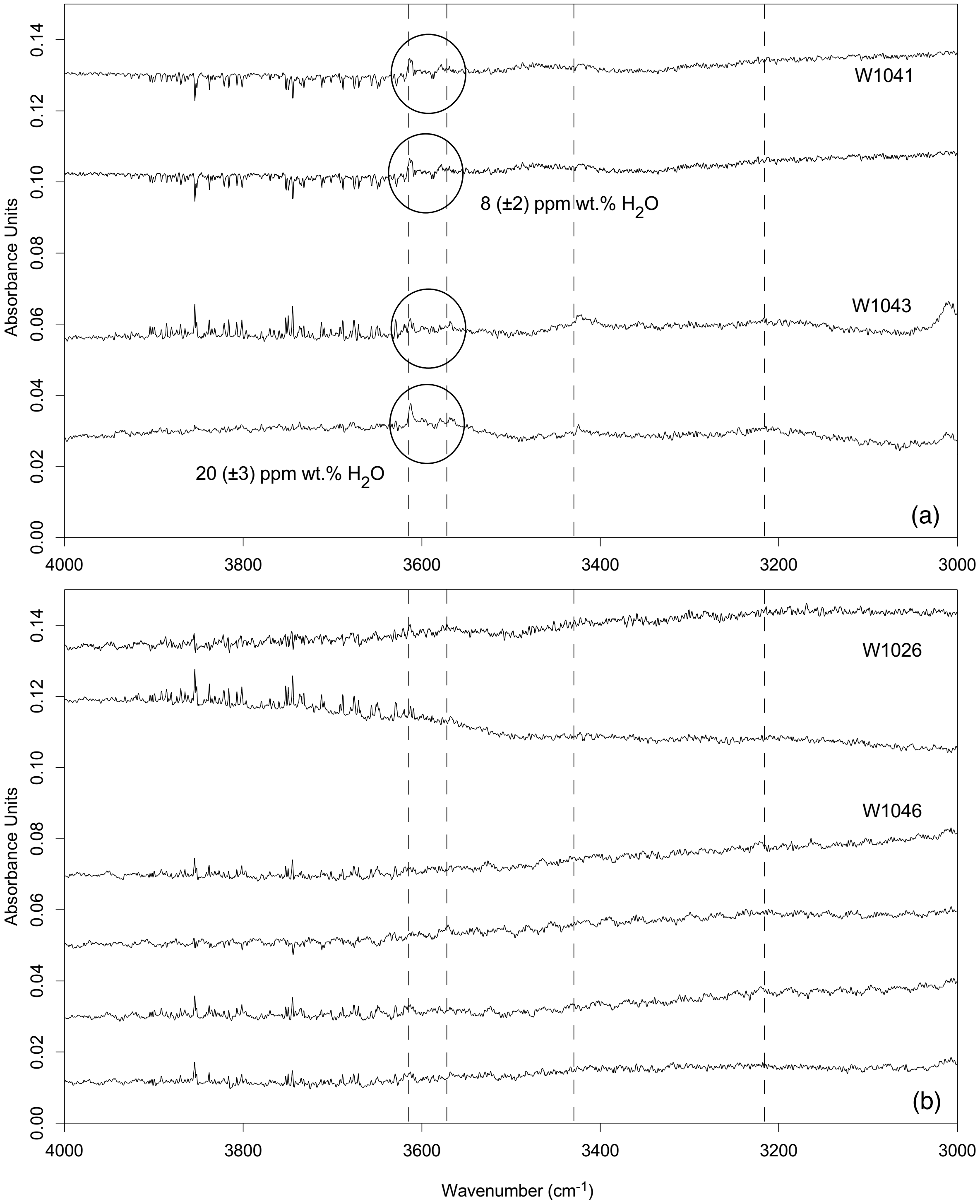

Figure C.5: FTIR spectra of deformed (a) and hydrostatic (b) An-Fo samples with Åheim forcing blocks. Samples and forcing blocks were dried for 12 hrs at 1000°C.

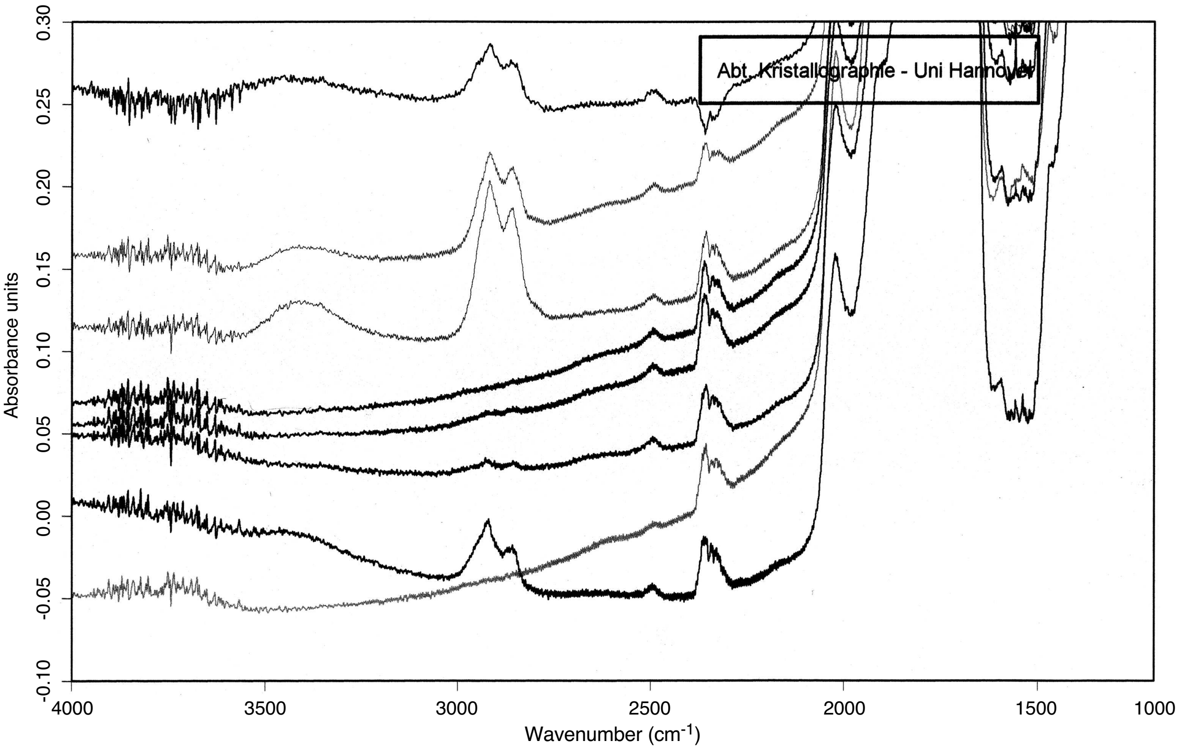

Figure C.6: FTIR spectra of hydrostatic An-Fo sample 34AA, measured at the Institute of Mineralogy, University of Hannover (Germany). As-is sample (>72 hrs, oven dried 110°C) and dried forcing blocks (24 hrs, 1000°C).

Acknowledgements

I am grateful to many people for help, both direct and indirect, during my PhD research. First and foremost, I want to thank my supervisor Holger Stünitz for his help and encouragement. His enthusiasm and knowledge in the wide range of combined deformation processes and metamorphism were a source of inspiration. Holger has an invaluable patience and I appreciated that he allowed me to run into his office with numerous questions, regardless of their importance. Halfway through my PhD, I participated in setting up the rock deformation laboratory at the department of Earth Sciences in Basel. Holger's motivation to get this laboratory up and running made it possible to complete the experiments that I required for the thesis. Holger also performed all the transmission electron microscope work in this thesis, which was indispensable for the decisive interpretations of this study.

I worked for five months at Brown University in the first two summers of my PhD-research. Jan Tullis extensively introduced me to laboratory work and experimental rock deformation. My experiences at Brown were the basis for the success of this study, and important for the subsequent set-up of the laboratory at Basel. I thank Jan for making me feel very welcome at Brown. She has an overflowing and encouraging energy for science, and she always found time to discuss my work by email, at conferences or at Brown, for which I am ever thankful.

I want to express my gratitude to Renée Heilbronner for all the discussions and work on our published strain analysis paper. Renée introduced me to many new aspects of image analysis and the interpretation of mechanical data and strain. I enjoyed the microstructure-group dinners at Renée and Holger's house, which were pleasant distractions from the work at the university. Working together with Renée, Holger and Jan taught me many new aspects of how to look at microstructures and the physical processes in rocks. They reviewed all the manuscripts in this thesis and their contributions to the discussions significantly improved the final result.

I also thank Dick Yund for all his help and advice during my work at Brown Uni-

versity (from powder grinding to fixing burned power supplies). I loved the dinners at his house with hummingbirds in the garden. Many thanks go out to Peter Ulmer, who helped setting up this interesting project together with Holger. He gave a lot of good advice during the development of the rock deformation laboratory in Basel, and provided the Blumone gabbro that I used for the experiments.

My research and personal motivation benefited greatly from the scientific interest of and discussions with Martyn Drury, Hans de Bresser, Misha Bystricki, Ralph Milke, Rainer Abart, Christian di Capitani, Julie Newman, Karsten Kunze, James Jackson and Keith Priestley. I thank all of them.

I have been very lucky in receiving much technical support. Especially I would like to express my gratitude to Hans-Ruedi Rüegg for all his new ideas and help during the development of the lab at Basel. I thank Willie Tschudin and Bill Collins (thin sections), Sylvie Demouchy (FTIR), Lukas Keller and Romain Bousquet (Electron Microprobe), Heinz Hürliman (sample preparation), Thomas Fisher and Claude Schneider (electrical engineering) and Daniel Matthys and Marcel Duggelin (SEM). I thank Joelle Glanzmann and Verena Scheuring for assisting me in various administrative problems and in the library.

The support and encouragement of many friends has been indispensable. I thank Auke Barhoorn for his friendship and our discussions on our PhD-topics. It was great to share our PhD's together, and being distracted from them as well during skiing, walking and other trips in Switzerland.

I am grateful to all my fellow PhD-colleagues and the students at the Geological Institute of Basel. I remember lots of good fun during parties in the institute and the town centre, game-evenings, cheese fondue, barbecues, skiing and climbing. I would particularly like to thank Nils Oesterling for helping out in many aspects and I enjoyed his company and fun in the office. I also thank Nynke Keulen for sharing the experiences in the lab and for taking care of my plants when I was on yet another trip to England. Caleb Holeoke, Giulio di Toro, David Goldsby and Michael Stipp are thanked for our enjoyable summers in Providence.

The love and support of my parents Arie and Anneke de Ronde and my sister Elma were of major importance to me during everything that happened over the last four years. They are always interested in the things that I do, and I am certain that this thesis will make them feel happy and proud. I thank Hans and Teja Deuss for their kindness and for making me feel at home during visits to Tilburg.

Finally, I would like to thank the one closest to me. Arwen has been a great source

of strength and inspiration all through my work. Her love, support and cheerfulness kept me going emotionally through the completion of this thesis and all those long years apart in different countries. My thesis would certainly not have existed without her. Now that it is finished, away with the long distance phones calls and frequent flyers, I am filled with happiness that we can share all our time together.

Curriculum Vitae

Name	Almar Arie de Ronde
Date of Birth	25 March, 1975
Place of Birth	Hoorn, the Netherlands
Nationality	Dutch

University education

2000–2004, University of Basel (Switzerland):
Research and teaching assistant at the Department of Earth Sciences.
PhD thesis: ‘Mineral reaction and deformation in plagioclase-olivine composites; an experimental study’
Advisors: PD. Dr. H. Stünitz, Prof. Dr. R. Heilbronner,
Prof. Dr. J. Tullis (Brown University, U.S.A.),

1994–1999, University of Utrecht (the Netherlands):
Doctoraal (MSc) study in Geology at the Department of Earth Sciences.
Thesis: ‘Reaction rims around garnet in the Ugelvik garnet peridotite (Western Gneiss Region, Norway)’
Advisors: Dr. M.R. Drury and Dr. H.L.M. van Roermund

Secondary education

Regionale Scholengemeenschap, Enkhuizen (The Netherlands)
1992–1994: Atheneum (V.W.O.)
1987–1992: H.A.V.O (pre-V.W.O.)

Primary education

1981–1987: O.B.S. ’t Padland, Venhuizen (the Netherlands)